## AD-A 133 626

RADC-TR-83-5
Final Technical Report
January 1983

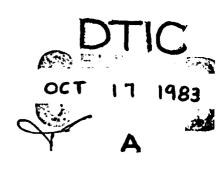


# ANALYSIS OF ELECTROMAGNETIC BACKSCATTER FROM AN INLET CAVITY CONFIGURATION

The Ohio State University

Prabhakar H. Pathak Ching-Chao Huang C. Y. Lai David L. Moffatt

APPROYED FOR PUBLIC RELEASE; DISTRIBUTION UNLIMITED



ROME AIR DEVELOPMENT CENTER Air Force Systems Command Griffiss Air Force Base, NY 13441

ITIE FILE COPY

This report has been reviewed by the RADC Public Affairs Office (PA) and is releasable to the National Technical Information Service (NTIS). At NTIS it will be releasable to the general public, including foreign nations.

RADC-TR-83-5 has been reviewed and is approved for publication.

APPROVED:

PHILIPP BLACKSMITH Project Engineer

APPROVED: Wiland Scheel

ALLAN C. SCHELL

Chief, Electromagnetic Sciences Division

FOR THE COMMANDER:

JOHN P. HUSS

Acting Chief, Plans Office

In P. There

If your address has changed or if you wish to be removed from the RADC mailing list, or if the addressee is no longer employed by your organization, please notify RADC (EECT), Hanscom AFB MA 01731. This will assist us in maintaining a current mailing list.

Do not return copies of this report unless contractual obligations or notices on a specific document requires that it be returned.

## UNCLASSIFIED

SECURITY CLASSIFICATION OF THIS PAGE (When Date Entered)

RADC-TR-83-5  4. TITLE (and Substitio)	BEFORE COMPLETING FORM
	N NO. 3. RECIPIENT'S CATALOG NUMBER
1. TITLE (and Subtitio)	3626
	S. TYPE OF REPORT & PERIOD COVERED
ANALYSIS OF ELECTROMAGNETIC BACKSCATTER FROM	Final Technical Report 1 Apr 80 - 1 Apr 82
AN INLET CAVITY CONFIGURATION	6. PERFORMING ONG. REPORT NUMBER
IIIII GOM TOOMITON	ESL 712661-4
: AUTHOR(a)	8. CONTRACT OR GRANT NUMBER(s)
Drobbokov U Dobbok C V I I	
Prabhaker H. Pathak C. Y. Lai Ching-Chao Huang David L. Moffatt	F19628-80-C-0056
PERFORMING ORGANIZATION NAME AND ADDRESS	10. PROGRAM ELEMENT, PROJECT, TASK AREA & WORK UNIT NUMBERS
The Ohio State University	61102F
Department of Electrical Engineering	2305J445
COlumbus OH 43212  CONTROLLING OFFICE NAME AND ADDRESS	12. REPORT DATE
	January 1983
Rome Air Development Center (EECT)	13. NUMBER OF PAGES
Hanscom AFB MA 01731	302
4. MONITORING AGENCY NAME & ADDRESS(II different from Controlling Offi	ce) 15. SECURITY CLASS, (of this report)
	UNCLASSIFIED
Same	15. DECLASSIFICATION/DOWNERADING
Same	154. DECLASSIFICATION/DOWNGRADING
6. DISTRIBUTION STATEMENT (of this Report)	15. DECLASSIFICATION/DOWNGRADING N/A
6. DISTRIBUTION STATEMENT (of this Report)  Approved for public release; distribution un  7. DISTRIBUTION STATEMENT (of the abetract entered in Block 20, 11 differen	N/A limited.
Approved for public release; distribution un	N/A limited.
6. DISTRIBUTION STATEMENT (of this Report)  Approved for public release; distribution un  7. DISTRIBUTION STATEMENT (of the shetrect entered in Block 20, 11 differen	N/A limited.
Approved for public release; distribution un  7. DISTRIBUTION STATEMENT (of the abstract entered in Block 20, if different  Same  8. SUPPLEMENTARY NOTES	ISA. DECLASSIFICATION/DOWNGRADING SCHEDULE N/A  limited.
Approved for public release; distribution un  7. DISTRIBUTION STATEMENT (of the abetract entered in Block 20, 11 different  Same  B. SUPPLEMENTARY NOTES  RADC Project Engineer: Ronald G. Newburgh (	ISA. DECLASSIFICATION/DOWNGRADING N/A  limited.  from Report)  EECT)
Approved for public release; distribution un  7. DISTRIBUTION STATEMENT (of the abetract entered in Block 20, If different Same  8. SUPPLEMENTARY NOTES  RADC Project Engineer: Ronald G. Newburgh (	ISA. DECLASSIFICATION/DOWNGRADING N/A  limited.  from Report)  EECT)
Approved for public release; distribution un  DISTRIBUTION STATEMENT (of the abetract entered in Block 20, If different  Same  Supplementary notes  RADC Project Engineer: Ronald G. Newburgh (  KEY WORDS (Continue on reverse side if necessary and identity by block nue  Uniform Geometrical Theory Of Diffraction	ISA. DECLASSIFICATION/DOWNGRADING N/A  limited.  ne (rom Report)  EECT)  nber)  Circular Waveguides
6. DISTRIBUTION STATEMENT (of this Report)  Approved for public release; distribution un  7. DISTRIBUTION STATEMENT (of the abetract entered in Block 20, if different  Same	ISA. DECLASSIFICATION/DOWNGRADING N/A  limited.  from Report)  EECT)

The electromagnetic backscatter from a simplified jet intake model is analyzed via the Uniform Geometrical Theory of Diffraction (UTD) ray method together with its modifications (at caustics) which are employed in conjunction with a self-consistent treatment of the multiple scattering method (MSM). The UTD analysis is chosen because it yields a solution which is simple, efficient, and accurate even for the dominant mode regime in the circular waveguide (or intake) region. Furthermore, the MSM which

DD 1 JAN 73 1473 EDITION OF 1 NOV 65 IS DESOLETE

UNCLASSIFIED

SECURITY CLASSIFICATION OF THIS PAGE (When Date Entered)

SECURITY CLASSIFICATION OF THIS PAGE(When Date Entered)

accounts for the wave interactions between the intake opening and blade discontinuity within allows one to isolate the dominant scattering mechanisms. Some interesting numerical results for the on- and off- axis RCS are presented as a function of the blade geometry, and are compared with corresponding RCS results and measurements for a hollow cylinder of finite length L with open and closed terminations. Some results for the RCS modulation spectrum resulting from blade rotation in the presence of a stator are also indicated. In addition, time domain responses have been obtained for the electromagnetic backscatter from the simple inlet model chosen here. The time domain response is synthesized from the high frequency ray based UTD-MSM solution which is used in conjunction with the Wiener-Hopf solutions for low frequencies. The low and high frequency responses are joined using rational function estimates. Furthermore, the dominant complex natural resonance of finite and open circular wave-guides have been extracted.

UNCLASSIFIED

SECURITY CLASSIFICATION OF THIP PAGE(When Date Entered)

## **ACKNOWLEDGEMENT**

The authors would like to thank Professor Leon Peters, Jr. for his helpful comments. Thanks are also due to Rockwell International for their financial support of some of the later phases of the work reported here.

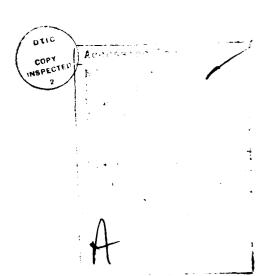


	TABLE OF CONTENTS	Page
INTRODU	CTION	1
PART I:	RAY ANALYSIS OF EM BACKSCATTER FROM A CAVITY CONFIGURATION	3
SECTION	1: PRELIMINARY DISCUSSION FOR PART I	4
SECTION	2: SELF-CONSISTENT MSM FORMULATION	15
SECTION	3: ANALYTICAL DEVELOPMENT OF THE ELEMENTS OF THE SCATTERING MATRICES IN MSM	30
Α.	Ray Analysis for [S <sub>11</sub> ]	32
	(i) First Order (or Singly) Diffracted Ray Contributions to [S11]	33
	(ii) Higher Order (or Multiply) Diffracted Ray Contributions to [S11]	39
В.	Ray Analysis for [S <sub>12</sub> ]	70
С.	Ray Analysis for [S <sub>21</sub> ]	98
0.	Ray Analysis for [S <sub>22</sub> ]	109
ε.	Ray Analysis for [S <sub>b</sub> ]	122
	a) [ $S_b$ ] for an Open Termination at $z=-L$	123
	b) [ $S_b$ ] for a Closed Termination at $z=-L$	123
	c) [Sb] for a Planar Termination at $z=-L$	124

	Page
d) $[S_b]$ for a Disc-Blade Termination at z=-L	128
SECTION 4: NUMERICAL RESULTS AND DISCUSSION	132
PART II: CANONICAL RESPONSE WAVEFORMS OF FINITE AND OPEN LOADED CIRCULAR WAVEGUIDES	161
SECTION 1: PRELIMINARY DISCUSSION FOR PART II	162
SECTION 2: SEMI-INFINITE OPEN CIRCULAR WAVEGUIDE	166
SECTION 3: FINITE CIRCULAR WAVEGUIDES WITH OPEN OR SHORT REAR TERMINATIONS	183
SECTION 4: INTERNALLY LOADED OPEN CIRCULAR WAVEGUIDES	205
4.1 Open Circular Waveguide	209
4.2 Shorted Open Circular Waveguide	212
4.3 Non-shorting Disc in Open Circular Waveguide	212
4.4 Planar Blade Geometry in Open Circular Waveguide (40 blades)	226
4.5 Planar Blade Geometry in Open Circular Waveguide (2 blades)	232
SECTION 5: COMPLEX NATURAL RESONANCES OF OPEN AND FINITE CIRCULAR WAVEGUIDES	241
SECTION 6: SUMMARY FOR PART II	<b>25</b> 3
CONCLUSIONS	256
APPENDIX A: SUMMARY OF CIRCULAR WAVEGUIDE MODES AND CUTOFF ka	260
APPENDIX B: INCLUSION OF ALL MULTIPLE INTERACTIONS ACROSS THE APERTURE	264
APPENDIX C: TO DETERMINE [S21] FROM [S12] USING THE RECIPROCITY THEOREM	270
APPENDIX D: RADAR RECOGNITION OF CAVITY STRUCTURES	274
REFERENCES	278

## LIST OF TABLES

TABLE			PAGE
PART	I:	RAY ANALYSIS OF EM BACKSCATTER FROM A CAVITY CONFIGURATION	
1		PROPERTIES OF MODES IN CIRCULAR WAVEGUIDES	72
2		NUMBER OF MODES INCLUDED VERSUS CPU TIME REQUIRED	138
PART	II:	CANONICAL RESPONSE WAVEFORMS OF FINITE AND OPEN LOADED CIRCULAR WAVEGUIDES	
3		COMPARISON OF RADAR CROSS SECTION (dB) OF EXACT SOLUTION (JOHNSON), ASYMPTOTIC SOLUTION (BOWMAN) AND MODIFIED ASYMPTOTIC SOLUTION (Eqn. 2-19, MOFFATT).	178
4		RESULTS FOR $L_{+}(k)$ AND $M_{+}(k)$ FOR THE $n=1$ CASE.	196
5		COMPLEX NATURAL RESONANCES EXTRACTED USING MODEL OF EQUATION (5-1) AND MOMENT METHOD SOLUTION OF BELOW CUTOFF REGION OF FINITE CIRCULAR GUIDE.	246

## LIST OF FIGURES

Figure		Page
1	A simplified jet intake model.	5
2	Geometry of a simple jet inlet-model with a planar stator-rotor combination within.	7
3	Backscattering from a finite hollow pipe which is open at $z=0$ and closed at $z=-L$ .	8
4	Backscattering from a finite hollow pipe with both ends open.	8
5	Scattering junctions I and II for the geometries in Figures 1-4.	16
6	Canonical scattering problem for determining $S_{11}$ and $S_{21} \boldsymbol{\cdot}$	16
7	Canonical radiation problem for determing $S_{12}$ and $S_{22}$ .	17
8	Canonical problem for determining $\ensuremath{S_b}$ associated with the configuration in Figures 1-4.	17
9	Multiple interactions between junctions (I) and (II) for calculating the total backscattered field.	26
10	Geometry of rays diffracted from point $\textbf{Q}_1$ and $\textbf{Q}_2$ on the edge.	35
11	Aperture and rim coordinates at z=0.	35
12	Mechanisms of 4 doubly diffracted rays across the aperture of the hollow circular cylinder.	42
13	The doubly diffracted ray for the equivalent current solution.	45
14	The relationship of $\phi'$ and $v'$ with $\theta$ varied from $10^\circ$ to $80^\circ$ in $10^\circ$ step.	47

Figure		Page
15	On-axis backscattering from the open end of a semi-infinite conducting hollow pipe.	53
16	Mechanisms of the scattering from the open end of a semi-infinite conducting hollow pipe.	57
17	Off-axis RCS (normalized to $\pi a^2$ ) of a semi-infinite, hollow, perfectly conducting circular with ka=7.261.	64
18	Off-axis RCS (normalized to $\pi a^2$ ) of a semi-infinite, hollow, perfectly conducting circular with ka=14.4.	66
19	On-axis RCS (normalized to $\pi a^2$ ) of a semi-infinite, hollow, perfectly-conducting circular cylinder with various terms included in UTD calculations.	68
20	Conversion of waveguide modal field into the conical ray field.	75
21	Diffraction from the rim of the perfectly conducting circular waveguide by an incident conical ray field.	76
22	Diffraction mechanism from a perfectly-conducting half plane.	88
23	Diffraction from a curved edge.	95
24	Radiation patterns of an open circular waveguide with ka=12.77.	99
25	Radiation patterns of an open circular waveguide based on UTD and its modifications.	102
26	Geometry for determining [S $_{21}$ ] from [S $_{12}$ ] using the reciprocity theorem.	107
27	Coupling into the circular waveguide due to a unit plane wave field incident on axis.	110
28	Total coupled transverse (to z) electric field along x or y at $z=-L$ for a unit plane wave incident on-axis.	111
29	Reflection from the open end of a circular waveguide.	113
30	Magnitude of the self reflection coefficient for a TE <sub>nm</sub> mode incident on an open-ended circular wavequide	120

Figure		Page
31	Magnitude of the self reflection coefficient for a TM <sub>nm</sub> mode incident on an open-ended circular waveguide.	121
32	Backscattering from a semi-infinite hollow pipe loaded with a dielectric material of relative permittivity $\epsilon_\Gamma$ in the region z<-L.	125
33	On-axis RCS (normalized to $\pi a^2$ ) of the simplified jet intake model with N blades attached to a circular disc as shown in Figure 1.	133
34	On-axis RCS (normalized to $\pi a^2$ ) of a hollow, perfectly conducting finite length circular cylinder open at the front end and closed (shorted) at the back end.	134
35	On-axis RCS (normalized to $\pi a^2$ ) of a hollow, perfectly conducting finite length circular cylinder open at both ends.	135
36	RCS (normalized to $\pi a^2$ ) of a finite length hollow metallic circular cylinder open at one end but closed at the other end.	140
37	RCS (normalized to $\pi a^2$ ) of a finite length hollow metallic circular cylinder open at one end but closed at the other end.	141
38	RCS (normalized to $\pi a^2$ ) of a semi-infinite hollow metallic circular cylinder open at one end but closed at the other end.	142
39	RCS (normalized to $\pi a^2)$ modulation from a jet intake model.	143
40	RCS (normalized to $\pi a^2)$ modulation from a jet intake model.	144
41	RCS (normalized to $\pi a^2)$ modulation from a jet intake model.	145
42	Power density frequency spectrum of the polarized backscattered electric field for the problem in Figure 2 with 0=40°, ka=3.8, number of stator vanes=60, number of rotor blades=30, disc radius b=0.2a, and the blade length c=0.9a.	150

igure		Page
43	Power density frequency spectrum of the backscattered electric field for the problem in Figure 2 with 0=0°, ka=3.8, number of stator vanes=40, number of rotor blades=40, disc radius b=0.2a, and the blade length c=0.9a.	152
44	Power density frequency spectrum of the backscattered electric field for the problem in Figure 2 with $\theta$ =0°, ka=3.8, number of stator vanes= 20, number of rotor blades=40, disc radius b=0.2a, and the blade length c=0.9a.	154
45	Power density frequency spectrum of the backscattered electric field for the problem in Figure 2 with $\theta$ =0°, ka=5, number of stator vanes=20, number of rotor blades=40, disc radius b=0.2a, and the blade length c=0.9a.	156
45	Power density frequency spectrum of the backscattered electric field for the problem in Figure 2 with $\theta$ =0°, ka=5, number of stator vanes=8, number of rotor blades=40, disc radius b=0.2a, and the blade length c=0.9a.	158
47	Finite circular waveguide, L=10a.	164
48	Coordinate system for Wiener-Hopf solution semi-infinite cylinder.	167
49	Inverse Laplace transform on cn-axis backscatter; asymptotic approximation.	171
50	Inverse Laplace transform of on-axis backscatter, comparing exact numerical results with asymptotic approximation.	173
51	On-axis normalized radar cross section for semi- infinite circular cylinder.	174
52	Modified impulse response of on-axis backscatter with asymptotic approximation, $\alpha t_0 = 8.$	176
53	Normalized axial radar cross section of finite hollow cylinders (open and shorted at far end), a circular disk and a semi-infinite circular waveguide.	184

rigure		Page
54a	On-axis backscatter impulse response from finite finite open circular cylinder.	186
54b	On-axis backscatter impulse response from finite circular cylinder shorted at the rear.	187
55a	Impulse response for finite open cylinder with direct diffraction from rear removed.	190
556	Impulse response for shorted finite cylinder with direct diffraction from rear removed.	191
56	Impulse response for shorted finite cylinder with direct and double diffraction from rear removed.	192
57	Coordinate system for scattering by shorted open circular waveguide.	194
58 <b>a</b>	Step response for open finite cylinder.	199
58b	Step response for shorted finite cylinder.	200
59a	Ramp response for open finite cylinder.	201
595	Ramp response for shorted finite cylinder.	202
60a	Impulse response due only to short inside circular semi-infinite waveguide.	203
60ъ	Step response due only to short inside circular semi-infinite waveguide.	204
61	Configurations of various loadings inside semi-infinite circular cylinder.	208
62a	Frequency spectrum (magnitude) of semi-infinite hollow cylinder.	210
62b	Frequency spectrum (phase) of semi-infinite hollow cylinder.	211
63a	Impulse response for semi-infinite hollow cylinder.	213
63b	Sten response for semi-infinite hollow cylinder.	214

igure		Page
64a	Impulse response for shorted semi-infinite cylinder.	215
64b	Step response for shorted semi-infinite cylinder.	216
65	Example of an incorrect impulse response due to incorrect rational function fit.	218
66a	Frequency spectrum (magnitude) for cylinder loaded with non-shorting disc showing behavior of rational function fit (solid line) inside and outside the unknown region.	219
ő6b	Frequency spectrum (phase) for cylinder loaded with non-shorting disc showing behavior of rational function fit (solid line) inside and outside the unknown region.	220
67a	Frequency spectrum (magnitude) for the non-shorting disc.	221
67b	Frequency spectrum (phase) for the non-shorting disc.	222
68a	Impulse response for semi-infinite cylinder loaded with non-shorting disc.	224
68b	Step response for <b>semi-</b> infinite cylinder loaded with non-shorting disc.	· 225
69	Impulse response due only to non-shorting disc inside semi-infinite cylinder.	227
70a	Frequency spectrum (magnitude) for cylinder loaded with a 40-blade planar geometry.	228
70b	Frequency spectrum (phase) for cylinder loaded with a 40-blade planar geometry.	229
71a	Impulse response for semi-infinite cylinder loaded with a 40-blade planar geometry.	230
71h	Step response for semi-infinite cylinder loaded with a 40-blade planar geometry.	231

Figu	re	Page
72	a Frequency spectrum (magnitude) for cylinder loaded with a 2-blade planar geometry.	233
72	b Frequency spectrum (phase) for cylinder loaded with a 2-blade planar geometry.	234
73	a Impulse response for semi-infinite cylinder loaded with a 2-blade planar geometry.	235
73	Step response for semi-infinite cylinder loaded with a 2-blade planar geometry.	236
74	Impulse response due only to 2-blade planar geometry inside cylinder with blades parallel to polarization of incident electric field.	237
74	b Impulse response due only to 2-blade planar geometry inside cylinder with blade at 45° with respect to polarization of incident electric field.	238
74	c Impulse response due only to 2-blade planar geometry inside cylinder with blades at 90° with respect to polarization of incident electric field.	239
75	Electric field lines for ${\sf TE}_{11}$ mode inside circular waveguide.	240
76	Poles extracted from impulse response from rim of finite waveguide.	243
<b>7</b> 7	<ul> <li>Poles extracted from impulse response from rear of finite waveguide with both ends open.</li> </ul>	244
78	Poles extracted from impulse response from rear of finith waveguide with rear end shorted.	245
79	Zeros fo 1-f <sub>1</sub> =0.	250
80	Zeros of 1+f <sub>1</sub> =0.	251

## INTRODUCTION

The radar cross section of jet engine configurations on modern aircraft is a most perverse problem analytically. An ability to predict the radar cross section of loaded cavity structures, even when such structures are only very crude models of the actual engine, has been seriously lacking. At the same time it is well known that above a certain spectral range the engine configuration largely controls the radar cross section of the aircraft over a large span of nose and often stern aspects. Recently, the radar signal modulation produced by the engines has become of important analytical concern. The research reported in this document on the radar cross section of a loaded cavity structure is felt therefore to answer significant needs of the Air Force.

Analysis of EM Backscatter from a Cavity Configuration contains the major thrust of our research and basically details an asymptotic frequency domain analysis of various loaded cavity structures. Part II, "Canonical Response Waveforms of Finite and Open Circular Waveguides" is essentially a time domain analysis of the same types of problems. Both Part I and Part II are self contained. The parts are interrelated however in the sense that results from one are used in the other. For

example, Part II reproduces a portion of the exact Wiener-Hopf computations for an open circular waveguide. These results were used to verify a portion of the theory in Part I. Conversely, frequency computations from the analysis in Part I are used in Part II as part of a Fourier synthesis procedure to obtain canonical response waveforms.

It is suggested that the reader peruse Part I and Part II in that order. Only when the real complexity of the problem is understood can the approximations used in Part II be appreciated. Both Part I and Part II have separate preliminary discussions and separate summaries. A final section of this report summarizes our main accomplishments and makes recommendations for future research.

## PART I

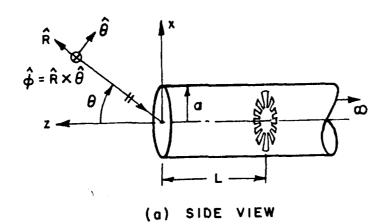
## RAY ANALYSIS OF EM BACKSCATTER FROM A CAVITY CONFIGURATION

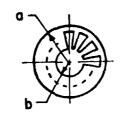
Ching-Chao Huang Prabhakar H. Pathak

### SECTION 1

## PRELIMINARY DISCUSSION FOR PART I

The jet inlet structure is a significant scatterer that must be taken into account when computing the radar cross section (RCS) of modern aircraft. While this is in general a difficult problem, it is strongly felt that this difficulty can be substantially reduced if one proceeds from relatively simple to more complex inlet geometries, and develops a thorough understanding of the basic scattering mechanisms involved in such geometries. These analyses can then be modified or extended so that a realistic analytical model of the actual inlet (or intake) should be obtainable. With the above view in mind, the low frequency RCS of a simplified jet inlet configuration is analyzed in this report. The method of analysis employed here is based on the Uniform Geometrical Theory of Diffraction (UTD) [1] ray technique and its modifications which are required within caustic regions, together with the self-consistent multiple scattering method (MSM). The modifications of the UTD at caustics which are incorporated in this work involve the use of equivalent currents and aperture integrals; it is noted that the aperture integrals referred to here are more closely associated with the Physical Theory of Diffraction (PTD) [24]. However. the PID in general can be shown to be related to the Geometrical Theory of Diffraction (GTD) [21] and its uniform version (UTD) [1] if one



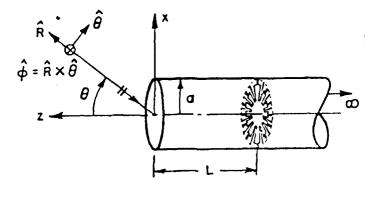


(b) FRONT VIEW

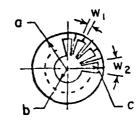
Figure 1. A simplified jet intake model.

evaluates the integrals of PTD asymptotically in the high frequency limit. Due to the latter relationship between GTD (UTD) and PTD, it is convenient to think of the use of equivalent currents and aperture integrals simply as modifications of the UTD at caustics, rather than as being a part of the PTD.

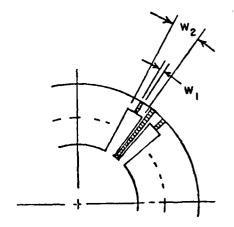
The simplified jet inlet model chosen here consists of a semi-infinite, perfectly-conducting hollow circular pipe (or waveguide) with a planar periodic blade structure placed within it at a distance, l, from the open end of the pipe as illustrated in Figure 1. The axis of the blade structure coincides with the axis of the circular pipe. The inlet model is illuminated by an external electromagnetic plane wave as shown in Figure 1, and the medium surrounding the inlet is assumed to be free space. In the present case, the blade geometry in Figure 1 only crudely models either the actual fan in the case of a turbo-fan type jet engine, or the first compressor ring of blades in a conventional (non-turbo-fan) jet engine. A second configuration which is also considered in this work is one which contains a combination of two planar, non-identical sets of blades extremely close together to simulate a stator-rotor combination in which the planar stator vanes are fixed and the planar rotor blades are allowed to turn relative to the fixed stator. The stator-rotor jet inlet model is illustrated in Figure 2. An analysis of the RCS for the problem in Figure 2 yields an estimate of the RCS modulation resulting from the motion of the rotor blades relative to the stator vanes. It is noted that the stator-rotor



## (a) SIDE VIEW



## (b) FRONT VIEW



W1 : WIDTH OF STATOR VANE

W2: WIDTH OF ROTOR BLADE

## (c) ENLARGED FRONT VIEW

Figure 2. Geometry of a simple jet inlet-model with a planar stator-rotor combination within. Stator and rotor lie in the same plane for convenience of analysis.

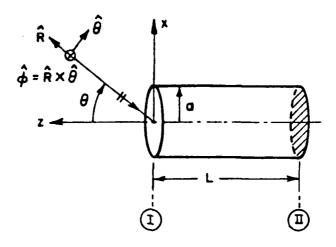


Figure 3. Backscattering from a finite hollow pipe which is open at z=0 and closed at z=-L.

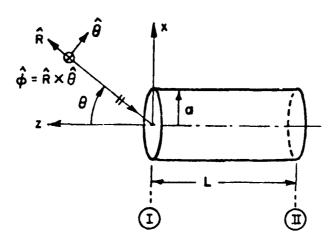


Figure 4. Backscattering from a finite hollow pipe with both ends open.

blade configuration of Figure 2 serves to improve the basic model of Figure 1 because a set of stator vanes is generally present immediately behind the fan in the case of a turbo-fan type jet engine, and they are also generally present immediately in front of the first compressor ring of blades in a conventional (or non-turbo fan) jet engine. Additional problems which are also considered in this work deal with the RCS analysis of finite length hollow circular cylinders open at the front end, but either closed (shorted), or open at the back end as shown in Figures 3 and 4, respectively. The solutions to the latter problems are of interest in that they allow a useful comparison of the effect on the RCS resulting from the scattering by the blade structure in the configurations of Figures 1 and 2, as opposed to the short and open terminations of Figures 3 and 4. In the present work, the RCS is of interest for the range of angles  $\theta$  which satisfy  $\theta < \pi/2$ ; the angle  $\theta$  is illustrated in Figures 1-4.

Some of the earlier published work available in the open literature on the types of problems considered in this report is briefly reviewed. The electromagnetic (EM) radiation from open-ended, semi-infinite circular and rectangular waveguides was treated by Chu [2] via a Kirchhoff approximation for the fields in the aperture at the open end. A formally exact solution for the problems of radiation and/or scattering from an open-ended, semi-infinite, hollow circular pipe was obtained via the Wiener-Hopf procedure by Levine and Schwinger [3], Jones [4], and Noble [5] for the acoustic case, and by Pearson [6] for

the perfectly-conducting EM case. Later Weinstein [7] treated in great detail both, the acoustic, and EM problems of radiation and scattering by an open-ended semi-infinite hollow circular pipe via the Weiner-Hopf technique; furthermore, Weinstein discussed the limitations of the Kirchhoff method for solving these problems. Subsequently Bowman [8], Lee et al [9], Mittra et al [10], Chuang et al [11], and Johnson and Moffatt [12] essentially dealt with improving the numerical efficiency and accuracy of the asymptotic high frequency approximation to the Wiener-Hopf factors given by Weinstein in his Wiener-Hopf solution for the EM radiation and scattering from an open-ended circular waveguide configuration. Witt and Price [13] analyzed the EM scattering by finite length perfectly-conducting hollow circular and rectangular pipes using a Kirchhoff type approximation. However, their procedure appears to be incorrect because the dominant term in their solution which pertains to the scattering by just the open front end exhibits the wrong frequency dependence for the circular pipe geometry when compared with an accurate asymptotic approximation of the Wiener-Hopf solution for the same problem [12]. Moll and Seecamp [14] analyzed the RCS of an inlet geometry modeled by an open-ended, semi-infinite hollow perfectly-conducting circular pipe with a planar blade structure inside; their blade model is somewhat similar, but not identical to the one chosen in the present work (as illustrated in Figures 1 and 2). However, Moll and Seecamp [14] employ the procedure of Witt and Price [13] which appears to be incorrect as mentioned earlier; furthermore, they include additional approximations (e.g., they neglect all TM modes

inside the duct) which appears to lead to additional errors. Kao [15] presents a numerical type solution for the scattering by finite length cylinders; however, his work is restricted to broadside incidence on the cylinder. Finally, it may be remarked that Mittra et al [10] also consider the effect on the RCS resulting from a uniform planar termination inside the semi-infinite hollow circular pipe in which the planar termination is characterized by a surface impedance type boundary condition. Their analysis of this problem is based on combining their Wiener-Hopf solution with the Generalized Scattering Matrix Technique (GSMT). It is noted that the MSM based procedure employed in the present work is essentially the same as the GSMT [16,17]. Both, the GSMT and the self-consistent MSM allow one to account for the multiple wave interactions between the open end of the circular pipe and the termination (or discontinuity) placed within the circular pipe. A ray analysis of the EM radiation from an open ended circular waveguide has been presented by Narasimhan [18]; whereas, Felsen and Yee [19] have performed a ray analysis of the acoustic modal reflection coefficient associated with an open ended rigid circular pipe which is excited from within. The ray analyses of Narasimhan [18], and Felsen and Yee [19] will be briefly reviewed in Section 3, wherein their work will also be compared and contrasted with the present UTD ray analysis and it's modifications for the EM radiation and reflection from an open-ended circular waveguide. The latter analysis is necessary in the present development of the explicit expressions for the RCS of the geometries in Figures 1-4.

In the present work, a ray analysis based on the Uniform Geometrical Theory of Diffraction (UTD) and its modifications is combined with the multiple scattering method (MSM) to arrive at a very efficient solution for evaluating the RCS of the inlet configurations in Figures 1-4. This method of analysis will simply be abbreviated as UTD-MSM, for convenience. Basically, the MSM allows one to systematically take into account all interactions between the open front end of the pipe and the termination (or discontinuity) at the back end located a distance L from the open end as shown in Figures 1-4. In the MSM, the wave interactions are described by "scattering matrices" pertaining to the canonical scattering events which occur at the front (Z=0) and back (Z=-L). These multiple interactions can be summed in a closed form via a self-consistent procedure. The elements of the scattering matrices in the MSM analysis are obtained here by using the UTD and its appropriate modifications which are required within caustic regions, and within the confluence of caustic and ray optical shadow boundary transition regions. It is important to note that the conventional waveguide modal fields in the pipe region need to be converted into a set of equivalent rays near the edge (or rim) of the open end in order to systematically employ the UTD ray technique for obtaining the elements of the scattering matrices. The UTD ray analysis provides simple and accurate expressions for the elements of the scattering matrices, and hence for the scattered and diffracted fields. The UTD analysis also provides a physical description for the scattering processes in terms of rays.

These UTD based scattering matrix elements for the EM radiation and scattering by an open-ended semi-infinite hollow circular pipe are found to agree extremely well with those obtained from the exact Wiener-Hopf solution for the same problem; the Wiener-Hopf solution is available in the open literature [7,9,10,12] as mentioned earlier. This agreement holds up even for the dominant mode regime in the circular pipe. A distinct advantage of the UTD solution, besides being physically appealing and accurate, is that it is far less complicated to use than the Wiener-Hopf solution. Furthermore, the present UTD analysis can be extended to jet intake or inlet shapes other than those which can be analyzed by the Wiener-Hopf method. Nevertheless, the Wiener-Hopf solution for the hollow, semi-infinite circular pipe is very useful in that it is a formally exact solution, and it therefore provides an important check on the approximate UTD ray solution.

A general description of the self-consistent MSM formulation of the solutions to the RCS problems shown in Figures 1-4 are described in Section 2. The elements of the various scattering matrices required in the MSM are obtained via the UTD and its appropriate modifications in Section 3. Several interesting numerical results based on the UTD-MSM solutions for the problems in Figures 1-4 are then presented and discussed in Section 4. Here, the UTD-MSM solution therefore implies that the backscattered field or the RCS of any of the problems in Figures 1-4 is obtained via the self-consistent MSM based formulation which contains scattering matrices whose elements are obtained via the UTD ray technique and its appropriate modifications. In addition, some

topics worthy of future investigation which would serve to improve the jet inlet model of Figures 1 and 2, and to extend the present analysis to inlet shapes other than the ones considered in Figures 1 and 2, are also briefly discussed.

## SECTION 2

## SELF-CONSISTENT MSM FORMULATION

As mentioned in Section 1, the method of RCS analysis of the configurations in Figures 1-4 is based primarily on the Uniform Geometrical Theory of Diffraction (UTD) ray technique and it's modifications which are used in conjunction with the multiple scattering method (MSM). In the MSM based analysis, the basic scattering mechanisms are "isolated", and "identified" as being associated with the scattering junctions. For example, these junctions are marked (I) and (II) in Figures 3-5. The multiple scattering between the junctions is calculated via a self consistent procedure. Such a procedure requires a knowledge of the generalized scattering matrices  $[S_{11}]$ ,  $[S_{12}]$ ,  $[S_{21}]$ , [ $S_{22}$ ], and [ $S_{b}$ ] for the scattering junctions (I) and (II). These generalized scattering matrices [16,17] are directly associated with the canonical scattering events shown in Figures 6, 7, and 8. The scattering matrix in microwave circuit analysis [20] arises in the description of interior region scattering (e.g., in waveguides) and it is defined in terms of interior propagating modes; whereas, the polarization scattering matrix [31,32,33] is defined for exterior region scattering. The generalized scattering matrix discussed here extends

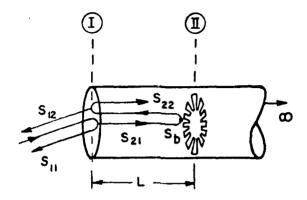


Figure 5. Scattering junctions I and II for the geometries in Figures 1-4.

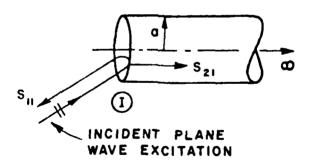


Figure 6. Canonical scattering problem for determining  $S_{11}$  and  $S_{21}$ .

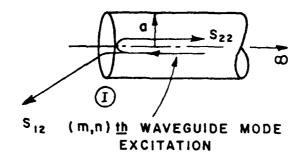


Figure 7. Canonical radiation problem for determining  $S_{12}$  and  $S_{22}$ .

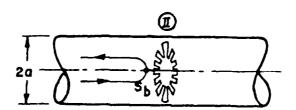


Figure 8. Canonical problem for determining  $S_{\mbox{\scriptsize h}}$  associated with the configuration in Figures 1-4.

the concept of microwave circuit scattering matrix to include evanescent modes, and to also include the polarization scattering matrix for exterior scattering. Thus, the generalized scattering matrix is essential for solving scattering problems which involve a coupling between interior and exterior regions as in the problem of the backscatter from jet inlet configurations. The elements of these generalized scattering matrices which will hence forth be referred to simply as the scattering matrices are defined next in the paragraphs to follow.

Let  $\overline{E}^i$  denote the electric field intensity of the incident electromagnetic plane wave. Using the coordinates given in Figures 1-4, one may express  $\overline{E}^i$  as

$$\overline{E}^{i} = (\hat{\theta} E_{\theta}^{i} + \hat{\phi} E_{\phi}^{i}) e^{jk(x \sin \theta + z \cos \theta)}.$$
 (1)

where  $E^{\frac{1}{9}}$  and  $E^{\frac{1}{9}}$  are the  ${}^{\frac{9}{9}}$  and  ${}^{\frac{9}{9}}$  polarized components of  $E^{\frac{1}{9}}$ , respectively at z=0, and k denotes the free space wave number. The unit vectors  ${}^{\frac{9}{9}}$  and  ${}^{\frac{2}{9}}$  lie in the plane of incidence defined by the cylinder axis (z) and the incident ray direction. The unit vector  ${}^{\frac{9}{9}}$  is orthogonal to the plane of incidence as shown in Figures 1-4. Likewise, let  $E^{\frac{1}{9}}$  denote the total far-zone backscattered electric field and  $E^{\frac{1}{9}}$  denote the far-zone electric field backscattered from only the open front end (at z=0) of the configurations in Figures 1-4. One can also express  $E^{\frac{1}{9}}$  and  $E^{\frac{1}{9}}$  in terms of their  ${}^{\frac{9}{9}}$  and  ${}^{\frac{1}{9}}$  components as

$$\overline{E}^{S} = \hat{\theta} E_{\theta}^{S} + \hat{\phi} E_{\phi}^{S} \qquad (?)$$

and

$$\overline{E}_0^S = \theta E_{\theta 0}^S + \phi E_{\phi 0}^S \qquad (3)$$

One may now describe the scattering matrix [S11]. The scattering matrix [S11] relates the field  $\overline{E}_0^S$  to  $\overline{E}^i$  (at z=0) as follows.

$$\begin{bmatrix} E_{\theta O}^{S} \\ E_{\phi O}^{S} \end{bmatrix} = \begin{bmatrix} S_{11} \end{bmatrix} \begin{bmatrix} E_{\theta}^{i} \\ E_{\phi}^{i} \end{bmatrix} \frac{e^{-jkR}}{R} , \qquad (4)$$

where R denotes the distance from the origin to the far zone observation point in the  $\hat{R}$  direction as shown in Figures 1-4. Thus,

$$\begin{bmatrix} S_{11} \end{bmatrix} = \begin{bmatrix} S_{\theta\theta} & S_{\theta\phi} \\ S_{\phi\theta} & S_{\phi\phi} \end{bmatrix} . \tag{5}$$

The scattering matrix [S12] converts the circular waveguide (intake) modal fields that are incident on the opening (at z=0) from the region z<0 into the fields radiated by these modes from the open end. The modal electric field  $\overline{E}_g^\pm$  within the circular waveguide region (z<0), i.e., within the intake region, may be represented in the usual manner by [20]

$$\overline{E}_{g}^{\pm} = \sum_{m,n} \left[ A_{nm}^{\pm} \overline{e}_{nin} e^{\mp j\beta_{nin}^{\dagger} z} + B_{nm}^{\pm} (\overline{e}_{nin} \pm \overline{e}_{zn:n}) e^{\mp j\beta_{nin}^{\dagger} z} \right], \quad (6)$$

where  $\overline{e}'_{nm}$  and  $\overline{e}_{nm}$  denote the transverse (to z) electric vector mode

functions for the  $TE_{nm}$  and  $TM_{nm}$  modes, respectively. Likewise,  $\beta'_{nm}$  and  $\beta_{nin}$  denote the propagation constants of the  $TE_{nm}$  and  $TM_{nm}$  modes, respectively. As usual, n and m denote the modal indices associated with the circumferential and radial variations of the modes (or eigenfunctions). Also,  $\overline{e}_{znm}$  denotes the z directed  $TM_{nm}$  electric mode field. The corresponding magnetic field  $\overline{H}_g^{\pm}$  within the circular guide is

$$\overline{H}_{g}^{\pm} = \sum_{m} \sum_{n} \left[ A_{nm}^{\pm} \left( \pm \overline{h}_{nm} + \overline{h}_{nmz}^{\dagger} \right)^{\mp j \beta_{nm}^{\dagger} z} + B_{nm}^{\pm} \left( \pm \overline{h}_{nm} \right) e^{\mp j \beta_{nm}^{\dagger} z} \right] . \quad (7)$$

The superscripts  $\pm$  in Eqs. (6)-(7) refer to modes propagating in the  $\pm z$  direction. To be specific, let  $\hat{\phi}' \cdot \overline{e}_{nm}$  behave as  $\begin{pmatrix} \cos n \phi' \\ \sin n \phi' \end{pmatrix}$  in the waveguide aperture at z=0 (see Figure 1-4). Then  $\hat{\phi}' \cdot \overline{h}_{nm}$  behaves as  $\begin{pmatrix} -\sin n \phi' \\ \cos n \phi' \end{pmatrix}$ ; likewise  $\hat{\phi}' \cdot \overline{e}_{nm}$  behaves as  $\begin{pmatrix} -\sin n \phi' \\ \cos n \phi' \end{pmatrix}$  and  $\hat{\phi}' \cdot \overline{h}_{nm}$ 

behaves as  $\binom{\cos n\phi^i}{\sin n\phi^i}$ . In Appendix A, a list of the circular waveguide modes and also the values of ka at mode cutoffs are given in chronological order.

Let  $E_{\theta}$  and  $E_{\phi}$  denote the  $\hat{\theta}$  and  $\hat{\phi}$  directed components of the electric field radiated by the waveguide fields  $(E_g^+, \overline{H}_g^+)$  after they impinge upon the open end (z=0) from the region z<0. Then

$$\begin{bmatrix} E_{\theta}^{\Gamma} \\ --- \\ E_{\phi}^{\Gamma} \end{bmatrix}_{2\times 1} = \begin{bmatrix} S_{12} \end{bmatrix}_{2\times \infty} \begin{bmatrix} A_{nin}^{+} \\ B_{nm}^{+} \end{bmatrix}_{\infty \times 1} \frac{e^{-jkR}}{R}, \qquad (8)$$

where a typical subscript of the type MxN on the matrices implies M rows

where a typical subscript of the type MxN on the matrices implies M roand N columns, and 
$$\begin{bmatrix} A_{01}^+ \\ A_{02}^+ \\ A_{11}^+ \\ A_{12}^+ \\ B_{01}^+ \\ B_{02}^+ \\ \vdots \\ B_{11}^+ \\ B_{12}^+ \\ \vdots \end{bmatrix}_{\infty x1}$$

It follows that

$$[S_{12}] = \begin{bmatrix} \frac{S_{\theta nm}^{*}}{S_{\theta nm}^{*}} & \frac{S_{\theta nm}^{*}}{S_{\theta nm}^{*}} \\ \frac{S_{\theta 01}^{*}S_{\theta 02}^{*} - S_{\theta 01}^{*}S_{\theta 02}^{*} - S_{\theta 01}^{*}S_{\theta 02}^{*} - S_{\theta 01}^{*}S_{\theta 02}^{*} \\ \frac{S_{\theta 01}^{*}S_{\theta 02}^{*} - S_{\theta 11}^{*}S_{\theta 12}^{*} - S_{\theta 01}^{*}S_{\theta 02}^{*} - S_{\theta 01}^{*}S_{\theta 02}^{*} - S_{\theta 01}^{*}S_{\theta 02}^{*} \\ \frac{S_{\theta 01}^{*}S_{\theta 02}^{*} - S_{\theta 11}^{*}S_{\theta 12}^{*} - S_{\theta 01}^{*}S_{\theta 02}^{*} - S_{\theta 01}^{*}S_{\theta$$

The scattering matrix  $[S_{21}]$  describes the transformation or coupling of the incident plane wave field into the waveguide modes as illustrated in Figure 6. Symbolically,  $[S_{21}]$  is defined by the relation

$$\begin{bmatrix} A_{nm}^{-} \\ B_{nm}^{-} \end{bmatrix}_{\infty \times 1} = \begin{bmatrix} S_{21} \\ S_{21} \end{bmatrix}_{\infty \times 2} \begin{bmatrix} E_{\theta}^{i} \\ E_{\phi}^{i} \end{bmatrix}_{2 \times 1}$$
 (11)

where  $A_{nm}$  and  $B_{nm}$  denote the amplitudes of the  $TE_{nm}$  and  $TM_{nm}$  modes transmitted into the waveguide (i.e., in the  $-\hat{z}$  direction) by the external plane wave field  $\overline{E}^i = E_{\theta}^{i} \hat{\theta} + E_{\phi}^{i} \hat{\phi}$  which is incident on the open end of the semi-infinite circular pipe. From Eq. (11), it follows that [S21] is given by

$$[S_{21}] = \begin{bmatrix} \widetilde{S}_{\theta nm} \\ \widetilde{S}_{\theta nm} \end{bmatrix} \begin{bmatrix} \widetilde{S}_{\phi nm} \\ \widetilde{S}_{\theta nm} \end{bmatrix}$$

$$[\widetilde{S}_{\theta nm}] \begin{bmatrix} \widetilde{S}_{\phi nm} \\ \widetilde{S}_{\phi nm} \end{bmatrix}$$

$$(12)$$

Clearly the problem of determining [ $S_{21}$ ] is the reciprocal of the problem of determining [ $S_{12}$ ] (see Figures 6 and 7). Thus, a knowldege of [ $S_{12}$ ]; i.e.,  $S_{0nm}^{i}$ ,  $S_{0nm}^{i}$ ,  $S_{0nm}^{i}$ , and  $S_{0nm}^{i}$ , together with the use of the reciprocity theorem for electromagnetic fields allows one to calculate  $\widetilde{S}_{0nm}^{i}$ ,  $\widetilde{S}_{0nm}^{i}$ ,  $\widetilde{S}_{0nm}^{i}$ , and  $\widetilde{S}_{0nm}^{i}$ , and to hence obtain [ $S_{21}$ ] in terms of [ $S_{12}$ ]. In short, the elements of [ $S_{21}$ ] are simply related to

the elements of  $[S_{12}]^T$ ; here T denotes the transpose matrix operator. The precise relation between  $[S_{21}]$  and  $[S_{12}]$  will be discussed in Section 3.

The scattering matrix [S22] is a modal reflection coefficient matrix which is associated with the interaction shown in Figure 7. In particular, the elements of [S22] describe the reflection coefficients associated with  $TE_{nm}$  and  $TM_{nm}$  modes reflected back from the opening (at z=0) into the semi-infinite waveguide region (z<0) when either a  $TE_{nm}$ , or a  $TM_{nm}$  mode is incident on the open end from within the waveguide region . The matrix [S22] is defined symbolically by the relation

$$\begin{bmatrix} \begin{bmatrix} A_{nm}^{-} \end{bmatrix} \\ \begin{bmatrix} B_{nm}^{-} \end{bmatrix} \end{bmatrix} = \begin{bmatrix} S_{22} \end{bmatrix} \quad \text{on} \quad \text{on} \quad \begin{bmatrix} A_{pq}^{+} \end{bmatrix} \\ \begin{bmatrix} B_{pq}^{+} \end{bmatrix} \end{bmatrix} \quad \text{on} \quad \text{on}$$

where, it is noted that [S22] can be further symbolically expressed as,

$$[S_{22}] = \begin{bmatrix} [R_{nm;pq}^{hh}] & [R_{nm;pq}^{he}] \\ [R_{nm;pq}^{eh}] & [R_{nm;pq}^{ee}] \end{bmatrix} \qquad (14)$$

The meaning of  $R_{nm;pq}^{he}$ ; for example, in the above equation is the following. A  $TM_{pq}$  (or e) type mode with amplitude  $R_{pq}^{+}$  which is incident at the open end (z=0) is partly transformed (or coupled) into a reflected  $TE_{nm}$  (or h) type mode with amplitude  $A_{nm}^{-} = R_{nm;pq}^{he} B_{pq}^{+}$ .

The scattering matrix  $[S_b]$ , like  $[S_{22}]$ , is also a reflection type matrix associated with the discontinuity at junction (2) in Figure 8. From Eqs. (13)-(14), one may therefore write

$$\begin{bmatrix}
A_{nm}^{+} \\
B_{nm}^{+}
\end{bmatrix} = \begin{bmatrix} S_{b} \\
\infty x^{\infty}
\begin{bmatrix}
A_{pq}^{-} \\
B_{pq}^{-}
\end{bmatrix}$$
(15)

and

The in which  $R_{nm;pq}$ , for example, has the same meaning as  $R_{nm;pq}$  of  $R_{nm;pq}$  of  $R_{nm;pq}$  are quite different those of  $R_{nm;pq}$ .

At a given operating frequency, the inlet duct or waveguide region in Figures 1-4 can support a finite number of propagating modes, and an infinite number of evanescent (or non-propagating) modes. Consequently, the matrices associated with  $[S_{12}]$ ,  $[S_{21}]$ ,  $[S_{22}]$ , and  $[S_b]$  are of infinite order to include the infinite number of evanescent modes. It may be remarked that although the matrices  $[S_{12}]$ ,  $[S_{21}]$ ,  $[S_{22}]$ , and  $[S_b]$  are of infinite order in a formal sense, one needs to retain only a finite number of the elements of these scattering matrices in practice

because the distance "L" shown in Figures 1-4 is generally large enough to where the infinite number of "evanescent" waveguide modes generated at junction (I) are not observed at junction (II), and vice versa. The finite number of elements retained in practice thus correspond to only the finite number of all the propagating (non-evanescent) modes which can exist in the waveguide or the cavity region. If the distance L in Figures 1-4 is small enough so that lower order evanscent modes become important, then one must include these modes but still ignore all the higher order evanescent modes in practice since their contribution must become vanishingly small. In any case, one retains only a finite number of elements in the scattering matrices. In the present work, "L" is chosen such that the contribution from all the evanescent waveguide modes can be ignored.

$$[E_0^s] = [S_{11}] [E^i] \frac{e^{-jkR}}{R} \qquad (17)$$

Part of the incident field which is scattered by (I) into region B becomes incident at junction (II) from which it is subsequently reflected; this reflected field is incident back at (I) where it undergoes further scattering into regions A and B, and so on, thereby giving rise to multiple wave interactions between junctions (I) and (II). The fields resulting from these multiple interactions may be expressed in a convergent Neumann series as done by Pace and Mittra [16];

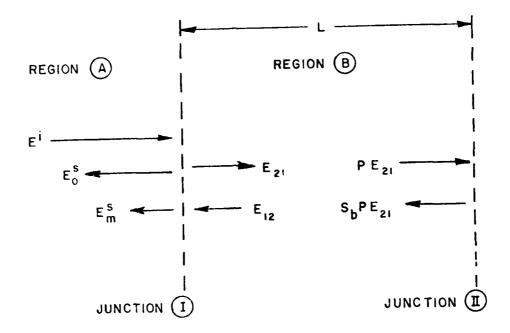


Figure 9. Multiple interactions between junctions (I) and (II) for calculating the total backscattered field.

however, an alternate procedure based on a self-consistent method leads directly to the same result. The latter, i.e., the self-consistent MSM method for summing up the multiple interactions, will be used in this analysis. Let  $[E_{12}]$  represent the net value of the field incident at (I) from (II) after taking all the multiple interactions into consideration. Similarly, let  $[E_{21}]$  represent the net value of the field incident at (II) from (I) after taking all the multiple interactions into account. Then the total scattered field in region A denoted by  $[E^S]$  consists of a superposition of the field  $[E_{12}]$ , and  $[E_{11}]$ , where  $[E_{11}]$  is the field scattered into A when  $[E_{11}]$  is incident on (I). Thus,

$$[\xi^{S}] = \begin{bmatrix} \xi^{S} \end{bmatrix} + \begin{bmatrix} \xi^{S} \end{bmatrix} . \tag{18}$$

where  $\begin{bmatrix} \mathbf{E}_{\mathbf{m}}^{\mathbf{S}} \end{bmatrix}$  may be expressed as

$$[E_m^s] = [S_{12}] [E_{12}] \frac{e^{-jkR}}{R}$$
 (19)

The expressions for [E $_{12}$ ] and [E $_{21}$ ] are given in terms of [S $_{21}$ ] and [S $_{22}$ ] by

$$[E_{21}] = [S_{21}][E^{\dagger}] + [S_{22}][E_{12}]$$
 (20)

$$[E_{12}] = [P][S_b][P][E_{21}]$$
 (21)

where  $[S_b]$  is the generalized matrix corresponding to the reflection coefficient at junction (II) as indicated earlier, and [P] is a diagonal matrix accounting for the phase delay in the propagation path L. Eliminating  $[E_{12}]$  between Eqs. (20) and (21) yields

$$([I]-[S_{22}][P][S_b][P]) [E_{21}] = [S_{21}][E^{\dagger}]$$
 (22)

where [I] is an infinite-order identity matrix. Hence, it follows that

$$[E_{21}] = ([I]-[S_{22}][P][S_b][P])^{-1} [S_{21}][E^{\dagger}] .$$
 (23)

From Eqs. (21) and (23),  $[E_{12}]$  becomes

$$[E_{12}] = [P][S_b][P] ([I]-[S_{22}][P][S_b][P])^{-1} [S_{21}][E^{\dagger}]$$
 (24)

Incorporating Eq. (24) into (19) yields

$$[\varepsilon_{m}^{s}] = [S_{12}][P][S_{b}][P] ([I]-[S_{22}][P][S_{b}][P])^{-1} [S_{21}][E^{i}] = \frac{e^{-jkR}}{R}.$$
(25)

Finally, combining Eqs. (17) and (25) according to Eq. (18) yields the self-consistent expression for the total scattered field [ES] as

$$[E^{s}] = \{[s_{11}] + [s_{12}][p][s_{b}][p]([I] - [s_{22}][p][s_{b}][p])^{-1} [s_{21}]\} [E^{i}] = \frac{e^{-jkR}}{R} .$$

$$(26)$$

In the special case of the geometry in Figure 4 where the field backscattered from a hollow finite cylinder open at both ends is of interest, an additional interaction becomes important and it must be

included. The latter interaction corresponds to waves coupled from the interior waveguide region to the exterior region via diffraction at the end z=-L, and vice versa. The fields of these interactions can also be found via the UTD in a manner similar to that done for  $\{S_{21}\}$ ; this field contribution to the backscattered field resulting from the internal-external coupling must be added to the result in Eq. (26). It should be observed that the latter is of little interest in terms of jet intake configuration of Figures 1 and 2.

It now remains to find explicit expressions for  $[S_{11}]$ ,  $[S_{12}]$ ,  $[S_{21}]$ ,  $[S_{22}]$ , and  $[S_b]$  to complete the calculation in Eq. (26). These scattering matrices are formed via the UTD ray technique as discussed next in Section 3.

## SECTION 3

## ANALYTICAL DEVELOPMENT OF THE ELEMENTS OF THE SCATTERING MATRICES IN MSM

The scattering matrices [S11], [S12], [S21], [S22], and [Sb] associated with the canonical scattering events shown in Figures 6-8 were defined in the previous section. In the present section, the elements of these scattering matrices are found via the uniform geometrical theory of diffraction (or UTD) ray technique [1] and its modifications at caustics. The present ray analysis is restricted so as to be valid only in the range  $\theta < \pi/2$ , where  $\theta$  is shown in Figures 1-4. The reason for this restriction is that in the present work, the RCS is of interest only for  $\theta < \pi/2$ . This analysis can of course be extended to  $\theta > \pi/2$ ; however, that extension is not reported in this work. The UTD ray analysis is appealing because it leads to a simple localized physical description for the scattering process in terms of rays, and it also provides relatively simple and accurate expressions for the scattered fields, and hence for the scattering matrices. In order to exploit ray methods systematically, the modal fields within the circular

intake (or waveguide) region have been converted into a set of equivalent rays, and vice versa. These scattering matrix calculations based on the UTD and its modifications at caustics are found to agree extremely well with those obtained from the exact Wiener-Hopf solutions available in the open literature [7,9,10,11,12] for the problem of diffraction of waves by a hollow semi-infinite circular pipe. This agreement holds even for the dominant mode regime within the circular pipe. It is noted that while the exact Wiener-Hopf solutions for the hollow, semi-infinite circular pipe provide very valuable checks on the UTD solutions, they are far more complicated to use than the present UTD solutions. Furthermore, the present UTD analysis can be extended to intake shapes other than those which can be analyzed via the Wiener-Hopf method. The reflection from the blades (i.e., blade scatter) in Figure 8 is found by employing a geometric optical type of approximation for the blade current induced by the modal fields which are excited within the intake by the incident plane wave. This approximation for the blade current is simple to apply, and it is expected to be reasonably accurate for a large number of blades closely spaced together as is generally the case in actual jet inlets. It would be worth investigating a more rigorous representation for the blade currents in a future study. The UTD ray analysis and its modifications at caustics which are required in the development of the elements of the scattering matrices is described next.

## A. Ray Analysis for [S11]

The scattering matrix  $[S_{11}]$  describes the fields scattered from only the open end (z=0) of the geometries in Figures 1-4 when these configurations are illuminated by a plane wave. In particular,  $[S_{11}]$  describes the fields scattered from junction (I) corresponding to the canonical scattering event as depicted in Figure 6 pertaining to a hollow, semi-infinite circular pipe illuminated by an EM plane wave. The latter problem in Figure 6 can be analyzed efficiently via the UTD ray method and its modifications which are required along ray caustics.

Consider the plane of incidence formed by the incident ray and the cylinder axis (z-axis) and let the x-coordinate lie in this plane. This x-z plane of incidence intersects the rim at the open end (z=0) of the cylinder at two points denoted by Q<sub>1</sub> and Q<sub>2</sub> whose coordinates are (x=a, y=0, z=0) and (x=-a, y=0, z=0), respectively. Only  $\theta < \pi/2$  is considered here for reasons mentioned earlier. According to Keller's  $\lfloor 21 
floor$  generalization of Fermat's principle, Q1 and Q2 constitute the two points of first order or single diffraction from the circular edge (rim) of the open-ended cylinder. Additional higher-order diffracted rays which emanate from the curved rim after undergoing multiple diffractions across the aperture formed by that rim at the open front end (z=0) also exist, and their contribution must be included in calculating the total field backscattered from the open front end. In general, these higher order (or multiply) diffracted ray contributions beyond the second order (or doubly) diffracted ray interaction may be ignored for backscattering aspects away from the z-axis (or 0=0 direction). However, for on-axis

 $(\theta=0)$  backscattering calculation the higher order diffracted ray contributions can become important especially as the radius (a) of the cylinder is decreased. It is noted that the axial (or  $\theta=0$ ) direction is a caustic of the rays which are singly and multiply diffracted from the circular rim (or edge) at the open front end (z=0) in the case of axial backscatter.

Initially, the UTD analysis of the problem in Figure 6 will be described for the first order or singly diffracted fields which contribute to the backscatter. This analysis will then be followed by an analysis of the multiply diffracted ray fields which can also contribute to the backscatter.

## (i) First Order (or Singly) Diffracted Ray Contributions to $[S_{11}]$

The UTD ray field  $\overline{E}^{hs1}$  which is singly diffracted from points  $\Omega_1$  and  $\Omega_2$  on the circular rim (edge) at the open front end (z=0) is given by [1,21]

$$\frac{bs1}{E} = E_{\phi 0} \quad \phi + E_{\theta 0} \quad \theta \qquad . \tag{27}$$

where

$$E_{\phi 0}^{bs1} = \pm \sum_{\ell=1}^{2} E_{\phi}^{i} D_{S}(\psi_{\ell}, \psi'_{\ell}; \beta_{0}) e^{-j2kasin\theta_{\xi}} \sqrt{\frac{a}{2sin\theta}} P_{\ell}(j) \frac{e^{-jkR}}{R};$$
(28)

θ not close to zero

and
$$D_{s}(\psi_{\ell}, \psi_{\ell}^{\prime}; \beta_{0}) = -\frac{e^{-j\frac{\pi}{4}}}{e^{2\sqrt{2\pi k} \sin \beta_{0}}} \left\{ \sec\left(\frac{\psi_{\ell} - \psi_{\ell}^{\prime}}{2}\right) F[2kL\cos^{2}(\frac{\psi_{\ell} - \psi_{\ell}^{\prime}}{2})] + \sec\left(\frac{\psi_{\ell} - \psi_{\ell}^{\prime}}{2}\right) F[2kL\cos^{2}(\frac{\psi_{\ell} - \psi_{\ell}^{\prime}}{2})] \right\}$$

$$33$$
(29)

A STATE OF THE STA

for a half plane. In Eq. (29), the "L" is an appropriate distance parameter within the "F" function which involves a Fresnel integral; "L" and "F" are as defined in [1]. When  $2kL\cos^2(\frac{\psi_{\ell} \mp \psi_{\ell}}{2})>3$ ,  $F[2kL\cos^2(\frac{\psi_{\ell} \mp \psi_{\ell}}{2})]\approx 1;$  and in the following, "F" is set equal to unity whenever the latter condition is true.

In Eq. (28),  $\Omega_S$  denotes  $\{ \substack{\text{hard} \\ \text{hard} } \}$  edge diffraction coefficient  $\{ \substack{\text{l}, \text{loop} \\ \text{loop} } \}$  at  $\{ \substack{\text{l}, \text{loop} \\ \text{loop} } \}$  and  $\{ \substack{\text{l}, \text{loop} } \}$  and  $\{ \substack{\text{l}, \text{loop} \\ \text{loop} } \}$  and  $\{ \substack{\text{l}, \text{loop} } \}$  and  $\{ \substack{\text{l}, \text{loop} \\ \text{loop} } \}$  and  $\{ \substack{l$ 

$$\Psi_{\ell} = \Psi_{\ell}' ; \beta_{O} = \pi/2 . \tag{30}$$

$$\theta_{\ell} = \{ \begin{cases} -\theta, & \text{if } \ell=1 \text{ (i.e., for ray diffracted at } Q_1 \\ \theta, & \text{if } \ell=2 \text{ (i.e., for ray diffracted at } Q_2 \} \end{cases}$$
 (31)

The factor  $P_{\ell}(j)$  is defined by

$$P_{\ell}(j) = \begin{cases} 1, & \text{when an edge diffracted ray from } Q_{\ell}(\ell=1, \text{ or } 2) \text{ does} \\ & \text{not cross the axial caustic } (z-axis) \\ \\ j, & \text{when an edge diffracted ray from } Q_{\ell}(\ell=1, \text{ or } 2) \text{ crosses} \\ \\ & \text{the axial caustic } (z-axis) \end{cases}$$

The factor  $P_{\ell}(j)$  is required since the cylinder axis is a caustic of the rays diffracted from the circular edge (at z=0). Upon crossing such a caustic, the phase associated with that diffracted ray undergoes a jump of +  $\pi/2$  radians which is properly taken into account via the factor j appearing in the RHS of Eq. (32). The quantity R in Eq. (28) denotes the usual distance from 0 to the far zone observation point in the  $\hat{R}$  direction. From Eq. (28), Eqs. (4)-(5), and the explicit form of  $D_{\Sigma}$  in

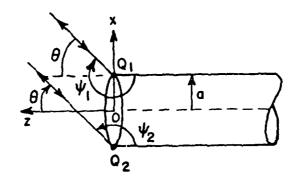


Figure 10. Geometry of rays diffracted from points  $\mathsf{Q}_1$  and  $\mathsf{Q}_2$  on the edge.

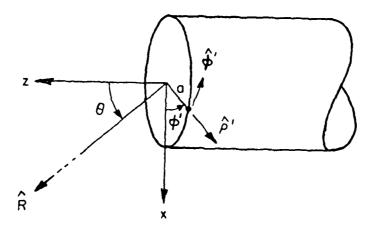


Figure 11. Aperture and rim coordinates at z=0.

[1,21], it readily follows that, for a unit amplitude plane wave incident on junction (I),

$$S_{\theta\theta} = \frac{a}{2} \left( 1 - \frac{1}{\cos \theta} \right) \sqrt{\frac{2}{\pi 2 ka \sin \theta}} \cos \left( 2 ka \sin \theta - \frac{\pi}{4} \right) \quad ; \quad \theta \neq 0 \quad , \tag{33}$$

and

$$S_{\phi\phi} = \frac{-a}{2} \left( 1 + \frac{1}{\cos \theta} \right) \sqrt{\frac{2}{\pi 2 kasin \theta}} \cos \left( 2kasin \theta - \frac{\pi}{4} \right) \quad ; \quad \theta \neq 0 \quad , \tag{34}$$

Near the caustic direction (0+0), Eq. (28), and hence Eqs. (33)-(34) break down. A uniform asymptotic approximation for  $S_{\theta\theta}$  and  $S_{\varphi\varphi}$  which is valid near and at 0=0 may be obtained via the method of "equivalent" edge currents which indirectly make use of  $D_{\Sigma}$  as indicated in [22].

The equivalent electric and magnetic edge currents  $I_1$  and  $M_1$ , respectively are positioned on the circular edge or the rim at the open end (z=0) of the semi-infinite cylinder, and they are given by [22]

$$I_{1}(\phi') = -\gamma_{0} \sqrt{\frac{3\pi}{jk}} \frac{D_{S}(\psi, \psi'; \beta_{0}^{*})}{\sin \beta_{0}} (\overline{E}^{i} \cdot \hat{\phi}')_{rim} \qquad (35)$$

and

$$M_{1}(\phi') = -\frac{7}{0}\sqrt{\frac{8\pi}{jk}} \frac{D_{h}(\psi,\psi';\beta'_{0})}{\sin\beta_{0}} (\overrightarrow{H}^{i} \cdot \phi')_{rim} \qquad (36)$$

where  $\phi'$  is the unit tangent vector to the circular edge or rim (at z=0) in the usual cylindrical coordinates at  $\phi'$ , and  $\psi'$ ,  $\psi$ ,  $\beta'$ ,  $\beta$  and  $(\overline{\frac{F}{H^i}})$ .  $\hat{\phi}'$  change as a function of position on the rim. The coordinates of any point on the rim are ( $\rho'$ =a,  $\phi'$ , z'=0); the primes denote the source coordinates associated with the equivalent sources  $I_1$  and  $M_1$ .

The quantities  $\psi$  and  $\psi'$  in  $D_S$  are interpreted as the usual projected incident and diffracted ray angles which are obtained by projecting the incident and diffracted rays on the rim, and  $\beta'_0$  is the acute angle between the incident ray and the edge tangent  $\hat{\phi}'$ . The incident magnetic field  $\widehat{H}^i$  is related to  $\widehat{E}^i$  via  $\widehat{H}^i = -Y_0 \widehat{R} x \widehat{E}^i$  in which  $Z_0$  is the free space impedance, and  $Y_0 = (Z_0)^{-1}$ . When the above equivalent currents are incorporated into the usual radiation integrals, one obtains the fields radiated by these currents as

$$\frac{-bs1}{E} = \frac{jkZ_0}{4\pi} \left[ \int_0^{2\pi} d\phi' a(\hat{R} \times \hat{R} \times I_1 \hat{\phi}' + Y_0 \hat{R} \times M_1 \hat{\phi}') \frac{e^{jk\rho' \cdot R}}{R} \right] \frac{e^{-jkR}}{R};$$
(37)

where k denotes the free space wave number and  $\bar{\rho}' = a \hat{\rho}'$ . The quantities  $\phi', \hat{\phi}', \hat{\rho}'$  and  $\hat{R}$  are shown in Figure 11.

For ka sin  $\theta >>1$ , Eq. (37) can be evaluated asymptotically via the method of stationary phase. This procedure yields the stationary points to be at  $Q_1$  and  $Q_2$  on the rim (see Figure 10), and the corresponding stationary phase solution agrees exactly with Eq. (28), as it should. While the integral in Eq. (37) can be evaluated exactly in closed form only for  $\theta = 0$ , it can be evaluated approximately but accurately in closed form for  $\theta$  small as follows.

As a first step in the approximate evaluation of the integral in Eq. (37) for 0 small, one may fix the  $D_S$  in  $I_1$  and  $D_h$  in  $M_1$  to their values close to the caustic direction (0=0) because, the diffraction coefficients  $D_S$  are slowly varying with respect to 0. Thus, for 9 very h small, the integral in Eq. (37) is given approximately by

$$\frac{-bs1}{E} = \frac{-jk}{4\pi} \sqrt{\frac{8\pi}{jk}} a \frac{e^{-jkR}}{R} \left\{ D_s (\theta \approx 0) \int_0^2 d\phi' \left[ \hat{R} x \hat{R} x \hat{\phi}' \right] \left( E_{\phi}^{\dagger} \cos \phi' - E_{\theta}^{\dagger} \cos \theta \sin \phi' \right) \right] e^{-jkR} d\phi' \left[ (\hat{R} x \hat{\phi}') \left( E_{\phi}^{\dagger} \cos \theta \sin \phi' + E_{\theta}^{\dagger} \cos \phi' \right) \right] e^{-jkR} d\phi' \left[ (\hat{R} x \hat{\phi}') \left( E_{\phi}^{\dagger} \cos \theta \sin \phi' + E_{\theta}^{\dagger} \cos \phi' \right) \right] e^{-jkR} d\phi' \left[ (\hat{R} x \hat{\phi}') \left( E_{\phi}^{\dagger} \cos \theta \sin \phi' + E_{\theta}^{\dagger} \cos \phi' \right) \right] e^{-jkR} d\phi' \left[ (\hat{R} x \hat{\phi}') \left( E_{\phi}^{\dagger} \cos \theta \sin \phi' + E_{\theta}^{\dagger} \cos \phi' \right) \right] e^{-jkR} d\phi' \left[ (\hat{R} x \hat{\phi}') \left( E_{\phi}^{\dagger} \cos \theta \sin \phi' + E_{\theta}^{\dagger} \cos \phi' \right) \right] e^{-jkR} d\phi' \left[ (\hat{R} x \hat{\phi}') \left( E_{\phi}^{\dagger} \cos \theta \sin \phi' + E_{\theta}^{\dagger} \cos \phi' \right) \right] e^{-jkR} d\phi' \left[ (\hat{R} x \hat{\phi}') \left( E_{\phi}^{\dagger} \cos \theta \sin \phi' + E_{\theta}^{\dagger} \cos \phi' \right) \right] e^{-jkR} d\phi' \left[ (\hat{R} x \hat{\phi}') \left( E_{\phi}^{\dagger} \cos \theta \sin \phi' + E_{\theta}^{\dagger} \cos \phi' \right) \right] e^{-jkR} d\phi' \left[ (\hat{R} x \hat{\phi}') \left( E_{\phi}^{\dagger} \cos \theta \sin \phi' + E_{\theta}^{\dagger} \cos \phi' \right) \right] e^{-jkR} d\phi' \left[ (\hat{R} x \hat{\phi}') \left( E_{\phi}^{\dagger} \cos \theta \sin \phi' + E_{\theta}^{\dagger} \cos \phi' \right) \right] e^{-jkR} d\phi' \left[ (\hat{R} x \hat{\phi}') \left( E_{\phi}^{\dagger} \cos \theta \sin \phi' + E_{\theta}^{\dagger} \cos \phi' \right) \right] e^{-jkR} d\phi' \left[ (\hat{R} x \hat{\phi}') \left( E_{\phi}^{\dagger} \cos \theta \sin \phi' + E_{\theta}^{\dagger} \cos \phi' \right) \right] e^{-jkR} d\phi' \left[ (\hat{R} x \hat{\phi}') \left( E_{\phi}^{\dagger} \cos \theta \sin \phi' + E_{\theta}^{\dagger} \cos \phi' \right) \right] e^{-jkR} d\phi' \left[ (\hat{R} x \hat{\phi}') \left( E_{\phi}^{\dagger} \cos \theta \sin \phi' + E_{\theta}^{\dagger} \cos \phi' \right) \right] e^{-jkR} d\phi' \left[ (\hat{R} x \hat{\phi}') \left( E_{\phi}^{\dagger} \cos \theta \sin \phi' + E_{\theta}^{\dagger} \cos \phi' \right) \right] e^{-jkR} d\phi' \left[ (\hat{R} x \hat{\phi}') \left( E_{\phi}^{\dagger} \cos \theta \sin \phi' + E_{\theta}^{\dagger} \cos \phi' \right) \right] e^{-jkR} d\phi' \left[ (\hat{R} x \hat{\phi}') \left( E_{\phi}^{\dagger} \cos \theta \sin \phi' + E_{\theta}^{\dagger} \cos \phi' \right) \right] e^{-jkR} d\phi' \left[ (\hat{R} x \hat{\phi}') \left( E_{\phi}^{\dagger} \cos \theta \sin \phi' + E_{\phi}^{\dagger} \cos \phi' \right) \right] e^{-jkR} d\phi' \left[ (\hat{R} x \hat{\phi}') \left( E_{\phi}^{\dagger} \cos \phi' + E_{\phi}^{\dagger} \cos \phi' \right) \right] e^{-jkR} d\phi' \left[ (\hat{R} x \hat{\phi}') \left( E_{\phi}^{\dagger} \cos \phi' + E_{\phi}^{\dagger} \cos \phi' \right) \right] e^{-jkR} d\phi' \left[ (\hat{R} x \hat{\phi}') \left( E_{\phi}^{\dagger} \cos \phi' + E_{\phi}^{\dagger} \cos \phi' \right) \right] e^{-jkR} d\phi' \left[ (\hat{R} x \hat{\phi}') \left( E_{\phi}^{\dagger} \cos \phi' + E_{\phi}^{\dagger} \cos \phi' \right) \right] e^{-jkR} d\phi' \left[ (\hat{R} x \hat{\phi}') \left( E_{\phi}^{\dagger} \cos \phi' + E_{\phi}^{\dagger} \cos \phi' \right) \right] e^{-jkR} d\phi' \left[ (\hat{R} x \hat{\phi}') \left( E_{\phi}^{\dagger} \cos \phi' + E_{\phi}^{\dagger} \cos \phi' \right) \right] e^{-jkR} d\phi' \left[ (\hat{R} x \hat{\phi}') \left( E_{\phi}^{\dagger} \cos \phi' + E_{\phi}^{\dagger} \cos \phi' \right) \right] e^{-jkR} d\phi' \left[ (\hat{R}$$

The above integral can now be evaluated in closed form to yield

$$E_{\theta 0}^{bs1} = -E_{\theta}^{i} (\sqrt{2\pi k} e^{-i\alpha}) \{D_{h}(\theta \approx 0)J_{1}^{i}(2kasin\theta) - D_{s}(\theta \approx 0)cos^{2}\theta \frac{J_{1}(2kasin\theta)}{2kasin\theta}\} \frac{e}{R}$$
(39)

$$E_{\phi 0}^{bs1} = E_{\phi}^{i} (\sqrt{2\pi k} e^{-a}) \{D_{s}(\theta \approx 0)J_{1}(2kasin\theta) + D_{h}(\theta \approx 0)cos^{2}\theta \frac{J_{1}(2kasin\theta)}{2kasin\theta}\} \frac{-jkR}{R}$$
(40)

It is clear that the above result which is valid at and near the caustic, i.e., for  $\theta$  at and near zero can blend into the two-point result of Eq. (28) which is valid for  $\theta$  not close to zero (i.e., far from the caustic direction) if the  $D_S(\theta \approx 0)$  in the above result for small  $\theta$  is now allowed to be a function of  $\theta$ . Thus, one may heuristically replace  $D_S(\theta \approx 0)$  in Eqs. (39)-(40) by  $D_S(\theta)$  to yield

$$E_{\theta\theta}^{\text{bs1}} = E_{\theta}^{\text{i}} \frac{a}{2} \left\{ \left(1 - \frac{1}{\cos \theta}\right) J_{1}^{\text{i}} \left(2 \text{kasin} \theta\right) - \left(1 + \frac{1}{\cos \theta}\right) \cos^{2} \theta \frac{J_{1} \left(2 \text{kasin} \theta\right)}{2 \text{kasin} \theta} \right\} \frac{-\text{jkR}}{R}$$
and

 $E_{\phi 0} = -E_{\phi}^{i} \frac{a}{2} \left\{ (1 + \frac{1}{\cos \theta}) J_{1}^{i} (2ka\sin \theta) + (1 - \frac{1}{\cos \theta})\cos^{2}\theta \frac{J_{1}(2ka\sin \theta)}{2ka\sin \theta} \right\} \cdot \frac{-jkR}{e}$ 

The above result for  $E_{\phi 0}^{bs1}$  corresponding to the singly diffracted electric field is now valid for  $\theta$  small and large. Thus,  $E_{\phi 0}^{bs1}$  in Eqs. (41)-(42) is "uniform" in the sense  $\theta_0$  that it remains valid at and near the caustic where the ordinary ray solution of Eq. (28) fails, and it reduces uniformly to Eq. (28) far from the caustic where the latter expression is indeed valid and accurate. Furthermore, it can be shown to remain quite accurate even for intermediate values of  $\theta$  by comparing it with the exact Wiener-Hopf solution when only the first order terms are retained in the asymptotic approximation of the latter solution.

For ka small, higher order (or multiply) diffracted rays can contribute significantly to the backscatter from the open front end. The expressions for these higher order diffracted field contributions are discussed next.

(ii) Higher Order (or Multiply) Diffracted Ray Contributions to  $[S_{11}]$ 

Let  $\overline{E}^{bsm}$  denote the electric field associated with the rays backscattered from just the open front end (at z=0) after undergoing multiple diffractions across the aperture corresponding to the open front end. It is convenient to express  $\overline{E}^{bsm}$  as

$$\overline{E}^{bsm} = E_{\phi o}^{bsin} \hat{\phi} + E_{\theta o}^{bsin} \hat{\theta} \qquad (43)$$

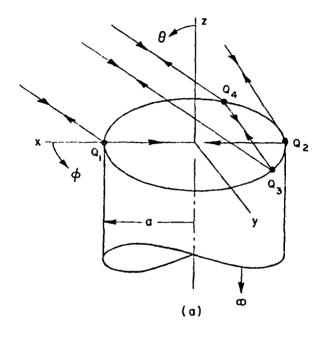
In determining  $E^{hsm}$  for backscatter directions which are not close to the axial (8=0) direction, only the doubly diffracted ray contributions

need to be included for accuracy when ka is not sufficiently large, because the contribution from all the other higher order multiply diffracted rays in general becomes sufficiently weak in this case as to be ignorable. It is noted that m=2 in the doubly diffracted ray contribution to Ebsm. i.e., Ebs2 is the doubly diffracted ray contribution to Ebsm. If ka is sufficiently large, then even the doubly diffracted ray contributions become insignificant in comparison to the singly diffracted ray contributions for the off-axis (or  $\theta$  not close to zero) backscatter directions. It is noted that the entire rim contributes to the diffraction at axial backscatter in contrast to just a few isolated points of diffraction on the rim which contribute to the backscatter in the off-axis case, because in the case of on-axis illumination the cylinder axis ( $\theta=0$ ) is a caustic of the rays diffracted by the rim. Consequently, an equivalent rim current solution must be obtained for 8 at and near zero in order to express Ebs2 at and close to the axial caustic as done for the first order or singly diffracted contribution Ebs! near the caustic. The equivalent current caustic solution for Ebs2 will be shown to generally yield numerical values which are approximately the same as those obtained from the off-axis solution for Ebs2 (which is based on a few isolated points of diffraction on the rim) in their common domain of overlap in 0. Thus one could switch from the caustic solution to the off-axis solution for  $\overline{E}^{\text{DS}2}$  in their domain of overlap. For the special case on axis (0=0), a separate solution for Ehsm is also provided (in addition to the caustic solution for Ebs2 mentioned earlier) which includes not only doubly, but

also triply and all the higher-order diffracted rays. The latter solution  $\overline{E}^{DSm}$  for  $\theta$ =0 which is admittedly more accurate than the caustic solution for  $\overline{E}^{DS2}$  at  $\theta$ =0, especially when ka is not sufficiently large, is also more cumbersome to use in practical applications. Furthermore, even when ka is not sufficiently large,  $\overline{E}^{DS2}$  is usually within one or two dBs of the value predicted by  $\overline{E}^{DSm}$ . Consequently, in the MSM based analysis for the problem configurations in Figures 1-4, only the second order  $\overline{E}^{DS2}$  solution will be employed for both,  $\theta$  near and far from zero to yield the higher-order diffraction contributions to the total backscattered field  $\overline{E}^{DSm}$ .

In the off-axis backscatter case, it is seen via Figure 12 that in general, a set of four rays contribute to the backscattered field after undergoing double diffraction. The total doubly diffracted backscattered field contribution can be expressed as

where the superscript, i-1-2-r, for instance, denotes that the incident field (-i-) is diffracted from point  $Q_1(-1-)$  to  $Q_2(-2-)$ , and then to the far field (-r-), and vice versa. It is found that points  $Q_3$  and  $Q_4$  are symmetrically located with respect to the xz-plane, and the cylindrical coordinates of  $Q_3$  ( $\rho$ =a,  $\phi$ = $\phi_3$ , z=0), and  $Q_4(\rho$ =a,  $\phi$ = $\phi_4$ , z=0) are obtained by letting



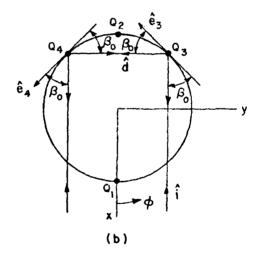


Figure 12. Mechanisms of 4 doubly diffracted rays across the aperture of the hollow circular cylinder.

$$\hat{i} \cdot \hat{e}_3 = \hat{d} \cdot \hat{e}_3$$
 (45)  
 $\hat{d} \cdot \hat{e}_4 = -\hat{i} \cdot \hat{e}_4$  (46)

$$\hat{d} \cdot \hat{e}_4 = -\hat{i} \cdot \hat{e}_4$$
 (46)

to satisfy the generalized Fermat's principle at points  $Q_3$  and  $Q_4$ . Here,  $\hat{i}$  and  $\hat{d}$  are the unit vectors of the incident direction and the diffracted ray direction across the aperture. eg and eq are the unit edge vectors at Q3 and Q4, respectively. i, d, e3, and e4 are given by

$$\hat{i} = -\hat{x} \sin \theta - \hat{z} \cos \theta$$
 (47)

$$\hat{d} = \hat{x} \cos \alpha + \hat{y} \sin \alpha \qquad . \tag{48}$$

$$\hat{\mathbf{e}}_3 = -\hat{\mathbf{x}} \sin \phi_3 + \hat{\mathbf{y}} \cos \phi_3 \quad . \tag{49}$$

$$\hat{e}_4 = -\hat{x} \sin \phi_4 + \hat{y} \cos \phi_4$$
 (50)

and,

$$\tan \alpha = \frac{\sin \phi_4 - \sin \phi_3}{\cos \phi_4 - \cos \phi_3} \quad . \tag{51}$$

Thus, by substituting Eqs. (47)-(51) into Eqs. (45)-(46), one obtains

$$\phi_3 = \frac{\pi}{2} + \tan^{-1}(\sin\theta) \quad . \tag{52}$$

and 
$$\phi_4 = -\phi_3$$
 (53)

It can be shown that

$$E_{\phi}^{112r} = E_{\phi}^{121r}; E_{\phi}^{134r} = E_{\phi}^{143r}$$

$$\vdots$$

which is to be expected from reciprocity. Therefore, Eq. (44) becomes

where

$$E_{\phi}^{i 12r} = E_{\phi}^{i} \frac{1}{2} \frac{-j2ka}{\pi kasin9} \frac{\cos^{2}{\theta}}{\cos^{2}{\theta}} \frac{-jkR}{R}$$
(56)

$$E_{\theta}^{i12r} = E_{\theta}^{i} \frac{a}{2} \frac{e}{\pi kasin\theta} \frac{sin^{2}\frac{3}{2}}{\cos^{2}\theta} \frac{e^{-jkR}}{R}$$
 (57)

$$E_{\phi}^{i34r} = -E_{\phi}^{i}(D_{s}^{2}\sin^{2}\theta + D_{h}^{2}\cos^{2}\theta)e^{j2ka\sin\theta\cos\phi_{3}} \cdot \sqrt{\frac{i34}{s(\rho^{i34} + s)}}e^{-jks}\sqrt{\rho^{34r}} \frac{e^{-jkR}}{R}.$$
(58)

$$E_{\theta}^{i34r} = E_{\theta}^{i}(0_{h}^{2}\sin^{2}\theta + 0_{s}^{2}\cos^{2}\theta)e^{j2ka\sin\theta\cos\phi}, \sqrt{\frac{i34}{s(\rho^{i34} + s)}}e^{-jks}\sqrt{\rho^{34r}} = \frac{e^{-jkR}}{R}.$$
(59)

and,

$$D_{s} = \frac{-e}{2\sqrt{2\pi k} \sin \beta_{0}^{t}} \left[ \sec \left( \frac{\pi}{4} - \frac{\xi}{2} \right) \pm \sec \left( \frac{\pi}{4} + \frac{\xi}{2} \right) \right] ; \qquad (60a)$$

$$\sin \beta_0' = \frac{1}{\sqrt{1+\sin^2 \theta}}$$
;  $\xi = \tan^{-1} \left( \frac{\sin^2 \theta}{\sqrt{1-\sin^4 \theta}} \right)$ ; (60b)

$$s = \frac{2a}{\sqrt{1 + \sin^2 \theta}}$$
 (60c)

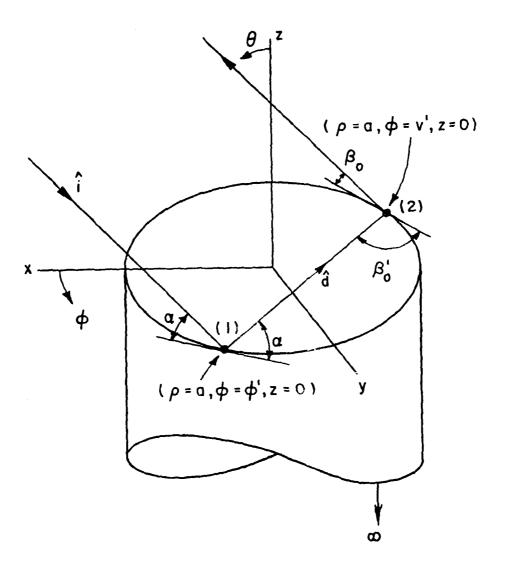


Figure 13. The doubly diffracted ray for the equivalent current solution. Here,  $\beta_0^{t}$  is not necessarily equal to  $\beta_0^{\cdot}$ 

$$\rho^{i34} = \frac{-a}{(1+\sin^2\theta)^{3/2}}; \quad \rho^{34r} = -a \frac{1+2\sin^2\theta}{2\sin^2\theta} (1+\sin^2\theta)^{-3/2}. \quad (60d)$$

Near the caustic region (0+0), Eqs. (56)-(59) break down and the equivalent current formulation is employed to correct the results as follows. Let  $(a, \phi', 0)$  and (a, v', 0) be the cylindrical coordinates of the first and second diffraction points on the rim as illustrated in Figure 13. To satisfy the generalized Fermat's principle at point (1), it can be found that

$$\hat{d} = \hat{x} \cos \beta + \hat{y} \sin \beta . \tag{61}$$

where

$$\beta = \pi + \phi' - \sin^{-1} \left( \sin \theta \sin \phi' \right) . \tag{62}$$

Thus, v' and  $\phi'$  are related by

$$v' = \pi + \phi' - 2\sin^{-1}(\sin\theta\sin\phi') . \tag{63}$$

which is illustrated in Figure 14. The doubly diffracted field in the backscatter direction can be expressed in terms of the equivalent current form as

$$\overline{E}^{bs2} = \frac{jkZ_0}{4\pi} \left[ \int_0^{2\pi} dv' \ a(\widehat{R}x\widehat{R}xI_2\widehat{v}' + Y_0\widehat{R}xM_2\widehat{v}')e^{jk\rho\cdot\widehat{R}} \right] \frac{e^{-jkR}}{R} . \quad (64)$$

where

$$I_2(v') = -Y_0 \sqrt{\frac{8\pi}{Jk}} \frac{D_S(\psi, \psi'; \beta'_0)}{\sin \beta_0} (E^{i12} \cdot \hat{v}')_{rim}$$
 (65)

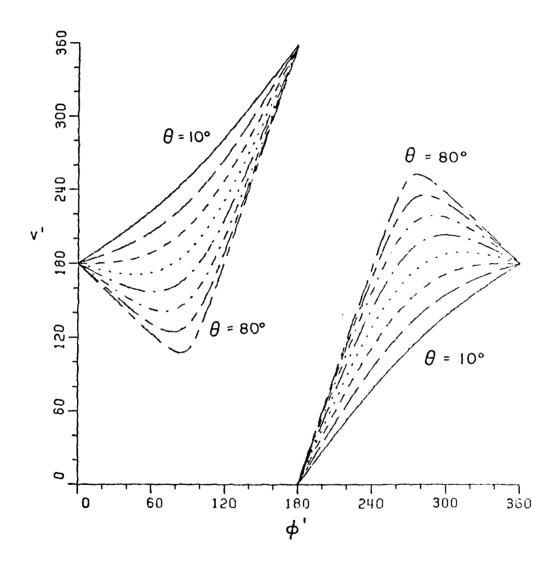


Figure 14. The relationship of  $\phi'$  and v' with  $\theta$  varied from  $10^\circ$  to  $80^\circ$  in  $10^\circ$  step.

$$M_2(v') = -Z_0 \sqrt{\frac{g_{\pi}}{jk}} \frac{D_h(\psi, \psi'; \beta_0')}{\sin \beta_0} (\widetilde{H}^{12} \cdot \hat{v}')_{rim} \qquad (66)$$

and

$$\psi' = \frac{\pi}{2}$$
,  $\psi' = \pi + \tan^{-1}(\tan \theta \cos v')$ ; (67a)

$$\sin \beta_0 = \sqrt{1 - \sin^2 \theta \sin^2 \phi'} , \quad \sin \beta_0 = \sqrt{1 - \sin^2 \theta \sin^2 v'} ; \quad (67b)$$

$$\hat{\mathbf{v}}' = -\hat{\mathbf{x}} \sin \mathbf{v}' + \hat{\mathbf{y}} \cos \mathbf{v}' ; \qquad (67c)$$

$$\widehat{R} \times \widehat{R} \times \widehat{V}' = -\theta \cos \theta \sin (\phi - V') - \phi \cos (\phi - V') , \qquad (67d)$$

$$\hat{R}xv' = -\theta\cos(\phi - v') + \phi\cos\theta\sin(\phi - v') , \qquad (67e)$$

with  $\hat{\theta} = \hat{x}\cos\theta - \hat{z}\sin\theta$ ,  $\hat{\phi} = \hat{y}$  and  $\phi = 0$  in this case.

 $\overline{E}^{i12}$  and  $\overline{H}^{i12}$  are the electric and magnetic fields incident at the second diffraction point (2), after being diffracted from point (1).  $\overline{E}^{i12}$  and  $\overline{H}^{i12}$  can be evaluated via [1] as follows.

$$\overline{E}^{112} = \hat{\beta}_0 E_{\beta_0}^{112} + \hat{\psi} E_{\psi_0}^{112} . \tag{68}$$

$$\vec{H}^{112} = \hat{\beta}_0 H_{\beta_0}^{112} + \hat{\psi} H_{\psi_0}^{112} . \tag{69}$$

where

$$\hat{\beta}_0 = \hat{x} \sin \gamma - \hat{y} \cos \gamma$$

$$\hat{\Psi} = \hat{z} \qquad . \tag{70a}$$

and

$$\gamma = \pi + \phi' - \sin^{-1}(\sin\theta\sin\phi') \quad . \tag{70b}$$

Since  $\hat{v}'$  .  $\hat{\psi}$  =0, one only needs to evaluate  $E_{\beta_0}^{i2}$  and  $H_{\beta_0}^{i2}$  . Thus, one obtains [1]

$$E_{\beta_0}^{i12} = -E_{\beta_0}^{i} D_s \sqrt{\frac{\rho}{s(\rho+s)}} e^{-jks} \qquad (71)$$

$$H_{\beta_0}^{i12} = -H_{\beta_0}^{i} D_h \sqrt{\frac{\rho}{s(\rho+s)}} e^{-jks} \qquad (72)$$

where

$$E_{\beta_0}^{i} = [E_{\theta}^{i} \sin \phi' \cos \delta - E_{\phi}^{i} (\sin \theta \sin \delta + \cos \phi' \cos \theta \cos \delta)]e^{jka\sin \theta \cos \phi'}.$$
(73a)

and

$$H_{\beta_0}^{\dagger} = [H_{\theta}^{\dagger} \sin \phi' \cos \delta - H_{\phi}^{\dagger} (\sin \theta \sin \delta + \cos \phi' \cos \theta \cos \delta)] e^{jka\sin \theta \cos \phi'}.$$
(73b)

with

$$\tan \delta = \frac{\sin \theta \cos \phi'}{\cos \theta} \qquad (74)$$

Also,

$$\rho = \frac{a \sin^2 \beta_0}{\sin \theta \cos \phi' - \sin \beta_0}, \qquad (75a)$$

and

$$s = 2a \sin \beta_0$$
 (75b)

The  $D_s$  in Eqs. (71)-(72) is given by

$$\frac{\partial}{\partial s} = \frac{-j\frac{\pi}{4}}{2\sqrt{2\pi k} \sin \beta_0} \left[ \sec\left(\frac{\psi - \psi'}{2}\right) \mp \sec\left(\frac{\psi + \psi'}{2}\right) \right] ,$$
(76a)

with

$$\psi' = \pi + \tan^{-1} \left( \frac{\sin \theta \cos \phi'}{\cos \theta} \right) , \quad \psi = \frac{\pi}{2} ; \qquad (76b)$$

$$\sin\beta_0 = \sqrt{1 - \sin^2\theta \sin^2\phi'} . \tag{76c}$$

It is noted that the integrations in Eq. (64) can be carried out numerically only for  $0<30^\circ$ . When  $0>30^\circ$ , a complication arises in that more than one singly diffracted ray can strike the second diffraction point (2) as may be readily seen from Figure 14. In the equivalent current solution, this proximity of the ray fields at the point (2) leads to a singular result. On the other hand,  $0>30^\circ$  is usually a sufficient condition to meet the criterion ka sin 0>>1, so that the

equivalent current solution of Eq. (64) asymptotically reduces to the four-point result in Eqs. (56)-(59) which is valid far from the axis (at  $\theta$ =0). Furthermore, the four point doubly diffracted ray contribution remains bounded and accurate even in the case for which the equivalent current solution becomes singular. Thus, in practical computations, it is recommended that the equivalent current solution for Ebs2 which remains valid at and near the axial caustic (at  $\theta$ =0) be switched to the off-axis 4-point solution for Ebs2 whenever  $\theta$ >30°.

Although the doubly diffracted ray contribution to the backscattered electric field Ebs2 has been evaluated above for both, the off-axis or  $0\neq 0$  case and also for the paraxial case where 9 is at or close to zero (and  $\theta=0$  is the caustic direction), a separate solution will also be obtained below for the general mth-order multiply diffracted field Ebsm in the special case of on-axis incidence (i.e., axial backscatter) as mentioned above. The reason for developing an expression for  $\overline{E}^{bsm}$  for the special case of axial (0=0) backscatter is that it would enable one to estimate the importance of the triple and higher order multiple diffraction effects which are not present in the expression for the doubly diffracted field Ebs?. Ebsm will be developed below only for the case of axial (0=0) backscatter because it is tractable in this case. Such an mth-order result for Ebsm which would be valid for the off-axis (or 0±0) case cannot be obtained in any tractable fashion. Furthermore, multiple diffraction effects beyond the doubly diffracted ones are in general quite weak for the off-axis (or

 $0\neq 0$ ) case and hence there is, in general, no need to consider the mth-order solution (for m>2) in the latter case.

The general mth-order solution  $\overline{E}^{bsm}$  for the 0=0 (axial backscatter) case will be constructed in terms of the previously described equivalent rim current concept as follows. First the singly diffracted contribution  $\overline{E}^{bs1}(\theta=0)$  will be listed to be followed by the expressions which will be developed for the doubly and the triply diffracted contributions  $\overline{E}^{bs2}(\theta=0)$  and  $\overline{E}^{bs3}(\theta=0)$ . A sequence will then be shown to emerge from  $\overline{E}^{bs1}(\theta=0)$ ,  $\overline{E}^{bs2}(\theta=0)$ , and  $\overline{E}^{bs3}(\theta=0)$  which can be directly generalized to  $\overline{E}^{bs4}(\theta=0)$ ,  $\overline{E}^{bs5}(\theta=0)$ , etc., and hence to  $\overline{E}^{bsm}(\theta=0)$  via the process of induction. One begins with the first-order (or singly diffracted) contribution  $\overline{E}^{bs1}(\theta=0)$  which is developed as follows. Referring to Figure 15, the incident field is given for the case of axial incidence by

$$\mathbf{\bar{E}}^{i} = -\hat{\mathbf{x}} \, \mathbf{E}_{0} \, \mathbf{e}^{jkz} \quad . \tag{77}$$

Since  $\psi = \pi$  in Eqs. (35)-(36), only the equivalent electric current contributes to the axially backscattered field; i.e., the equivalent magnetic current gives a vanishing contribution. Thus, as in Eq. (37),

$$\overline{F}^{hs1}(\theta=0) = \frac{jkZ_0}{4\pi} \cdot \frac{e^{-jkR}}{R} \int_0^{2\pi} e^{jk\overline{\rho}' \cdot \hat{R}} (\widehat{RxRxI}_1 \hat{\phi}') ad\phi' . \qquad (78)$$

with

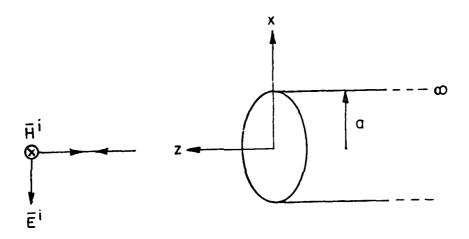


Figure 15. On-axis backscattering from the open end of a semi-infinite conducting hollow pipe.

$$\hat{R} = \hat{z} ,$$

$$\bar{p}' = a(\hat{x} \cos \phi' + \hat{y} \sin \phi') ,$$

$$\hat{\phi}' = -\hat{x} \sin \phi' + \hat{y} \cos \phi' .$$
(79)

It follows that

$$\overline{E}^{bs1}(\theta=0) = \frac{jkZ_0}{4\pi} \cdot \frac{e}{R} \int_0^{2\pi} (\hat{x}\sin\phi' - \hat{y}\cos\phi') I_1 d\phi' . \qquad (80)$$

where

$$I_{1} = -\frac{\hat{\phi}' \cdot \overline{E}'}{N_{O}} D_{S}(\psi' = \psi = \pi) \cdot \sqrt{\frac{8\pi}{k}} e$$

$$= -j \frac{2E_{O}}{kZ_{O}} \sin \phi' \quad \text{at } z \approx 0 . \tag{81}$$

Thus, one obtains

$$E = (\theta=0) = \hat{x} E_0 \cdot \frac{a}{2} \cdot \frac{e}{R}$$
 when  $\theta=0$  (82)

fnis result checks with that in Eqs. (41)-(42), as it should, when the latter is specialized to 0=0.

One can extend the above approach to obtain the axially backscattered field due to the 2nd-order (or doubly diffracted) ray interaction as

$$\frac{-bs2}{E} (\theta=0) = \frac{jka}{4\pi} \cdot Z_0 \cdot \frac{e}{R} \int_0^{-jkR} (\hat{x} \sin \phi' - \hat{y} \cos \phi') I_2 d\phi' \cdot$$
(83)

in which only the equivalent electric current  $I_2$  is non-zero (the equivalent magnetic current contribution vanishes again). Specifically,

$$I_2 = -\frac{\hat{\phi}' \cdot E_2^{\dagger}}{Z_0} \cdot D_S(\psi' = \frac{\pi}{2} \cdot \psi = \pi) \sqrt{\frac{8\pi}{k}} e^{-j\frac{\pi}{4}}$$
 (84)

and

$$\overline{E}_{2}^{i} = \hat{\phi}' E_{0} \cdot \sin \phi' \cdot D_{s}(\psi' = \frac{\pi}{2}, \psi = \pi) \sqrt{\frac{\rho}{2a(\rho + 2a)}} e^{-2jka}$$

$$\rho = -a \qquad (85)$$

Therefore,

$$I_2 = -\frac{2E_0}{kZ_0} \cdot \sin \phi' \frac{1}{\sqrt{\pi ka}} \cdot e^{-j(2ka + \frac{\pi}{4})} \qquad (86)$$

By comparing  $I_2$  in Eq. (86) with  $I_1$  in Eq. (81), one can readily obtain

$$\overline{E}^{hs2}$$
 ( $\theta=0$ ) =  $u_2 \cdot \overline{E}^{hs1}$  ( $\theta=0$ ) • (37)

where u2 is given by

$$u_2 = -\frac{1}{\sqrt{\pi k a}} e^{-j(2ka - \frac{\pi}{4})}$$
 (88)

Likewise, one may obtain the axially backscattered field  $\overline{E}^{hs3}(\theta=0)$  due to the 3rd-order (or triply diffracted) ray interaction via the equivalent current concept as

$$\overline{E}^{b \leq 3} \quad (\theta = \theta) = \frac{jka}{4\pi} \cdot Z_0 \cdot \frac{e^{-jkR}}{R} \int_0^{2\pi} (\hat{x} \sin \phi' - \hat{y} \cos \phi') I_3 d\phi' \cdot$$
(89)

with

$$I_3 = -\frac{\hat{\phi}' \cdot E_3^{\frac{1}{3}}}{Z_0} \cdot n_S \quad (\psi' = \frac{\pi}{2}, \psi = \pi) \cdot \sqrt{\frac{8\pi}{k}} e^{-\frac{j\pi}{4}} \text{ at } z=0$$
 (90)

As shown in Figure 16, it is noted that the ray singly diffracted from any point on the rim (edge) traverses across the aperture to be diffracted again from a diametrically opposite point on the rim, thereby producing a doubly diffracted ray. Likewise, the doubly diffracted ray which traverses the aperture can in turn be diffracted once again from a diametrically opposite point on the edge to produce the triply diffracted ray, and so on. Now, the doubly diffracted ray which traverses the aperture (to produce the triply diffracted ray) will lie on the reflection shadow boundary of the singly diffracted ray (which produces the doubly diffracted ray). Due to the fact that the doubly diffracted ray lies on the reflection shadow boundary, the field associated with that doubly diffracted ray in the aperture is non-ray optical. Thus, one cannot use the edge diffraction coefficient which is

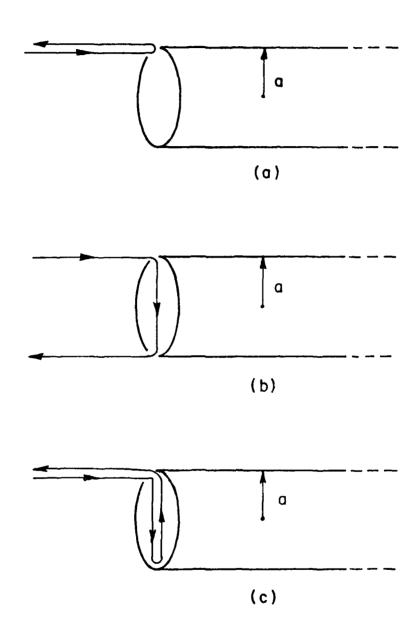


Figure 16. Mechanisms of the scattering from the open end of a semi-infinite conducting hollow pipe.

valid only for an incident ray optical field to directly calculate the field of the triply diffracted ray. However, it is possible in this special case to decompose the non-ray optical doubly diffracted field in the aperture into two distinct ray optical components. The diffraction of each of these two ray optical components can then be directly calculated using the edge diffraction coefficient which is valid only for a ray optical incident field. Let the two ray optical components of the non-ray optical doubly diffracted ray field along the aperture (i.e., along the reflection boundary), be denoted by  $E_{3,1}$  and  $E_{3,2}$ , respectively when the field is evaluated in the limit as the observation point moves to the aperture from the shadowed side of the reflection boundary. Let the total original non-ray optical field be denoted by  $E_{3,1}$  thus,

$$\overline{E}_{3}|_{1im} = \overline{E}_{3,1}^{i} + \overline{E}_{3,2}^{i}$$
 (91)  
from shadow side

If the limit of the total non-ray optical field value E3 in the aperture was evaluated from the lit side of the reflection boundary, one would obtain

$$\overline{E}_{3}|_{1im} = \overline{E}_{3,1} - \overline{E}_{3,2} + \overline{E}_{3}$$
 (92)

where  $\overline{E_3}^{(go)i}$  is the geometrical optics field "reflected" from the edge illuminated by the singly diffracted field in the aperture. This term must be included in the total field calculation since it is non-zero on the lit side of its reflection boundary. Furthermore, it can be shown that

$$\overline{E}_{3,2} = \frac{1}{2} \overline{E}_{3}(go)^{\dagger} \qquad (93)$$

so that

$$(\overline{E}_3)$$
 =  $\overline{E}_3$  |  $\overline{E}_3$  . (94)  
Shadow side |  $\overline{E}_3$  .

as expected since the field in the aperture after the second interaction must be continuous across the aperture. The ray optical components  $\overline{E}_{3,1}^i$  and  $\overline{E}_{3,2}^i$  are explicitly given by

$$\frac{1}{E_{3,1}} = \frac{1}{E_2} \int_{0}^{1} \int_{0}^{1} \sqrt{\frac{\rho}{2a(\rho+2a)}} e^{-j2ka} e^{-j2ka}$$
(95)

and

$$\bar{E}_{3,2}^{i} = \frac{1}{2} \bar{E}_{2}^{i} (-1) \sqrt{\frac{\rho_{1}^{r} \rho_{2}^{r}}{(\rho_{1}^{r}+2a)(\rho_{2}^{r}+2a)}} e^{-j2ka} \qquad (96)$$

with

$$D_{S}^{i} = \frac{-e^{-j\frac{\pi}{4}}}{2\sqrt{2\pi k}} \qquad (97)$$

Here p is obtained by [1] to yield p=-a.  $p_1^r$  and  $p_2^r$  are the two principal radii of curvature of the reflected wavefront associated with  $\overline{E}_3^{(g_0)i}$ ; they are given as follows [1].

$$\frac{1}{\rho_1^{\Gamma}} = \frac{2}{r_c \cos \theta^{\dagger}} + \frac{1}{\ell_1} \qquad (98)$$

and

$$\frac{1}{\rho_2^{\Gamma}} = \frac{2 \cos \theta^{\dagger}}{\Gamma_c^{\dagger}} + \frac{1}{\ell_2} \qquad (99)$$

where  $r_c$  and  $r_c'$  are the two principal radii of curvature on the surface. In this case,  $\theta^1=0$ ,  $r_c=-a$ ,  $r_c'=\infty$ ,  $\ell_1=a$ , and  $\ell_2=2a$ . Consequently,

$$\rho_1^{\Gamma} = -a \quad ; \quad \rho_2^{\Gamma} = 2a \quad .$$
 (100)

One thus obtains

$$\overline{E}_3^j = u_3 \overline{E}_2^j \qquad . \tag{101}$$

where  $\overline{E}_2$  is as in Eq. (85) and ug is given by

$$u_3 = \frac{-j}{2\sqrt{2}} e^{-j2ka} \left(1 + \frac{e^{-j\frac{\pi}{4}}}{\sqrt{2\pi ka}}\right) . \tag{102}$$

Due to the similarities in the expressions between  $I_2$  and  $I_3$  (see Eqs. (84) and (90)), one readily obtains

$$\overline{E}^{bs3}(\theta=0) = u_3 \overline{E}^{bs2}(\theta=0) . \qquad (103)$$

Combining Eqs. (82), (87), and (103), one can obtain the on-axis backscattered field  $\overline{E_0}(\theta=0)$  up to and including the triply diffracted rays as follows.

$$\overline{E}_{o}^{s}(\theta=0) = \sum_{m=1}^{3} \overline{E}^{bsm}(\theta=0) = \hat{x} E_{o} \frac{a}{2} \frac{e^{-jkR}}{R} \{1+u_{2}(1+u_{3})\} . \tag{104}$$

Therefore, from Eqs. (4) and (104),

$$S_{\theta\theta} \mid_{\theta=0} = S_{\phi\phi} \mid_{\theta=0} = -\frac{a}{2} \{1 + u_2(1 + u_3)\}$$
 (105)

or, equivalently, the on-axis RCS from the open end of a semi-infinite, perfectly-conducting circular pipe is given by

$$\sigma \mid_{\theta=0} = \pi a^2 \mid 1 + u_2(1 + u_3) \mid^2 \qquad (106)$$

The above results for  $\overline{E}^{bs}I(\theta=0)$ ,  $\overline{E}^{bs}2(\theta=0)$ , and  $\overline{E}^{bs}3(\theta=0)$  can be extended to obtain the mth-order diffracted ray contribution to the axial backscattered field  $\overline{E}^{bs}_0$  as

$$\overline{E}^{\text{bsm}}(\theta=0) = \frac{jka}{4\pi} Z_0 \frac{e^{-jkR}}{R} \int_0^{2\pi} (\hat{x} \sin \phi' - \hat{y} \cos \phi') I_{\text{in}} d\phi' . \qquad (107)$$

and

$$I_{m} = -\frac{\hat{\phi}' \cdot E_{m}^{\dagger}}{Z_{0}} D_{S}(\psi' = \frac{\pi}{2}; \psi = \pi) \sqrt{\frac{8\pi}{k}} e^{-j\frac{\pi}{4}}; \begin{cases} ad \\ m \ge 2 \end{cases}$$
(108)

where  $\overline{E}_{m}^{i}$  is obtained by generalizing the procedure used in obtaining  $\overline{E}_{3}^{i}$  of Eq. (94). Each successive bounce (or diffraction) of a ray optical field component in the aperture gives rise to a non-ray optical field which in turn can be decomposed into two ray optical components as in Eq. (91). Furthermore, each of the latter two ray optical components generates two additional ray optical field components upon diffraction, and so on. Finally, as shown in Appendix B, the total on-axis backscattered field which includes all m multiple interactions, where  $m+\infty$ , is found to be

$$\frac{-s}{E_0}(\theta=0) = \sum_{m=1}^{\infty} \frac{-bsm}{E}(\theta=0) = \hat{x} E_0 \frac{a}{2} \frac{e^{-jkR}}{R} (1 + u_2 \frac{C}{1-AC}) .$$
 (109)

where

$$A = -\frac{e^{-j(2ka - \frac{\pi}{4})}}{4\sqrt{\pi ka}} \qquad (110)$$

$$C = 1 + \sum_{n=1}^{\infty} (jB)^n \sqrt{\frac{1}{n+1}}$$
 (111)

and

$$B = -\frac{1}{2}e^{-j2ka} (112)$$

Also, the on-axis RCS of the open front end (z=0) is obtained from Eq. (109) as

$$\sigma \mid_{\theta=0} = \pi a^{2} \mid_{\theta=0} 1 + u_{2} \frac{c}{1 - AC} \mid_{\theta=0} 2 \qquad (113)$$

Numerical results for the off-axis RCS (normalized to  $\pi a^2$ ) of just the rim, or the open front end (at z=0) of the configurations in Figures 1-4, is illustrated in Figures 17-18 as a function of 0 for fixed values of ka. These calculations are based on Eqs. (41)-(42), (55)-(59), and (64)-(76). It is noted that the RCS components  $\sigma_{00}$  and  $\sigma_{\phi\phi}$  in these figures are defined by

$$\sigma_{\theta\theta} = \lim_{R \to \infty} 4\pi R^2 \frac{\left| E_{\theta\theta}^{S} \right|^2}{\left| E_{\theta}^{i} \right|^2} = 4\pi \left| S_{\theta\theta} \right|^2 \qquad (114)$$

and

$$\sigma_{\phi\phi} = \lim_{R \to \infty} 4\pi R^2 \frac{\left|E_{\phi 0}^{S}\right|^2}{\left|E_{\phi}^{i}\right|^2} = 4\pi \left|S_{\phi\phi}\right|^2 \qquad (115)$$

with

$$E_{\phi 0}^{S} = E_{\phi 0}^{bs1} + E_{\phi 0}^{bs2} \qquad (116)$$

Some of these results are compared with corresponding results based on the exact Wiener-Hopf solution in Figure 13. The agreement between these two independent results is seen to be good. Likewise, numerical results for the on-axis RCS are shown in Figure 19, as a function of  $a/\lambda$  ( $\lambda$  is the wavelength). A result based on the Wiener-Hopf solution

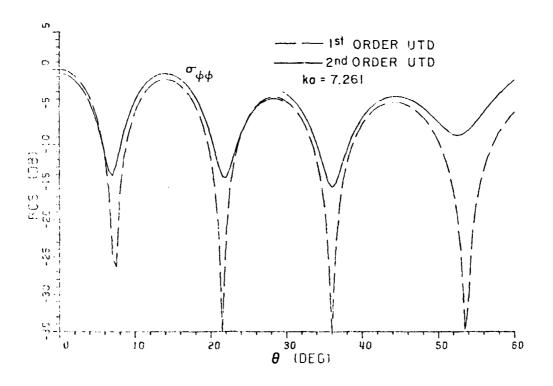
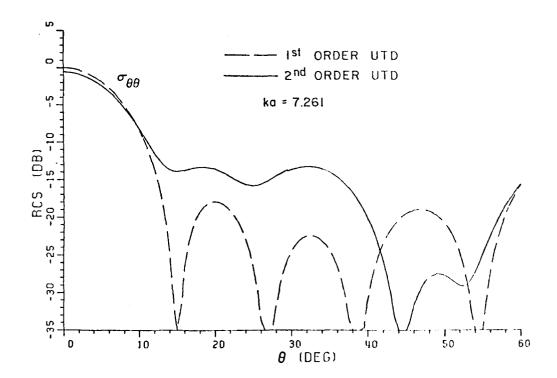


Figure 17. Off-axis RCS (normalized to  $\pi a^2$ ) of a semi-infinite, hollow, perfectly conducting circular with ka=7.261. The equivalent current technique is employed for  $\theta < 30^\circ$ .

(a)



(b)

Figure 17. (continued)

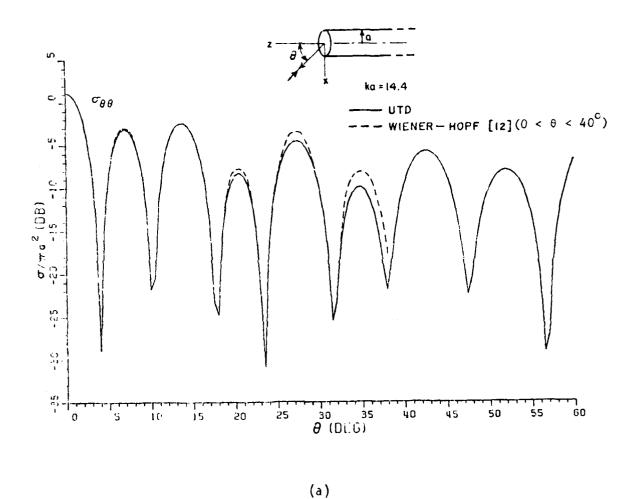


Figure 18. Off-axis RCS (normalized to  $\pi a^2$ ) of a semi-infinite, hollow, perfectly conducting circular cylinder with ka=14.4. The equivalent current technique is employed for 0<30° in UTD calculations.

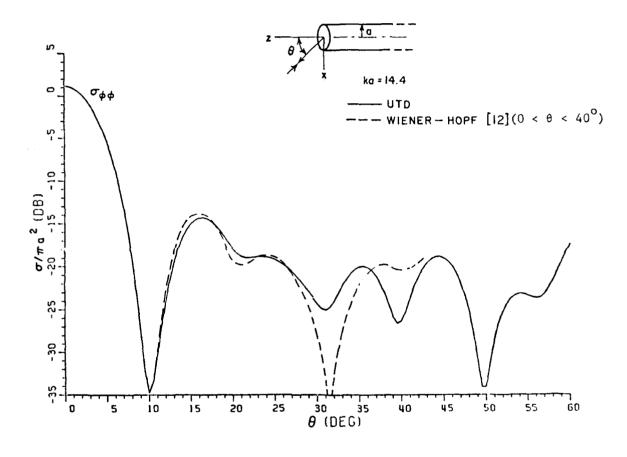
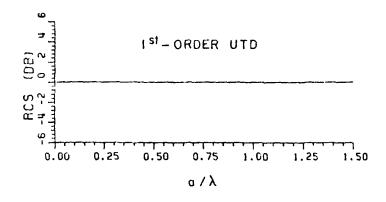
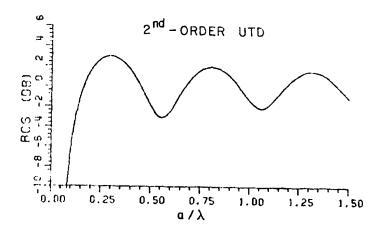


Figure 13. (continued)

(b)

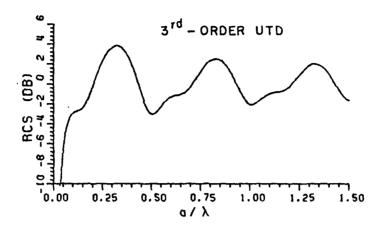


(a) 1st-order

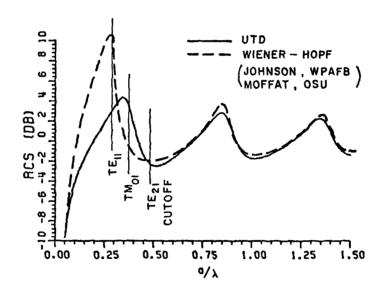


(b) 2nd-order

Figure 19. On-axis backscattered RCS (normalized to  $\pi a^2$ ) from a semi-infinite, hollow, perfectly-conducting circular cylinder with various terms included in UTD calculations.



(c) 3rd-order



(d) all interaction terms included

Figure 19. (continued)

for the on-axis illumination is also compared with the present on-axis solution which includes multiply diffracted rays of all orders (see Eq. (113)). Again the agreement between the two solutions is seen to be good. It is possible that the inclusion of slope diffraction effects on the multiply diffracted fields could improve the accuracy of the present solution for smaller ka even further in the case of on-axis illumination.

## B. Ray Analysis for $[S_{12}]$

The elements of the scattering matrix  $[S_{12}]$  describe the manner in which the modal fields propagating within the waveguide region radiate into the exterior free space region from the open front end (at z=0) of the semi-infinite circular pipe (waveguide), as depicted in Figure 7. The elements of  $[S_{12}]$  are found here via the UTD together with its modifications which are required within caustic regions. However, in order to use the UTD ray technique systematically in this case, it is necessary to convert each propagating waveguide modal field into an equivalent ray optical field at the rim (edge) associated with the open front end (at z=0). This procedure is in contrast to the UTD ray technique employed by Narasimhan [18] for analyzing the same problem as the one being considered in the present UTD ray analysis of  $[S_{12}]$ . Narasimhan [18] does not convert his waveguide modal field into an equivalent ray optical field in his UTD analysis. Consequently, the UTD, which requires that the edge diffraction coefficient be employed only for a "ray-optical" incident field, cannot be strictly applied to a "modal" field incident at the edge (or rim). On the other hand, it appears that if the propagation constant of a mode approaches the free space wave number, as is the case for a mode which is very far from cutoff, then the modal field behaves almost like a ray optical field and Narasimhan's [18] procedure may work reasonably well in that case. However, Narasimhan's [18] procedure is expected to become inaccurate for a mode even moderately near cutoff; whereas, the present UTD procedure which is described below will not suffer from the limitation present in Narasimhan's procedure [18].

Table 1 indicates the various electric and magnetic field components for the  ${\sf TE}_{nm}$  and  ${\sf TM}_{nm}$  modes in a circular waveguide. The propagation constants of the  ${\sf TE}_{nm}$  and the  ${\sf TM}_{nm}$  modes are given by

$$\beta_{nm} = \sqrt{k^2 - (\frac{p_{nm}^2}{a})^2}$$
 and  $\beta_{nm} = \sqrt{k^2 - (\frac{p_{nm}}{a})^2}$ , respectively. Consider a

typical modal field component whose  $\rho$  and z variation is given by

$$J_{n}(\xi_{nm}) = \begin{cases} \xi_{nm} = \begin{cases} P'_{nm} & \text{for } TE_{nm} \text{ mode} \\ P_{nm} & \text{for } TM_{nm} \text{ mode} \end{cases}$$

$$\gamma_{nm} = \begin{cases} \beta'_{nm} & \text{for } TE_{nm} \text{ mode} \\ \beta_{nm} & \text{for } TM_{nm} \text{ mode} \end{cases}$$
(117)

One may decompose  $J_n(\xi_{nm}\rho)$  in Eq. (117) as  $J_n(x) = \frac{H_n^{(2)}(x) + H_n^{(1)}(x)}{2}$ ; thus, Eq. (117) becomes

$$J_{n}(\xi_{nm}\rho)e^{-j\gamma_{nm}|z|} = \frac{H_{n}^{(2)}(\xi_{nm}\rho)}{2} e^{-j\gamma_{nm}|z|} + \frac{H_{n}^{(1)}(\xi_{nm}\rho)}{2} e^{-j\gamma_{nm}|z|}.$$
(118)

TABLE 1
PROPERTIES OF MODES IN CIRCULAR WAVEGUIDES

	TE modes	TM modes
h <sub>z</sub>	$jN_{nin}' \kappa_{nin}'^2 J_n(\frac{p_{nmp}}{a}) \begin{cases} \cos n\phi \\ \sin n\phi \end{cases}$	0
e <sub>z</sub>	0	$jN_{nm}\kappa_{nm}^2 J_n \left(\frac{p_{nm}\rho}{a}\right) \begin{cases} \cos n\phi \\ \sin n\phi \end{cases}$
h <sub>p</sub>	$N_{nm}' \frac{\beta_{nm}\rho_{nm}}{a} J_n'(\frac{\rho_{nm}\rho}{a}) \begin{cases} \cos n\phi \\ \sin n\phi \end{cases}$	- e <sub>φ</sub> Z <sub>e,nm</sub>
hφ	$N'_{nm} \frac{n \beta_{nm}}{\rho} J_n \frac{(P'_{nm}\rho)}{a} \begin{cases} -\sin n\phi \\ \cos n\phi \end{cases}$	e <sub>p</sub> Z <sub>e,nm</sub>
e p	Z <sub>h,nm</sub> h <sub>φ</sub>	$N_{nm} \frac{\beta_{nm} p_{nm}}{a} J_n'(\frac{p_{nm} p}{a}) \begin{cases} \cos n q \\ \sin n q \end{cases}$
e ø	-Z <sub>h,nm</sub> h	$N_{nm} \frac{n\beta_{nm}}{\rho} J_n(\frac{p_{nm}\rho}{a}) \begin{cases} -\sin n\phi \\ \cos n\phi \end{cases}$
Z <sub>h</sub> ,nm	$\frac{k}{\beta_{\min}} Z_0$	
Z <sub>e,nm</sub>		$\frac{3 \text{nm}}{k} Z_0$
κ' nm	Pnm	

TABLE 1
(CONTINUED)

TE modes  $\frac{p_{nm}}{a}$   $\frac{p_{nm}}{a}$   $\frac{2}{J_n(p_{nm}^i)\sqrt{\pi\omega\mu\beta_{nm}^i\varepsilon_{on}(p_{nm}^{i-2}-n^2)}}$   $\frac{2}{p_{nm}J_n^i(p_{nm})\sqrt{\pi\omega\varepsilon\beta_{nm}\varepsilon_{on}}}$ 

The normalization factors  $N_{nm}$  and  $N_{nm}$  yield unit power in each mode. Here,  $\varepsilon_{0n}$  = 2 for n = 0, and 1 for n > 0. From the large argument asymptotic form of H(2)( $\xi_{nin}$ P) and for real  $\gamma_{\text{DM}}$ , it is easily verified that the first term in Eq. (118) containing  $\mathrm{H}_\mathrm{n}^{(2)}(\xi_\mathrm{nm}
ho)$  represents a conical wavefront propagating away from the guide center, (i.e., away from the guide axis) as shown in Figure 20; whereas, the second term which contains  $H_n^{(1)}(\xi_{nm}\rho)$  is a conical wavefront (also for real  $\gamma_{nm}$ ) propagating toward the guide center (or collapsing on the guide axis). Clearly, the field of the conical wave which propagates away from the guide axis, i.e., which propagates toward the rim at the open front end (at z=0), constitutes the ray optical field which is incident at the rim (edge). This incident field undergoes diffraction at the circular edge and thus contributes to the field radiated into the exterior region by the modal field within the waveguide. Far from the waveguide axis ( $\theta$ =0), one may use the UTD to calculate the field radiated from the open end in terms of the two diffracted rays shown in Figure 21. In accordance with the generalized Fermat's principle, these two rays originate at the two points of diffraction on the circular rim (at z=0) which correspond to the intersection of the rim with the plane defined by the far zone observation point and the axis of the open-ended circular waveguide. The first order, or the singly diffracted field associated with the two rays diffracted from the rim is directly produced by the incident ray optical field which is incident there. A part of this singly diffracted field also initiates multiply diffracted rays which bounce back and forth across the aperture; at each bounce, a part of the energy is again radiated to the far zone observation point along the

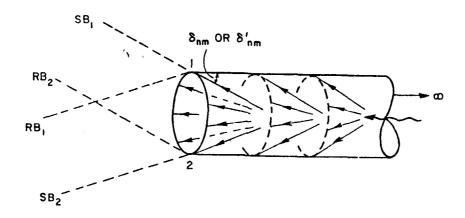


Figure 20. Conversion of waveguide modal field into the conical ray field.

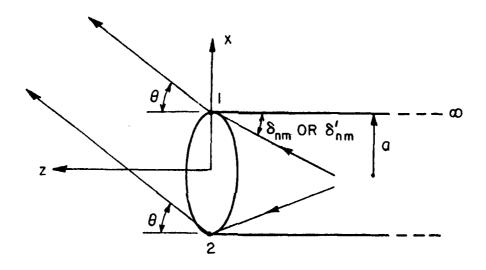


Figure 21. Diffraction from the rim of the perfectly conducting circular waveguide by an incident conical ray field.

aforementioned same two ray paths after being multiply diffracted from the same two points of diffraction on the rim. The latter contribution to the radiation field which results from the multiply diffracted rays may be included for improved accuracy when ka is not sufficiently large. If ka is sufficiently large, then the field of only the singly diffracted rays remains significant; thus, the singly diffracted fields are the dominant contributors to the far zone radiated fields, when  $\theta$  is not close to zero. The UTD electric field  $\overline{\mathbb{E}}^\Gamma$  which is associated with these two singly diffracted rays is given by

$$\vec{E}^{\Gamma} = \begin{cases}
\vec{E}_{\theta}^{\Gamma} + \vec{E}_{\phi}^{\Gamma}, & \text{for TE modes} \\
\vec{E}_{\theta}^{\Gamma} + \vec{E}_{\phi}^{\Gamma}, & \text{for TM modes}
\end{cases}$$
(119)

Here,

$$E_{\phi}^{r'} \sim j^{n+2} A_{nm}^{+} kZ_{o} P_{nm}^{+} H_{n}^{(2)'} (P_{nm}^{+})(jN_{nm}^{+}) \left[ \frac{\frac{\theta}{\cos 2} \frac{\delta_{nm}}{\sin 2}}{\cos \delta_{nm}^{+} - \cos \theta} \right]$$

$$\cdot (\frac{\cos n\phi}{\sin n\phi}) \sqrt{\frac{2}{\pi kasin\theta}} \sin(kasin\theta - \frac{n\pi}{2} - \frac{\pi}{4}) \frac{e^{-jkR}}{R}, \qquad (120)$$

. {Note that  $H_n^{(2)}(P_{nm}) = -jY_n(P_{nm}) \sim -jJ_n(P_{nm})$  since  $J_n(P_{nm})=0$  for  $TE_{nm}$  modes.};

$$E_{\theta}^{r'} \sim j^{n+2} A_{nm}^{+} H_{n}^{(2)} (P_{nm}^{'}) \operatorname{nkZ}_{0} N_{nm}^{'} \cos \delta_{nm}^{'} \left[ \frac{\sin \frac{\delta}{2} \cos \frac{\delta}{2}}{\cos \theta - \cos \delta_{nm}^{'}} \right]$$

$$\cdot (\frac{-\sin n\phi}{\cos n\phi}) \sqrt{\frac{2}{\pi kasin\theta}} \cos (kasin\theta - \frac{n\pi}{2} - \frac{\pi}{4}) \frac{e^{-jkR}}{R} ,$$
(121)

{Note that  $H_n^{(2)}(P_{nm}) \sim J_n(P_{nm})$  in this case.};

$$E_{\theta}^{r} \sim j^{n+2} B_{nim}^{+} k P_{nm} H_{n}^{(2)} (P_{nim}) N_{nim} \left[ \frac{\sin \frac{\delta}{2} \cos \frac{\delta_{nm}}{2}}{\cos \theta - \cos \delta_{nm}} \right]$$

$$\cdot \left( \frac{\cos n \phi}{\sin n \phi} \right) \sqrt{\frac{2}{\pi k a \sin \theta}} \cos \left( k a \sin \theta - \frac{n \pi}{2} - \frac{\pi}{4} \right) \frac{e^{-jkR}}{R} , \qquad (122)$$

[Note that  $H_n^{(2)}(P_{nin}) \sim J_n(P_{nim})$  in this case.];

$$E_{\phi}^{\Gamma} \sim j^{n+2} B_{nm}^{+} n_{nm}^{3} H_{n}^{(2)} (P_{nm}) (jN_{nm}) \left[ \frac{\cos \frac{\theta}{2} \sin \frac{\delta_{nm}}{2}}{\cos \theta - \cos \delta_{nm}} \right]$$

$$\cdot \left( \frac{-\sin n_{\phi}}{\cos n_{\phi}} \right) \sqrt{\frac{2}{\pi k a \sin \theta}} \sin(ka \sin \theta - \frac{n\pi}{2} - \frac{\pi}{4}) \frac{e^{-jkR}}{R} , \qquad (123)$$

{Note that  $H_0^{(2)}(P_{nm})=-jY_0(P_{nm})\sim jJ_0(P_{nm})$  in this case.};

where the terms within the square brackets in Eqs. (120)-(123) are the UTD edge diffraction coefficients multiplied by a constant; in particular.

$$\left[\frac{\cos\frac{\theta}{2}\sin\frac{\delta}{2}}{\cos\theta-\cos\delta}\right] = -\sqrt{2\pi k j} \cdot \frac{1}{2}D_{S}(\pi+\theta, \delta; \frac{\pi}{2}) , \qquad (124a)$$

and

$$\left[\frac{\sin \frac{\theta}{2} \cos \frac{\delta}{2}}{\cos \theta - \cos \delta}\right] = -\sqrt{2\pi k j} \cdot \frac{1}{2} D_{h}(\pi + \theta, \delta; \frac{\pi}{2}) \quad , \tag{124b}$$

with

$$\delta = \left\{ \begin{array}{l} \delta_{nm}^{\prime} = \cos^{-1}(\beta_{nm}^{\prime}/k) \text{ for TE}_{nm} \text{modes} \\ \delta_{nm}^{\prime} = \cos^{-1}(\beta_{nm}/k) \text{ for TM}_{nm} \text{modes} \end{array} \right. \tag{125}$$

It is noted that the half cone angles of the conical wavefront associated with the rays incident on the rim (at z=0) as shown in Figures 20-21 are denoted by  $\delta_{nm}$  and  $\delta_{nm}$  for the TE<sub>nm</sub> and the TM<sub>nm</sub> modes, respectively. These angles  $\delta_{nm}^{'}$  and  $\delta_{nm}^{}$  appear in Eqs. (120)-(123). Note that  $\theta = \{\delta_{nm} \text{ or } \delta_{nm}\}$  corresponds to the incident and reflected shadow boundary directions associated with the incident conical wave at the edge as shown in Figure 20. The above Eqs. (120)-(123) are presented for  $2k\widetilde{L}\cos^2(\frac{\theta \mp \delta}{2})>3$  where  $\widetilde{L}=a/\sin\delta$ . Consequently, these equations need to be modified if  $\theta\!\!\to\!\!\delta_{nm}$  or  $\delta_{nm}$ by including the "F" functions in  $\mathrm{D}_{\mathrm{S}}$  as indicated in Eq. (29). Since  $\theta$ =0 is a caustic direction for the diffracted rays, the two point first order diffraction solution for the radiated fields in Eqs. (120)-(123) becomes singular at  $\theta=0$  and therefore cannot be employed at and near that direction. The equivalent ring current concept used previously for evaluating the fields near the caustic direction (0=0) cannot be employed in this case because the incident conical wavefront which undergoes diffraction at the rim edge (at z=0) gives rise to a non-cylindrical wavefront in the immediate vicinity of that edge. It is noted that the diffracted wavefront in the immediate vicinity of the diffracting edge must be cylindrical in order for the equivalent ring current concept to be valid. The reasons for the existence of a non-cylindrical diffracted wave near the circular edge in this radiation problem are two-fold. First, the total field in the immediate vicinity of the diffracting edge consists not only of the edge diffracted field which may possess a cylindrical wavefront, but also consists of the incident and reflected conical wavefronts associated with the incident and reflected rays which exit directly from the aperture. The latter incident and reflected conical rays represent the ray equivalent of the modal field which impinges on the edge (at z=0) from within the wavequide region as described earlier. Secondly, the wavefront of the edge diffracted field in the immediate vicinity of the diffracting edge may also become non-cylindrical if it is produced by an incident conical wave corresponding to a waveguide mode far from cutoff (i.e., when  $\delta_{\min}$  and  $\delta_{\min}$  are close to zero) because in this case an observation point in the close vicinity of the diffracting edge (at z=0) can lie within the incident and reflection shadow boundary transition regions associated with the incident and reflected conical rays at the edge. Therefore, a procedure different from the equivalent current concept must be employed to find the field  $\overline{E}^r$  near  $\theta=0$ , which is radiated from the open-ended waveguide.

A procedure is described below for obtaining  $\overline{\mathbb{E}}^\Gamma$  which remains valid for 0 not only at and near zero, but also for 0 far from zero. Furthermore, for 0 far from zero, this result reduces to the first order (singly diffracted) two point UTD diffraction solution for  $\overline{\mathbb{E}}^\Gamma$  obtained earlier in Eqs. (119) -(123) where the latter is indeed expected to be accurate. This procedure is based on a modification of Ufimtsev's Physical Theory of Diffraction [24]; it is described next.

The radiated field  $\overline{E}'$  can be expressed in terms of the Stratton-Chu radiation integral [25] over the equivalent surface currents that exist on the surface & which tightly encapsulates the semi-infinite open-ended circular waveguide. Let & denote the circular disc shaped aperture surface at z=0 and & denote the surface formed by the exterior walls of the waveguide. Thus,  $\overline{E}'$  is given by [25]

$$\overline{E} = \frac{jkZ_0}{4\pi} \frac{e^{-jkR}}{R} \int_{\mathcal{S}} \int_{\mathcal{S}} \frac{dS'}{a + \mathcal{S}_C} \left[ \widehat{R} x \widehat{R} x \overline{J}_{eq} + Y_0 \widehat{R} x \overline{M}_{eq} \right] e^{jk\overline{R'} \cdot \widehat{R}}$$
 (126)

where  $\overline{R}'$  is a vector from the origin (0) to any point on g. Since one is concerned with the use of rays in this study, it is convenient to replace the equivalent electric and magnetic current densities  $\overline{J}_{eq}$  and  $\overline{M}_{eq}$  by their asymptotic approximations valid for large ka. Hence, to a first order of asymptotic approximation,

$$\overline{J}_{eq}$$
  $\sim \overline{J}_{eq}^{\text{modal}} + \overline{J}^{d}$  (127)

$$M_{eq} \mid_{\mathcal{B}_a} \sim M_{eq}^{\text{modal}} + M^{d}$$
 (128)

$$J_{eq} \mid_{A_c} \sim J^d \qquad . \tag{129}$$

It is noted that  $\overline{M}_{eq} \mid_{\mathcal{S}_{C}} = 0$  because  $\underline{\mathcal{S}_{C}}$  is a perfectly conducting exterior wall of the waveguide. In Eqs. (127) and (128),

$$\frac{1}{J_{eq}} = \frac{1}{z} \times \frac{1}{H_{modal}}; \frac{1}{M_{eq}} = \frac{1}{E_{modal}} \times \frac{1}{z}.$$
 (130)

where  $\overline{H}_{modal}$  is the magnetic field associated with the waveguide modes which impinge upon the circular edge (at z=0) from within the waveguide. Likewise,  $\overline{E}_{modal}$  is the electric field associated with  $\overline{H}_{modal}$ . On the other hand, the current densities  $\overline{J}$  and  $\overline{M}$  in Eqs. (127)-(129) denote the corrections to  $\overline{J}_{eq}$  and  $\overline{M}_{eq}$  that result from the effects of diffraction of the incident modal fields ( $\overline{E}_{modal}$ ,  $\overline{H}_{modal}$ ) at the circular rim (edge). The  $\overline{J}^d$  and  $\overline{M}^d$  will be described subsequently in more detail.

It is obvious from the above definition in Eq. (130) that  $\overline{J}_{eq}^{modal}$  =0 on  $\&_{C}$ . Consequently, the result in Eq. (126) can be decomposed into

$$\overline{E}^{r} = \overline{E}_{PO}^{r} + \overline{E}_{U}^{r} \qquad . \tag{131}$$

where

$$\overline{E}_{PO}^{\Gamma} = \frac{jkZ_{O}}{4\pi} \frac{e^{-jkR}}{R} \int_{\mathbb{R}_{a}}^{\mathbb{R}_{a}} dS' \left[ \hat{R} \times \hat{R} \times \hat{J}_{eq} + Y_{O} \hat{R} \times \hat{M}_{eq} \right] e^{jk\rho' \cdot \hat{R}}$$
(132)

since  $\overline{R}' = \overline{\rho}'$  on  $\mathcal{B}_a$ , and,

$$\frac{\vec{E}_{U}}{\vec{E}_{U}} = \frac{jkZ_{o}}{4\pi} \frac{e^{-jkR}}{R} \oint_{a} dS' \left[ \hat{R}x\hat{R}x\hat{J} + Y_{o}\hat{R}x\hat{M} \right] e^{-jkR} + \frac{jkZ_{o}}{4\pi} \frac{e^{-jkR}}{R} \oint_{a} dS' \left[ \hat{R}x\hat{R}x\hat{J} \right] e^{-jkR'} \cdot \hat{R} \qquad (133)$$

Obviously, the term  $\overline{\mathbb{E}_{p_0}}$  represents the vector Kirchhoff-Huygen's aperture integral for field radiated by the open end of the waveguide in which one employs the common approximation that the field in the aperture at the open end consists of only the waveguide modal fields which are incident (on the aperture) from within. The diffraction current densities  $\overline{J}^d$  and  $\overline{M}^d$  in Eq. (133) for  $\overline{\mathbb{E}_U}$  provide the correction to the incident mode current approximation in  $\overline{\mathbb{E}_{p_0}}$ . The integral for  $\overline{\mathbb{E}_{p_0}}$  in Eq. (132) has been essentially evaluated by Chu [2] and is also described by Silver [24]. The result can be rewritten in a more convenient form for the present analysis as

$$E_{p0}^{r} = \underbrace{(E_{p0\theta}^{r} \hat{\theta} + E_{p0\phi}^{r} \hat{\phi})}_{\text{radiation from TM}_{nm modes}} + \underbrace{(E_{p0\theta}^{r} \hat{\theta} + E_{p0\phi}^{r} \hat{\phi})}_{\text{radiation from TE}_{nm modes}}.$$
 (134)

where

$$E_{PO\theta}^{r'} = -A_{nm}^{+} \int_{nk}^{n+2} \int_{nk}^{n} \left[ \frac{\sin \frac{\theta}{2} \cos \frac{\theta}{2}}{\cos \theta - \cos \delta_{nm}} \right] - \frac{\cos \theta \sin^{2} \delta_{nm}}{2 \sin \theta (\cos \theta - \cos \delta_{nm})} \cos \delta_{nm}^{r'}$$

$$\cdot N_{nm}^{r'} \int_{n}^{n} (P_{nm}^{r'}) \int_{n}^{n} (ka \sin \theta) \left( \frac{-\sin n\phi}{\cos n\phi} \right) \frac{e^{-jkR}}{R} , \qquad (135)$$

$$E_{PO\phi}^{r'} = A_{nin}^{r} j^{+} (kZ_{o}) P_{nin}^{r} \left[ \frac{\sin \frac{\delta^{1}}{2} \cos \frac{\delta^{1}}{2}}{\cos \theta - \cos \delta_{nm}} \right] N_{nm}^{r} J_{n}(P_{nm}^{r})$$

$$\cdot J_{n}^{r} (kasin\theta) (\frac{\cos n\phi}{\sin n\phi}) \frac{e^{-jkR}}{R} , \qquad (136)$$

$$E_{P00} = B_{nm}^{+} \int_{nm}^{n+2} (kP_{nm}) \left[ \frac{\sin \frac{\theta}{2} \cos \frac{\theta}{2}}{\cos \theta - \cos \delta_{nm}} \right] N_{nm} \int_{nm}^{n} (P_{nm})$$

• 
$$J_n(kasin\theta)(\frac{cosn\phi}{sinn\phi}) \frac{e^{-jkR}}{R}$$
, (136)

$$E_{PO\phi}^{r} = 0 \qquad . \tag{137}$$

It is further convenient to identify the terms within the square brackets of Eqs. (134)-(137) as follows.

$$\left[\frac{\sin \frac{\delta}{2} \cos \frac{\delta}{2}}{\cos \theta - \cos \delta}\right] \approx -\sqrt{2\pi k j} \frac{1}{2} D_{S}^{PO} \left(\pi + \theta, \delta; \frac{\pi}{2}\right), \tag{139a}$$

and

$$\begin{bmatrix} \sin \frac{\theta}{2} \cos \frac{\theta}{2} \\ \cos \theta - \cos \delta \end{bmatrix} = -\sqrt{2\pi k j} \frac{1}{2} D_{h}^{PO} (\pi + \theta, \delta; \frac{\pi}{2}), \qquad (139b)$$

with

$$\delta = \left\{ \begin{array}{c} \delta_{nm}^{i} \text{ , for TE}_{nm} \text{ modes} \\ \delta_{nm} \text{ , for TM}_{nm} \text{ modes} \end{array} \right.$$

where  ${}^{D}_{S}^{PO}$  and  ${}^{D}_{h}^{PO}$  are the soft and hard physical optics (PO) edge diffraction coefficients. Far from the axis ( $\theta$ =0); i.e., for large ka sin  $\theta$ , and  $\theta$  not close to  $\{\delta_{nm} \text{ or } \delta_{nm}\}$ , the above results for  $\overline{E}_{PO}$ in Eqs. (134)-(137) reduce to the two point diffraction form as in Eqs. (120)-(122), but with Ds appearing in place of Ds as one might have anticipated. It will be shown below that only when the  $\overline{\mathsf{E}}_{\mathsf{u}}$ contribution of Eq. (133) is added to the  $\overline{\text{Ep}}_0$  of Eqs. (134)-(137) to obtain E as in Eq. (126), and the result for E is subsequently asymptotically approximated for large ka sin  $\theta$  and  $\theta$  not close to  $\{\delta_{nm} \text{ or } \delta_{nm}\}\text{, then the resulting asymptotic form agrees with the two$ point UTD diffraction solutions in Eqs. (120)-(122) which is in terms of Ds. Returning next to the evaluation of  $\overline{E}_U^r$  in Eq. (133), it is noted that  $\overline{J}^d$  and  $\overline{M}^d$  in that equation represent the current densities associated with the edge diffracted field components. The surface integrals over  $\mathcal{A}_a$  and  $\mathcal{A}_c$  must be evaluated asymptotically along the coordinate transverse to the circular rim thereby reducing those surface integrals to a line integral over the circular rim (edge) at z=0. A stationary phase evaluation of that line integral (or the rim integral) for ka sin  $\theta$  large yields a closed form result for  $E_{ij}$ . However that closed form result for large ka sin  $\theta$  is not valid at and near the caustic direction (0=0). Clearly, the rim integral therefore cannot be evaluated via stationary phase at and near the caustic;

instead, it must be evaluated numerically for  $\theta$  at and near zero. While the reduction of the surface integral for  $\overline{E_U}$  to the line or rim integral is conceptually straightforward, it is quite tedious since  $\overline{J}^d$  and  $\overline{M}^d$  must be expressed in the proper coordinate systems to carry out the asymptotic end point evaluation of the integral along the coordinate transverse to the rim. Of course,  $\overline{J}^d$  and  $\overline{M}^d$  are known from the UTD edge diffracted fields in the problem of plane wave diffraction by a half plane [1]. These fields are also identical to those obtained by Sommerfeld in his solution to the problem of plane wave diffraction by a half plane [26]. In particular,

$$\frac{d}{d} = \begin{cases}
\hat{z} \times \hat{H} & \text{on } & \hat{z} \\
\hat{\rho} \times \hat{H} & \text{on } & \hat{z}
\end{cases}$$
(140)

in which  $\overline{E}^d$  and  $\overline{H}^d$  are the edge diffracted electric and magnetic fields produced by the diffraction of the incident conical wave (which is locally plane for large ka) at the edge (see Figure 21). A far more convenient alternative to the Ufimtsev based formulation for  $\overline{E}^r$  in Eq. (131) which is given in terms of the surface integral representation for  $\overline{E}^r_U$  in Eq. (133) is to use the concept of equivalent Ufimtsev edge currents to obtain  $\overline{E}^r_U$  directly in terms of a rim integral rather than the surface integral. This modification of the Ufimtsev based formulation in Eq. (133) is described below.

Consider the problem of the plane wave scattering (and diffraction) by a half plane in Figure 22 for which the exact solution is well known. It is not difficult to see in this case that when the incident, reflected, and diffracted fields present in that exact solution are employed to calculate the equivalent electric and magnetic current densities in the Stratton-Chu integral [2,25] for the electric field  $\mathbf{E}_{hp}^{r}$  radiated (or scattered) by the half plane, then one should again recover the original exact solution for the fields scattered (and diffracted) by that half plane. The Stratton-Chu formulation [2,25] for  $\mathbf{E}_{hp}^{r}$  is the same as in Eq. (126), and the contours  $\mathbf{A}_{a}$  and  $\mathbf{A}_{c}$  for the present half plane case are as shown in Figure 22. Note that  $\mathbf{A}_{a}$  of Figure 22 locally simulates the aperture  $\mathbf{A}_{a}$  of the circular waveguide (see Eq. (126)). Again, the field  $\mathbf{E}_{hp}^{r}$  can be decomposed into

$$\overline{E}_{hp} = \overline{E}_{PO}(hp) + \overline{E}_{U}(hp) . \qquad (141)$$

as in Eq. (131). The equivalent electric and magnetic current densities  $\overline{J}_{eq}$  and  $\overline{M}_{eq}$  that appear in the Stratton-Chu integrals for  $\overline{E}_{PO}^{\Gamma}(hp)$  and  $\overline{E}_{U}^{\Gamma}(hp)$  are given by

$$J_{eq} = [\hat{z} \times (\overline{H}^{i} + \overline{H}^{r})]_{a} + (\hat{z} \times \overline{H}^{d})_{a}. \qquad (142)$$

$$\overline{M}_{eq} \downarrow_{\mathcal{B}_a} = [(\overline{E}^i + \overline{E}^r) \times \hat{z}]_{\mathcal{B}_a} + (\overline{E}^d \times \hat{z})_{\mathcal{B}_a}.$$
 (143)

$$J_{eq} \mid_{\mathcal{B}_a} = (-\hat{x} \times \overline{H}^d)_{\mathcal{B}_c} ; \overline{M}_{eq} \mid_{\mathcal{B}_c} = 0 . \qquad (144)$$

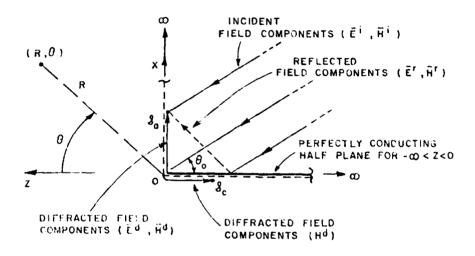


Figure 22. Diffraction mechanism from a perfectly-conducting half plane.

where  $\overline{E}^i$ ,  $\overline{E}^i$ , and  $\overline{E}^d$  are the incident, reflected and diffracted components, respectively, of the electric field present in the exact solution to half plane diffraction problem of Figure 22 and likewise the  $\overline{H}^i$ ,  $\overline{H}^i$ , and  $\overline{H}^d$  are the magnetic field components associated with  $\overline{E}^i$ ,  $\overline{E}^i$ , and  $\overline{E}^d$ . It can be shown that an evaluation of the  $\overline{E}_{PO(hp)}^i$  integral in terms of  $\overline{J}_{eq}$  and  $\overline{M}_{eq}$  of Eqs. (142)-(144) yields

$$\overline{E}_{PO(hp)} = \overline{E}^{i} U(|\psi - \psi'| - \pi) + \overline{E}^{r} U(|\psi + \psi'| - \pi) + \overline{E}_{PO} , \qquad (145)$$

where  $\psi' = \theta_0$ ,  $\psi = \pi \pm \theta$ ;

$$U(\xi) = \begin{cases} 1 & , & \xi > 0 \\ 1/2 & , & \xi = 0 \\ 0 & , & \xi < 0 \end{cases}$$
 (146)

and

$$\frac{d}{Ep_0} = \frac{i}{E} \left| \begin{array}{c} = P0 \\ at 0 \end{array} \right| \left( \pi \pm \theta, \theta_0 ; \frac{\pi}{2} \right) \frac{e^{-jkR}}{\sqrt{R}} \qquad (147)$$

in which  $\overline{\tilde{D}}^{PO}(\pi \pm \theta \ \theta_0; \overline{Z})$  is the uniform physical optics edge diffraction coefficient in dyadic form and it corresponds to the receiver location at x > 0. This dyadic  $\overline{\tilde{D}}^{PO}$  can be expressed in terms of the  $\begin{cases} soft \\ hard \end{cases}$  scalar diffraction coefficient  $\overset{\sim}{D}_s^{PO}$  in a manner similar to that for  $\overset{\sim}{D}$  as indicated in [1]. The  $\overset{\sim}{D}_s^{PO}$  is explicitly given by

When  $2kR \cos^2(\frac{\psi^\mp\psi^\dagger}{2})>3$ , the "F" functions in Eq. (148) are po essentially unity, then Ds  $(\psi^\dagger,\psi;\frac{\pi}{2})$  reduces to Ds  $(\psi,\psi^\dagger;\frac{\pi}{2})$  defined h earlier in Eq. (139); i.e.,

$$\frac{e^{-j\frac{\pi}{4}}}{h} = \frac{-e^{-j\frac{\pi}{4}}}{2\sqrt{2\pi k}} \left[ \tan\left(\frac{\psi-\psi'}{2}\right) \mp \tan\left(\frac{\psi+\psi'}{2}\right) \right] = -\left\{ \frac{e^{-j\frac{\pi}{4}}}{2\sqrt{2\pi k}} \left[ \frac{4\sin\frac{\psi'}{2}\cos\frac{\psi'}{2}}{\cos\psi + \cos\psi'} \right] - \frac{e^{-j\frac{\pi}{4}}}{2\sqrt{2\pi k}} \left[ \frac{4\sin\frac{\psi}{2}\cos\frac{\psi}{2}}{\cos\psi + \cos\psi'} \right] \right\}$$
(149)

and

if 
$$2kR \cos^2\left(\frac{\psi + \psi'}{2}\right) > 3$$
.

Also, an evaluation of  $\overline{E_U}(hp)$  in terms of the  $\overline{J}_{eq}$  and  $\overline{M}_{eq}$  of Eqs. (142)-(144) must yield

$$\overline{E}_{U(hp)}^{r} = \overline{E}_{U}^{d} , \qquad (151)$$

where

The D may be referred to as a "Ufimtsev" half plane edge diffraction coefficient in dyadic form. This dyadic D can also be expressed in terms of the  ${soft hard}$  scalar diffraction coefficient Ds , where

$$D_{s}^{U}(\psi,\psi';\frac{\pi}{2}) = -\frac{e^{-j\frac{\pi}{4}}}{2\sqrt{2\pi k}} \left[ \left( \sec\left(\frac{\psi-\psi'}{2}\right) - \tan\left(\frac{\psi-\psi'}{2}\right) \right) \mp \left( \sec\left(\frac{\psi+\psi'}{2}\right) - \tan\left(\frac{\psi+\psi'}{2}\right) \right) \right]$$
(153)

It is noted that in contrast to  $D_h^{PO}$ , the  $D_h^{S}$  is valid at and near the incident and reflection shadow boundaries in the problem of Figure 22; these shadow boundaries occur at  $|\psi+\psi'|=\pi$ . Consequently, the wavefront associated with  $\overline{E}_{IJ}^{d}$  and  $\overline{H}_{IJ}^{d}$  is always cylindrical and one can always view the field  $\overline{E}_{IJ}^{O}(hp)$  as being produced by an equivalent edge (line) current referred to as an equivalent Ufimtsev edge current; in particular, one may write

$$\frac{d}{E_U} = -ykZ_0 I_U \sqrt{\frac{j}{8\pi k}} \frac{e^{-jkR}}{\sqrt{R}} , \qquad (154)$$

if  $\overline{E} = y E$  only; and

$$\vec{H}_{U} = -\hat{y}_{k} Y_{0} M_{U} \sqrt{\frac{j}{8\pi k}} \frac{e^{-jkR}}{\sqrt{R}} , \qquad (155)$$

if  $H = \hat{y} H$  only. Thus, the equivalent electric and magnetic Ufimtsev

half plane edge currents Iy and My, respectively are given by

$$I_{U} = -Y_{0}\sqrt{\frac{3\pi}{Jk}} D_{S}^{U}(\psi,\psi';\frac{\pi}{2})(\overline{E}^{i}\cdot\hat{y}) . \qquad (156)$$

$$M_{U} = -Z_{0}\sqrt{\frac{8\pi}{jk}} D_{h}^{U} (\psi, \psi'; \frac{\pi}{2}) (\overrightarrow{H} \cdot \hat{y}) . \qquad (157)$$

The above Iy and My are obtained by a direct comparison of Eq. (152), with Eqs. (154)-(155), respectively. These currents Iy and My which are valid for normal incidence on the half plane can also be directly generalized to oblique angles of incidence and diffraction on the edge [23]. Next, comparing the half-plane geometry in Figure 22 with the local geometry at any point on the circular edge of the open-ended circular waveguide as shown in Figure 21, it is not difficult to see that one can define a  $\theta_0 = \{\delta_{nm}^+ \text{ or } \delta_{nin}\}$  at any point on the circular edge (at z=0) so that the field  $\overline{E_U}$  in Eq. (133) can now be viewed as being produced by the equivalent electric and magnetic Ufimtsev half plane edge currents Iy and My. Thus, using the equivalent current concept, one may directly employ the Stratton-Chu radiation integral for  $\overline{E_U}$  in terms of these rim currents Iy and My, to obtain

$$\overline{E}_{U}^{r} = \frac{jkZ_{0}}{4\pi} \frac{e^{-jkR}}{R} \oint \left[\widehat{R} \times \widehat{R} \times I_{U} + Y_{0} \widehat{R} \times M_{U}\right] \widehat{\ell}' e^{jk\overline{\rho}' \cdot R_{d}\ell'} . \tag{158}$$

with  $\hat{\ell}'d\ell' = \hat{\phi}'ad\phi'$  for a circular rim, and  $\overline{\rho}'=\hat{\rho}'a$ . Eq. (158) is in contrast to the surface integral in Eq. (133) which can be reduced to a rim integral only after asymptotically evaluating the integral along the coordinate orthogonal to the rim. Thus, according to the proposed modification of the Ufimtsev based formulation for obtaining  $\overline{\ell}'$ , one may write

$$\overline{E} = \overline{E}_{PO} + \frac{jkZ_0}{4\pi} \frac{e^{-jkR}}{R} \oint d\ell' \left[ \hat{R} \hat{x} \hat{R} \hat{x} I_U \hat{\ell}' + Y_0 \hat{R} \hat{x} M_U \hat{\ell}' \right] e^{jkD' \cdot \hat{R}}$$
(159)

where  $\overline{E_{PO}}$  is still the same as in Eq. (132). Only the  $\overline{E_U}$  term in Eq. (133) which occurs in Eq. (131) is now replaced by the line integral around the edge as in Eq. (158) above. Specifically, the equivalent Ufimtsev edge currents  $\overline{I_U}$  and  $\overline{M_U}$  in Eqs. (156)-(157) which are modified so as to make them valid for oblique angles of incidence and diffraction on the edge, without the restriction of generalized Fermat's principle for edges [23] are now defined by

$$I_{U} = -Y_{0}\sqrt{\frac{8\pi}{jk}} \frac{1}{\sin\beta_{0}} D_{S}^{U} (\psi, \psi'; \beta_{0}') (\overline{E}^{1} \cdot \hat{\ell}') \qquad (160)$$

and

$$M_{U} = -Z_{o}\sqrt{\frac{8\pi}{jk}} \frac{1}{\sin \beta_{o}} D_{h}^{U} (\psi, \psi'; \beta_{o}') (\widehat{H}^{i} \cdot \hat{\ell}') \qquad (161)$$

As shown in Figure 23,  $\beta_0$  and  $\beta_0$  are the acute angles made by the incident and diffracted rays with the tangent  $(\hat{\ell})$  to the edge at the point of edge diffraction, respectively. In the present case of conical wave incidence at the edge, the axis (or caustic) of the conical wave coincides with the waveguide axis and hence  $\beta_0 = \pi/2$  or  $\sin \beta_0 = 1$  in Eqs. (160)-(161); on the other hand,  $\beta_0$  is given by

$$\sin \beta_0 = \sqrt{1 - \sin^2 \theta \sin^2 \phi'} \qquad . \tag{162}$$

The above  $I_U$  and  $M_U$  in Eqs. (160)-(161) reduce to those given previously in Eqs. (156)-(157) for normal incidence on the edge in which  $\beta_0'=\pi/2$  and  $\beta_0=\pi/2$ .

It is important to note that the result in Eq. (159) involving the equivalent Ufimtsev edge current represents a useful modification of the original Ufimtsev formulation in Eq. (131)-(133). Furthermore, this modified result in Eq. (159) is quite general in that it can be directly extended to other antenna and scattering problem configurations involving edges. Basically, the modified result in Eq. (159) implies that the radiation or scattering can be calculated according to a physical optics approximation and be corrected by the equivalent Ufimtsev edge current integral which is then added to the physical optics contribution of Eq. (159). The result in Eq. (159) is to be used for all  $\theta$  (both near and far from zero) and it is expected to be accurate as long as  $\overline{\text{Ep}}_0$  is not vanishingly small. For  $\theta + \pi/2$ , a doubly diffracted ray becomes important; its contribution can be calculated separately via the UTD and it is simply added to the solution

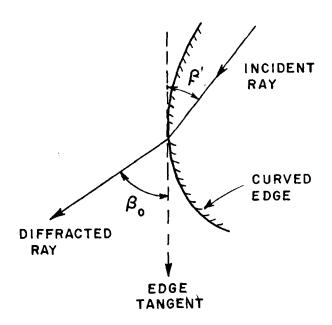


Figure 23. Diffraction from a curved edge.

for E in Eq. (159). For large ka sin  $\theta$ , the physical optics contribution in Eq. (159) together with Eqs. (134)-(138) can be approximated such that the Bessel functions involving ka sin  $\theta$  and the Hankel functions therein are replaced by their large argument asymptotic forms. When this asymptotic approximation is made, the physical optics result has the same form as the two point UTD diffraction solution of Eqs. (120)-(122) except that it now contains the physical optics edge diffraction coefficients  $\overline{D}_{s}^{P0}$  instead of the UTD edge diffraction coefficients Ds of Eqs. (120)-(122) as mentioned earlier. Furthermore, the rim integral in Eq. (159) can also be asymptotically evaluated for large  $ka \sin \theta$  via the method of stationary phase to yield a result which is again like the two point UTD diffraction solution except that it contains the Ufimtsev ede diffraction coefficients  $\mathbf{D}_{\boldsymbol{s}}^{\boldsymbol{U}}$  instead of  $\ensuremath{\mathsf{Ds}}$  . However, the sum of the asymptotic approximations, for large ka sin 0, of the physical optics and the equivalent Ufimtsev rim current integrals agrees with the two point UTD diffraction solution in Eqs. (120)-(122) because

$$D_{s} = D_{s}^{PO} + D_{s}^{U}$$
 (163)

It may be remarked that while the two point UTD diffraction solution in Eqs. (120)-(122) is accurate for ka sin 0 large, the solution in Eq. (159) is valid even when ka sin 0 is not large; furthermore, it is expected to be more accurate than the UTD solution for 0 +  $\delta_{nm}$  or  $\delta_{nm}$  even if the "F" functions present in Ds of Eq. (29) are included in the latter. One notes that the Bessel functions  $J_n$  (ka sin 0) or

 $J_n$  (ka sin  $\theta$ ) in the physical optics solutions of Eqs. (135)-(138) for the TM<sub>nm</sub> and TE<sub>nm</sub> cases vanish at  $\theta = \delta_{nm}$  and  $\theta = \delta_{nm}$ , respectively; thereby keeping the solutions bounded even when  $D_{\Sigma}^{PO}$  at  $\theta$  +  $\delta_{nm}$ or  $\delta_{\text{nm}}\text{.}$  Clearly the Bessel functions which keep  $\overset{\text{\tiny 17}}{\text{D}_{\text{N}}}$  bounded are to be viewed as incident and reflection shadow boundary transition functions which yield a result for Epo that is uniformly valid across the incident and reflection shadow boundaries associated with  $\theta = \{\delta_{nm} \text{ or } \delta_{nm}^{\dagger}\}$ . It appears that the Bessel-type transition functions are more accurate than the Fresnel integral ("F"-type) transition functions of the UTD at least for the present wavequide problem and especially for ka sin 0 small. Finally, it may be remarked that the two point UTD diffraction solution valid for large ka sin 0 can in some problems be generalized heuristically to be valid at and near the caustic at  $\theta=0$  by recognizing the two-point solution to be an asymptotic approximation of some functional form which yields a bounded result at the caustic. However, such a heuristic procedure for generalizing the two-point UTD diffraction solution to the caustic region is risky in the present open-ended circular waveguide case and it can lead to an erroneous result. In conclusion therefore, the result for  $\overline{E}$  in Eq. (159) is to be employed for all  $\theta$ .

A direct application of either the UTD result of Eq. (119) (for  $\theta$  not close to zero) or even the use of the expression for  $\overline{E}$  in Eq. (159) will generally fail to predict the correct value of  $\overline{E}$  if any component of  $\overline{E}$  vanishes at all aspects (see Eq. (134) for  $\overline{E}$  component of  $\overline{E}$  for the radiation by an open-ended circular waveguide

excited in the TM<sub>nm</sub> mode. In the latter case, the term  $E_{P0\phi}$  is identically zero in Eq. (134). From a practical point of view, even though  $E_{P0\phi}^{\Gamma}$  =0, its overall effect in the RCS calculation is small in comparison to the other scattering effects which dominate; hence an unavailability at the present time of an accurate estimate based on ray methods and its modifications for  $E^{\Gamma} \cdot \hat{\phi}$  radiated from the open end of a circular waveguide excited by a TM<sub>nm</sub> mode, is not a serious problem in the present RCS study. Some typical results for  $E^{\Gamma}$  based on Eq. (159) are shown in Figures 24-25 where they are seen to compare well with those based on the exact Wiener-Hopf solution [12], provided the  $\hat{\theta}$  and  $\hat{\phi}$  components of  $E_{P0}^{\Gamma}$  are non-zero.

## C. Ray Analysis for [S21]

The scattering matrix [S21] describes the transformation or coupling of the incident plane wave field into the waveguide modes as illustrated in Figure 6. This scattering matrix [S21] was defined earlier in Eq. (11). The problem of determining [S21] is the reciprocal of the problem of determining [S12] (see Figures 6-7). Thus, a knowledge of [S12], or more specifically  $S_{0nm}$ ,  $S_{0nm}$ ,  $S_{0nm}$ , and  $S_{0nm}$ , and the use of the reciprocity theorem for electromagnetic fields allows one to calculate the elements  $S_{0nm}$ ,  $S_{0nm}$ ,  $S_{0nm}$ , and  $S_{0nm}$  of [S21], and to hence calculate [S21] in terms of [S12]. Thus, it can be shown that the elements of [S21] are simply related to the elements of [S12]; here T denotes the transpose matrix operator. The reciprocity theorem is applied as follows.

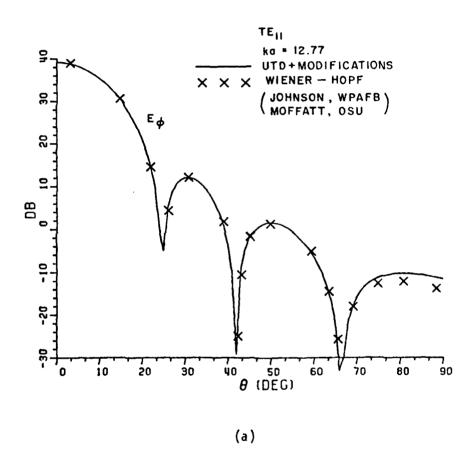
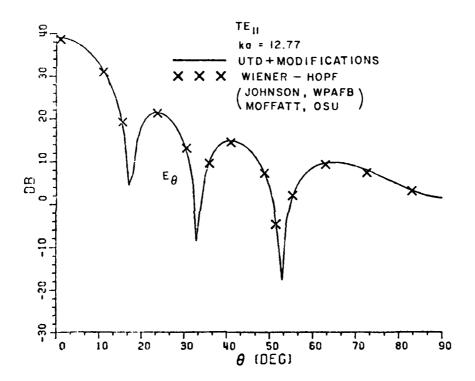
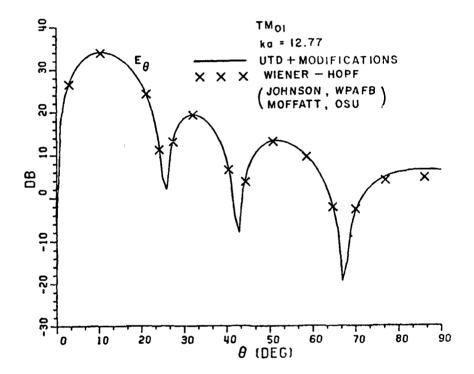


Figure 24. Radiation patterns of an open circular waveguide with ka=12.77.



(b)

Figure 24. (continued)



(c)

Figure 24. (continued)

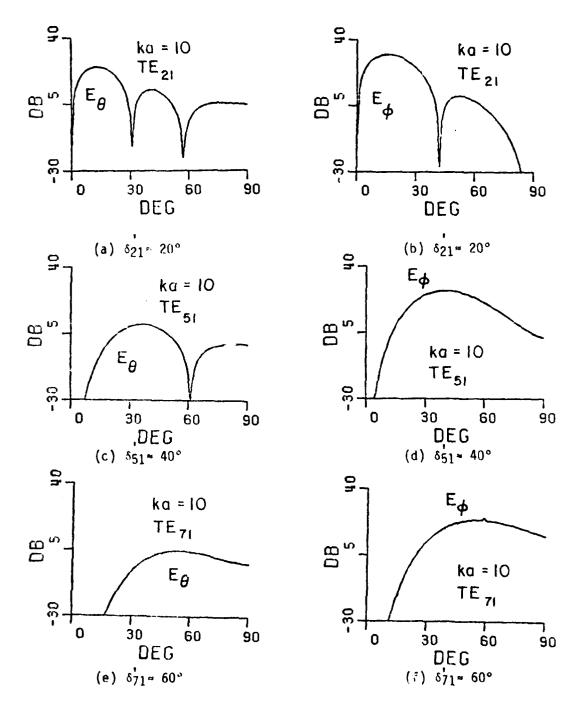


Figure 25. Radiation patterns of an open circular waveguide based on UTD and its modifications.  $\delta_{nm}$  shown in the figure is the corresponding cone angle for each mode.

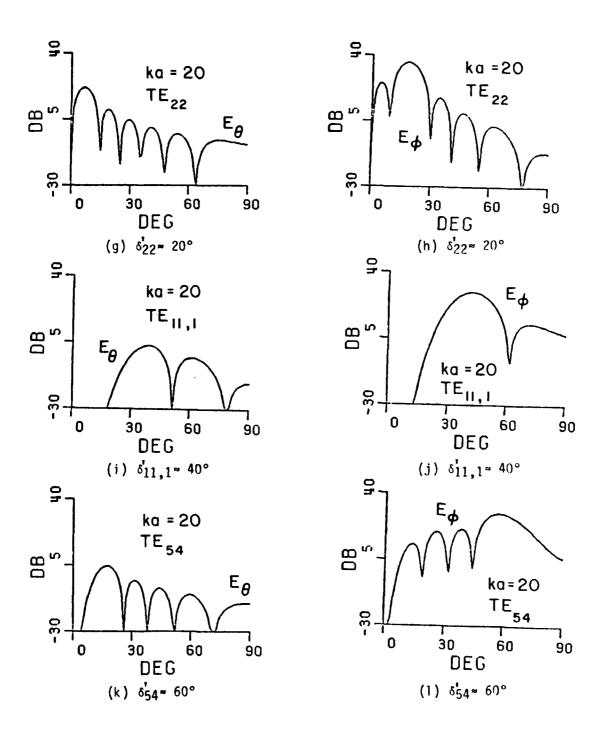


Figure 25. (continued)

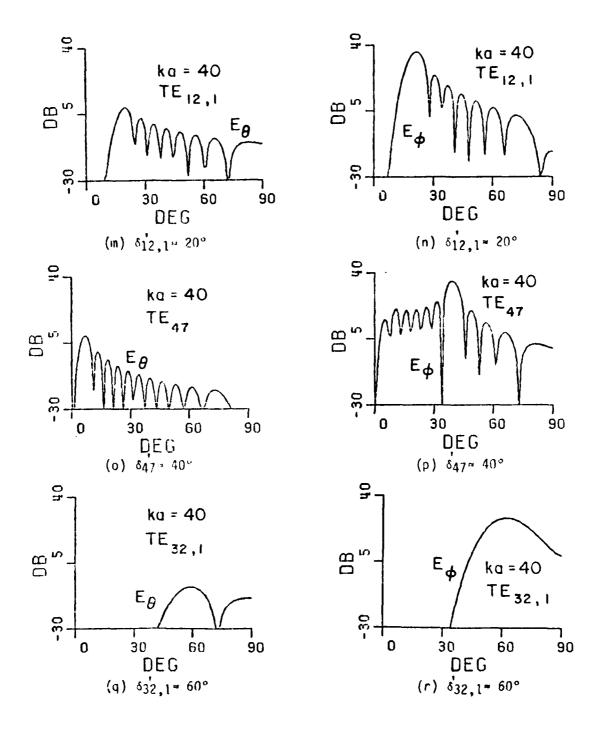


Figure 25. (continued)

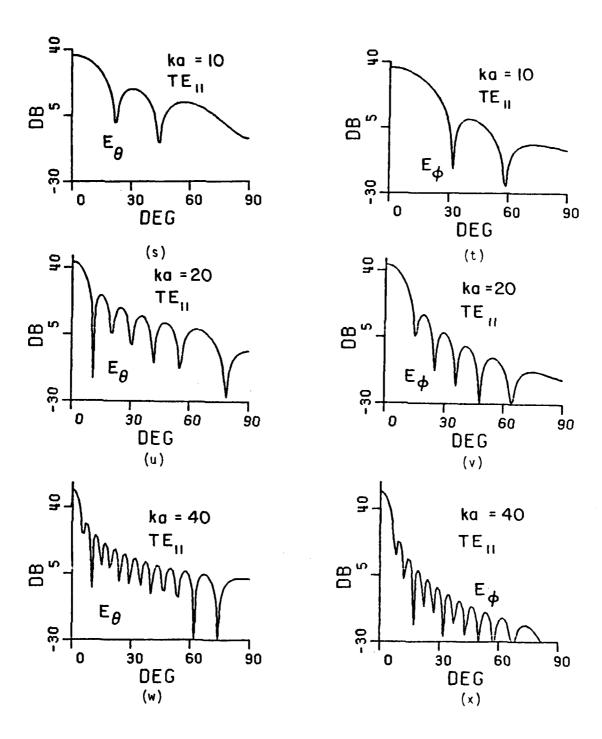


Figure 25. (continued)

First consider the geometric plane defined by z=-L inside the semi-infinite pipe, and let So denote the area of this waveguide cross section at z=-L as shown in Figure 26. Then let S denote the surface area which tightly encapsulates the complete outer (exterior) surface of the semi-infinite pipe, and also a portion of the inner walls of this pipe up to the distance z=-L within the pipe. The surface S does not include the plane at z=-L within the pipe. Let  $\Sigma$  denote the sphere at infinity which surrounds the semi-infinite pipe such that S on the exterior or outer wall of the semi-infinite pipe is connected to the surface  $\Sigma$  at  $z \rightarrow -\infty$  as in Figure 26. Next consider the following two cases. In the first case, the semi-infinite circular waveguide is excited from within by the modal fields with amplitudes  $A_{\text{nin}}^{\dagger}$  and  $B_{\text{nin}}^{\dagger}$  which propagate in the  $\hat{z}$  direction. However, in the second case the same geometry is excited by an external electric field  $\frac{1}{E} = \frac{1}{\theta E_0} + \frac{1}{\phi E_\phi}$  which for convenience is assumed to be produced by an electric test source  $\overline{J}_e$  at  $\overline{R}_p$  exterior to and in the far zone of the semi-infinite pipe. It is assumed that the spherical wave factor  $\frac{e^{-jkRp}}{R^2}$ in E is suppressed so that E represents a locally plane wave part of the field generated by  $\overline{J}_e$ . Let  $\overline{J}_e = (\hat{\mathfrak{g}} E_\theta^i + \hat{\mathfrak{g}} E_\phi^i) \delta(|\overline{R} - \overline{R}p|) \cdot (\frac{-4\pi}{j\omega\mu})$ , where  $\mathcal{E}(|\overline{R}-\overline{R}p|)$  refers to Dirac's delta function. The modal fields with amplitudes  $A_{nin}^+$  and  $B_{nin}^+$  radiate the fields  $\overline{E}_{nim}^- = E_{\theta nm}^-\hat{\theta} + E_{\phi nm}^-\hat{\phi}$  from the open end of the pipe in the first case. Likewise the field  $\overline{E}^1$  which is locally plane at the open end of the pipe launches the modal fields with amplitudes  $A_{nm}^-$  and  $B_{nm}^-$  within the semi-infinite pipe in the second case. As shown in detail in Appendix C, one can apply the reciprocity

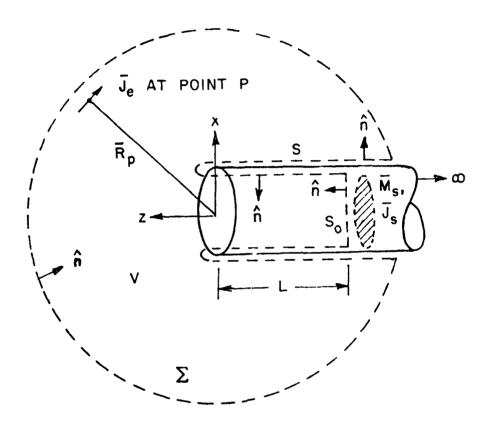


Figure 26. Geometry for determining [ $S_{21}$ ] from [ $S_{12}$ ] using the reciprocity theorem.

theorem to the pair of fields  $\overline{E}_{nm}$  and  $\overline{E}$  within the region V bounded by S,  $S_0$  and  $\Sigma$ , and then enforce the radiation condition on  $\Sigma$ , as well as the boundary condition on S (e.g., tangential electric field vanishes on the perfectly conducting surface S). This yields the required modal amplitudes  $A_{nm}^-$  and  $B_{nm}^-$  in terms of  $\overline{E}_{nm}^\Gamma$  (related to  $[S_{12}]$ ) as follows:

$$\Lambda_{nin}^{-} = \frac{\left(\frac{\theta E_{0}^{\dagger} + \phi E_{0}^{\dagger}\right) \cdot \overline{E} f_{E}(\overline{R}p) \cdot Rp e^{jkRp}}{2A_{nin}^{+} \int_{S_{0}}^{\infty} e_{nin}^{\dagger} \times \overline{h}_{nin}^{\dagger} \cdot \hat{z} ds} \cdot \frac{4\pi}{j\omega\mu}$$
(164)

$$B_{\text{nim}}^{-} = \frac{\left(\widehat{\mathfrak{g}}E_{0}^{\dagger} + \widehat{\mathfrak{g}}E_{0}^{\dagger}\right) \cdot \widetilde{E}_{\text{IM}}^{T}(\widetilde{R}p)Rp \cdot e^{jkRp}}{2B_{\text{nim}}^{\dagger} \int_{S_{0}}^{S} e_{\text{nim}} \times \widetilde{h}_{\text{nim}} \cdot \widehat{z} ds} \cdot \frac{4\pi}{j\omega u}$$
 (165)

Here, the subscripts TE and TM in Eqs. (164)-(165) denote that  $\overline{E}_{TE}^r$  is radiated by  $A_{nm}^+$  alone, and  $\overline{E}_{TM}^r$  is radiated by  $B_{nm}^+$  alone, respectively. Ine radiated fields for  $\overline{E}_{TE}^r$  and  $\overline{E}_{TM}^r$  have been shown in Section (3). Because of the normalization factor  $N_{nm}^-$  and  $N_{nm}^+$  introduced in Table 1, it is noticed that

$$\frac{1}{2} \iint_{S_0} \overline{e_{nm}} \times \overline{b_{pm}} \cdot \hat{z} ds = 1 . \qquad (166)$$

Inc elements of [521] may be easily obtained, by inspection, from Eqs. (11)-(12) and (164)-(165) respectively.

Figure 27 illustrates an example for the coupling into the circular waveguide due to a unit plane wave incident on axis with electric field polarized in the  $\hat{y}$  direction. It is noted that only  $TE_{1m}$  and  $TM_{1m}$  modes yield non-vanishing radiated fields in the axial (0=0) direction, thus only  $TE_{1m}$  and  $TM_{1m}$  modes can be coupled into the circular waveguide for the configuration of Figure 27. The total transverse electric fields evaluated on x (or y) axis are then reduced to only  $E_{\varphi}$  (or  $E_{p}$ ), because all the coupled fields of Figure 27 possess a  $\binom{\cos \varphi}{\sin \varphi}$  - type of variations. Figure 28 illustrates the total transverse electric fields on x (or y) axis at various z=-L inside the circular waveguide (with ka=35) due to a unit plane wave incident on axis as shown in Figure 27.

#### D. Ray Analysis for [S22]

The scattering matrix [S22] is a modal reflection coefficient matrix which is associated with the interaction shown in Figure 7 which occurs at the open front end (or z=0). This matrix [S22] was defined earlier in Eqs. (13)-(14). The order of the sub-matrix elements of the or eh [S22]; i.e., of [Rnin; pq], and [Rnm; pq], are found by employing the UTD in the following manner. As before, the equivalent ray cone corresponding to the modes with amplitudes  $A_{pq}^+$  and  $B_{pq}^+$  which are incident on the circular edge at the opening of the semi-infinite guide make an angle  $\delta_{pq}^-$  and  $\delta_{pq}^-$ , with the walls, respectively (see Figure 29). Then from UTD considerations, each of these rays diffracts back into the waveguide region at any angle  $\psi$  with the walls. Except for a mode near cutoff, the angle  $\psi$  will be far from any incident or

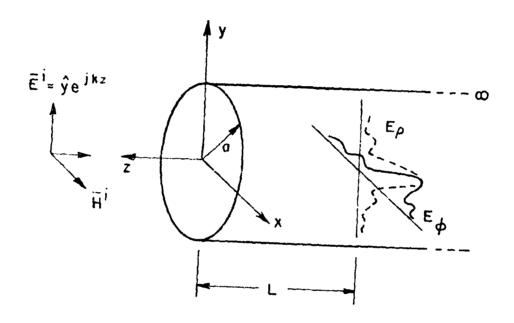


Figure 21. Coupling into the circular waveguide due to a unit plane wave field incident on axis.

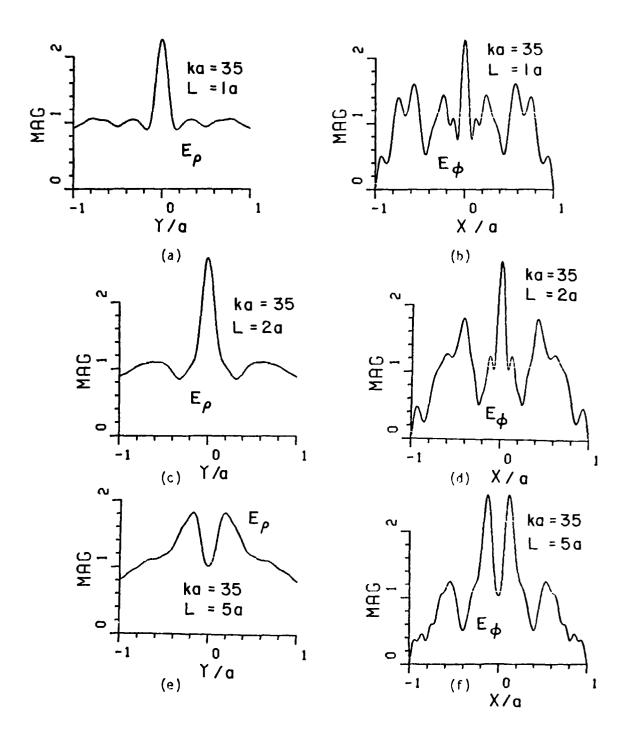


Figure 28. Total coupled transverse (to z) electric field along x or y at z=-L for a unit plane wave incident on-axis.

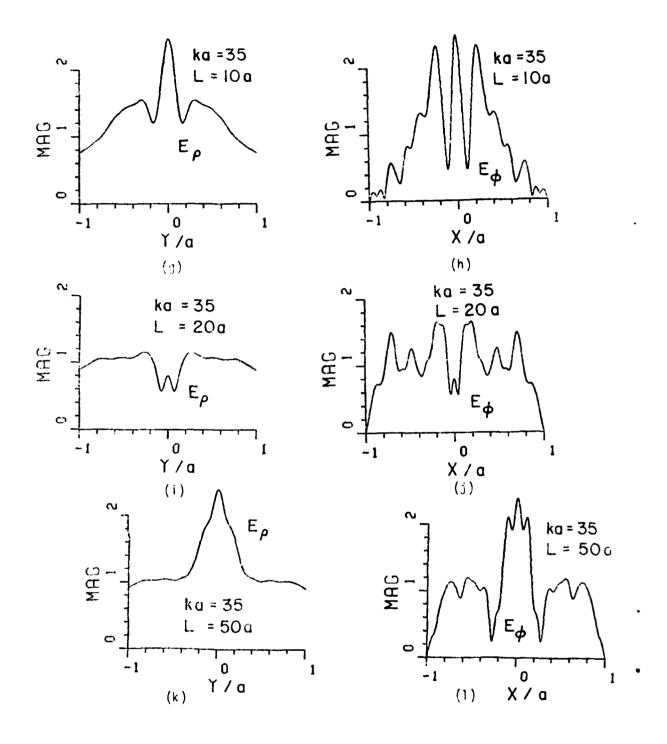


Figure 28. (continued)

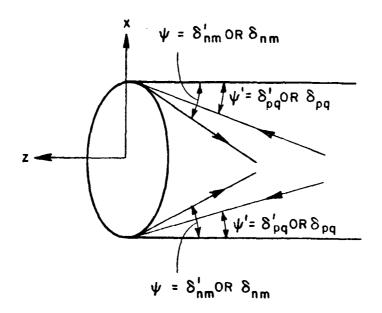


Figure 29. Reflection from the open end of a circular waveguide.

reflection shadow boundary that is associated with the cone of incident rays at the edge. One may thus define equivalent magnetic and magnetic dipole edge currents of strength M and  $M_{
m d}$ , respectively, on the circular rim (or edge) which generate the same diffracted fields within the waveguide, but near the edge, as those produced by the incident ray cone. Unlike the equivalent magnetic and electric edge currents shown in Section (B) which radiate into free space, the equivalent magnetic and magnetic dipole currents mentioned above radiate within the guide; i.e., in the presence of the perfectly-conducting waveguide walls. Consequently the equivalent electric edge current for the exterior field calculation is now replaced by the equivalent magnetic dipole edge current  $M_{
m d}$  for calculating the field in the interior waveguide region. Therefore, care must be exercised in defining these equivalent currents which radiate into the waveguide region. It can be shown that the general form of M is the same as in Eq. (36) except that a factor of 1/2 must be included in the definition of this current and also for  $M_{
m d}$ to account properly for the presence of the perfectly-conducting waveguide walls [28,29] when calculating the field in the interior wavequide region. Specifically, the equivalent magnetic current is given by.

$$\overline{M}(\psi,\psi') = -\hat{\phi}'(\overline{H}_{\text{modal}}^{\text{inc}} \cdot \hat{\phi}') \cdot \frac{Z_0}{2} \cdot \sqrt{\frac{8\pi}{jk}} \cdot D_h(\psi,\psi'; \beta_0 = \frac{\pi}{2}) \cdot (167)$$

and the equivalent magnetic dipole current is given by [27,28],

$$\overline{M}_{d}(x,\psi') = z \cdot (\overline{L}_{modal}^{inc} \cdot \hat{\phi}') \cdot \frac{1}{2} \cdot \sqrt{\frac{8\pi}{jk}} \cdot \frac{D_{S}(\psi,\psi'; \beta_{O} = \frac{\pi}{2})}{\sin \psi} \cdot (168)$$

where  $\psi' = \delta_{pq}$  or  $\delta'_{pq}$ . Clearly one requires  $\psi' = \delta_{pq}$  or  $\delta_{pq}$  in Eqs. (167)-(168) corresponding to the angle made by the incident ray cone with the waveguide walls. Then the fields radiated into the waveguide region by the above rim currents may be expressed in terms of modes in the usual manner by simply invoking the reciprocity theorem to find which modes are excited by the source [20], i.e., by the rim current. Since one is interested in calculating the amplitudes  $\Lambda_{nm}^{-}$ or  ${\rm B}^{-}_{nm}$  of the reflected  ${\rm TE}_{nm}$  or  ${\rm TM}_{nm}$  modes, respectively, it therefore follows from physical considerations that one must require  $\psi$  =  $\delta_{\text{nin}}$  or  $\delta_{nm}^{1}$  in Eqs. (167)-(168) for these cases, based on the aforementioned ray-mode equivalence. Thus, one must require that  $\psi$  take on the proper value corresponding to the ray-cone angle  $\delta_{nm}$  or  $\delta_{nm}'$  which is associated with the reflected waveguide mode when employing reciprocity to find the strength of the reflected modes generated by  $\overline{M}$  and  $\overline{M}_d$  of Eqs. (167)-(168) via [20]. Without presenting any details, one obtains the required amplitudes  $A^-_{\mbox{\scriptsize nin}}$  and  $B^-_{\mbox{\scriptsize nin}}$  via the above procedure from which the elements of [S22] can be directly extracted (by inspection) via Eq. (13). In particular,

$$R_{\text{nm;pq}}^{\text{hh}} = \frac{\oint \frac{\text{rim}\left[\overline{h'_{\text{nm}}}, \overline{M}\left(\delta'_{\text{nm}}, \delta'_{\text{pq}}\right) + \overline{h'_{\text{znm}}}, \overline{M}^{\text{d}}\left(\delta'_{\text{nm}}, \delta'_{\text{pq}}\right)\right] d\ell}{2\iint \frac{e'_{\text{nm}}}{S_{\text{o}}} \times \overline{h'_{\text{nm}}} \cdot \hat{z} ds}$$
(169)

$$\frac{ee}{R_{nm;pq}} = \frac{\oint \frac{rim[\overline{h}_{nin}.\overline{M}(\delta_{nm},\delta_{pq})]d\ell}{2\iint \overline{e}_{nm} \times \overline{h}_{nin} \cdot \hat{z} ds} .$$
(170)

$$\frac{eh}{R} = \frac{\frac{\Phi}{rim[h_{nin} \cdot M(\delta_{nin}, \delta_{pq})]d\ell}}{2\iint_{S_0} e_{nm} \times h_{nm} \cdot \hat{z} ds} .$$
(171)

$$\frac{he}{n_{\text{in};pq}} = \frac{\frac{\phi}{\text{rim}[h_{\text{nin}} \cdot M(\delta_{\text{nin}}, \delta_{\text{pq}}) + h_{\text{znin}} \cdot M^{d}(\delta_{\text{nin}}, \delta_{\text{pq}})]d\ell}}{2\iint \frac{e_{\text{nin}} \cdot x h_{\text{nin}} \cdot \hat{z} ds}{\delta_{\text{o}}}} .$$
(172)

It is important to note that the integrals over the rim in Eqs. (169)-(172) can be evaluated in closed form; likewise the integrals over the guide cross section  $S_0$  (at z=0) can also be evaluated in closed form (see Eq. (166)). Employing the orthogonality properties of the waveguide modes, it can be easily seen that the numerators of Eqs. (169)-(172) vanish when  $a \neq n$ . Thus, the elements of [S22] vanish when p\*n. For the dominant mode regime, it is necessary to modify the above equivalent rim currents to include the effects of rays multiply diffracted across the aperture. Taking cognizance of the fact that the multiple diffractions occur along the reflection boundaries of the interacting rays, it follows that multiple diffraction calculations must be treated carefully by decomposing the non-ray optical fields near the reflection boundaries into their ray optical components as done previously in the calculation of [S11] at 0=0. Following a similar procedure as in Appendix 8 to include all orders of rays multiply diffracted across the rim, one can show that the final expression for  $R_{\mathsf{nm};\mathsf{nq}}$  which denotes the reflection coefficient of the  $\mathsf{TE}_{\mathsf{nm}}$  mode that is reflected back into the waveguide when a TE<sub>ng</sub> mode is incident at z=0, and which is based on Eq. (169), is given by

$$R_{nm;nq} = R_{o} \left[ 1 + u_{2} \left( \delta_{nm}^{\prime}, \delta_{nq}^{\prime} \right) \cdot \frac{D}{1 + (-1)^{n} \Lambda \cdot D} \right] \cdot + A_{o} R_{o} \left[ 1 - u_{2} \left( \delta_{nm}^{\prime}, \delta_{nq}^{\prime} \right) \cdot \frac{C}{1 + (-1)^{n} \Lambda C} \right] \cdot$$
(173)

where

$$R_{0} = \frac{N_{nq}^{\prime}}{N_{nm}^{\prime}} \frac{j}{4ka} \frac{n^{2}}{n^{2} - p_{nm}^{\prime}^{2}} \frac{H_{n}^{(2)}(p_{nq}^{\prime})}{J_{n}(p_{nm}^{\prime})} \cos \delta_{nq}^{\prime}$$

$$\cdot \left[ \sec \left( \frac{\delta_{nm} - \delta_{nq}^{\prime}}{2} \right) + \sec \left( \frac{\delta_{nm} + \delta_{nq}^{\prime}}{2} \right) \right] \qquad (174)$$

$$A_0 = -j \frac{(ka)^2}{n}^2 \tan \delta_{nq}^i \tan \delta_{nm}^i \tan \frac{\delta_{nq}}{2} \tan \frac{\delta_{nm}}{2} \frac{H_1^{(2)}(p_{nq}^i)}{H_1^{(2)}(p_{nq}^i)}$$
(175)

$$u_2(\psi, \psi') = (-1)^n \cdot \frac{1}{2\sqrt{\pi k a}} e^{-j(2ka - \frac{\pi}{4})} (\sec \psi + \sec \psi')$$
 (176)

$$C = 1 + \sum_{n=1}^{\infty} (jB)^n \cdot \sqrt{\frac{1}{n+1}}$$
 (177)

$$0 = 1 + \sum_{n=1}^{\infty} (-jB)^n \cdot \sqrt{\frac{1}{n+1}} \qquad (1/8)$$

and

$$A = -\frac{e^{-j(2ka-\frac{\pi}{4})}}{4\sqrt{\pi ka}} \qquad (179)$$

$$B = -\frac{1}{2} e^{-j2ka} . (180)$$

Similarly, the final expression for  $R_{\text{nin};nq}^{\text{ee}}$ , which denotes the reflection coefficient for the  $TM_{\text{nin}}$  mode reflected back into the waveguide when a  $TM_{nq}$  mode is incident at z=0, is given by

$$R_{nm;nq} = R_0 \cdot \left[1 + u_2(\delta_{nm}, \delta_{nq}) \cdot \frac{D}{1 + (-1)^n A \cdot D}\right] \quad (181)$$

where

$$R_{0} = -\frac{N_{nq}}{N_{nm}} \frac{j}{4ka} \frac{H_{n}^{(2)}(p_{nq})}{J_{n}^{+}(p_{nm})} \frac{\sin \delta_{nq}}{\sin \delta_{nm}} \cdot \frac{1}{\cos \delta_{nm}}$$

$$\cdot \left[ \sec \left( \frac{\delta_{nm} - \delta_{nq}}{2} \right) + \sec \left( \frac{\delta_{nm} + \delta_{nq}}{2} \right) \right] \cdot (182)$$

Also, the final expression for  $R_{nm;nq}^{eh}$ , which corresponds to the reflection coefficient for the  $TM_{nm}$  mode which is reflected back into the waveguide when a  $TE_{nq}$  mode is incident at z=0, is given by

$$R_{\text{nin}; nq} = \pm R_{1} \left[ 1 + u_{2}(\delta_{\text{nin}}^{1}, \delta_{\text{nq}}) \cdot \frac{D}{1 + (-1)^{n} A \cdot D} \right]$$
 (183)

where

$$R_{1} = \frac{N_{nq}}{N_{nm}} \frac{jnZ_{0}}{4ka} \frac{H_{n}^{(2)}(p_{nq})}{p_{nm}} \frac{cos \delta_{nq}}{cos \delta_{nm}}$$

$$\cdot \left[sec \left(\frac{\delta_{nm} - \delta_{nq}}{2}\right) + sec \left(\frac{\delta_{nm} + \delta_{nq}}{2}\right)\right] \qquad (184)$$

fine upper sign "+" in Eq. (183) corresponds to the incident  $TE_{nq}$  mode in the upper row, and reflected  $TM_{nm}$  mode in the lower row of Table 1. The lower sign "-" in Eq. (183) corresponds to the incident  $TE_{nm}$  mode in the lower row, and reflected  $TM_{nm}$  mode in the upper row of Table 1.

Likewise, the final expression for  $R_{nm;nq}$ , which corresponds to the reflection coefficient for the  $TE_{nm}$  mode which is reflected back into the waveguide when a  $TM_{nq}$  mode is incident at z=0, is given by

he
$$R_{nm;nq} = \pm R_1 \left[ 1 + u_2(\delta_{nm}, \delta_{nq}) \cdot \frac{D}{1 + (-1)^n AD} \right]$$

$$\pm \tilde{A}_0 R_1 \left[ 1 - u_2(\delta_{nm}, \delta_{nq}) \cdot \frac{C}{1 + (-1)^n AC} \right] \qquad (185)$$

where

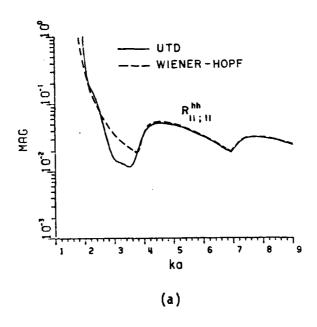
$$\frac{\kappa}{R_1} = \frac{N_{nq}}{N_{nm}} \frac{j}{4Z_0} \frac{n}{n^2 - p_{nm}^2} \frac{H_n^{(2)}(p_{nq})}{J_n(p_{nm})} \sin \delta_{nq}$$

$$\cdot \left[ \sec \left( \frac{\delta_{nm} - \delta_{nq}}{2} \right) + \sec \left( \frac{\delta_{nm} + \delta_{nq}}{2} \right) \right] \cdot (186)$$

$$\tilde{A}_{0} = -j \frac{H_{n}^{(2)}(p_{nq})}{H_{n}^{(2)}(p_{nq})} \tan \delta_{nm} \cot \delta_{nq} \tan \frac{\delta_{nq}}{2} \tan \frac{\delta_{nm}}{2}$$
 (187)

The upper sign "+" in Eq. (185) corresponds to the incident  $TM_{nq}$  mode in the upper row, and reflected  $TE_{nm}$  mode in the lower row of Table 1. The lower sign "-" in Eq. (185) corresponds to the incident  $TM_{nq}$  mode in the lower row, and reflected  $TE_{nm}$  mode in the upper row of Table 1.

Plots of the magnitudes of  $R_{11;11}$ ,  $R_{01;01}$ ,  $R_{11;11}$ , and  $R_{01;01}$  in Eqs. (173)-(182) are shown in Figures 30-31, respectively, as a function of ka. These UTD based results are also compared with those based on



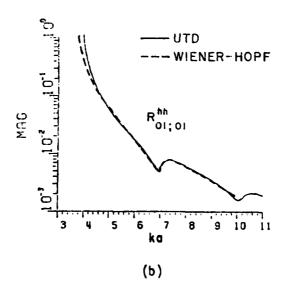
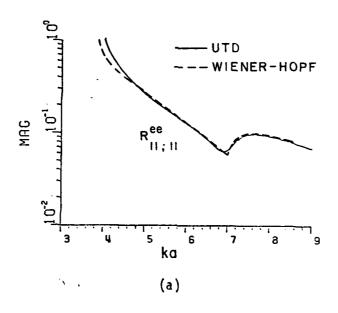


Figure 30. Magnitude of the self reflection coefficient for a  ${\rm TE}_{nm}$  mode incident on an open-ended circular waveguide.



ì

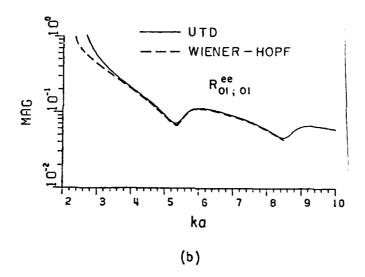


Figure 31. Magnitude of the self reflection coefficient for a  $\mathsf{TM}_{\mathsf{nin}}$  mode incident on an open-ended circular waveguide.

Weinstein's Wiener-Hopf solution to this problem. One observes from these figures that the agreement between the UTD and the exact Wiener-Hopf solution for the reflection coefficients is good. It is noted that Felsen and Yee [19] have obtained the modal reflection coefficients associated with acoustic modes reflected from the open end of a semi-infinite acoustically rigid pipe. They [19] also employed ray methods, and they used a Poisson sum technique to convert the reflected ray cones into waveguide modes. On the other hand, the ray to mode conversion for the more general electromagnetic case accomplished in the present work involves simply invoking the reciprocity theorem to determine which modes are excited by a given source inside the waveguide; in particular, the sources employed in this work are the equivalent rim currents. While our procedure may be somewhat less rigorous than the one in [19] (which employs a Poisson sum technique), it appears to be simpler and yields results which are also quite accurate.

# E. Ray Analysis for [Sh]

The scattering matrix  $[S_b]$ , like  $[S_{22}]$ , is also a reflection coefficient matrix which is associated with the discontinuity at the back end, or at z=-L, as shown in Figure 8. Clearly, the elements of  $[S_b]$  depend on the exact nature of the discontinuity at z=-L; as observed from Figures 1-4, the nature of the discontinuity is different for the different terminations at z=-L in those figures. Presently, the following terminations or discontinuities at z=-L are considered;

namely, an open circuit or open end at z=-L for a finite pipe, a planar dielectric interface at z=-L in a semi-infinite pipe, a disc-blade termination in a semi-infinite pipe, and a short circuit or closed end at z=-L for the semi-infinite as well as the finite length pipe, respectively.

#### a) $[S_b]$ for an Open Termination at z=-L

When a finite pipe is open at both ends, it is apparent that  $[S_b]$  is the same as  $[S_{22}]$ . Thus,

$$[S_b] = [S_{22}]$$
 (188)

## b) $[S_b]$ for a Closed Termination at z=-L

As shown in Figure 3, there exists an electric field which is incident on the termination from the left side or the region (z>-L); that field is denoted here by  $\overline{E}_{\overline{k}}$ , where  $\overline{E}_{\overline{k}}$  may represent a TE or TM electric modal field. Then the total electric field E in the region z>-L can be expressed as

$$\overline{E} = \overline{E}_{k}^{-} + \sum_{n=1}^{\infty} c_{n}^{+} \overline{E}_{n}^{+} \quad \text{for } z > -L \quad . \tag{189}$$

where  $c_n^+$  ( $n=1,2,\ldots,\infty$ ) denotes the reflection coefficient for the modal field  $\overline{E}_n^+$  which is reflected from the termination at z=-L when the modal field  $\overline{E}_k^-$  is incident there. One needs to solve for the

coefficients  $c_n^+$  in Eq. (189) for obtaining the elements of  $[S_b]$  in this case as follows. On the perfectly conducting termination at z=-L, the following boundary condition must be satisfied; namely,

Now the unknowns  $c_0^+$  can be determined quite easily from Eqs. (189)-(190) together with the orthogonality properties of the waveguide modes; thus,

$$c_n^+ = \begin{cases} -1 & n=k \\ 0 & \text{otherwise} \end{cases}$$
 (191)

It follows that

$$[S_b] = -[I] , \qquad (192)$$

where [I] is an identity matrix of order ∞ x ∞.

# c) [ $S_b$ ] for a Planar Termination at z=-L

As shown in Figure 32, the guide is loaded with a dielectric material of relative permittivity  $\varepsilon_\Gamma$  in the region z<-L. The dielectric interface at z=-L is planar, and perpendicular to the guide axis. Consider a modal electric field  $\overline{E}_{\overline{k}}$  incident upon this termination at z=-L from the region z<-L, then the total electric field E in the region z<-L within the guide can be expressed as,

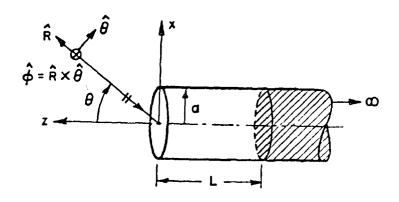


Figure 32. Backscattering from a semi-infinite hollow pipe loaded with a dielectric material of relative permittivity  $\epsilon_\Gamma$  in the region z<-L.

$$\overline{E} = \begin{cases}
\overline{E}_{k} + \sum_{n=1}^{\infty} c_{n}^{+} E_{n}^{+} & -L < z < 0 \\
\sum_{n=1}^{\infty} c_{n}^{-} E_{n}^{-} & z < -L \end{cases}$$
(193)

likewise the total magnetic field  $\overline{H}$  corresponding to  $\overline{E}$  may be expressed as

$$\overrightarrow{H} = \begin{cases}
\overrightarrow{H}_{k} + \sum_{n=1}^{\infty} c_{n}^{+} H_{n}^{+} & -L < z < 0 \\
\xrightarrow{\infty} \sim \\
\sum_{n=1}^{\infty} c_{n}^{-} H_{n}^{-} & z < -L
\end{cases}$$
(194)

Here  $c_n^+(or c_n^-)$  denotes the modal reflection (or transmission) coefficient at the junction z=-L. It is noted that, for -L<z<0.

$$\overline{E}_n^{\pm} = c_n^{\pm} (\overline{e}_n \pm \overline{e}_{nz}) e^{\mp j \gamma_{nm} z} . \qquad (195)$$

$$\overline{H}_{n}^{\pm} = c_{n}^{\pm} \left( \pm \overline{h}_{n} + \overline{h}_{nz} \right) e^{\mp j \gamma_{nm} z} . \tag{196}$$

where  $\overline{e}_n$  (or  $\overline{h}_n$ ), and  $\overline{e}_{nz}$  (or  $\overline{h}_{nz}$ ) denote the transverse and longitudinal electric (or magnetic) modal fields, respectively, and can be found in Table 1.  $\gamma_{nm}$  can be  $\beta_{nm}$  or  $\beta_{nm}$  to denote the TE or TM modes. For z<-L (in the dielectric region),

$$\tilde{\epsilon}_{n}^{\pm} = \tilde{c}_{n}^{\pm} (\tilde{e}_{n}^{-} \pm \tilde{e}_{nz}^{-}) e^{\mp j \tilde{\gamma}_{nin} z} \qquad (197)$$

$$\widehat{H}_{n}^{\pm} = \widehat{c}_{n}^{\pm} \left( \pm \widehat{h}_{n} + \widehat{h}_{nz} \right) e^{\mp j \widehat{\gamma}_{nin} z} \qquad (198)$$

where the expressions for  $e_n$ ,  $h_n$ ,  $e_{nz}$ , and  $h_{nz}$  can be found from Table 1 except that the free space permittivity  $\epsilon$  has to be replaced by  $\epsilon$   $\epsilon_r$ . Therefore,  $k^2$  are replaced by  $k^2\epsilon_r$ , and  $\beta_{nm}$  (or  $\beta_{nm}$ ) by  $\widetilde{\beta}_{nm}$  (or  $\widetilde{\beta}_{nm}$ ), where

$$\beta_{nm}^{i} = \sqrt{k^{2} \varepsilon_{r} - (\frac{P_{nm}^{i}}{a})^{2}} \quad \text{for TE}_{nm} \text{ modes.}$$

$$\beta_{nm}^{i} = \sqrt{k^{2} \varepsilon_{r} - (\frac{P_{nm}}{a})^{2}} \quad \text{for TM}_{nm} \text{ modes.}$$
(199)

Then, by enforcing the boundary conditions at the dielectric interface which require that  $\hat{z} \times E$  and  $\hat{z} \times H$  are continuous at z=-L, and employing the orthogonality properties of the waveguide modes, one obtains,

$$R_{nm;nm} = \frac{\beta_{nm}^{\prime} - \overline{\beta_{nm}^{\prime}}}{\beta_{nm}^{\prime} + \overline{\beta_{nm}^{\prime}}}, \qquad (200)$$

$$\stackrel{\text{ee}}{R}_{\text{nm;nm}} = \frac{\widetilde{\beta}_{\text{nm}} - \varepsilon_{\Gamma} \beta_{\text{nm}}}{\widetilde{\beta}_{\text{nm}} + \varepsilon_{\Gamma} \beta_{\text{nm}}} \qquad (201)$$

All the other elements of  $[S_b]$  vanish identically. Thus,  $[S_b]$  is reduced to a diagonal matrix, i.e.,

$$[S_b] = \begin{bmatrix} \widehat{R}_{nm;nm}^{hh} & [0] \\ [0] & [\widehat{R}_{nm;nm}^{ee} \end{bmatrix}$$

$$\infty \times \infty . \qquad (202)$$

#### d) [ $S_b$ ] for a Disc-Blade Termination at z=-L

As shown in Figure 1, the planar disc-blade discontinuity comprises of N blades, placed with an azimuthal periodicity around a central disc. The blades of length c and the disc of radius b are assumed to be perfectly conducting and to lie in the plane z=-L. Each blade spans an angle  $\psi$ , and the distance (a-c) between the blades and the cylinder is assumed to be small. For a sufficiently large number of blades, the surface current density  $J_b$  induced on the composite disc-blade geometry may be given to a first approximation by

$$\overline{J}_b \approx 2 \hat{z} \times \overline{H}_q^-$$
, on the disc and blades only, (203)

in which  $\overline{H_g}$  is the sum of all the propagating  $TE_{nm}$  and  $TM_{nm}$  modes which are incident on the disc-blade discontinuity. An expression for  $\overline{H_g}$  is provided in Eq. (7). The approximation in Eq. (203) corresponds to the geometrical optics approximation for the current. The fields generated by  $\overline{J_b}$  propagate in the  $+\hat{z}$  direction; for propagation in the  $+\hat{z}$  direction, these fields constitute the reflected waveguide modes in the region 0>z>-L, and for the  $-\hat{z}$  directed propagation case, they constitute the transmitted waveguide modes in the region z<-L. Once again, as in the calculation of the elements of [S<sub>22</sub>], the reflected and transmitted waveguide modes generated by  $\overline{J_b}$  may be readily calculated by invoking the reciprocity theorem to determine which modes will be excited by a given source within the guide [20]. Thus, the amplitudes  $+\frac{1}{2}$  and  $+\frac{1}{2}$  of the TE<sub>nm</sub> and TM<sub>nm</sub> modes, respectively, which are reflected from the disc-blade discontinuity are found to be [20]

$$A_{nm}^{+} = \frac{-\iint_{S_d} \vec{e}_{nm} \cdot \vec{J}_b dS}{2\iint_{S_0} \vec{e}_{nm} \times \vec{h}_{nm} \cdot \hat{z} dS} \qquad (204)$$

and

$$B_{nm}^{+} = \frac{-\iint \overline{e}_{nm} \cdot \overline{J}_{b} dS}{2\iint \overline{e}_{nm} \times \overline{h}_{nm} \cdot \hat{z} dS} \qquad (205)$$

in which  $S_d$  denotes the surface area of the disc-blade geometry. The elements of  $[S_b]_{\infty X_\infty}$  can be directly obtained from Eqs. (204)-(205), which are found as follows.

$$\widehat{R}_{nm;pq}^{hh} = -\frac{\iint_{S_d} e_{nm} \times \widehat{h}_{pq} \cdot \widehat{z} ds}{\iint_{S_d} e_{nm} \times \widehat{h}_{nm} \cdot \widehat{z} ds}$$
(206)

$$\widehat{R}_{nm;pq}^{ee} = -\frac{\iint_{S_d} \overline{e}_{nm} \times \overline{h}_{pq} \cdot \widehat{z} ds}{\iint_{S_d} \overline{e}_{nm} \times \overline{h}_{nm} \cdot \widehat{z} ds} \qquad (207)$$

$$\hat{R}_{nm;pq}^{eh} = -\frac{\iint_{S_d} e_{nm} \times h_{pq} \cdot \hat{z} ds}{\iint_{S_0} e_{nm} \times h_{nm} \cdot \hat{z} ds}$$
(208)

and

$$\hat{R}_{nm;pq}^{he} = -\frac{\iint_{S_d} \vec{e}_{nm} \times \vec{h}_{pq} \cdot \hat{z} ds}{\iint_{S_0} \vec{e}_{nm} \times \vec{h}_{nm} \cdot \hat{z} ds}$$
(209)

It is noted that the integrals in the latter equations can be evaluated in closed form.

Some interesting effects are observed in the reflection from a rotationally symmetric object inside a circular waveguide. It has been shown [34] that if an object is rotating about the axis of the waveguide and has periodic characteristics in the azimuthal direction with period  $2\pi/N$  (N: integer), an incident  $TE_{pq}$  (or  $TM_{pq}$ ) mode can only excite reflected  $TE_{nm}$  (or  $TM_{nm}$ ) modes where n=p or n= $\ell$ N±p ( $\ell$ : integer). Furthermore, only the reflected modes withe n= $\ell$ N±p, but not n=p, contain information on the modulation of the reflected wave due to the rotation of the periodic object. Therefore, if the disc-blade model in Figure 1 contains a large number of fan blades (N), as is usually the case in a true jet intake, and if the waveguide is not big enough to propagate the high-order modes with mode number n= $\ell$ N±p, then one will generally not be able to observe any modulation effect in the reflected wave.

In the configuration of Figure 2 where the stator and the rotor are both taken into account, Eqs. (206)–(209) still apply except that the area of integration  $S_d$  appearing in the numerators is now a function of the relative position of the stator and rotor. When the geometry of the rotor-stator combination is no longer symmetric, all possible modes can be reflected corresponding to an incident mode. However, the conversion of an incident mode into a different reflected mode is usually small

compared with the self reflection coefficient. The modulation effects are mostly due to the change in the total area covered by the rotorstator combination.

Finally, the matrix [P] which is associated with the phase delay in the propagation path L can be conveniently written as

#### SECTION 4

### NUMERICAL RESULTS AND SUMMARY FOR PART I

Numerical results for the on-axis RCS of the intake blade geometry in Figure 1, which are based on the MSM, in conjunction with the UTD together with its modifications at caustics, are shown in Figure 33 as a function of  $a/\lambda$ , with the length L (from the intake opening to the blades) being kept such that L=10a. All of the RCS plots here are normalized to  $\pi a^2$ . The number of blades, N=40 for the plot in Figure 33. The mean RCS level in Figure 33 is basically controlled by the blade scattering, and the ripple structure results from the interference between the blade backscatter and the backscatter from the intake opening. The effect of evanescent (non-propagating) modes in the intake is ignored in these calculations because it is expected to be negligible as long as L does not become extremely small (or approach zero). The scattering matrices in the MSM become fairly simple in this case because first, they are of finite order having neglected the evanescent modes, and secondly, there are only a few elements involved for the range of  $a/\lambda$  values being considered, since only the first few propagating modes exist in this case. It is interesting to compare the intake-blade RCS results of Figure 33 with the RCS of two other related geometries as shown in Figures 3 and 4, respectively. Thus, Figure 34

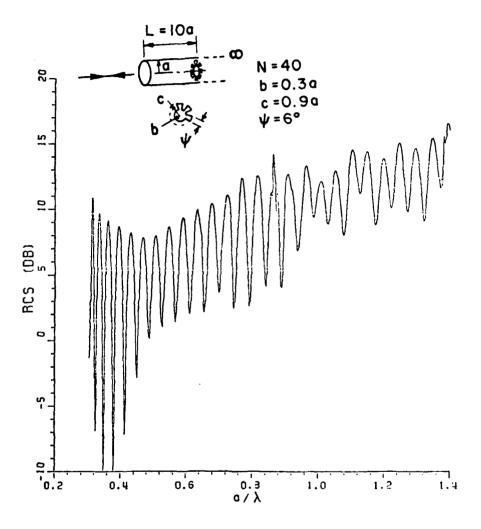


Figure 33. On-axis RCS (normalized to  $\pi a^2$ ) of the simplified jet intake model with N blades attached to a circular disc as shown in Figure 1.

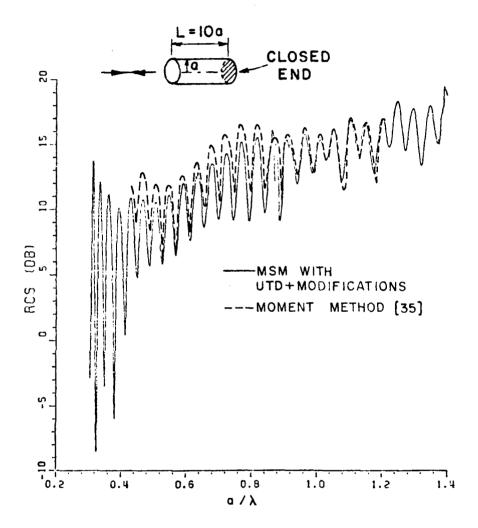


Figure 34. On-axis RCS (normalized to  $\pi a^2$ ) of a hollow, perfectly conducting finite length circular cylinder open at the front end and closed (shorted) at the back end.

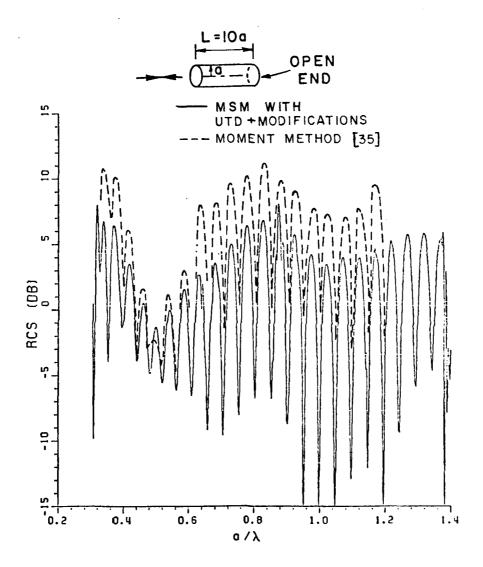


Figure 35. On-axis RCS (norm lized to  $\pi a^2$ ) of a hollow, perfectly conducting finite length circular cylinder open at both ends.

illustrates the on-axis RCS of a hollow, perfectly-conducting cylinder of finite length L with the front end open (as in the intake case) and with the back end closed (or shorted) with a perfectly-conducting planar disk. Likewise, Figure 35 illustrates the on-axis RCS of the same finite length hollow cylinder as in Figure 4 except that it is now open at both ends. The RCS in Figures 34-35 have also been calculated via the MSM used in conjunction with the UTD. Clearly, as one would expect, the mean RCS level is higher for the finite cylinder with a closed (snorted) back end (Figure 3) than for the same cylinder with both ends open (Figure 4). In the case of the finite cylinder with a closed back end (Figure 3), the mean RCS level is controlled by the backscatter from the closed end, and the ripple structure again results primarily from the interference between the backscatter from the closed back end and the backscatter from the open front end. In contrast, the mean RCS in Figure 35 of the finite length hollow cylinder open at both ends is controlled primarily by the backscatter from the open front end. However, the ripple structure is primarily the result of interference between the backscatter from the open front end and the backscatter resulting from the wave coupling from the internal to the external regions of the hollow pipe, and vice versa.

It is important to note that only the  $TE_{1m}$  and  $TM_{1m}$  modes inside a circular waveguide yield non-vanishing radiated fields in the axial (0=0) direction. Therefore, from the foregoing discussions of the scattering matrix [S21] in Section 3, only the  $TE_{1m}$  and  $TM_{1m}$  modes can be induced inside the circular waveguide of Figures 1-3 when a plane

wave is incident in the axial (-z) direction. Furthermore, the  $\mathsf{TM}_{1m}$ modes yield very low-level fields in the direction  $\theta=0$  and the mode conversion between the  $TE_{1m}$  and  $TM_{1m}$  modes are small in the discontinuity at z=-L; for practical purposes, only the  $TE_{1m}$  modes need to be considered in the calculations of the on-axis backscattered fields of Figures 1-3. On the other hand, the  $TM_{1m}$  modes may become important for calculating the RCS for the problem in Figure 4 where these modes are coupled from the exterior region to the interior at z=-L (and vice versa). These TM<sub>1m</sub> modes have been ignored in the calculations leading to Figure 35 and could possibly account for only a part of the almost 3 dB shift between the results based on (MSM-UTD with modifications) and the independent moment-method calculations [35] in Figure 35 for the following reason. It is expected that the mean RCS level in Figure 35 should correspond to the field backscattered from the open front end as accurately predicted via the (MSM-UTD with modifications) as shown earlier in Figure 19; consequently, the effect of the  $TM_{1m}$  modes would have to virtually be almost in phase with the backscatter from the open end to yield a better agreement with the moment method solution by providing a constant shift in the mean RCS level, but such an in-phase behavior of the TM<sub>1m</sub> modes may not actually take place over the entire range of  $a/\lambda$  values considered in Figure 35 and will therefore not completely explain the puzzling approximate 3 dR shift between the two independent calculations.

The on-axis solutions of Figures 33-34 can indeed be extended to a very large  $a/\lambda$ . As an example, which can be readily seen from Appendix

A, only 11 modes (i.e.,  $TE_{11}$  through  $TE_{1,11}$ ), instead of all the 320 modes, need be included when ka=35.2187.

Some additional interesting preliminary results of the work are shown in Figures 36-41. Figures 36-37 indicate the UTD-MSM based RCS calculations for a finite or semi-infinite hollow metallic circular cylinder open at the front end and closed (shorted) at the termination. These UTD-MSM based calculations are shown to agree very well with experimental results obtained from elsewhere [13,29].

The computational speed can be examined from Table 2.

TABLE 2

NUMBER OF MODES INCLUDED VERSUS CPU TIME REQUIRED

No. of modes included	Approximate CPU time required on a VAX-11/780 computer system to generate the numerical values of the RCS for the problems in Figures 1-4 and for a given aspect angle (8)
5	0.18 sec
10	0.57 sec
15	1.50 sec
20	3.01 sec
25	6.66 sec

Because the required CPU time increases sharply as one increases the number of modes, some measures must be taken to extend the solution for large values ka. To obtain the RCS at any desired angle, it is possible for the sake of computational efficiency to discard the modes which radiate weakly in that direction. A weak radiated field also means a weak induced field in the waveguide via reciprocity. It is noted that the distance L between the open end and the termination of the waveguide is so chosen that all the evanescent modes can be negligible.

Figures 39-41 indicate the UTD-MSM based calculations for the modulation envelope of both the the off-axis and the on-axis RCS for the configuration in Figure 1, but with two identical sets of planar blades which are physically located at the same position inside the circular intake duct. One set of these blades is kept fixed as a stator, while the other set is allowed to rotate (i.e., it forms a rotor). The RCS modulation envelope then indicates the extent of the change in RCS resulting from the motion of the rotor relative to the stator. Another example is shown in Figure 2 to illustrate the RCS of a semi-infinite hollow circular cylinder with a rotor-stator combination inside in which the stator and rotor blades are non-identical. This configuration which is shown in Figure 2 resembles most jet intake geometries. Consider the case where the stator and the rotor are assumed to have 60 and 30 blades, and the various angular widths for the stator and the rotor are 2° and 8°, respectively. The stator blades are connected to the intake wall, the length of the rotor blades is c=0.9a, and the radius of the center disk is assumed to be b=0.2a. Since the relative position of the

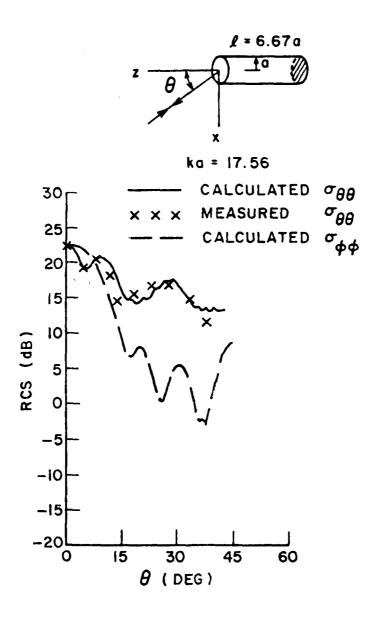


Figure 36. RCS (normalized to  $\pi a^2)$  of a finite length hollow metallic circular cylinder open at one end but closed at the other end.

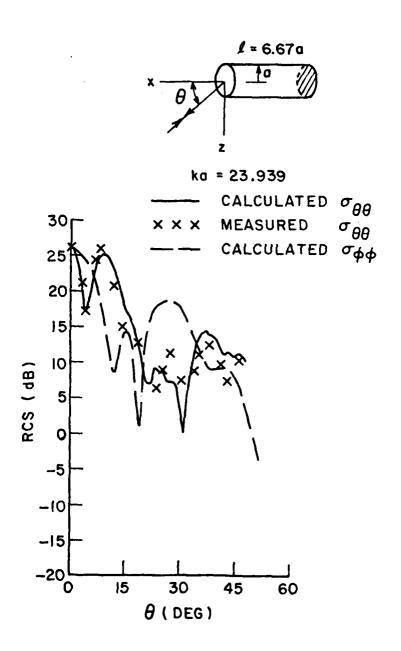


Figure 37. RCS (normalized to  $\pi a^2$ ) of a finite length hollow metallic circular cylinder open at one end but closed at the other end.

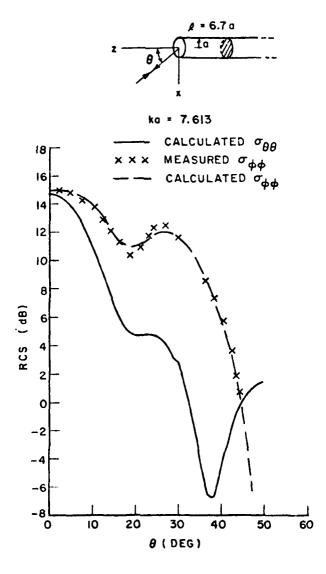


Figure 38. RCS (normalized to  $\pi a^2$ ) of a semi-infinite hollow metallic circular cylinder open at one end but closed at the other end.

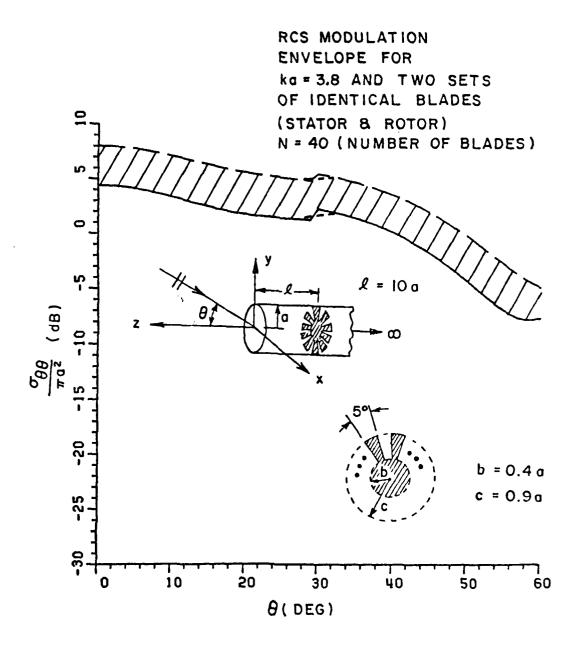


Figure 39. RCS (normalized to  $\pi a^2)$  modulation from a jet intake model.

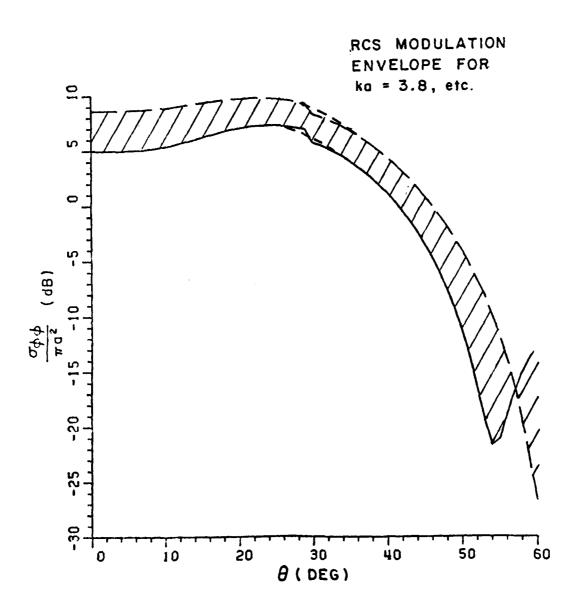


Figure 40. RCS (normalized to  $\pi a^2$ ) modulation from a jet intake model.

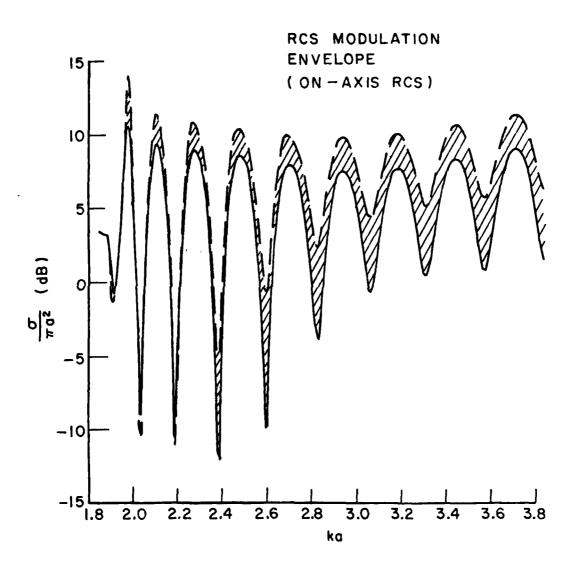


Figure 41. RCS (normalized to  $\pi a^2$ ) modulation from a jet intake model.

rotor blades with reference to the stator blades is a periodic function of time (t) with a period T, the reflection coefficient matrix  $[S_b]$  associated with that composite rotor-stator blade structure discontinuity, and also, the total backscattered field E has the same periodic property. The angular frequencies present in the backscattered electric field E are obtained in this case. Frequencies other than those corresponding to the one associated with the incident wave will be present in E because of blade rotation. In particular, these additional angular frequencies in E resulting from blade rotation (relative to the stator) comprise the so-called modulation frequencies, and they give rise to the RCS modulation frequency spectrum. A short analysis leading to the determination of the RCS modulation frequencies is provided next as in [30]. Let

$$\overline{E}^{S} = \overline{\Sigma}(t) e^{j\omega_0 t} \qquad (211)$$

where  $\omega_0$  is the angular frequency of the incident plane wave and  $\overline{\Sigma}(t)$  is a complex function of t with period T. It can be seen that

$$T = \frac{6^{\circ}}{\omega_{\Gamma}} \qquad (212)$$

where  $\omega_r$  is the angular velocity with which the blades rotate.

 $\overline{\Sigma}(t)$  is a periodic function; therefore, it can be represented by a summation of its Fourier series,

$$\overline{\Sigma}(t) = \sum_{m=-\infty}^{\infty} \overline{F}(m) e \qquad (213)$$

If  $|\overline{F}(m)| \approx 0$ , for  $|m| > N_0/2$ , then Eq. (213) can be adequately approximated by

$$\overline{\Sigma}(t) = \sum_{m=-N_0/2}^{N_0/2-1} \overline{F}(m) e^{j2\pi mt/T}$$

$$= \sum_{m=0}^{N_0-1} \overline{F}(m-N_0/2) e^{j2\pi(m-N_0/2)t/T} . \qquad (214)$$

Let

$$\overline{\Sigma}(t) e^{j\pi N_0 t/T} = \overline{\Sigma}_1(t) . \qquad (215)$$

and

$$\overline{F}(m-N_0/2) = \overline{F}_1(m) \qquad . \tag{216}$$

Then

$$\overline{\Sigma}_{1}(t) = \sum_{m=0}^{N_{0}-1} \overline{F}_{1}(m) e \qquad (217)$$

The inverse transform is

$$\overline{F}_{1}(m) = \frac{1}{N_{0}} \sum_{t N_{0}/T=0}^{N_{0}-1} \overline{\Sigma}_{1}(t) e^{-j2\pi mt/T} . \qquad (218)$$

The  $\overline{F}_1(m)$  in Eq. (218) can be obtained via the Fast Fourier Transform (FFT) algorithm applied to the RHS of Eq. (218). From Eqs. (211)-(213), we have

$$\overline{E}^{bs} = \sum_{m=-\infty}^{\infty} \overline{F}(m) e \qquad (219)$$

The power density spectrum of Eq. (219) is defined by

$$S(\omega) = \frac{1}{2T_0} \left| \int_{-T_0}^{T_0} \int_{m=-\infty}^{\infty} F(m) e^{j[(\omega-\omega_0)-2\pi m/T]t} dt \right|^2$$

$$= \frac{2}{T_0} \int_{m=-\infty}^{\infty} \overline{F}(m) \frac{\sin[(\omega-\omega_0)-2\pi m/T]T_0}{(\omega-\omega_0)-2\pi m/T}$$

$$\stackrel{\circ}{\underset{m'=-\infty}{\sum}} \overline{F}^*(m') \frac{\sin[(\omega-\omega_0)-2\pi m'/T]T_0}{(\omega-\omega_0)-2\pi m'/T}$$
(220)

As  $T_0 \rightarrow \infty$ ,

$$S(\omega) = 2\pi \sum_{m=-\infty}^{\infty} |\overline{F}(m)|^2 \delta[(\omega - \omega_0) - 2\pi m/T] . \qquad (221)$$

Thus, the angular frequencies or spectral lines of  $\overline{E}^{SS}$  are located at

$$\omega = \omega_0 + 2\pi m/T = \omega_0 + m\omega_0$$
; m=0, ±1, ±2, ..., (222)

Clearly mup represent the modulation frequency spectrum for  $\overline{E}^{bS}$ . The power density spectral lines for the backscattered field at  $\theta$ =40° (see Figure 2 for  $\theta$ ) are shown in Figure 42 where it is seen that the results for the  $\hat{\theta}$  and  $\hat{\phi}$  polarized returns are almost identical for the special case of  $\theta$ =40°.

Additional results for the modulation frequency spectra are shown for various combinations of M rotor blades and N stator blades, and for different 0, and also different ka values in Figures 43-46. The dimensions of the rotor and stator blades as well as of the central disc

are also shown in these figures. The various angular widths for the stator vane and the rotor blade are all kept at 2° and 8°, respectively. Note that the period T depends on the rotor-stator combination, and except for Figure 42, is not necessarily given by Eq. (212). It is seen from these RCS modulation spectra that their amplitudes in certain cases (particularly for certain combinations of the number of rotor and stator blades) can be significant. Clearly, a more realistic rotor-stator model would be worth investigating to obtain a more realistic RCS modulation spectrum of jet inlet configurations. This task is not simple, but it is hoped that based on some of the results of the initial study on the RCS of a simplied jet inlet model reported here, it is a topic which is certainly worth pursuing in the future. The accuracy of the RCS analysis of the simplified models chosen in Figures 1-4 is based in turn on the good accuracy obtained in the UTD ray solutions developed here for the elements of the various scattering matrices in the MSM based formulation of these problems. The good accuracy of the UTD ray solutions and their modifications at caustics is established in Section 3 where the results based on the UTD are compared against results based on available exact (but more cumbersome) solutions in some cases and based on measurements in other cases. It is also noted that the MSM has proved to be quite accurate wherever it has been employed elsewhere for solving various other scattering problems [10]; consequently the present UTD-MSM analysis is also expected to yield the same type of accuracy in dealing with the problems in Figures 1-4. An advantage of the present UTD ray representation for the elements of the scattering

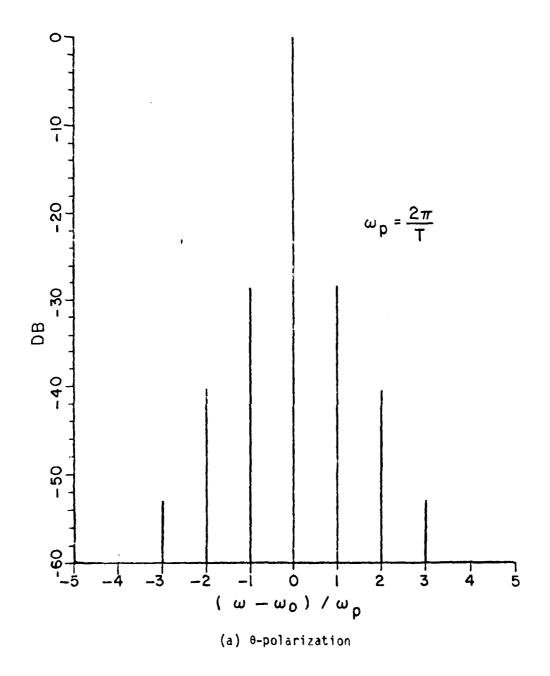
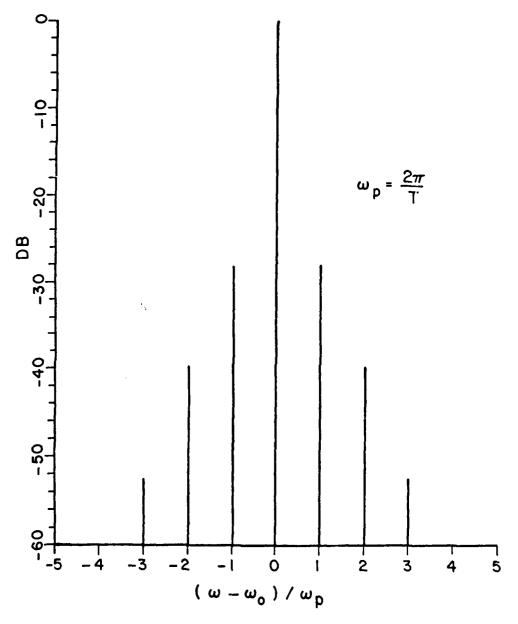


Figure 42. Power density frequency spectrum of the polarized backscattered electric field for the problem in Figure 2 with  $\theta$ =40°, ka=3.8, number of stator vanes=60, number of rotor blades=30, disc radius b=0.2a, and the blade length c=0.9a.



(b)  $\phi$ -polarization

Figure 42. (continued)

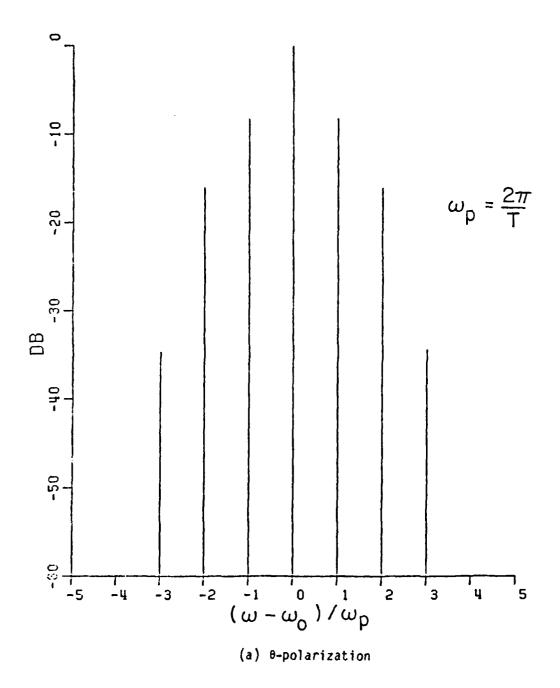
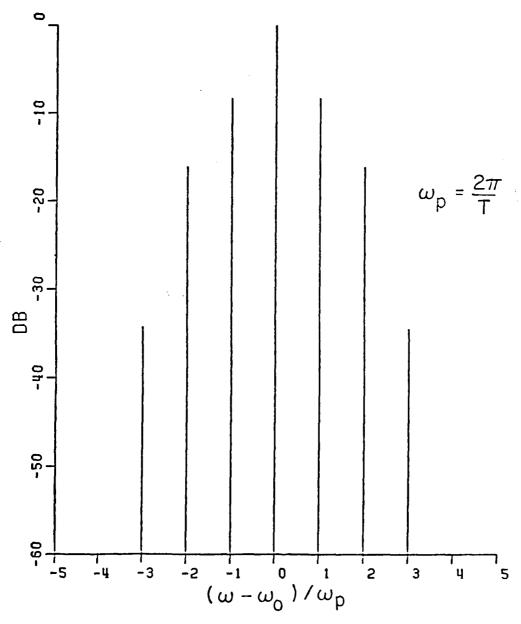


Figure 43. Power density frequency spectrum of the backscattered electric field for the problem in Figure 2 with  $\theta$ =0°, ka=3.8, number of stator vanes =40, number of rotor blades=40, and disc radius, b=0.2a. The blade length, c=0.9a.



(b)  $\phi$ -polarization

Figure 43. (continued)

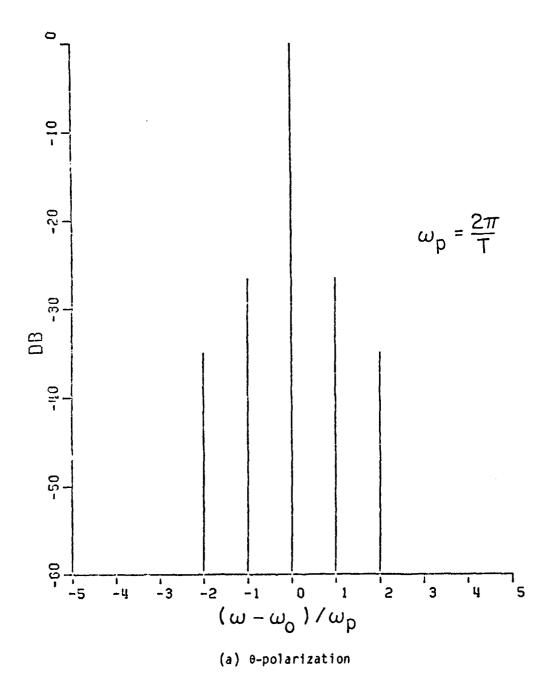


Figure 44. Power density frequency spectrum of the backscattered electric field for the problem in Figure 2 with 0=0°, ka=3.8, number of stator vanes =20, number of rotor blades=40, and disc radius, b=0.2a. The blade length, c=0.9a.

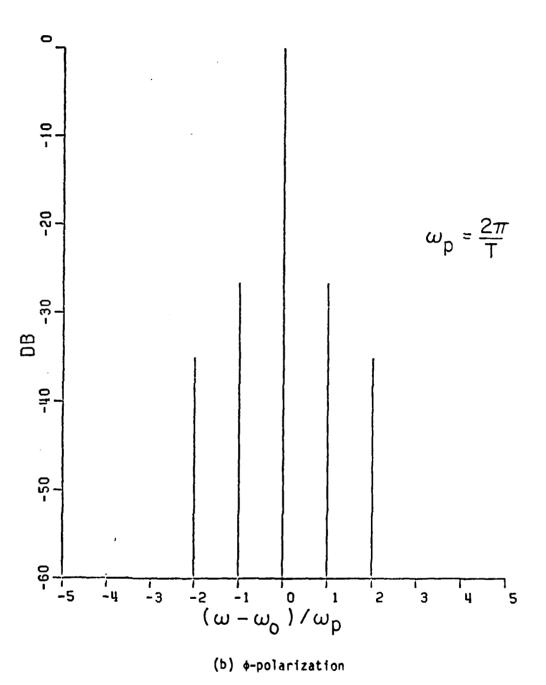


Figure 44. (continued)

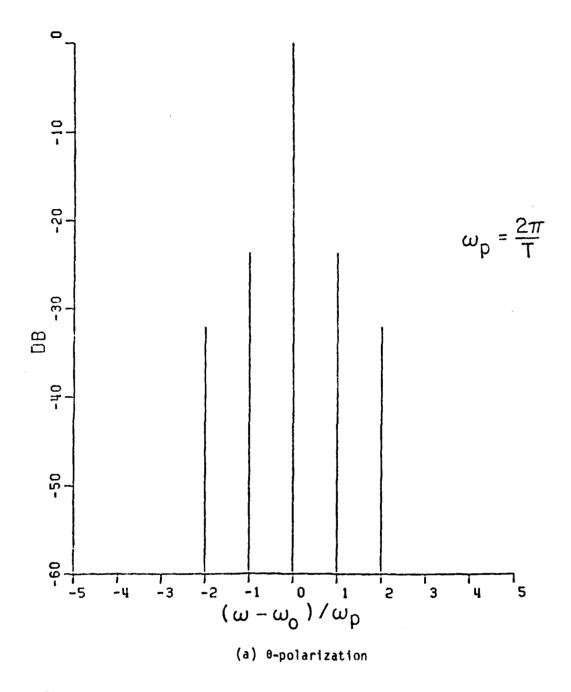
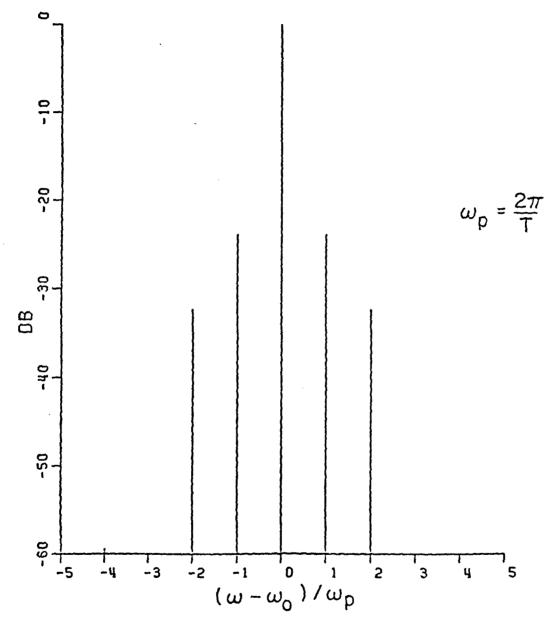


Figure 45. Power density frequency spectrum of the backscattered electric field for the problem in Figure 2 with  $\theta$ =0°, ka=5, number of stator vanes =20, number of rotor blades =40, and disc radius, b=0.2a. The blade length, c=0.9a.



(b) 4-polarization

Figure 45. (continued)

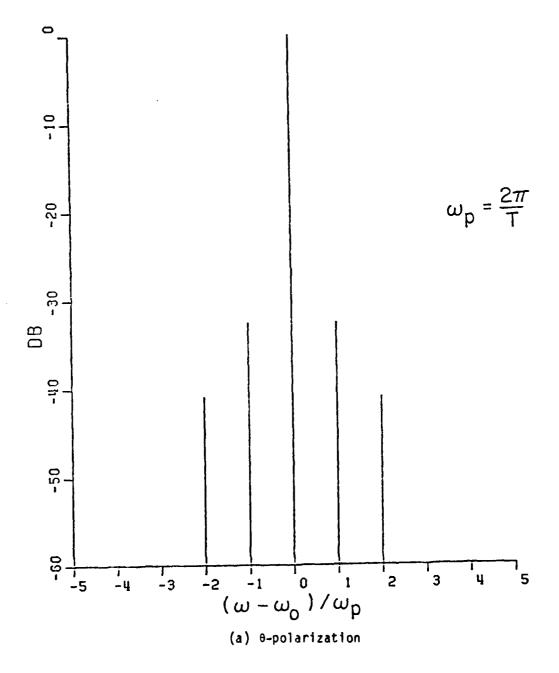
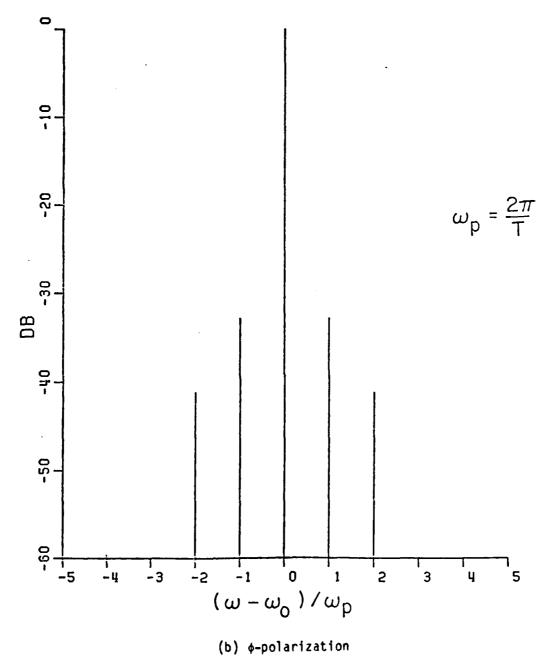


Figure 46. Power density frequency spectrum of the backscattered electric field for the problem in Figure 2 with 0=0°, ka=5, number of stator vanes=8, number of rotor blades=40, and disc radius, b=0.2a. The blade length, c=0.9a.



(0) Y POIL (010)

Figure 46. (continued)

matrices required in the MSM is that they are not only simple (in comparison to those available from the exact Wiener-Hopf solution), and quite accurate, but they also yield a physical insight into the dominant scattering mechanisms present in the problems of Figures 1-4. The latter aspect of the UTD ray analysis offers the potential for controlling the RCS.

While it would be worthwhile extending the present work to deal with more realistic stator-rotor models, it is also worthwhile as a part of future research to study the effects on the RCS of changing the cross-sectional shapes of the inlet duct, e.g., from the present circular form to rectangular, skewed rectangular, semi-circular, or elliptical forms. In addition, it is also of interest to consider the continuous changes in the duct cross-section along the length of the inlet duct, e.g., from rectangular to circular, or a semi-circular to a circular one with a bend. The latter cross-sectional shapes and changes in the cross-section along the length of the inlet duct commonly occur in practice. A related study, which has been under investigation by Volakis [36], is on estimating the RCS of a jet intake mounted on a convex surface. All of the above mentioned problems are difficult, challenging, and worthy of future investigation in the area of RCS studies.

## PART II

# CANONICAL RESPONSE WAVEFORMS OF FINITE AND OPEN LOADED CIRCULAR WAVEGUIDES

Chun-Yue Lai
David L. Moffatt

### SECTION 1

### PRELIMINARY DISCUSSION FOR PART II

The interaction of electromagnetic waves with the jet intake and exhaust configurations on modern aerospace vehicles are important scattering mechanisms. While both cross section modification effects have been measured, a firm understanding of the scattering mechanisms has not followed. The purpose of this report is to first demonstrate the simplicity and diagnostic potential of the canonical response waveforms for a cavity structure and then to postulate an approximate time domain derived model to predict the scattering from circular waveguide geometries which is suitable for extension to more complex cavities.

This report is primarily concerned with the spectral rather than the spatial variation of the electromagnetic scattering properties of finite and semi-infinite circular waveguides at guide diameters less than 3.0 or 4.0 wavelengths. Consequently, the interrogating signal waveforms are limited to axial incidence.

In the second section of this report, the exact low frequency and the asymptotic high frequency spectral solutions to an unloaded semi-infinite open circular waveguide are summarized. The analytical impulse response waveform is also discussed.

The third section centers upon the backscatter from finite circular waveguides with open or short rear terminations. The analytical model chosen is the finite circular waveguide shown in Figure 47. The waveguide has a diameter 2a and a length L. The waveguide walls are assumed to be infinitely thin and perfectly conducting. Consider first the case of a plane electromagnetic wave with shock type time dependence axially incident on the waveguide. Regardless of the observation point, the time-dependent scattered waveform must be the same as that which would be obtained from an open circular waveguide of the same dimension until such time when the incident wavefront travels to the rear of the guide and the subsequent perturbation then reaches the observer. It is clear therefore that some short time portion of the canonical response waveforms of the finite circular waveguide can be taken from those for an open or semi-infinite circular waveguide. Simply stated, the excitation cannot anticipate the termination of the waveguide. Furthermore, the evanescent and propagating modes initially launched at the guide rim are independent of the rear termination. Therefore the initial incident waveguide modes on any postulated internal structure (e.g., blades) and the subsequent reradiation coupling also come from a solution for the open circular waveguide. This brief discussion illustrates one reason why a time domain analysis, where a single real time-dependent waveform of relatively simple shape sums up the

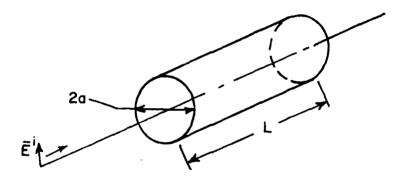


Figure 47. Finite circular waveguide, L≈10a.

scattering properties of an object at all frequencies, is felt to be a fundamental approach.

In the fourth section of this report, the effects of internal loading on open circular waveguides are studied. The different kinds of loading include short, disc and blade structures (2 and 40 blades). They are compared to the case of a hollow semi-infinite circular waveguide. This involves the joining of a high frequency and a low frequency spectrum through a rational function fit, thereby enabling the time domain responses to be found. Though there is no exact way to prove the correctness of the fit, the time domain waveforms produced thereby do satisfy both physical and moment conditions.

In the fifth section, the poles of the open circular waveguide are explored and some preliminary results are presented. They are based both on results in the previous sections and on a proposed characteristic equation of the open circular waveguide.

An appendix discusses the implications of the research in this report on the recognition by active radar sensors of targets with cavity structures with resonant dimension apertures.

## SECTION 2

## SEMI-INFINITE OPEN CIRCULAR WAVEGUIDE

The formulas and results presented in this section are partially abstracted from a report by Johnson and Moffatt [12] and from a paper [41] by the same authors. A relatively complete list of significant references to the Wiener-Hopf solution is given in the report. The open circular waveguide and the coordinate system are shown in Figure 48. With the unfortunate e-iwt time convention, the incident and scattered fields are given respectively as

$$\overline{E}^{i} = \frac{e^{ikr}}{r} (\theta E_{\theta}^{i} + \phi E_{\phi}^{i}) , \qquad (223)$$

$$\overline{E}^{S} = \frac{e^{-ikr}}{r} \left( \hat{\theta} E_{\theta}^{S} + \hat{\phi} E_{\phi}^{S} \right) , \qquad (224)$$

where

$$\begin{bmatrix} E_{ij}^{S} \\ E_{\phi}^{S} \end{bmatrix} = \begin{bmatrix} S_{\theta\theta} & S_{\theta\phi} \\ S_{\phi\theta} & S_{\phi\phi} \end{bmatrix} \begin{bmatrix} E_{\theta}^{i} \\ E_{\phi}^{i} \end{bmatrix}$$
(225)

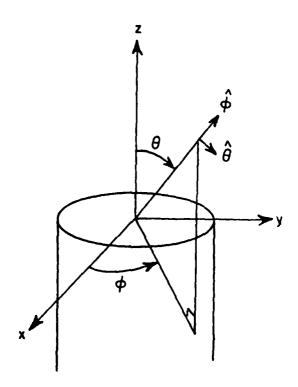


Figure 48. Coordinate system for Wiener-Hopf solution to semi-infinite cylinder.

The components of the far field scattering matrix in Equation (225) are

$$S_{\theta\theta} = -\frac{2i}{k} \sum_{n=0}^{\infty} \varepsilon_n \cos n\phi_s \frac{J_n(kasin\theta_i)}{sin\theta_i L_+(kcos\theta_i)} \frac{J_n(kasin\theta_s)}{sin\theta_s L_+(kcos\theta_s)}.$$

$$\left[\frac{(1-\cos\theta_{i})(1-\cos\theta_{s})}{2(\cos\theta_{i}+\cos\theta_{s})} - \frac{f_{n}^{2}}{1-f_{n}^{2}}\right]$$
(226)

$$S_{\phi\phi} = \frac{2i}{k(1+\cos\theta_i)(1+\cos\theta_S)} \sum_{n=0}^{\infty} \varepsilon_n \cos n\phi_S \frac{J_n'(ka\sin\theta_i)}{M_+(k\cos\theta_i)} \frac{J_n'(ka\sin\theta_S)}{M_+(k\cos\theta_S)}$$

$$\left[\frac{(1+\cos\theta_{i})(1+\cos\theta_{s})}{2(\cos\theta_{i}+\cos\theta_{s})} + \frac{f_{n}^{2}}{1-f_{n}^{2}}\right], \qquad (227)$$

$$S_{\theta\phi} = \frac{4i}{k(1+\cos\theta_i)} \sum_{n=1}^{\infty} \sin_{n\phi} \frac{J_n(ka\sin\theta_s)}{\sin\theta_s L_+(k\cos\theta_s)} \frac{J_n(ka\sin\theta_i)}{M_+(k\cos\theta_i)} \cdot \frac{f_n}{1-f_n^2},$$
(228)

$$S_{\phi\theta} = \frac{4i}{k(1+\cos\theta_S)} \sum_{n=1}^{\infty} \sin_{n\phi_S} \frac{J_n'(ka\sin\theta_S)}{M_+(k\cos\theta_S)} \frac{J_n(ka\sin\theta_i)}{\sin\theta_i L_+(k\cos\theta_i)} \frac{f_n}{1-f_n^2},$$
(229)

Where

$$f_n = \frac{nL_+(k)}{2kaM_+(k)}$$
(230)

and

$$\varepsilon_{n} = \begin{cases}
1 & n = 0 \\
2 & n = 1, 2, 3...
\end{cases}$$
(231)

The exact defining integrals for the Wiener-Hopf factorization functions  $(L_+(k), M_+(k))$  in Equation (230)\*) are given in Johnson and Moffatt [12]. In the same reference these functions are evaluated exactly (diameter/wavelength less than 3.0) using numerical integration.

For axial incidence ( $\theta_1=0,n=1$ ) the infinite summations for the polarization matrix coefficients disappear and

$$S_{\theta\theta} \mid_{\theta_{1}=0} = \frac{2ia\cos(\phi_{S})J_{1}(ka\sin\theta_{S}) L_{+}(k)}{\sin(\theta_{S})L_{+}(k\cos\theta_{S})[(2kaM_{+}(k))^{2}-(L_{+}(k))^{2}]}, \quad (232)$$

$$S_{\phi\phi} \mid_{\theta_{1}=0} = \frac{4ika^{2}cos(\phi_{S})J_{1}(kasin\theta_{S})M_{+}(k)}{[1+cos\theta_{S}]M_{+}(kcos\theta_{S})[(2kaM_{+}(k))^{2}-(L+(k))^{2}]}, \quad (233)$$

$$S_{\theta\phi} \mid_{\theta_{i}=0} = \frac{i4a\sin(\phi_{S})J_{1}(ka\sin\theta_{S})L_{+}(k)}{\sin(\theta_{S})L_{+}(k\cos\theta_{S})[(2kaM_{+}(k))^{2}-(L_{+}(k))^{2}]}, \quad (234)$$

and

$$S_{\phi\theta} \mid_{\theta_{i}=0} = \frac{4ik^{2}a^{3}\sin(\phi_{S})J_{1}(ka\sin\theta_{S})(M_{+}(k))^{2}}{[1+\cos\theta_{S}]M_{+}(k\cos\theta_{S})L_{+}(k)[(2kaM_{+}(k))^{2}-(L_{+}(k))^{2}]} \cdot (235)$$

<sup>\*</sup> more properly written as  $L_{+}(k,n)$ ,  $M_{+}(k,n)$ .

For axial backscatter ( $\theta_S=0$ )

$$S_{\theta\theta} \mid_{\theta_1 = \theta_S = 0} = S_{\phi\phi} \mid_{\theta_1 = \theta_S = 0} = \frac{kia^2}{[(2kaM_+(k))^2 - (L_+(k))^2]},$$
(236)

and, of course, the cross-polarized terms are zero. Bowman [8] has given an asymptotic result for the case of axial backscatter which yields an impulse response approximation through inverse Laplace transform

$$F_{I}(t) = \frac{-a}{2} \delta(t) - \frac{a}{2\pi \sqrt{t_0}} \sum_{m=1}^{\infty} \frac{(-j)^{m} [1 + (-1)^{m}] u(t - 2mt_0)}{m^{3/2} 2\sqrt{t - 2mt_0}} - \frac{1}{2\sqrt{t - 2mt_0}} \frac{(-j)^{m} [1 + (-1)^{m}] u(t - 2mt_0)}{(-j)^{m} [1 + (-1)^{m}] u(t - 2mt_0)}$$

$$\frac{a}{2\pi \sqrt{t_0}} \sum_{m=1}^{\infty} \frac{(j)^{m+1} (1-(-1)^m] u (2mt_0-t)}{m^{3/2} 2\sqrt{2mt_0-t}},$$
(237)

where  $t_0=^d/c$  is the transit time for the guide radius and the spatial propagation and delay have been suppressed. Beyond the reflected impulse the response consists of alternating (sign) paired causal and non-causal contributions delayed by integer multiples of the transit time for the guide diameter. A sketch of the response of Equation (237) is shown in Figure 49. While the peaks predicted are singularities, the attenuation is severe because of the weighting and only the first few terms contribute significantly. A comparison of the

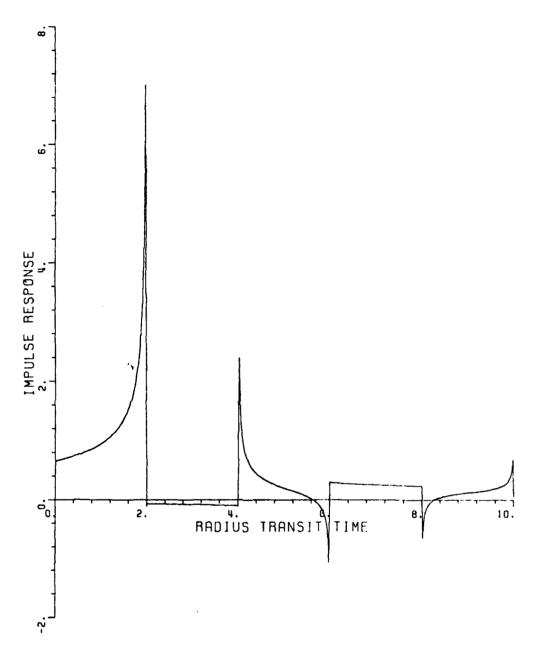


Figure 49. Inverse Laplace Transform of on-axis backscatter; asymptotic approximation.

impulse response of the open circular waveguide predicted using Fourier synthesis of the exact results in Equation (236) and Bowman's [8] asymptotic approximation is reproduced from the paper by Johnson and Moffatt [41] in Figure 50. Axial backscatter cross sections were also compared and are reproduced in Figure 51. The asymptotic frequency domain results of Bowman (1970) were also obtained by Chuang, Liang and Lee [11]\*. The impulse response comparisons in Figure 50 show that the major failure of the asymptotic waveform occurs between delays of 2 to 6 guide radii transit times. This translates into a major cross section error of roughly 8.0 dB at a guide diameter of 0.59 wavelengths which is the cutoff wavelength of the first propagating mode (TE<sub>11</sub>). Progressively, as the guide diameter increases, the peaks of the axial backscatter cross section occur at essentially the TE mode cutoffs (TE<sub>11</sub>, TE<sub>21</sub>, TE<sub>01</sub>, etc.) and the cross section nulls are slightly in advance (lower  $^{0}/_{\lambda}$ ) of the cutoffs for the TM modes (TM $_{01}$ , TM $_{11}$ , TM $_{21}$ etc.). From Figure 51, the asymptotic result is a reasonable approximation for guide diameters greater than one and an excellent one for guide diameters greater than two.

The simplicity of the time domain waveforms is emphasized. Despite the complexities of the Wiener-Hopf solution the time domain waveforms in Figures 49 and 50 are extremely simple. The noncausality of the odd order summation in Equation (237) precludes direct utilization of this model for terminated guides and guides with internal structures.

<sup>\*</sup>The exact results of Chuang, Liang and Lee [11] were in error, as reported in a corrections letter. Chuang et al. [39].

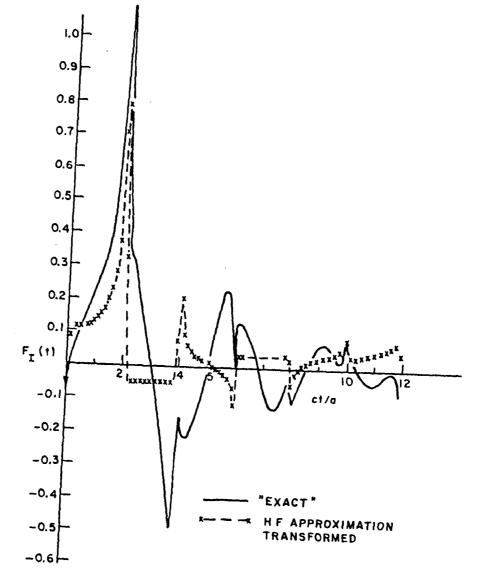


Figure 50. Inverse Laplace transform of on-axis backscatter, comparing exact numerical results with asymptotic approximation.

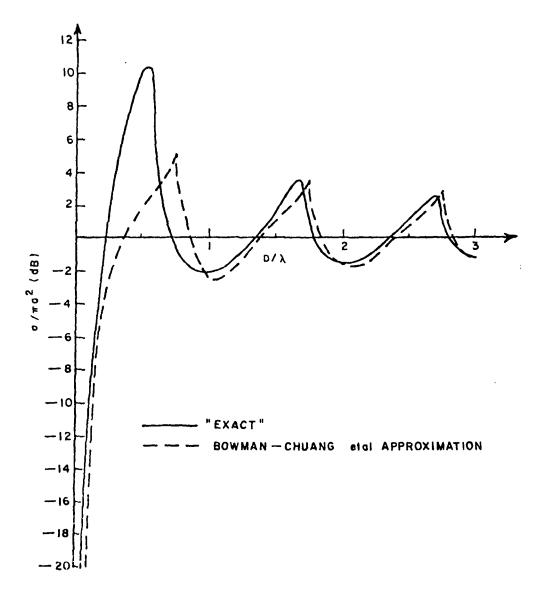


Figure 51. On-axis normalized radar cross section for semi-infinite circular cylinder.

If the approximation

$$\frac{-a}{2\pi \sqrt{t_0}} \sum_{m=1}^{\infty} \frac{(j)^{m+1} [1-(-1)^m] u (2mt_0-t)}{\sqrt[3]{2} 2\sqrt{2mt_0-t}} \simeq$$

$$\frac{-a}{2\pi \sqrt{t_0}} \sum_{m=1}^{\infty} \frac{(j)^{m+1} [1-(-1)^m] [u(t-2(m-1)t_0)-u(t-2mt_0)]}{m^{3/2} 2\sqrt{2mt_0-t}},$$
(238)

is made then the waveforms are identical for  $t \ge 2(m-1)t_0$  (m is odd) but a small step discontinuity results at  $t = 2(m-1)t_0$ . The asymptotic waveforms in Figures 49 and 50 have been terminated at zero but actually are nonzero for negative time and hence noncausal. The addition of a real axis pole, with high damping, to remove the step discontinuity in Equation (238) would appear to be feasible. Instead of the correction of Equation (238), we have

$$g_{c}(t) = \frac{-a}{2\pi \sqrt{t_{0}}} \sum_{m=1}^{\infty} \frac{(j)^{m+1} [1-(-1)^{m}] (1-e^{-\alpha(t-2(m-1)t_{0})})}{m^{3/2} 2\sqrt{2mt_{0}-t}} [u(t-2(m-1)t_{0}) -u(t-2mt_{0})].$$
(239)

where  $g_C(t)$  replaces the odd order summation in Equation (237). The resulting time waveform with the modification of Equation (239) is shown in Figure 52. It is found that when  $\alpha^t$ 0 is of the order of 10, the asymptotic results in the frequency domain are not altered significantly.

A comparison was made of the radar cross section of the circular guide as given by Bowman [8] with that using the modification of

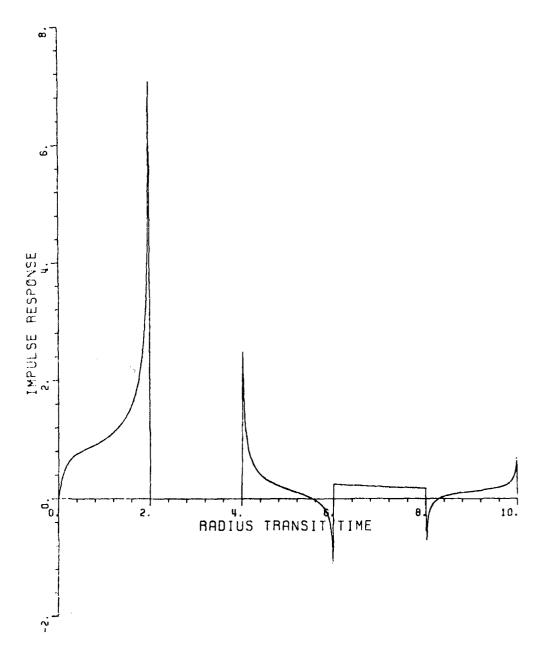


Figure 52. Modified impulse response of on-axis backscatter with asymptotic approximation,  $\alpha t_0 \! = \! 8$  .

Equation (239). The radar cross section according to Bowman is (converted to  $e^{jwt}$  time convention)

$$\frac{\sigma}{\pi a^2} \sim \left| 1 + \frac{e^{-j\pi/4}}{\sqrt{\pi k a}} \sum_{m=1}^{\infty} \frac{(-j)^m e^{-j2mka}}{\sqrt{m^3/2}} \right|^2$$
 (240)

The radar cross section with the modification of Equation (239) is

$$\frac{\sigma}{\pi a^2} \sim \left| 1 + \frac{e^{-j\pi/4}}{\sqrt{\pi k a}} \right|_{m=2}^{\infty} \frac{(-j)^m e^{-j2mka}}{\sqrt{3/2}}$$
m even

$$+ \sum_{m=1}^{\infty} \frac{(-j)^m}{m^{3/2}} \qquad \frac{e^{-j2mka}}{\sqrt{j\pi ka}} \left\{ \left[ 1 - \text{Erfc}(j\sqrt{j2ka}) \right] - \frac{e^{-j2mka - 2\alpha t_0}}{\sqrt{\pi} \sqrt{jka + \alpha t_0}} \left[ 1 - \text{Erfc}(j\sqrt{2jka} + 2\alpha t_0) \right] \right\} \right\}^{2}$$
(241)

In Table 3, these asymptotic forms are compared to the exact solution given by Johnson and Moffatt [12]. It is evident from Table 2-1 that for  $^{\rm D}/_{\lambda}>0.6$ , the cross sections corresponding to causal and noncausal time waveforms are equally good approximations of the exact solution.

Asymptotic results obtained from a ray optical approximation, Bowman [8], are identical to Equation (237) up to m=2 but thereafter differ in the weights of the terms. The asymptotic result in Figure 50

Equation (239). The radar cross section according to Bowman is (converted to  $e^{jwt}$  time convention)

$$\frac{\sigma}{\pi a^2} \sim \left| 1 + \frac{e^{-j\pi/4}}{\sqrt{\pi k a}} \right|_{m=1}^{\infty} \frac{(-j)^m e^{-j2mka}}{\sqrt[3]{2}} \left| \frac{2}{m^{3/2}} \right|_{m=1}^{\infty}$$
(240)

The radar cross section with the modification of Equation (239) is

$$\frac{\sigma}{\pi a^2} \sim \left| 1 + \frac{e^{-j\pi/4}}{\sqrt{\pi k a}} \right|_{m=2}^{\infty} \frac{(-j)^m e^{-j2mka}}{\frac{3}{2}}$$

$$+ \sum_{m=1}^{\infty} \frac{(-j)^m}{m^{3/2}} \qquad \frac{e^{-j2mka}}{\sqrt{j\pi ka}} \left\{ \left[ 1 - \text{Erfc}(j\sqrt{j2ka}) \right] - \frac{e^{-j2mka - 2\alpha t_0}}{\sqrt{\pi} \sqrt{jka + \alpha t_0}} \left[ 1 - \text{Erfc}(j\sqrt{2jka} + 2\alpha t_0) \right] \right\} \right\}$$

$$(241)$$

In Table 3, these asymptotic forms are compared to the exact solution given by Johnson and Moffatt [12]. It is evident from Table 2-1 that for  $^{\rm D}/_{\lambda}$  > 0.6, the cross sections corresponding to causal and noncausal time waveforms are equally good approximations of the exact solution.

Asymptotic results obtained from a ray optical approximation, Bowman [8], are identical to Equation (237) up to m=2 but thereafter differ in the weights of the terms. The asymptotic result in Figure 50

TABLE 3

COMPARISON OF RADAR CROSS SECTION (dB) OF EXACT SOLUTION (JOHNSON), ASYMPTOTIC SOLUTION (BOWMAN) AND MODIFIED ASYMPTOTIC SOLUTION (Eqn. 2-19, MOFFATT)

731	HI TOTTO SOCOTIO	· (Edir e	-15, MOLLALLY
D/X	Johnson	Bowman	Moffatt
0.100	-9.458848		
0.110	-8.520934		
0.120	<b>-7.6467</b> 16		
0.130	-6.824223		
0.140	-6.045925		
0.150	-5.305766		
0.160	-4.595446		
0.170	-3.913079		
0.180	-3.255218		
0.190	-2.617804		
0.200	-2.001531		
0.210 0.220	-1.408495		
0.230	-0.833483 -0.276990		
0.240	0.264939		
0.250	0.792181		
0.260	1.301408		
0.270	1.795182		
0.280	2.270724		
0.290	2.731840		
0.300	3.174628		
0.310 🔩	3.627388		
0.320	4.064384		
0.330	4.490535		
0.340	4.902714		
0.350	5.301191		
0.360	5.686905		
0.370	6.056279		
0.380	6.408279		
0.390	6.744378		
0.400	7.066416		
0.410	7.288048		
0.420	7.530067		
0.430 0.440	7.786634		
0.450	8.061458 8.346395		
0.460	8.636331		
0.470	8.927008		
0.460	9.213129		
0.490	9.493250		
0.500	9.743763		
0.510	9.976593		
0.520	10.161530		
0.530	10.306625		
0.540	10.395186		
0.550	10.413555		
0.560	10.367692		
0.570	10.254469		
0.580	9.873226		
0.590	8.092514		
0.600 0.610	6.002594 4.758259	2 071422	0 00000
0.620	3.745943	3.071432	2.880305
0.630	2.918265	3.244816	3.006446
0.640	2.248425	3.336831	3.090103 3.203558
0.650	1.711760	3.476034	3.363394
0.660	1,291267	3.585063	3.488144
0.670	0.976372	3.642307	3.560661
0.680	0.755607	3.740452	3.678851
0.690	0.615962	3.907654	3.866302
0.700	0.557735	4.030650	4.003542
0.710	5.867754	4.074891	4.060959
0.720	5.615556	4.203629	4.211191

0.730	5.300941	4.496467	4.528727
0.740	4.915490	4.701146	4.745268
0.750	4.462694	4.495789	4.531584
0.760	3.960338	3.819680	3.829793
0.770	3.412798	2.965487	2.946289
0.780	2.842850	2.349164	2.317832
0.790	2.256176	2.000432	1.971990
0.800	1.679505		1.605475
0.810	1.117669	1.635842 1.187165	1.147456
	0.591479		0.775175
0.820		0.819100	
0.830	0.107829	0.564319	0.523153
0.840	-0.325362	0.281201	0.238399
0.850	-0.703480	-0.053583	-0.104108
0.860	-1.026303	-0.324297	-0.378683
0.870	-1.288107 -1.497142	-0.521342 -0.749196	-0.574454
0.880	-1.655850	-1 000100	-0.805479
0.890 0.900	-1.767546	-1.009100 -1.208304	-1.073821
		-1.200304	-1.277504
0.910	-1.839869	-1.354398	-1.423762
0.920	-1.882918	-1.531832	-1.606125
0.930	-1.901502	-1.726239	-1.809954
0.940	-1.899772	-1.861168	-1.949681
0.950	-1.890381	-1.957783	-2.047384
0.960	-1.877861	-2.085210	-2.181114
0.970	-1.866457	-2.217362	-2.323117
0.980	-1.861093	-2.292324	-2.402434
0.990	-1.867049	-2.341610	-2.453027
1.000	-1.880707	-2.420392	-2.538843
1.010	-1.907961	-2.494346	-2.622281
1.020	-1.937236	-2.515522	-2.646585
1.030	-1.976914	-2.522350	-2.654363
1.040	-2.021478	-2.556740	-2.695997
1.050	-2.065371	-2.579477	-2.727279
1.060	-2.106021	-2.555760	-2.705028
1.070	-2.140774	-2.527534	-2.677213
1.080	-2.161213	-2.524461	-2.681547
1.090	-2.173288	-2.505359	-2.670043
1.100	-2.165415	-2.447143	-2.611728
1.110	-2.146071	-2.392444	-2.557278
1.120	-2.109116	-2.360129	-2.533267
1.130	-2.059807	-2.309289	-2.489850
1.140	-1.994752	-2.226755	-2.406308
1.150	-1.919178	-2.153824	-2.334631
1.160	-1.835327	-2.100295	-2.292448
1.170	-1.745910	-2.027018	-2.228523
1.180 1.190	-1.656677 -1.570702	-1.928881 -1.844659	-2.129956
1.200	-1.484781	-1.776799	-2.051133
1.210	-1.408654	-1.688724	-2.004253
1.220	-1.339279	-1.581738	-1.934084 -1.831867
1.230	-1.277167	-1.491552	-1.767274
1.240	-1.222956		
1.250	-1.222330	-1.414743 -1.317664	-1.771731 -1.782492
1.260	-1.173344 -1.131993	-1.206690	-1.732754
1.270 1.280	-1.089466	-1.114349 -1.032542	-1.629171
1.280	-1.045954	-0.930583	-1.506572
	-1.001394		-1.378139
1.300	-0.949340 -0.892804	-0.818919 -0.727010	-1.253332
1.310	-0.821347	-0.642964	-1.142442 -1.033542
1.320 1.330	-0.741740	-0.538906	-0.910714
1.340	-0.646153	-0.428665	-0.787844
1.350	-0.541254	-0.338876	-0.682887
1.330		-0.330070	-0.002001

1.360	-0.426064	-0.254430	-0.580401
1.370	-0.301055	-0.150045	-0.461617
1.380	-0.168339	-0.042492	-0.343499
1.390	-0.035823	0.044128	-0.244776
1.400	0.104695	0.127807	
1.410	0.237799	0.231507	-0.147102
1.420	0.367332		-0.031908
1.430	0.484647	0.335697	0.081024
1.440		0.418518	0.173686
	0.597126	0.500756	0.267246
1.450	0.692532	0.603329	0.379283
1.460	0.781571	0.703902	0.487138
1.470	0.859947	0.782561	0.573963
1.480	0.930879	0.863047	0.663914
1.490	0.995187	0.964523	0.773385
1.500	1.055551	1.061533	0.876530
1.510	1.116309	1.135811	0.957706
1.520	1.181357	1.214536	1.044577
1.530	1.251361	1.315421	1.152379
1.540	1.343095	1.409195	1.251371
1.550	1.441111	1.478916	1.327015
1.560	1.557706	1.556167	1.411466
1.570	1.694245	1.657583	1.519011
1.580	1.843339	1.748774	1.614656
1.590	2.005405	1.813689	1.684713
1.600	2.185416	1.890157	1.767725
1.610	2.370679	1.994319	1.877441
1.620	2.560735	2.084119	1.971007
1.630	2.746525	2.143686	2.035024
1.640	2.916111	2.220860	2.118327
1.650	3.073452	2.332511	2.235150
1.660	3.206708	2.423400	
1.670	3.309040		2.329006
1.680	3.373470	2.476077	2.385360
1.690	3.398627	2.557715	2.472930
1.700		2.689892	2.609956
1.710	3.383114 3.316839	2.788655	2.710307
1.720		2.827770	2.751536
1.730	3.205293	2.929719	2.859467
1.740	3.044869	3.150998	3.084904
1.750	2.833142	3.290674	3.218311
	2.592613	3.093302	3.003269
1.760	2.303109	2.531862	2.419261
1.770	1.991521	1.873926	1.745675
1.780	1.658170	1.433071	1.302936
1.790	1.305361	1.187997	1.060206
1.800	0.957284	0.921487	0.791057
1.810	0.610778	0.604546	0.470287
1.820	0.279078	0.359371	0.225954
1.830	-0.032145	0.191298	0.060154
1.840	-0.311415	-0.002104	-0.134483
1.850	-0.558779	-0.224069	-0.358561
1.860	-0.772689	-0.393827	-0.527132
1.870	-0.951250	-0.516808	-0.648159
1.880	<b>~1.0</b> 97941	-0.664287	-0.796644
1.890	~1.204541	-0.827888	-0.961813
1.900	-1.290164	-0.946561	-1.079222
1.910	-1.342392	-1.033748	-1.164748
1.920	-1.369620	-1.144185	-1.276220
1.930	-1.383562	-1.262092	-1.395434
1.940	-1.391595	-1.339409	-1.471423
1.950	-1.385437	-1.395425	-1.526003
1.960	-1.376858	-1.473282	-1.605004
1.970	-1.372984	-1.552135	-1.684992
1.980	-1.373787	-1.594074	-1.725501

1.990	-1.378723	-1.622507	-1.752666
2.000	-1.388200	-1.671246	-1.802734
2.010	-1.409455	-1.716079	
	-1.409433	-1.710079	-1.848584
2.020	-1.434915	~1.727710	-1.858684
2.030	-1.468116	~1.732179	-1.862118
2.040	-1.497193	-1.755308	-1.886827
2.050	-1.530067	~1.770888	-1.903411
2.060	-1.563129	-1.757145	-1.888087
2.070	-1.588005	-1.741491	-1.871730
2.080	-1.605111	-1.742748	-1.875067
2.090	-1.614407		-1.867363
		~1.733845	-1.00/303
2.100	-1.611845	-1.699564	-1.831599
2.110	-1.597379	-1.667681	-1.799615
2.120	-1.570827	-1.650900	-1.785888
2.130	-1.540240	<b>~1.</b> 622135	-1.758935
2.140	-1.492945	~1.571873	-1.707582
2.150	-1.4411.86	~1.527465	-1.664295
2.160	-1.380228	-1.496309	-1.638246
2.170	-1.318419	~1.451953	-1.597253
2.180	-1.255688	~1.389776	-1.535095
2.190	-1.187466	~1.336162	-1.485539
2.200	-1.126583	-1.293949	-1.453743
2.210	-1.073125	-1.237741	-1.405459
2.220	-1.018938	-1.167085	-1.338488
2.230	-0.976863	~1.107094	-1.294459
2.240	-0.934144	-1.056673	-1.283988
2.250	-0.899574	~0.991729	-1.264609
2.260	-0.869091	-0.915403	
		-0.913403	-1.207512
2.270	-0.842774	~0.851337	-1.130548
2.280	-0.811835	~0.795051	-1.052014
2.290	-0.781015	-0.723874	-0.967828
2.300	-0.745597	~0.644072	-0.881089
2.310	-0.705026	~0.577760	-0.804591
2.320	-0.650821	-0.517472	-0.731987
2.330	-0.596142	-0.441996	-0.647846
2.340	-0.526942	-0.360383	-0.560333
2.350	-0.447948		
		-0.293233	-0.485653
2.360	-0.367513	-0.230377	-0.414110
2.370	-0.271103	-0.152039	-0.329275
2.380	-0.178004	-0.069832	-0.242304
2.390	-0.073619	-0.002917	-0.169533
2.400	0.028423	0.061431	-0.098514
2.410	0.128111	0.141632	-0.013175
2.420	0.224486	0.223572	0.072640
2.430	0.318318	0.289447	0.143230
2.440	0.403315	0.354519	0.213689
2.450	0.479265	0.435962	0.299333
2.460	0.546875	0.517072	0.383632
2.470	0.609710	0.581285	0.451736
2.480	0.662336	0.646574	0.521530
2.490	0.715476	0.728991	0.607470
2.500	0.763727	0.808966	0.690081
2.510	0.811773	0.871008	0.755399
2.520	0.860367	0.936242	0.824500
2.530	0.919062	1.019756	0.911021
2.540	0.983261	1.098520	0.991961
2.550	1.064192	1.157938	1.054157
2.560	1.156561	1.223094	1.122714
2.570	1.261352	1.306351	1.210564
2.580	1.383782	1.386109	1.290070
2.590	1.514239	1.442373	1.348685
2.600	1.653584	1.507758	1.417113

predicts the positions of signularities and discontinuity quite well but fails to predict the damped sinusoid corresponding to the large error in cross section at the cutoff frequency of the first propagating mode  $TE_{11}$ .

If the open circular waveguide is shorted internally at a distance L down the guide then each propagating mode is reflected as the same propagating mode. For axial incidence the contribution of the  $TE_{11}$  mode to the backscatter is, according to Johnson and Moffatt [41],

$$E^{S} = -e^{i2\alpha L_{B_{11}}\theta C_{\Theta H}E^{i}}, \qquad (242)$$

where the coupling coefficient is

$$B_{11}^{\theta} = \frac{2i(k+\alpha_{11})M_{+}(\alpha_{11})}{\alpha_{11}^{\prime}(1-\frac{1}{j_{11}^{\prime}2})L_{+}(k)} \qquad \frac{f_{1}}{1-f_{1}^{2}} \qquad (243)$$

the radiation coefficient is

$$C_{\theta H} = \frac{+(ka)^2}{(k-\alpha_{11})} \frac{M_{+}(\alpha_{11})}{L_{+}(k)} \frac{1}{2} \frac{f_1}{1-f_1^2} , \qquad (224)$$

and

$$\alpha'_{11} = \sqrt{k^2 - (j'_{11}/a)^2}$$
 (225)

The j11 is the first (m=1) zero of the derivative of the Bessel function, i.e., 1.84118.

## SECTION 3

## FINITE CIRCULAR WAVEGUIDES WITH OPEN OR SHORT REAR TERMINATIONS

The axial backscatter by the finite circular waveguide shown in Figure 47 has been computed using a moment method program for rotationally symmetric objects.\* Both open and shorted rear termination of the waveguide were used. The normalized axial radar cross sections of both the open and shorted finite guides, a thin circular disk of radius a and the semi-infinite open waveguide (a few points) are shown in Figure 53. Several features should be noted. First, for guide diameters less than the cutoff wavelength of the first propagating mode (TE<sub>11</sub>) the radar cross sections of the open and shorted cylinders are essentially the same, i.e., the rear termination is unimportant. This would also be true for any structure in the interior of the guide provided they are sufficiently removed from the front of the guide (evanescent modes). Second, the disk cross section in this same range ( $^{\rm D}/\lambda$  < 0.6) is a good

<sup>\*</sup>These computations were made by Dr. W.S.C. Chang of the ElectroScience Laboratory, Department of Electrical Engineering, The Ohio State University, Contract No. NO0014-78-C-0049.

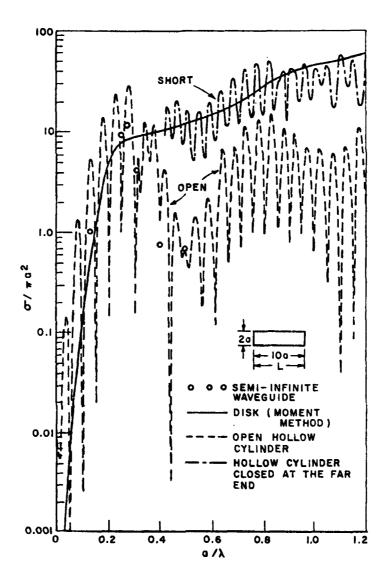


Figure 53. Normalized axial radar cross section of finite hollow cylinders (open and shorted at far end), a circular disk and a semi-infinite circular waveguide.

approximation for the average of the finite guide cross sections.

Third, the disk cross section is a reasonable approximation for the open waveguide cross section in this same range.

Using computations spanning  $^a/\lambda=0.01(0.01)1.20$  the axial impulse response waveforms of the open and shorted finite cylinders have been generated using a Fourier synthesis procedure, Kennaugh and Moffatt [43]. These response waveforms are shown in Figure 54 for respectively the open, 54a, and shorted, 54b, guides. The initial response, impulse plus ringing  $(0<^t/t_0<20)$ , is the same for both guides as was anticipated in the Introduction. This response is also the same as that for the open guide in Figure 50, but for the open guide much more resolution was obtained because computations to  $^a/\lambda$  of 6.0 were used. The negative impulse at the origin was removed in these and subsequent figures. The basic scattering mechanisms of the finite guides can be enumerated, some of which are isolated and identifiable in the waveforms of Figure 54. Recall that both the finite and semi-infinite guides have an infinitely thin wall thickness.

- 1. Specular (frequency independent) return which is a weighted impulse at  $t/t_0=0$ .
- 2. Rim scattering or diffraction back and forth across the front rim. This is the ringing for  $0<^t/t_0<20.0$ .
- 3. Singly diffracted return from the rear of the guide. This excitation and return travels at approximately the free space velocity exterior to the guide and is clearly identifiable as the spike (bandlimited approximation of an impulse) at  $t/t_0=20.0$ .

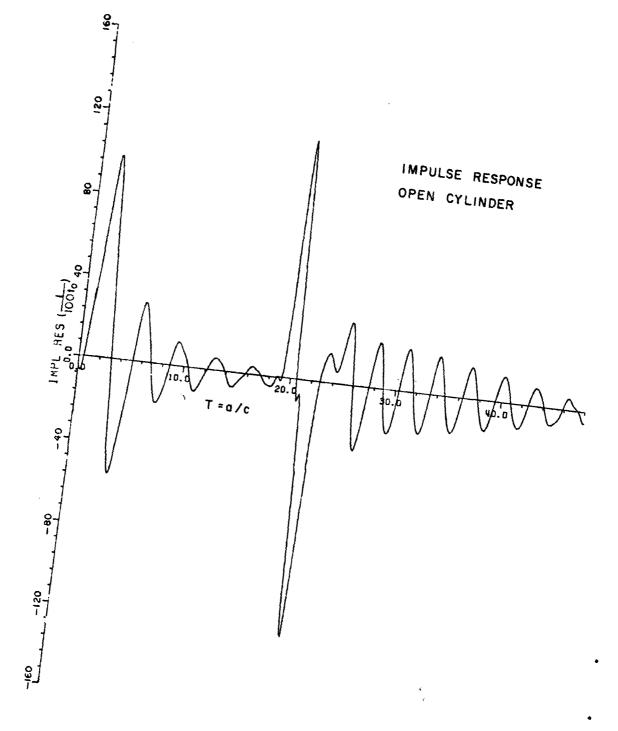


Figure 54a. On-axis backscatter impulse response from finite open circular cylinder.

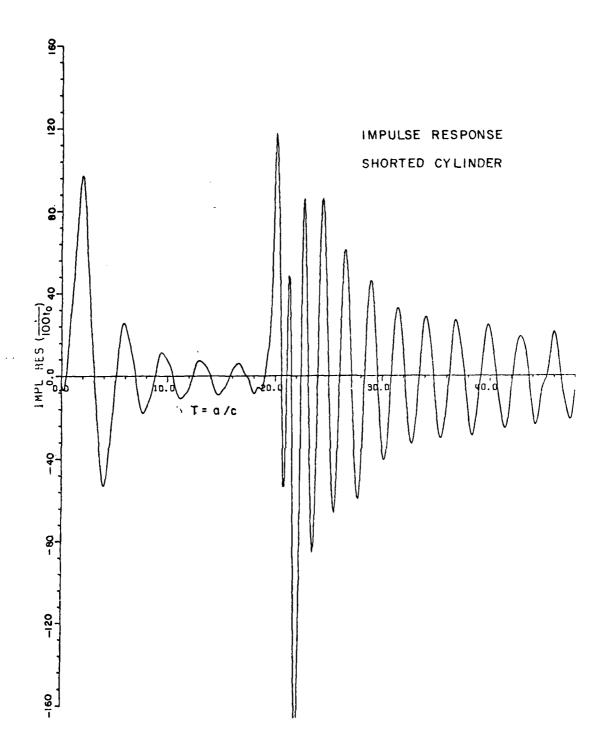


Figure 54b. On-axis backscatter impulse response from finite circular cylinder shorted at the rear.

- 4. Diffraction across the rear of the guide or a doubly diffracted contribution, which is masked with other effects in Figure 54. There are, of course, also evanescent waveguide modes for both guides which are unimportant for these geometries. The above four mechanisms are identical for both guides.
  - 5. Propagating modes are coupled into the guide structure, reflected at the termination and then reradiated at the front of the guide. The reflection coefficient at the rear is obviously different for the open and shorted guides. Note, however, that there is no mode conversion for these terminations. In time, these mechanisms must occur later than  $t/t_0=20.0$  because of the mode energy velocity in the guide.
  - 6. For the open finite guide another scattering mechanism exists which has two reciprocal forms. Coupling into the guide at the front as waveguide modes, guide propagation and then diffraction at the rear of the guide and free space propagation in the backscatter direction. Obviously the reverse or reciprocal mechanism also occurs.

A principal advantage of the time domain viewpoint is that the above scattering mechanisms can, in principle, be separately removed from the total response waveform. More importantly, approximate impulse response waveforms for these and similar cavity geometries can be constructed by simple addition of basic waveforms with appropriate delays. The impulse at the waveform origins in Figure 54 and Figure 50 is simply predicted by asymptotic theory. In fact, the impulses shown have been added artificially. The weight of this impulse, Equation

- 4. Diffraction across the rear of the guide or a doubly diffracted contribution, which is masked with other effects in Figure 54. There are, of course, also evanescent waveguide modes for both guides which are unimportant for these geometries. The above four mechanisms are identical for both guides.
  - 5. Propagating modes are coupled into the guide structure, reflected at the termination and then reradiated at the front of the guide. The reflection coefficient at the rear is obviously different for the open and shorted guides. Note, however, that there is no mode conversion for these terminations. In time, these mechanisms must occur later than  $t/t_0=20.0$  because of the mode energy velocity in the guide.
  - 6. For the open finite guide another scattering mechanism exists which has two reciprocal forms. Coupling into the guide at the front as waveguide modes, guide propagation and then diffraction at the rear of the guide and free space propagation in the backscatter direction. Obviously the reverse or reciprocal mechanism also occurs.

A principal advantage of the time domain viewpoint is that the above scattering mechanisms can, in principle, be separately removed from the total response waveform. More importantly, approximate impulse response waveforms for these and similar cavity geometries can be constructed by simple addition of basic waveforms with appropriate delays. The impulse at the waveform origins in Figure 54 and Figure 50 is simply predicted by asymptotic theory. In fact, the impulses shown have been added artificially. The weight of this impulse, Equation

(237), was subtracted from the frequency domain data before Fourier synthesis in order to improve details of the waveforms for short times. In a similar fashion, the singly diffracted contribution which is easily predicted via the geometrical theory of diffraction (GTD) as \*

$$E_{SD}^{S} = E_{o} \frac{a}{4} e^{-j2k1} \frac{e^{-jkR}}{R} \frac{4}{3\sqrt{3}}$$
 (246)

can be removed.

The impulse response waveforms of the finite open and shorted guides with the specular contribution removed are shown in Figure 3-3. It remains, in this time span, to approximate the sinusoidal delay for  $0 < t/t_0 < 20.0$ . This type of approximation is discussed later.

UTD provides excellent asymptotic frequency domain approximations for the doubly diffracted contribution. Unfortunately the finite guides have a cylindrical caustic on the guide axis. The proper constant phase shift correction at all frequencies for this caustic results in a nonphysical system and consequently a noncausal response in the time domain. Thus if this term is subtracted before synthesis a distortion of the resulting waveform at times before this contribution can poscibly arrive results. This is illustrated in Figure 56 for the finite shorted guide. Comparing Figure 56 and Figure 55b it is seen that a distortion before  $t/t_0=20.0$  has occurred and this cannot occur

<sup>\*</sup>Modern Unified Theory of Diffraction (UTD), Pathak and Kouyoumjian offers more sophisticated results but the simpler GTD formula is adequate here.

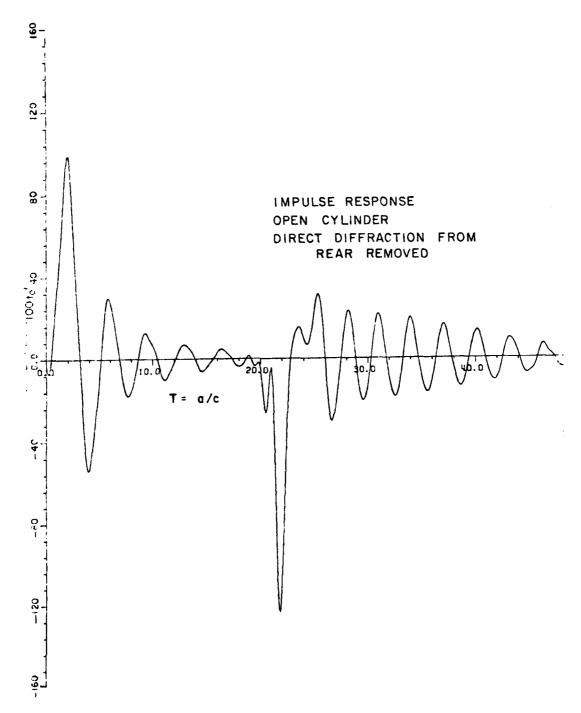


Figure 55a. Impulse response for finite open cylinder with direct diffraction from rear removed.

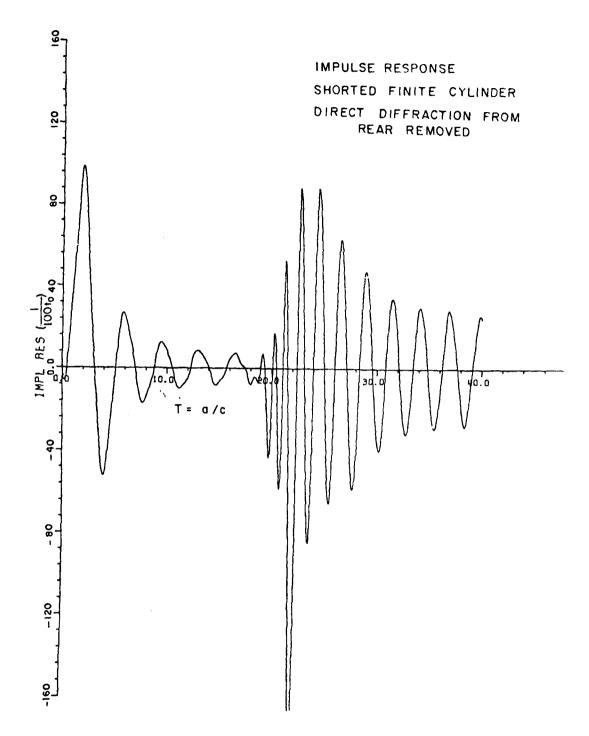


Figure 55b. Impulse response for shorted finite cylinder with direct diffraction from rear removed.

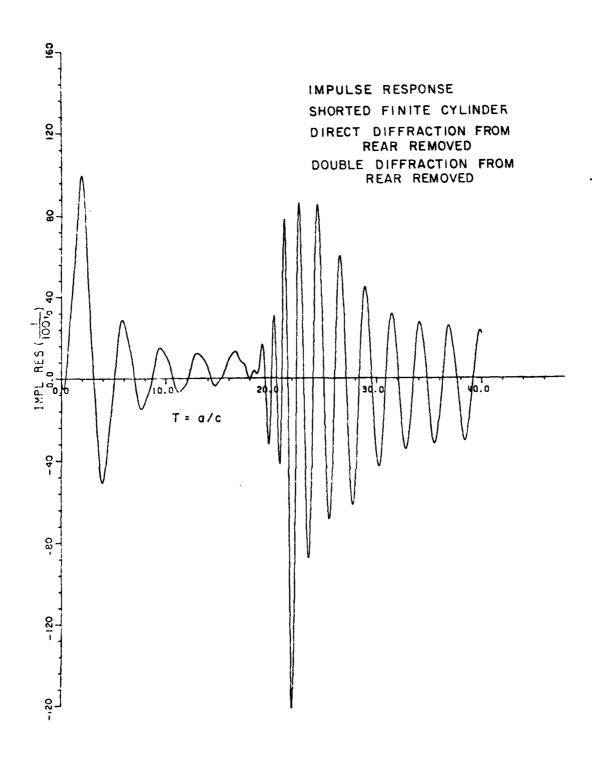


Figure 56. Impulse response for shorted finite cylinder with direct and double diffraction from rear removed.

physically. The asymptotic phenomenon occurring was shown in Figure 49 for a different type of response. Note carefully that in time the doubly diffracted contribution physically begins to occur at  $^t/t_0=20.0+\epsilon$ . According to the asymptotic theory it is identically zero for  $^t/t_0>22.0$ . It is precisely this caustic correction problem which prevents a large number of GTD and UTD results from being fully exploited in the time domain. The difficulty has been known for some time, Moffatt [53], but a simple effective solution has not ensued.

For the finite shorted guide we can consider removing mechanism 5, the propagating mode contributions, by utilizing results from the solution for the open circular waveguide with a shorting plate as shown in Figure 57. This contribution must be the same for the two structures. The axial backscatter, based on coupling and reradiation of the TE<sub>11</sub> mode and neglecting the rim scattering was given in Equation (242). Radar cross section calculations of the open waveguide in Figure 57 which include the TE<sub>11</sub> and TM<sub>11</sub> modes and the rim contribution have been made, Johnson and Moffatt [41]. Unfortunately the propagating mode contributions were not separated and the time waveform corresponding to Equation (242) will require some repeated calculations. Since these involve the Wiener-Hopf factorization functions they are not simple.

An extensive table of values of the factorization functions  $L_+(\alpha)$  and  $M_+(\alpha)$  computed by numerical integration is found in Johnson and Moffatt [12]. We are now interested in the case of n=1 (backscatter). For  $0.1<0/\lambda<0.7$ , the  $L_+$  and  $M_+$  functions vary smoothly except at a cusp in the imaginary part of the  $M_+$  function at  $0/\lambda=0.5861$ . An interpolation

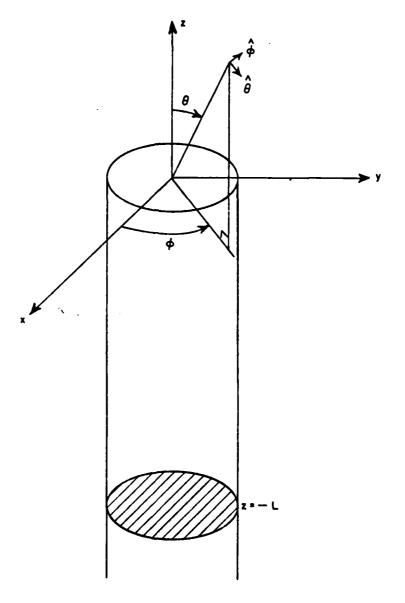


Figure 57. Coordinate system for scattering by shorted open circular waveguide.

program was written to obtain values of the factorization functions at inbetween frequencies. It avoids interpolation across the cusp which would lead to erroneous results. The results for  $L_+(k)$  and  $M_+(k)$  for the n=1 case are given in Table 4.

Based on the simplest asymptotic forms, the axial backscattered field is given by, Johnson and Moffatt [41]

$$E^{S} = \left[ \frac{-sa^{2}}{c[j_{11}^{2}-1]} + \frac{a(4+j_{11}^{2})}{(j_{11}^{2}-1)8s^{a}/c} \right] e^{-2sL/c} .$$
 (247)

The time waveform corresponding to Equation (3-2) is

$$F_{I}(t) = \frac{-a}{j_{11}^{2}-1} \delta'(t-\frac{2L}{c}) + \frac{a}{(j_{11}^{2}-1)} \left(\frac{4+j_{11}^{2}}{8}\right) u(t-\frac{2L}{c})$$
 (248)

The most obvious difficulty with Equation (248) is the delay--we know that it should be slightly greater than 2L/c. The precise inversion of

$$i2\alpha L = i2L \sqrt{(\frac{w}{c})^2 - j_{11}^2/a^2}$$
, (249)

yields

TABLE 4 RESULTS FOR  $L_{+}(k)$  AND  $M_{+}(k)$  FOR THE n=1 CASE.

			L <sub>+</sub> (k)		M <sub>+</sub> (	M <sub>+</sub> (k)	
n	D/A	a∕k	Real	Imag.	Real	Imag.	
1	.100	1.0	0.9595	0.1825	0.3033	1.6039	
1	.110	1.0	0.9523	0.1984	0.3020	1.4605	
1	.120	1.0	0.9446	0.2136	0.3007	1.3411	
1 1	.130 .140	1.0	0.9362 0.9273	0.2287 0.2433	0.2994 0.2981	1.2403	
i	.150	1.0	0.9179	0.2574	0.2968	1.0796	
ī	.160	1.0	0.9078	0.2711	0.2954	1.0145	
ĩ	.170	1.0	0.8972	0.2843	0.2941	0.9572	
1	.180	1.0	0.8861	0.2971	0.2928	0.9064	
1	.190	1.0	0.8743	0.3095	0.2915	0.8611	
ļ	.200	1.0	0.8620	0.3214	0.2902	0.8205	
1	.210 .220	1.0	0.8510 0.8398	0.3324	0.2884	0.7829	
1	.230	1.0	0.8284	0.3429 0.3528	0.2866 0.2848	0.7487 0.7175	
î	.240	1.0	0.8167	0.3622	0.2829	3383.0	
ī	.250	1.0	0.8048	0.3711	0.2810	0.6623	
1	.260	1.0	0.7927	0.3795	0.2791	0.6379	
1	.270	1.0	0.7804	0.3873	0.2771	0.6152	
1	.280	1.0	0.7678	0.3946	0.2752	0.5942	
1	.290 .300	1.0	0.7550 0.7420	0.4014	0.2732 0.2712	0.5745 0.5561	
î	.310	1.0	0.7300	0.4077 0.4139	0.2696	0.5378	
ī	.320	1.0	0.7181	0.4196	0.2679	0.5205	
1	.330	1.0	0.7061	0.4248	0.2664	0.5040	
1	.340	1.0	0.6941	0.4296	0.2648	0.4883	
l	.350	1.0	0.6822	0.4340	0.2632	0.4733	
1	.360 .370	1.0	0.6702 0.6583	0.4379	0.2617 0.2602	0.4589	
1	.380	1.0 1.0	0.6464	0.4413 0.4443	0.2587	0.4319	
î	.390	1.0	0.6344	0.4469	0.2573	0.4192	
1	.400	1.0	0.6225	0.4490	0.2558	0.4069	
1	.410	1.0	0.6112	0.4513	0.2530	0.3972	
1	.420	1.0	0.6001	0.4533	0.2509	0.3870	
1 1	.430 .440	1.0	0.5890 0.5781	0.4549	0.2494	0.3764	
ì	.450	1.0	0.5673	0.4563 0.4572	0.2486 0.2483	0.3653	
î	.460	1.0	0.5566	0.4579	0.2485	0.3420	
ī	.470	1.0	0.5460	0.4582	0.2493	0.3298	
1	.480	1.0	0.5356	0.4582	0.2505	0.3173	
1	.490	1.0	0.5253	0.4579	0.2521	0.3044	
1 1	.500	1.0	0.5151	0.4572	0.2542	0.2913	
1	.510 .520	1.0	0.5053 0.4956	0.4568 0.4562	0.2566 0.2595	0.2779	
î	.530	1.0	0.4861	0.4553	0.2626	0.2504	
1	.540	1.0	0.4768	0.4543	0.2661	0.2362	
1	.550	1.0	0.4676	0.4530	0.2699	0.2219	
1	.560	1.0	0.4586	0.4515	0.2740	0.2073	
1	.570	1.0	0.4498	0.4497	0.2783	0.1926	
ì	.580 .590	1.0	0.4411	0.4478 0.4456	0.2895 0.3196	0.1693 0.1553	
ī	.600	1.0	0.4243	0.4432	0.3523	0.1648	
1	.610	1.0	0.4162	0.4410	0.3720	0.1720	
1	.620	1.0	0.4083	0.4387	0.3882	0.1792	
1	.630	1.0	0.4005	0.4362	0.4011	0.1865	
ì	.640 .650	1.0 1.0	0.3929 0.3855	0.4336 0.4308	0.4108 0.4175	0.1938	
î	.660	1.0	0.3783	0.4279	0.4213	0.2085	
1	.670	1.0	0.3713	0.4249	0.4223	0.2159	
1	.680	1.0	0.3644	0.4217	0.4206	0.2234	
1	.690 .700	1.0	0.3577	0.4184	0.4165	0.2309	
	. , , , ,	4 . V	0.3512	0.4149	0.4000	0.2384	

This waveform would have to be convolved with the inverse transform of the  $B_{11}^{\theta}C_{\theta H}$  expression in Equation (242) to yield the true impulse response of the coupled and reradiated mode. The impulse term in Equation (250) is a precursor illustrating that even for guided waves the first presence of the signal (perfect detector) arrives with the velocity of light in a vacuum. The signal front buildup is dictated by the second term in Equation (250). For guided waves the topic of transients was discussed by Cerillo [37]. The present case is further complicated by the coupling and radiation expressions, which are also frequency dependent.

The doubly diffracted contribution in the time domain for the finite shorted cylinder is given by (asymptotic estimate)

$$F_{I}^{DD}(t) = \frac{-2}{3\sqrt{\pi t_0}} \frac{u(22t_0-t)}{\sqrt{22t_0}-t}$$
 (251)

According to this estimate the contribution endures only for  $^{t}/t_{o}$ <22.0 ( $^{t}o^{=a}/c$ ). The essential truth of this can be seen by comparing Figures 54b and 56. For  $^{t}o$ /t>22.0, the response waveforms are identical. Therefore for  $^{t}/t_{o}$ >22.0, the waveforms in Figures 54b, 55b and 56 are the coupling, guide propagation and radiation of basically the TE<sub>11</sub> and TM<sub>11</sub> circular waveguide modes. At the smallest wavelength calculated,  $^{a}/\lambda$ =1.2, there are actually 10 TE and 6 TM modes which can propagate but for axial backscatter, only the TE<sub>11</sub> and TM<sub>11</sub> modes are of any real consequences. At other aspects or for terminations which cause mode conversion this will no longer be true. We postulate therefore that on-axis the backscatter contribution from coupling and radiation consists

of a weighted doublet delayed by  $^{2L}$ /(energy velocity of TE $_{11}$  mode) and then damped sinusoid contributions which originate at times dictated by the energy velocity of the higher order modes. Impulse and step response waveforms due to the short inside the semi-infinite guide are obtained from inversion of Equation (242) for  $0.6 < ^{D}/\lambda < 2.6$  in steps of  $^{D}/\lambda = 0.01$ , as shown in Figure 60a and 60b respectively. (Recall that below  $^{D}/\lambda = 0.5861$ , the cutoff frequency of TE $_{11}$  mode of the circular waveguide, there is no return from the short.) These time waveforms agree well with our postulation.

For completeness of the canonical response waveforms, the step and ramp response waveforms of the open and shorted finite circular waveguides are shown in Figures 58 and 59 respectively. The smoothing effected by integration and, for the ramp response, the emphasis on low frequencies is very evident.

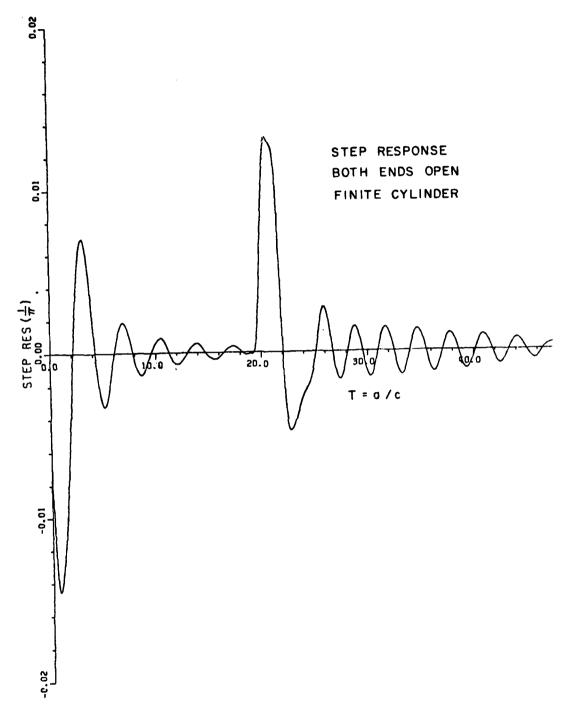


Figure 58a. Step response for open finite cylinder.

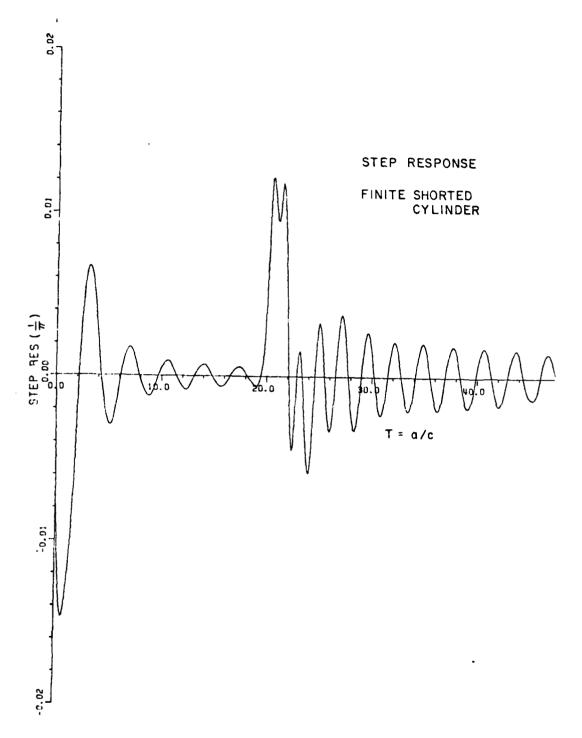


Figure 58b. Step response for shorted finite cylinder.

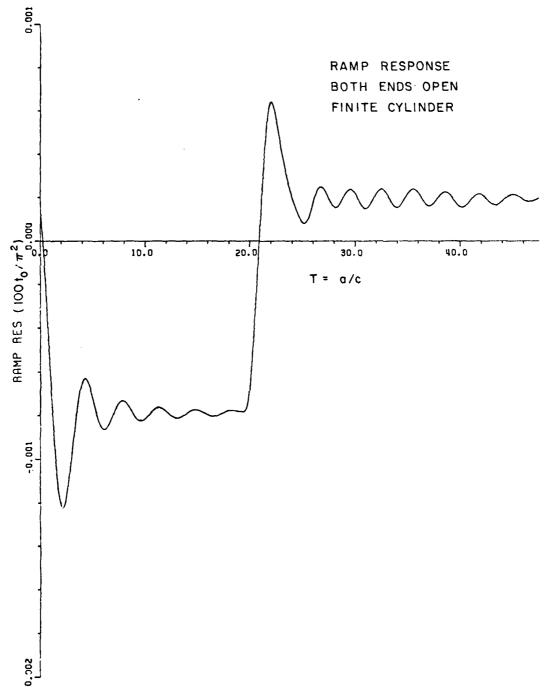


Figure 59a. Ramp response for open finite cylinder.

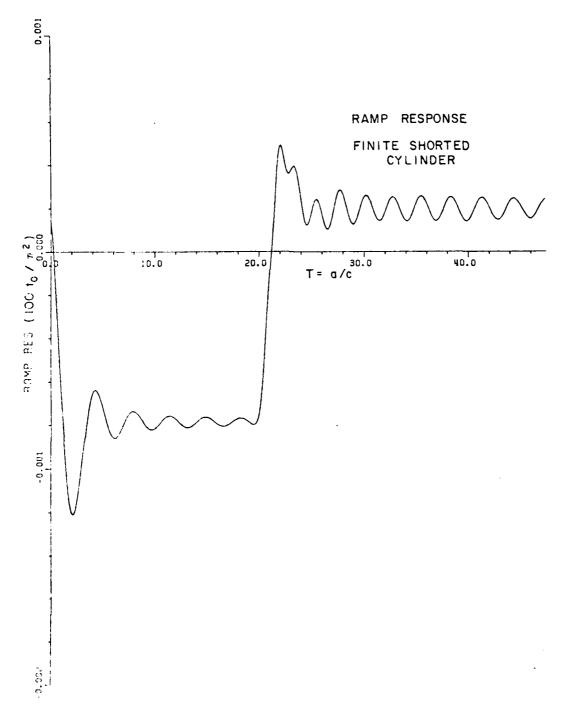


Figure 59b. Ramp response for shorted finite cylinder.

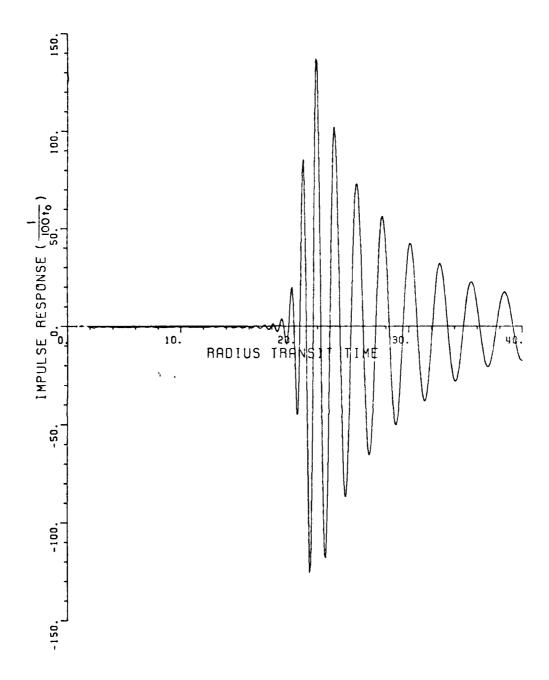


Figure 60a. Impulse response due only to short inside circular semi-infinite waveguide.

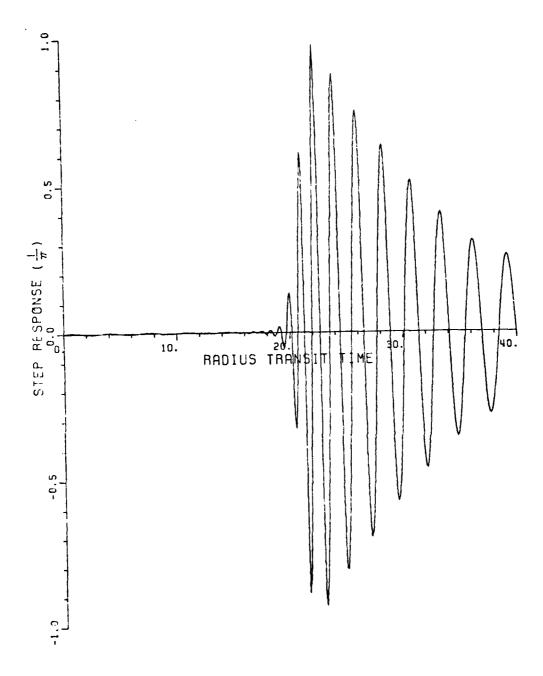


Figure 60b. Step response due only to short inside circular semi-infinite waveguide.

#### SECTION 4

#### INTERNALLY LOADED OPEN CIRCULAR WAVEGUIDES

In this section, we study the effects of loading inside a semiinfinite circular waveguide. We choose this waveguide instead of the finite guide because we thus eliminate a myraid of diffractions from the termination of the guide. Furthermore, the exact low frequency Wiener-Hopf solution is available for the semi-infinite circular waveguide. The loading is placed at a position five guide diameters down from the opening of the guide.

In particular, we are studying the time domain on-axis impulse response of the semi-infinite circular waveguide with or without loading. A Fourier synthesis procedure is used to obtain the time domain response. The frequency spectrum consists of three regions: 1) low frequency (below cutoff) region; 2) high frequency asymptotic region; and 3) a resonance region between the high and low frequency regions which will be approximated by a rational function fit.

The low frequency region was calculated for  $^{\rm D}/\lambda$ =0.01 to  $^{\rm D}/\lambda$ =0.58 in steps of 0.01. It is calculated using equations and data on the Wiener-Hopf factorization functions given in the report by Johnson and Moffatt

[12]. It is therefore the exact Wiener-Hopf solution. Since the cutoff wavelength for the TE<sub>11</sub> mode of the circular waveguide occurs at  $D/\lambda=0.586$ , this low frequency region is identical for all cases of loading, including the absence of loading.

The high frequency solution is computed via the methods of physical optics for the internal load and the geometrical theory of diffraction.\* It extends to  $0/\lambda=2.60$ . A detailed discussion is given by Pathak and Huang [50].

For the region between the high and low frequency regions, a rational function of the form

$$F(jka) = \frac{\sum_{n=0}^{g} A_n(jka)^n}{\sum_{\substack{h=1\\m=1}}^{h} B_m(jka)^m}$$
(252)

is used to fit points in the high and low frequency regions.

To ensure, in part, the correctness of the rational function fit, the following checks are made.

1. Since the load is placed five diameters down from the open end of the guide, the impulse response for  $0<^t/t_0<20.0$   $(t_0=a/c)$  and all cases of loading should be the same as the case of no loading in the same time period. Furthermore, the impulse response for  $0<^t/t_0<20.0$  should be the same as that of the

<sup>\*</sup>These computations were made by Mr. C.C. Huang of the ElectroScience Laboratory, Department of Electrical Engineering, The Ohio State University, Contract No. F19628-80-C-0056.

finite waveguide discussed in Section 3.

The impulse response and step response must satisfy the moment conditions.

$$\int_{0}^{\infty} F_{I}(t) dt = 0$$
 (253)

$$\int_{0}^{\infty} F_{U}(t) dt = 0$$
 (254)

where  $F_{\rm I}(t)$  and  $F_{\rm U}(t)$  are the impulse and step response respectively.

It must be understood that in the absence of experimental data it is not possible to completely verify the calculated results. Experimental data to verify the calculations would require either an experimental pulse range or very broadband scattering data to isolate the rim plus load return.

In the following sections, (4-1) to (4-5), results for the cases of open circular waveguide, shorted open circular waveguide, non-shorting disc in open circular waveguide and planar blade geometry in open circular waveguide (40 blades and 2 blades) are presented. These configurations are shown in Figure 61.

All the frequency data have spacings of  $D/\lambda=0.01$  and the following notation is used:

 $F_{asy}(s)[^D/\lambda=0.64, 2.6]$  means the asymptotic frequency response for  $0.64 < ^D/\lambda < 2.6$  in steps of  $^D/\lambda=0.01$ . It is equivalent to  $F_{asy}(s)[u(^D/\lambda-0.64)-u(^D/\lambda-2.61)]$  where  $u(^D/\lambda)$  is the discrete unit step function.

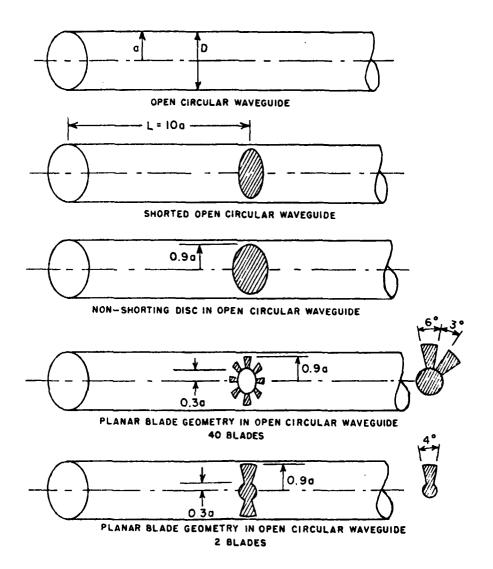


Figure 61. Configurations of various loadings inside semiinfinite circular cylinder.

# 4.1 Open Circular Waveguide

This is a well known geometry and will also be referred to as the hollow cylinder from here on. Frequency data used are given by

$$F_{hollow}(s) [^{D}/\lambda=0.01, 2.6] = F_{low}(s) [^{D}/\lambda=0.01, 0.58]$$
+  $F_{rat}(s) [^{D}/\lambda=0.59, 0.99] + F_{asy}(s) [^{D}/\lambda=1.0, 2.6]$ .

 $F_{10W}(s)$  is the exact Wiener-Hopf solution given by Johnson and Moffatt [12].  $F_{asy}(s)$  [D/ $\lambda$ =1.0, 2.6] is the asymptotic solution given by

$$\frac{E^{S}}{E^{\dagger}} = \frac{-a}{2} \left\{ 1 - \frac{e^{-j(2ka-\pi)}}{\sqrt{\pi ka}} \left[ 1 - \frac{j}{2\sqrt{2}} e^{-j2ka} \left( 1 + \frac{e^{-j\pi}}{\sqrt{2\pi ka}} \right) \right] \right\} \frac{e^{-jkR}}{R}$$
(256)

Lastly,  $F_{\text{rat}}(s)[^D/\lambda=0.59,\ 0.99]$  is the rational function fit spanning the two solutions. Figures 62a and 62b show the magnitude and phase respectively of  $F_{\text{hollow}}(s)$  up to  $^D/\lambda=1.4$ . The frequency response is a slowly varying function and the rational function fit is represented by the solid curve in Figure 62. The impulse and step responses obtained by inversion of Equation (255) are shown in Figures 63a and 63b respectively. Again the negative impulse at the origin of the impulse response curve is removed by adding an appropriate positive constant to the frequency response. This also applies to all subsequent plots. When Figure 63a is compared with the  $0 < t < 20t_0$  region of Figures 54 and 55, it is seen that agreement is excellent.

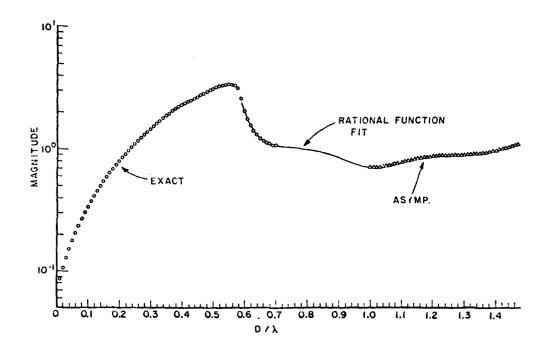


Figure 62a. Frequency spectrum (magnitude) of semi-infinite hollow cylinder.

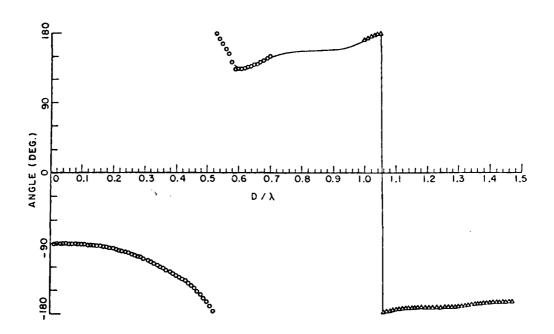


Figure 62b. Frequency spectrum (phase) of semi-infinite hollow cylinder.

### 4.2 Shorted Open Circular Waveguide

A short is placed 5 diameters down from the open end of the semi-infinite guide. An exact solution for the contributions of the short is given by Equation (242), which we shall call  $F_{sh}(s)$ . Therefore, the frequency data for this geometry are constructed as follows:

$$F_{short}(s)[D/\lambda=0.01,2.6] = F_{hollow}(s)[D/\lambda=0.01,2.6] + F_{sh}(s)[D/\lambda=0.6,2.6]$$
 (257)

 $F_{hollow}(s)$  is the same as that given by Equation (255) and  $F_{sh}(s)$  is added to  $F_{hollow}(s)$  term by term for  $0.6 < 0/\lambda < 2.6$ . Figures 64a and 64b show the impulse and step responses of the shorted open circular cylinder via inversion of Equation (257). It is notable that for  $0.0 < t < 20t_0(t_0 = a/c)$  the impulse response is the same as that of Figure 63a while for  $t/t_0 > 20.$ , the impulse response is the same as that of Figure 60a. This suggests that we can deal with the cylinder and the loading separately, thus greatly facilitating the computations.

### 4.3 Non-Shorting Disc in Open Circular Waveguide

This is a more complicated problem since the frequency response is a rapidly varying function above cutoff of the  $TE_{11}$  mode of the circular guide. There is no closed form expression for the high frequency response and an asymptotic solution  $(F_{di}(s))$  is obtained numerically using GTD and

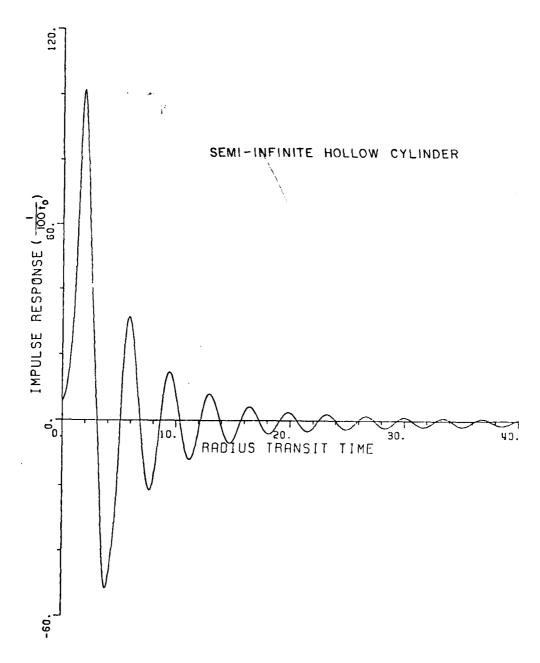


Figure 63a. Impulse response for semi-infinite hollow cylinder.

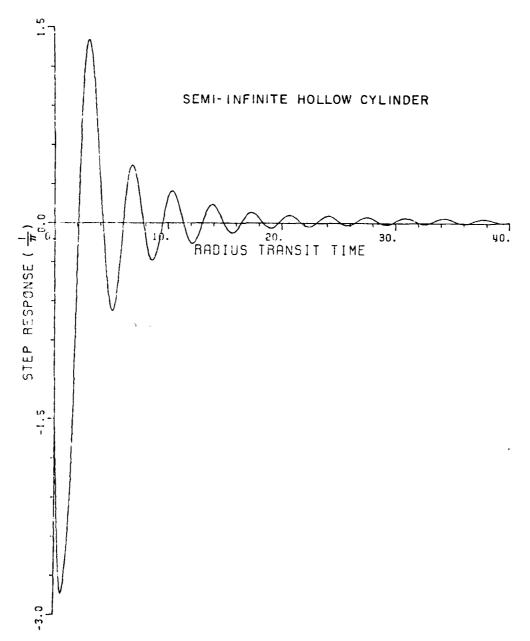


Figure 63b. Step response for semi-infinite hollow cylinder.

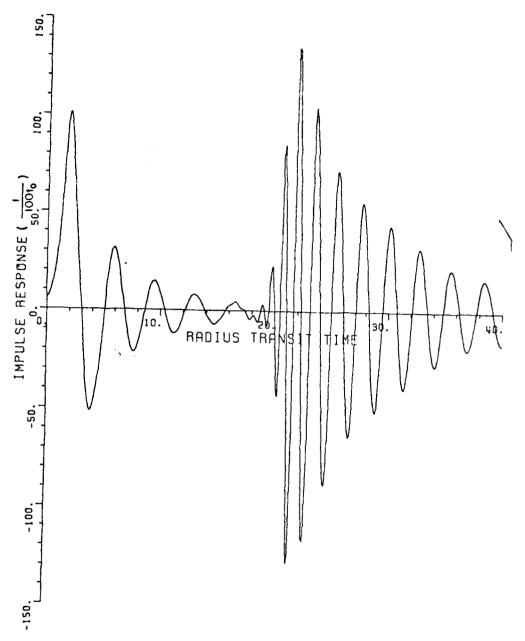


Figure 64a. Impulse response for shorted semi-infinite cylinder.

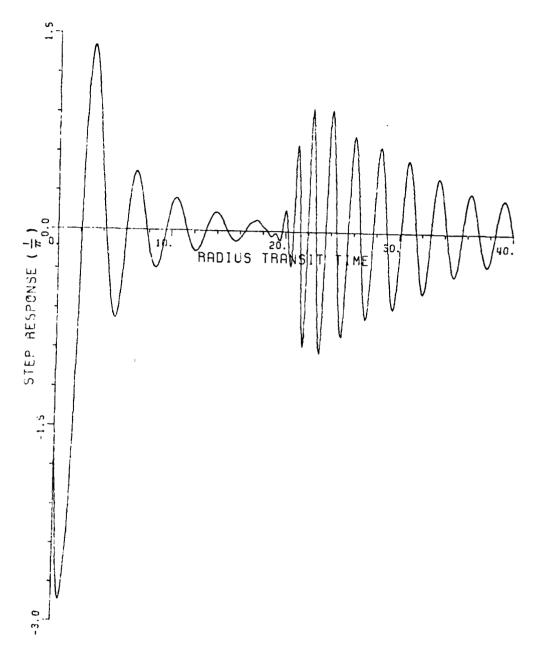


Figure 64b. Step response for shorted semi-infinite cylinder.

the physical optic approximation for the disc.\* For frequencies below cutoff,  $F_{low}(s)$  in Equation (255) is used.

The frequency data used are as follows:

$$F_{disc}(s)[^{D}/\lambda=0.01,2.6] = F_{low}(s)[^{D}/\lambda=0.01,0.58] + F_{rat}(s)[^{D}/\lambda=0.59,0.63] + F_{di}(s)[^{D}/\lambda=0.64,2.6]$$
(258)

The rational function fit is needed as we know that the asymptotic solution is not satisfactory for the region immediately above cutoff. A number of points from  $F_{low}(s)$  and  $F_{di}(s)$  are used as input to a program computing the coefficients of Equation (252) by a least square error algorithm. This is a trial and error method and the "correct" solution must satisfy both physical constraints and the moment conditions. Figure 65 shows the impulse response of an "incorrect" frequency solution. The waveform for  $0.<t/t_0<20$  does not agree with the corresponding waveform for the hollow cylinder, Figure 63a.

A satisfactory solution is given in Figure 66 and Figure 67. The circles represent the solution for the hollow cylinder, while the triangles represent the asymptotic solution. The solid line of Figure 66 shows how the rational function fit behaves inside and outside the unknown region 0.59 < 0.63. The squares in Figure 67 represent the rational function fit. The corresponding impulse and step responses are

<sup>\*</sup>These computations are made by Mr. C.C. Huang of the ElectroScience Laboratory, Department of Electrical Engineering, The Ohio State University under Contract No. F19628-80-C-0056.

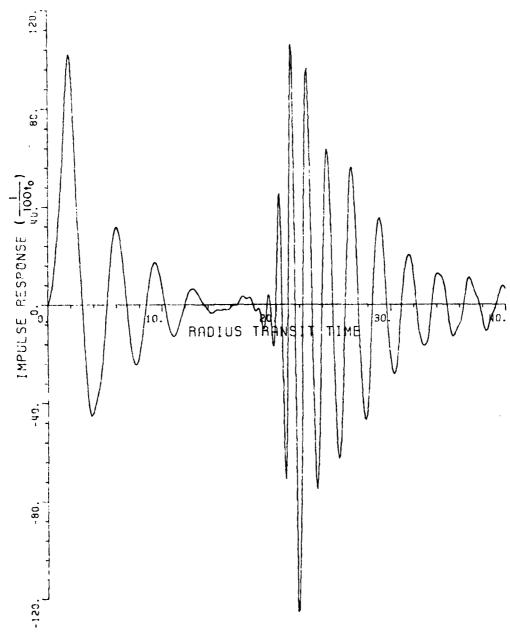


Figure 65. Example of an incorrect impulse response due to incorrect rational function fit.

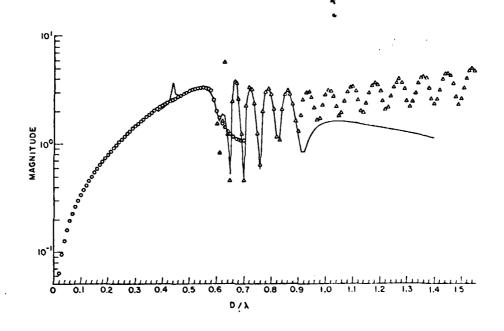


Figure 66a. Frequency spectrum (magnitude) for cylinder loaded with non-shorting disc showing behavior of rational function fit (solid line) inside and outside the unknown region.

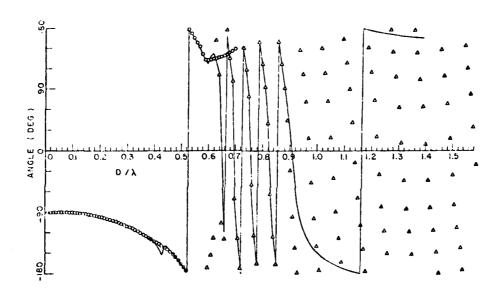


Figure 66b. Frequency spectrum (phase) for cylinder loaded with non-shorting disc showing behavior of rational function fit (solid line) inside and outside the unknown region.

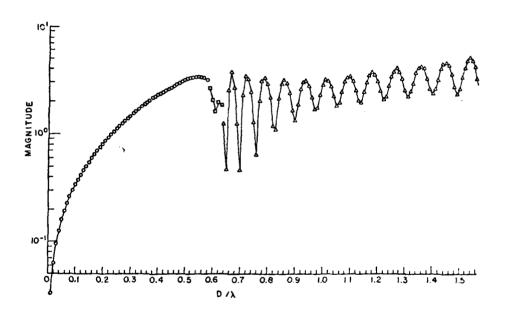


Figure 67a. Frequency spectrum (magnitude) for the non-shorting disc.

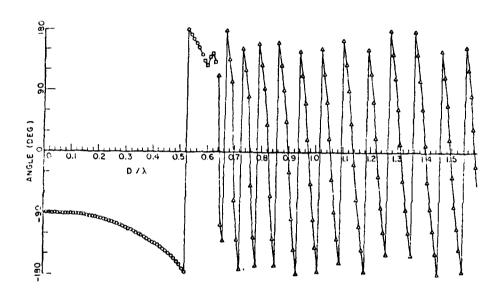


Figure 67b. Frequency spectrum (phase) for the non-shorting disc.

given in Figure 68a and 68b respectively. Again note that for  $0.<t/t_0<20.0$  the impulse response agrees with that of the hollow cylinder and the return from the disc starts only at  $t=20t_0$ .

In general, the high frequency asymptotic frequency data is excellent for  $D/\lambda$  greater than 1.0. For the case of the non-shorting disc, we have used the asymptotic solution down to  $D/\lambda=0.64$ ; Equation (258). The reason that this is possible is that the return from the disc is much stronger than that from the rim at these frequencies. This is clear when we examine the region  $D/\lambda>0.6$  of the semi-infinite hollow cylinder (Figure 62a) and that of the hollow cylinder loaded with a non-shorting disc (Figure 67a).

In target identification, we would be interested in the structure that is present inside the cylinder. In our present study the loadings are always placed five diameters down the guide so that by the time t=20t<sub>0</sub>, the ringing from the rim has died down substantially. Also in the case of the non-shorting disc the return from the loading starting at t=20t<sub>0</sub> is rather strong. When these two conditions are not met, that is, if the return from the loading occurs when the ringing from the rim has not died down enough (due to position of loading inside cylinder) or if the return from the loading is so small that it has comparable magnitude as the ringing from the rim at the instant, the waveform of the return from the loading is masked. Therefore, it is of special importance that the reflection from the loading inside the cylinder be isolated.

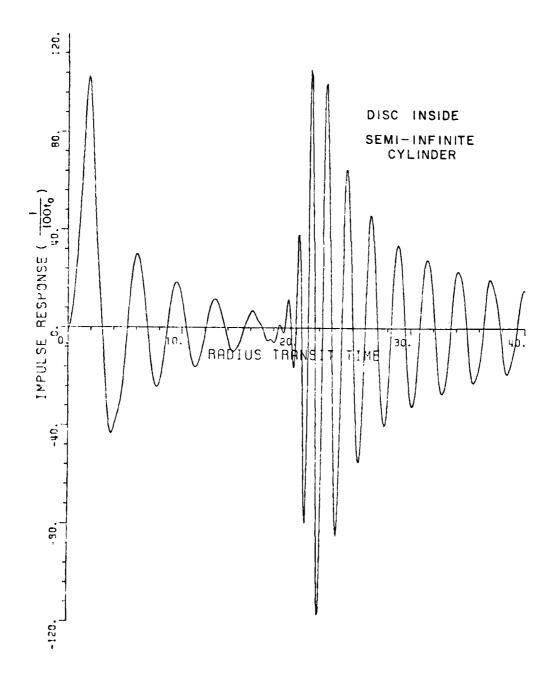


Figure 68a. Impulse response for semi-infinite cylinder loaded with non-shorting disc.

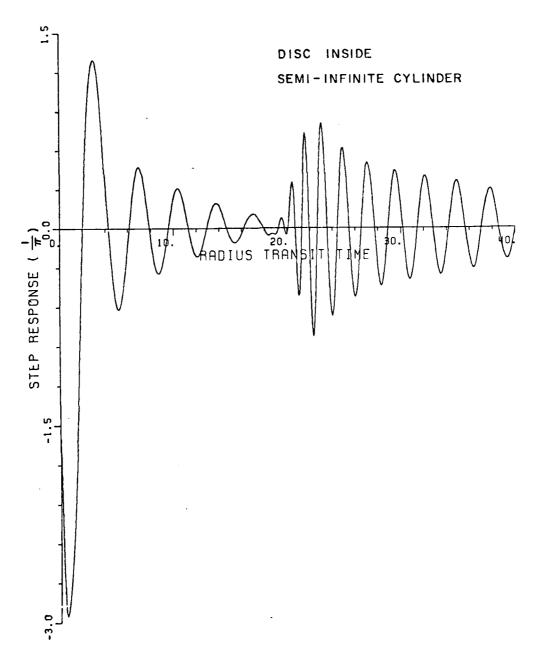


Figure 68b. Step response for semi-infinite cylinder loaded with non-shorting disc.

Furthermore, in the process of isolating the return waveform from the loading, we can partly verify the correctness of the frequency domain solution. A valid waveform would have to be zero for  $0.<^t/t_0<20$ . and starts at t=20t<sub>0</sub>.

We shall first obtain the frequency spectrum for the reflection due only to the non-shorting disc inside the guide which we shall call  $F_{\mbox{disc only}}(s). \mbox{ Note that below } D/\lambda = 0.5861 \mbox{ there is no wave propagating inside the guide and the spectrum is identically zero in this region.}$ 

F disc only(s)[
$$^{D}/\lambda=0.59,2.6$$
] =  
Fdisc(s)[ $^{D}/\lambda=0.01,2.6$ ] - Fhollow(s)[ $^{D}/\lambda=0.01,2.6$ ] . (259)

The impulse response obtained via inversion of Equation (259) is shown in Figure 69. When compared with Figure 68a, we see that this is an excellent way to study the effects of loading. It can be applied to experimental situations with other waveguide geometries and loadings.

# 4-4 Planar Blade Geometry in Open Circular Waveguide (40 blades)

The geometry of the loading is illustrated in Figure 61. There are forty blades around a small circular disc positioned 5 diameters down the guide. The frequency data are obtained in the same way as that of the non-shorting disc case and are shown in Figure 70a and 70b. The impulse response and the step response are shown in Figures 71a and 71b respectively. Note that they are very similar to the solution for the non-shorting disc (Figures 68a and 68b). This is attributed

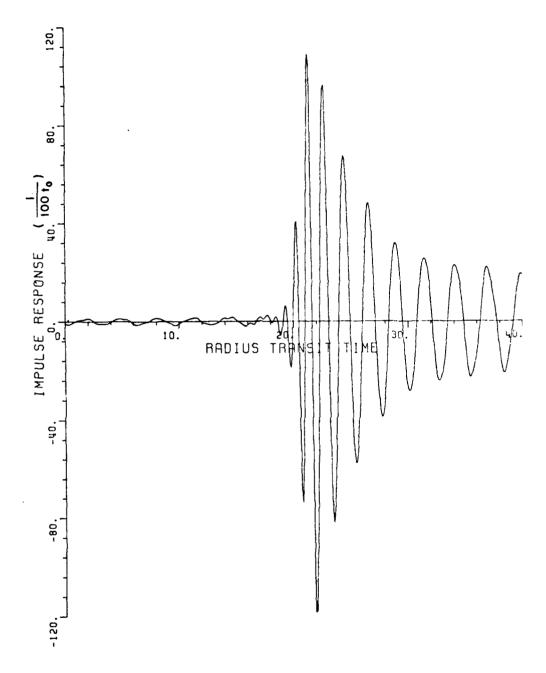


Figure 69. Impulse response due only to non-shorting disc inside semi-infinite cylinder.

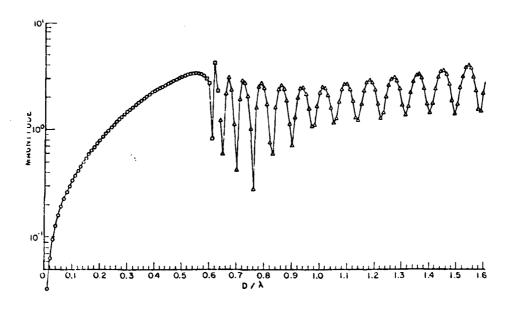


Figure 70a. Frequency spectrum (magnitude) for cylinder loaded with a 40-blade planar geometry.

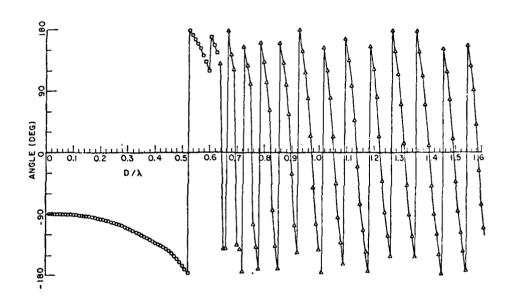


Figure 70b. Frequency spectrum (phase) for cylinder loaded with a 40-blade planar geometry.

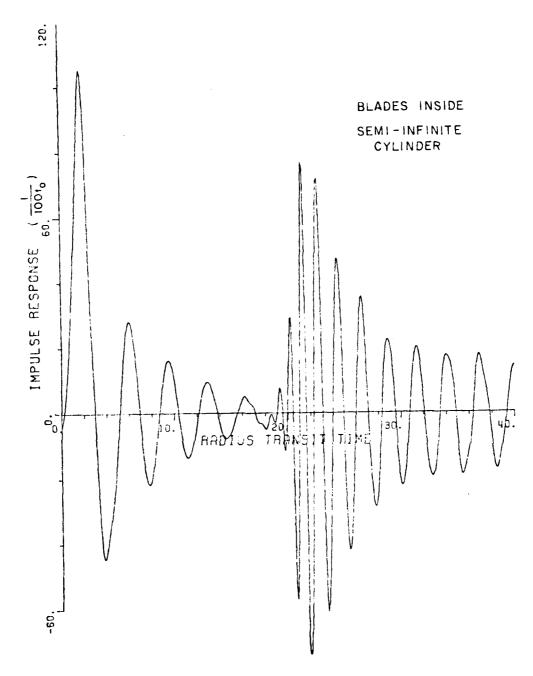


Figure 71a. Impulse response for semi-infinite cylinder loaded with a 40-blade planar geometry.

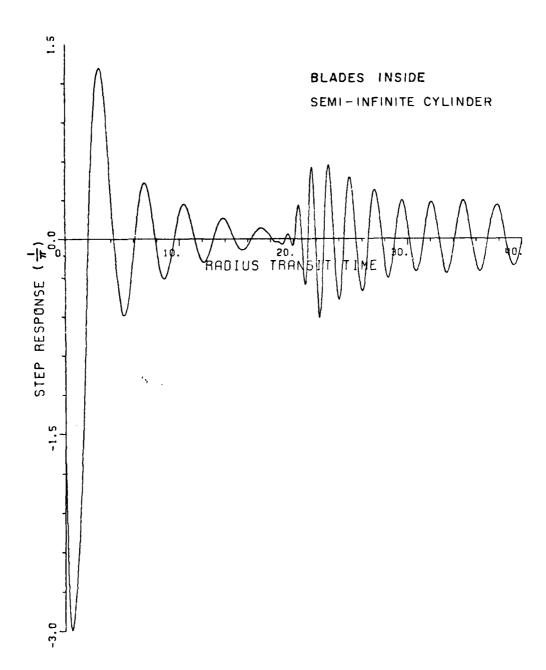


Figure 71b. Step response for semi-infinite cylinder loaded with a 40-blade planar geometry.

to the highly symmetrical property of the geometry and the large reflection area of the loading. Thus it is not very different from the non-shorting disc particularly as we are using the physical optics approximation for the loading.

# 4-5 Planar Blade Geometry in Open Circular Waveguide (2 blades)

The geometry for this case is shown in Figure 61. We shall study the loading with the blades at 0°, 45° and 90° with respect to the polarization of the incident electric field. The frequency spectrum for the 0° case is shown in Figures 72a and 72b. The corresponding impulse and step waveforms are shown in Figure 73a and 73b. It is apparent that the return from the loading is not strong and is therefore masked by the ringing from the rim. Here is an example where we would like to isolate the return due only to loading. Following the procedure described by Equation (259) in Section 4-3 we obtained the impulse responses for the 0°, 45° and 90° cases as shown in Figure 74a, 74b and 74c respectively.

The modulation effect is primarily evident in the amplitude of the waveform. We have used frequency data up to  $^{\rm D}/\lambda$ =2.6 and thus included altogether 18 TE and TM modes. However, the TE<sub>11</sub> is the dominant mode and its electric field lines diagram is shown in Figure 75. Therefore it is clear that for the 0° degree case, the return is strongest. Note that the area of the small circular disc at the center is  $0.09\pi a^2$  while the area of the two blades together is only  $0.016\pi a^2$ . Thus the modulation effect is not very dramatic since the small disc plays a leading role.

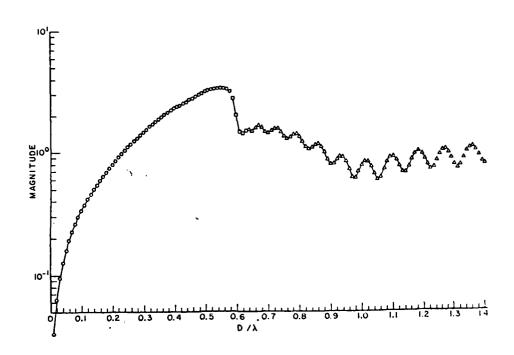


Figure 72a. Frequency spectrum (magnitude) for cylinder loaded with a 2-blade planar geometry.

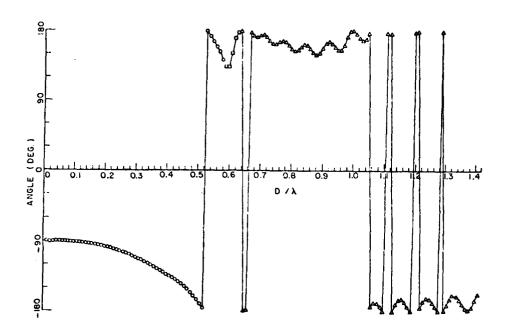


Figure 72b. Frequency spectrum (phase) for cylinder loaded with a 2-blade planar geometry.

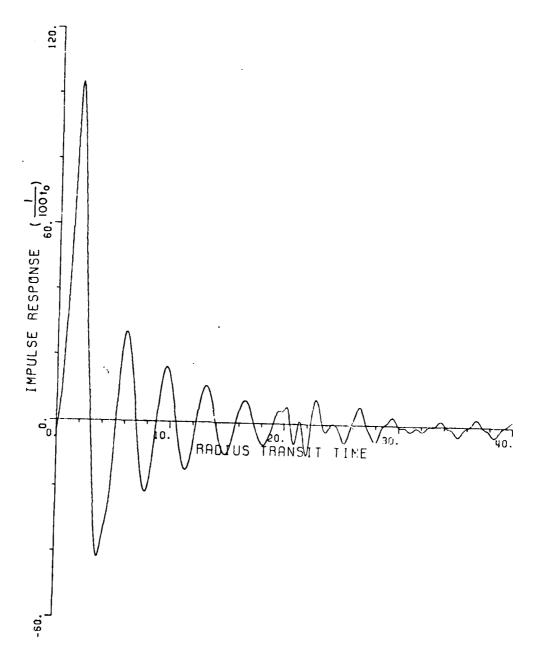


Figure 73a. Impulse response for semi-infinite cylinder loaded with a 2-blade planar geometry.

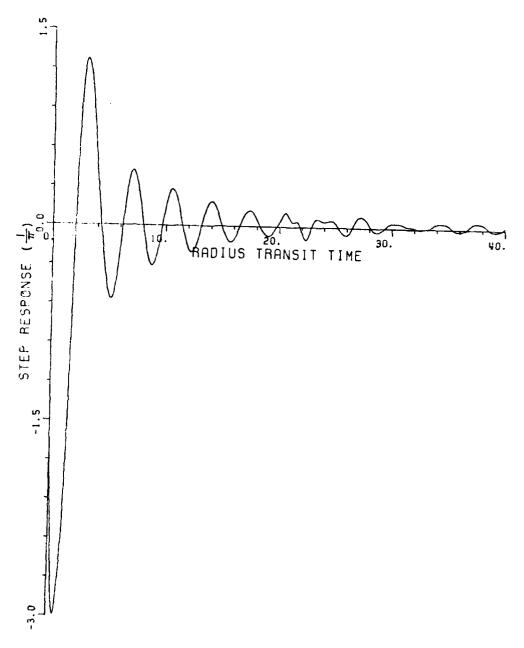


Figure 73b. Step response for semi-infinite cylinder loaded with a 2-blade planar geometry.

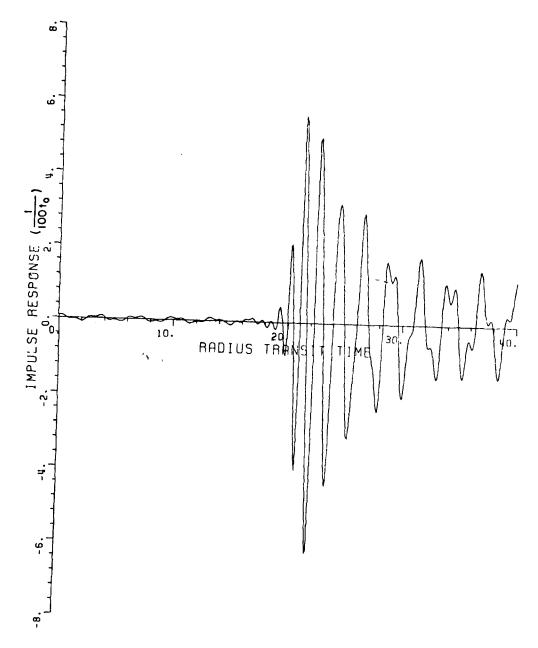


Figure 74a. Impulse response due only to 2-blade planar geometry inside cylinder with blades parallel to polarization of incident electric field.

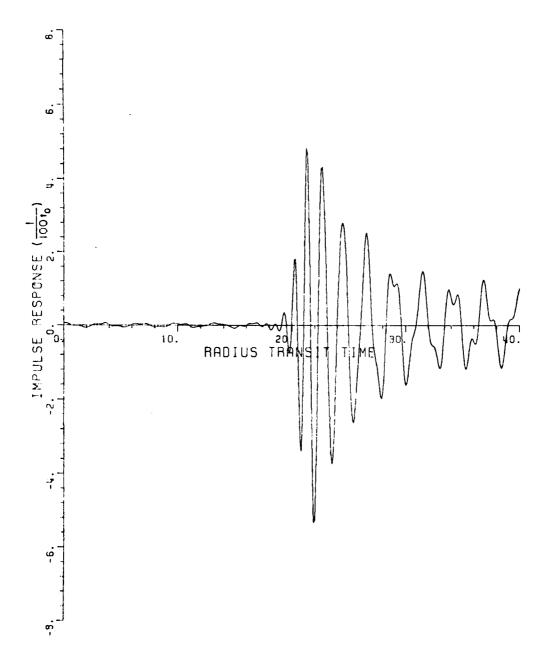


Figure 74b. Impulse response due only to 2-blade planar geometry inside cylidner with blade at 45° with respect to polarization of incident electric field.

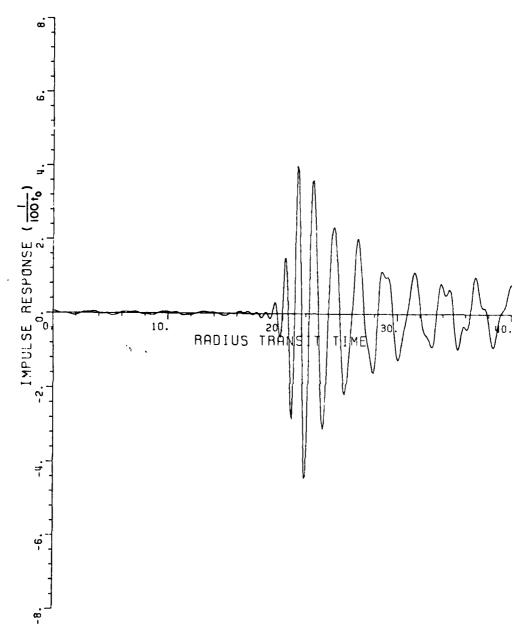


Figure 74c. Impulse response due only to 2-blade planar geometry inside cylinder with blades at 90° with respect to polarization of incident electric field.

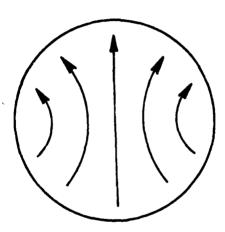


Figure 75. Electric field lines for  ${\sf TE}_{11}$  mode inside circular waveguide.

#### SECTION 5

## COMPLEX NATURAL RESONANCES OF OPEN AND FINITE CIRCULAR WAVEGUIDES

The complex natural resonances of a scatterer offer a unique way of identification, Moffatt [47]. They are also necessary for the make-up of the K-pulse, Kennaugh [44], a somewhat different target recognition tool. Although the importance of the complex natural resonances is recognized by many researchers, the resonance locations have been obtained only for a few simple geometries.

In this section, three different approaches are used to find the complex natural resonances of the open circular waveguide; eigenanalysis of time domain waveforms, rational function fit of frequency domain data and complex roots of a postulated characteristic equation.

The eigenanalysis solution of min-max problems involving squared error is described extensively in the literature, Guillemin [40]. It has also been shown, Moffatt et al. [49], to be less sensitive to noise than similar procedures, e.g., Prony's method.

Time domain impulse response waveforms of the finite cylinder (Figures 54a and 54b) are used in the present analysis. Since we note that for  $0.0<^t/t_0<20.0$  ( $t_0=^a/c$ , a=radius of circular guide, c=speed of

light), the impulse responses are the same for the open cylinder and the shorted cylinder, the result of eigenanalysis in this region is the same for both cases and is shown in Figure 76. The plot is in the complex ka (normalized s) plane and it is evident from the plot that the real part of the extracted pole locations vary over some range. The shaded area in the plot indicates that the pole can occur anywhere in the region. This is a common shortcoming of the eigenanalysis methods.

The uncertainty of the real part of pole locations according to the eigenanalysis method (including Prony's Method) is attributed to the fact that the exact order of the system is unknown while we look for a certain number of poles. Also it is known that the sampling interval affects the solution, Moffatt et al. [49].

Figure 77 and 78 show results of eigenanalysis of the region  $24.<^t/t_0<40$ . for the cases of a cylinder open at both ends and a cylinder with rear end shorted respectively.

In the second method, the moment method solution for the hollow finite guide shown in Figure 53 is used in a rational function fit. Frequency data are for  $0.02 < D/\lambda < 0.56$  in steps of 0.02 (D is diameter of guide,  $\lambda$  is wavelength). As we noted earlier, the cutoff frequency for the TE<sub>11</sub> mode of the circular waveguide is  $D/\lambda = 0.586$ , the frequency data includes only the effect of the rim and diffraction at the rear via propagation on the outside of the cylinder.

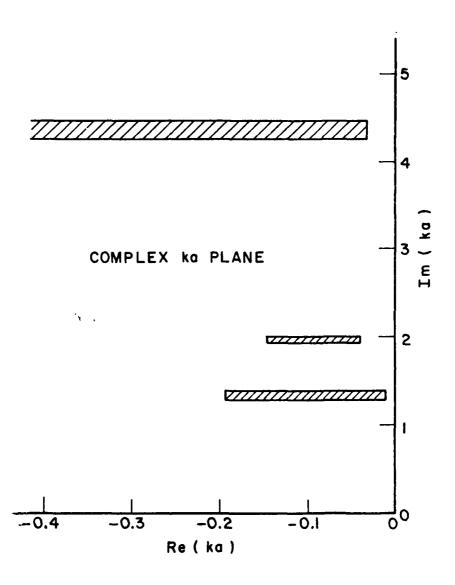


Figure 76. Poles extracted from impulse response from rim of finite waveguide.

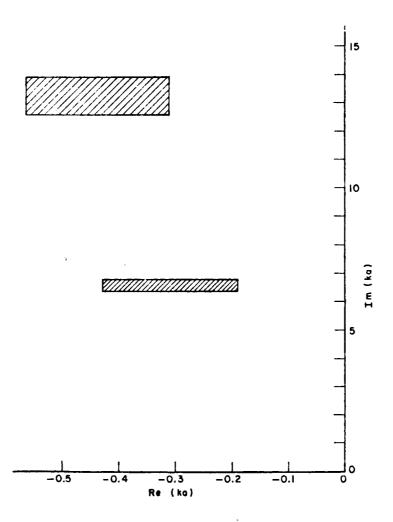


Figure 77. Poles extracted from impulse response from rear of finite waveguide with both ends open.

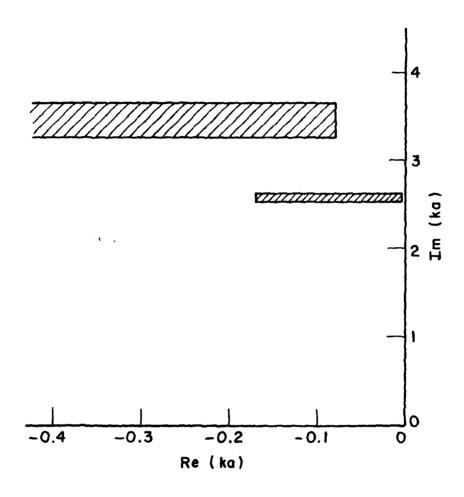


Figure 78. Poles extracted from impulse response from rear of finite waveguide with rear end shorted.

Thus a model represented by the rational function

$$F(ka) = \frac{\sum_{m=0}^{M} A_m(ka)^m + e^{-20jka} \sum_{n=0}^{N} B_n(ka)^n}{1 + \sum_{j=1}^{J} C_j(ka)^j},$$
 (260)

is proposed. The coefficients  $A_m$ ,  $B_n$  and  $C_j$  are real and are determined through a least square error algorithm. Then the expression in the denominator of Equation (260) is solved to obtain the complex natural resonances. The  $e^{-j20ka}$  term represents the time delay of contributions from the rear of guide. Two cases are presented here in Table 5.

TABLE 5. COMPLEX NATURAL RESONANCES EXTRACTED USING MODEL OF EQUATION (5-1) AND MOMENT METHOD SOLUTION OF BELOW CUTOFF REGION OF FINITE CIRCULAR GUIDE.

	M=N=5, J=6	M=N=4, J=5		
Complex natural resonances	-0.238 - j 1.832	-0.230 - j 1.688	C-+ A	
	-0.238 + j 1.832	-0.230 + j 1.688	Set A	
	-0.557 - j 1.086	-0.518 - j 1.16	Cat D	
	-0.557 + j 1.086	-0.518 + j 1.16	Set 8	

We recall that the resonance locations in Figure 76 did not include the diffraction from the rear, while the complex natural resonances in Table 5 include both rim scattering and diffraction from the rear of the finite guide. Comparing the imaginary parts of the

complex natural resonances of the two results, it appears that at frequencies below cutoff, the effect of rim scattering is strongest as the inclusion of rear diffraction in the model of Equation (260) did not alter the pole locations much.

When we examine the denominator of each component in the polarization scattering matrix (Equations 226, 227, 228 and 229), we note that all contain the factor  $1-f_{\rm n}^2$ . The same denominator factor is found in the coefficients which define the waveguide modes coupled into the guide and also appears in the radiation coupling coefficients for waveguide modes. We postulate therefore that the characteristic equation for the open circular waveguide is

$$1 - f_n^2 = (1 + f_n)(1 - f_n) = 0 (261)$$

The factored form of Equation (261) is interesting in that it appears to define even and odd complex natural resonances for the structure. For axial incidence, the infinite summations in the components of the scattering matrix reduce to the n=1 term and for axial incidence the complex natural resonances excited are given by

$$(1+f_1)(1-f_1) = 0$$
 , (262)

where

$$f_1 = \frac{L_+(k)}{2ka M_+(k)}$$
 (263)

Asymptotic forms for the factorization functions ( $L_+$ ,  $M_+$ ) have been given by Chuang et al. [11] as ( $e^{-iwt}$ convention)

$$L_{+}(k) \approx \frac{e^{i\pi/4}}{\sqrt{2ka}} \left\{ 1 - \frac{R}{2\sqrt{\pi ka} e^{-i\pi/4}} + \frac{R^{2}}{8\pi ka e^{-i\pi/2}} \right\},$$
(264)

and

$$M_{+}(k) \approx \frac{e^{i\pi/4}}{\sqrt{2ka}} \left\{ 1 - \frac{R'}{2\sqrt{\pi ka} e^{-i\pi/4}} + \frac{R'2}{8\pi ka e^{-i\pi/2}} \right\},$$
(265)

where

$$R = \sum_{m=1}^{\infty} \frac{(-i)^m e^{i2mka}}{m^{3/2}},$$
 (266)

and

$$R' = \sum_{m=1}^{\infty} \frac{(i)^m e^{i2mka}}{m^{3/2}} . \qquad (267)$$

Thus the complex natural resonances are defined by

$$\frac{1}{2ka} \left[ \frac{8\pi ka - 4\sqrt{\pi ka} e^{i\pi/4} R - iR^2}{8\pi ka - 4\sqrt{\pi ka} e^{i\pi/4} R' - iR'^2} \right] \pm 1 = 0$$
 (268)

As noted by Chuang et al. [11], the infinite summations R and R' converge relatively rapidly except when  $ka=3\pi/4$  and a few terms are sufficient to represent the series. However, we seek those complex values of ka which satisfy Equation (268) and each terms in R and R' adds additional zeros. This obviously complicates any search procedure.

A Cauchy integration program developed by Singaraju et al. [51] has been used to search for the zeros of Equation (268). The zeros of  $1-f_1=0$  and  $1+f_1=0$  are searched separately and they are plotted in the complex ka-plane in Figure 79 and Figure 80 respectively. Four terms each are used in the summations of R and R'. The solid line is drawn to show the cusp-like trend of the distribution of the zeros. Furthermore, the cusps have a period of  $\pi$  and suggests a simple relationship of the wavelength with the diameter. As is expected of an asymptotic expression, the locus of the zeros becomes more regular as the frequency increases. Due to the complexity of the characteristic equation, any solution becomes a formidable task.

The solution to Equation (268) has been attempted with different number of terms in R and R'. A particular zero appears consistently at around -0.35+j1.1. This is similar to the pole (set B of Table 5) obtained via the rational function model of the below cutoff region of the frequency spectrum. It is also similar to the dominant pole of the wire loop.

Due to the approximate nature of the equations and the complexity of the problem, the solutions are only approximate. However, it is encouraging to note that there is good agreement between the three methods.

The question of a characteristic equation and attendant complex natural resonances for the open circular waveguide is not considered settled. The topic, particularly as reexamination of the Wiener-Hopf solution, is beyond the scope of this report. Exact characteristic

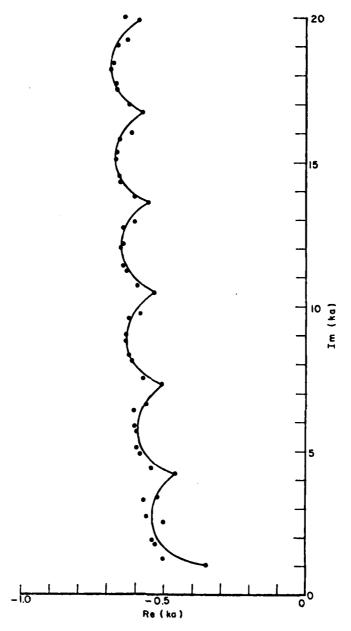


Figure 79. Zeros of  $1-f_1=0$ .

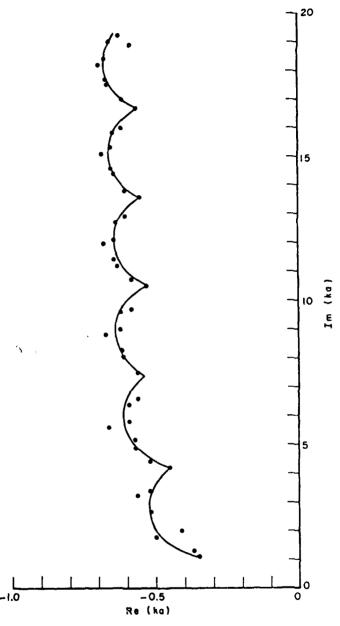


Figure 80. Zeros of  $1+f_1=0$ .

equations are known for only two scatterer geometries, spherical and cylindrical. The vector wave equation is also separable for the circular disc and some effort toward extraction of the characteristic equation has been made, Mithouard and Hodge [45]. It would now appear that the open circular waveguide can possibly also be treated.

## SECTION 6

#### SUMMARY FOR PART II

Backscatter calculations for the low resonance region of loaded cavity structures (open, loaded circular waveguides) have been obtained by combining exact (Wiener-Hopf) solutions at low frequencies with asymptotic estimates (GTD) at high frequencies. The spectral solutions were joined using rational function approximations to span the critical spectral region of the first propagating mode for the guide. A proper fit for the rational function model was obtained by satisfying both physical constraints and moments of the corresponding time domain estimates. The basic approach is not new, one of the earliest utilizations of the time domain concept by Kennaugh and Moffatt [43] was to combine Rayleigh and physical optics estimates to predict resonance region scattering. In this case, however, exact computations were used at low frequencies and the proper spectral region (below the cutoff frequency of the first propagating mode) was known a priori.

In the time domain the asymptotic estimates could not be utilized directly, the predicted time waveforms being noncausal. It has been demonstrated however that the noncausality of these solutions can be

removed without altering the correctness of the asymptotic model in its proper spectral range.

For an open, unloaded circular waveguide, asymptotic estimates provide a reasonable estimate of backscattering for guide diameters greater than 1.0 wavelength and an excellent estimate for guide diameters greater than 2.0 wavelengths, Johnson and Moffatt [12]. It has been demonstrated using physical constraints and moment conditions on the time domain models that when the guide is substantually loaded, i.e., a short or multiple blade load geometry, there the asymptotic estimates can be extended to lower frequencies (guide diameters of 0.7 to 0.75 wavelengths). The reason for this is that the rim scattering (unloaded waveguide) becomes relatively unimportant compared to the contributions from the load. The rim still must be accounted for however in the vicinity of the cutoff frequency for the first (TE11) propagating mode.

While the extension has not been made, the manipulations of spectral limited analytical solutions for the case of a open loaded circular waveguide have clearly demonstrated that in the low resonance region much more realistic jet engine geometries could be handled. The approach would be via moment method calculations of the structure at low frequencies which will not support propagating modes within the unloaded cavity and asymptotic estimates of the loaded cavity when only a few propagating modes are possible. These solutions could then be joined using rational function estimates to span the low resonance region of the aperture of the cavity. As in the cases demonstrated here, both

physical constraints and moment conditions can be applied to correct the corresponding time waveforms.

The dominant complex natural resonances of finite and open circular waveguides have been extracted using both time and frequency domain methods. An argument was given illustrating that the complex natural resonance string associated with the rim scattering (leading) is identical for all finite circular waveguides and is independent of rear terminations and of internal loading. This was demonstrated for the extracted poles. Therefore we can conclude that target recognition procedures based on the complex natural resonances of the aperture of the jet engine intake (see Appendix D) would be independent of the jet engine itself and would not require interrogating signals with spectral content above the first cutoff frequency for the intake.

A postulated characteristic equation for the open circular waveguide has been suggested based on the exact Wiener-Hopf solution. First estimates of the complex natural resonances corresponding to this characteristic equation have been obtained using asymptotic approximations for the Wiener-Hopf factorization functions. While some rough agreement with the poles extracted via time and frequency domain methods has been obtained, additional analysis is needed to properly interpret the complex natural resonances predicted by the proposed characteristic equation.

#### CONCLUSIONS AND RECOMMENDATIONS

The following conclusions can be drawn from the research detailed in this report; these are grouped below into catagories 1 and 2 corresponding to parts 1 and 2 of the report, respectively.

(la) The dominant scattering mechanisms have been identified and isolated in the frequency domain analysis of the problem of electromagnetic fields backscattered from the simplified inlet geometries of Figures 1 and 2. Junctions pertaining to these various dominant scattering mechanisms are defined, and the scattering from these junctions is described in terms of appropriate "generalized" scattering matrices. The elements of the generalized scattering matrices alluded to above are obtained in a relatively simple form via the uniform GTD (or UTD) ray analysis together with it's modifications which are required along ray caustics. The multiple scattering method (MSM) has been employed, in a self consistent fashion, to sum all the interactions between the scattering junctions. As noted above, the scattering junctions are characterized by the generalized scattering matrices whose elements are obtained via the ray method (see (1b)) together with it's modifications at ray caustics. The accuracy of the elements of the generalized scattering matrices has been established by comparison with the exact (but far more complicated) Wiener Hopf solution for these elements, and also by comparison with available

measurements in some cases. Consequently, it is concluded that the solution to the complete problem of the electromagnetic backscatter from the simple inlet model of Figures 1 and 2, which can be "built-up" from the use of the generalized scattering matrices via the self consistent MSM based procedure, is also expected to be reasonably accurate.

- (1b) The modulation of the backscattered electric field due to the blade rotation is also predicted for the simple inlet model in Figures 1 and 2. It is concluded, that this modulation can be significant in some cases for the simple inlet model chosen in the present work.
- (2a) The diagnostic and interpretation potential of the canonical (impulse, step, and ramp) response waveforms of cavity and loaded cavity-type structures have been vividly demonstrated. For a finite circular waveguide for example all of the scattering mechanisms have been recognized and in many cases resolved in the time domain.
- 2(b) It has been conclusively demonstrated that scattering data for cavity structures in the resonance region (cavity circumference of the wavelength) of the cavity aperture can be obtained by properly combining low frequency calculations and high frequency asymptotic estimates. The approach is particularly attractive because it provides a means to combine low frequency data where the only fields in the cavity are evanescent modes with solutions provided for example by the geometrical theory of diffraction. Computations at the low frequency end are inevitably simpler if propagating modes in the structure need not be considered.

- 2(c) It has been shown that the non-causal response waveforms predicted by certain asymptotic results for finite and semi-infinite guides can be corrected without altering their correct form at high frequencies.
- 2(d) A definite procedure using rational functions to join the low frequency calculations and high frequency asymptotic results was established for the case of loaded and unloaded semi-infinite circular waveguides. The rational functions are simple in form and both physical constraints and moment conditions on the time response waveforms have been given to assure the relative correctness of the rational functions.
- 2(e) A form for the characteristic equation for a semi-infinite circular waveguide has been postulated, and some initial estimates of the complex natural resonances made based on asymptotic formulas. The postulated characteristic equation came from an examination of the elements of the polarization scattering matrix for the exact Wiener-Hopf solution, and also from an examination of the coefficients for the modes coupled into the guide.

The following recommendations are made for future studies on the subject of electromagnetic backscatter from inlet geometries.

- 1(a) It is recommended that the present frequency domain analysis be extended to treat non-circular inlet rim shapes.
- 1(b) It would be worth analyzing the effect of a hub structure in front of the blades in the simple inlet geometries of Figures 1 and 2. It would also be worthwhile to consider more realistic blade structures

(e.g., those which include a pitch on the blades) in the inlet geometries of Figures 1 and 2.

- 1(c) It is recommended that the present analysis be extended to treat higher frequencies where a large number of modes can be excited within the inlet duct. Alternative representations for the high frequency fields within the duct regions should be sought because the use of a large number of modes, or a large number of equivalent rays, would lead to a very cumbersome solution. Also, it is recommended that the effect of tapers or transitions in the inlet duct shapes be studied since actual jet inlets do not maintain a constant cross-section within the duct regions.
- 2(a) It is recommended that the rational function procedure for obtaining resonance region scattering data be extended to finite cavity structures more closely modelling actual jet engine configurations. In this case one would be combining low frequency electric field integral equation calculations with high frequency asymptotic estimates.
- 2(b) The initial research on the characteristic equation and the related complex natural resonances of a semi-infinite circular waveguide should be completed.

All of these recommended problems in 1(a)-2(b) are very difficult and challenging, but are certainly important.

APPENDIX A
SUMMARY OF CIRCULAR WAVEGUIDE MODES
AND CUTOFF ka

NO	•	N	М	ka	NO	•	N	M	ka
1	TE	1	1	1.8412	41	TM	8	1	12.2251
2	TM	0	1	2.4049	42	TM	5	2	12.3386
3	TE	2	1	3.0542	43	TE	4	3	12.6819
4	TM	1	1	3.8318	44	TE	11	1	12.8264
5	TE	0	1	3.8318	45	TE	7	2	12.9324
6	TE	3	1	4.2012	46	TM	3	3	13.0152
7	TM	2	1	5.1357	47	TE	2	4	13.1704
8	TE	4	1	5.3175	48	TM	1	4	13.3237
9	TE	1	2	5.3315	49	TE	0	4	13.3237
10	TM	0	2	5.5201	50	TM	9	1	13.3543
11	TM	3	1	6.3802	51	TM	6	2	13.5893
12	TE	5	1	6.4155	52	TE	12	1	13,8787
13	TE	2	2	6.7062	53	TE	5	3	13,9872
14	TM	1	2	7.0156	54	TE	8	2	14.1155
15	TE	0	2	7.0156	55	TM	4	3	14.3726
16	TE	6	1	7.5013	56	TM	10	1	14.4755
17	TM	4	1	7.5884	57	TE	3	4	14.5859
18	TE	3	2	8.0153	58	TM	2	4	14.7960
19	TM	2	2	8.4173	59	TM	7	2	14.8213
20	ΤE	1	3	8.5363	60	TE	1	5	14.8636
21	TE	7	1	8.5777	61	TE	13	1	14.9283
22	TM	0	3	8.6537	62	TM	0	5	14.9309
23	TM	5	1	8.7715	63	TE	6	3	15.2682
24	TE	4	2	9.2824	64	TE	9	2	15.2867
25	TE	8	1	9.6474	65	TM	11	1	15.5899
26	TM	3	2	9.7610	66	TM	5	3	15.7002
27	TM	6	1	9.9361	67	TE	4	4	15.9641
28	TE	2	3	9.9695	68	TE	14	1	15.9753
29	TM	1	3	10.1735	69	TM	8	2	16.0378
30	TE	0	3	10.1735	70	TM	3	4	16.2235
31	TE	5	2	10.5199	71	ΤE	2	5	16.3475
32	TE	9	1	10.7114	72	TE	10	2	16.4479
33	TM	4	2	11.0647	73	TM	1	5	16.4706
34	TM	7	1	11.0864	74	ΤE	0	5	16.4706
35	TE	3	3	11.3459	75	TE	7	3	16.5294
36	TM	2	3	11.6199	76	TM	12	1	16.6983
37	TE	1	4	11.7060	77	TM	6	3	17.0038
38	TE	6	2	11.7349	78	TE	15	1	17.0202
39	TE	10	1	11.7708	79	TM	9	2	17.2412
40	TM	0	4	11.7915	80	TE	5	4	17.3129

NO.		N	M	ka	NO.		N	М	ka
81	TE	11	2	17.6003	121	TM	0	7	21.2116
82	TM	4	4	17.6160	122	ΤE	8	4	21.2291
83	TE	8	3	17.7740	123	ΤE	11	3	21.4309
84	TE	3	5	17.7888	124	TM	7	4	21.6415
85	TM	13	1	17.8014	125	ΤE	6	5	21.9317
86	TM	2	5	17.9598	126	TM	13	2	21.9563
87	TE	1	6	18.0155	127	TM	10	3	22.0470
88	TE	16	1	18.0632	128	TE	15	2	22.1422
89	TM	0	6	18.0711	129	TM	17	1	22.1725
90	TM	7	3	18.2876	130	TM	5	5	22.2178
91	TM	10	2	18.4335	131	TE	20	1	22.2190
92	TE	6	4	18.6375	132	TE	4	6	22.4010
93	TE	12	2	18.7451	133	TE	9	4	22.5014
94	TM	14	1	18.9000	134	TM	3	6	22.5827
95	TM	5	4	18.9801	135	TE	12	3	22.6293
96	TE	9	3	19.0046	136	ΤE	2	7	22.6716
97	TE	17	1	19.1044	137	TM	1	7	22.7601
98	ΤE	4	y 5	19.1960	138	TE	0	7	22.7601
99	TM	3	5	19.4094	139	TM	8	4	22.9452
100	TE	2	6	19.5129	140	TM	14	2	23.1158
101	TM	8	3	19.5545	141	TE	21	1	23.2548
102	TM	1	6	19.6159	142	TM	18	1	23.2568
103	TE	0	6	19.6159	143	TE	16	2	23.2643
104	TM	11	2	19.6160	144	TE	7	5	23.2681
105	TE	13	2	19.8832	145	TM	11	3	23,2759
106	TE	7	4	19.9419	146	TM	6	5	23.5861
107	TM	15	1	19.9944	147	TE	10	4	23.7607
108	TE	18	1	20.1440	148	TE	5	6	23.8036
109	TE	10	3	20.2230	149	TE	13	3	23.8194
110	TM	6	4	20.3208	150	TM	4	6	24.0190
111	ΤE	5	5	20.5755	151	TE	3	7	24.1449
112	TM	12	2	20.7899	152	TM	9	4	24.2339
113	TM	9	3	20.8071	153	TM	15	2	24.2692
114	TM	4	5	20.8269	154	TM	2	7	24.2701
115	TE	3	6	20.9725	155	TE	22	1	24.2893
116	TE	14	2	21.0154	156	TE	1	8	24.3113
117	TM	16	1	21.0852	157	TM	19	1	24.3383
118	TM	2	6	21.1170	158	TM	0	8	24.3525
119	TE	1	7	21.1644	159	TE	17	2	24.3819
120	TE	19	1	21.1822	160	TM	12	3	24.4949

```
NO.
NO.
            N
                         ka
                                              N
                                                            ka
                 5
                                                   5
161
      TE
            8
                      24.5872
                                  201
                                        TM
                                              9
                                                        27.5838
                                                        27.6979
                                                   2
162
      TM
            7
                 5
                      24.9349
                                  202
                                        TM
                                             18
                                                   2
163
      TE
           14
                 3
                      25.0020
                                  203
                                        TE
                                             20
                                                        27.7121
                                              8
                                                   6
164
           11
                 4
                      25.0085
                                  204
                                        TE
                                                        27.8893
      TE
                                        TM
                                             12
                                                   4
165
      TE
            6
                 6
                      25.1839
                                  205
                                                        28.0267
                                                   3
           23
                      25.3228
                                  206
                                        TM
                                             15
                                                        28.1024
166
      TE
                 1
                      25.4170
167
      TM
           16
                 2
                                  207
                                        TM
                                              7
                                                   6
                                                        28.1912
                      25.4172
                                  208
                                        TE
                                                   7
                                                        28.4098
168
      TM
           20
                                              6
                 1
            5
                      25.4304
      TM
                 6
                                  209
                                        TE
                                             26
                                                   1
                                                        28,4180
169
                 2
                      25.4956
                                                   5
170
      TE
           18
                                  210
                                        TE
                                             11
                                                        28.4609
                                                   3
171
      TM
           10
                 4
                      25.5095
                                  211
                                        TE
                                             17
                                                        28.5114
                 7
                                        TM
                                                   7
172
      TE
            4
                      25.5898
                                  212
                                              5
                                                        28.6266
173
      TM
           13
                 3
                      25.7051
                                  213
                                        TM
                                             23
                                                   1
                                                        28.6402
                 7
                                        TE
                                             14
                                                   4
174
      TM
            3
                      25.7482
                                  214
                                                        28.6943
            2
                 8
                                        TE
                                              4
                                                   8
175
      TE
                      25.8260
                                  215
                                                        28.7678
                                                   2
176
      TE
            9
                 5
                      25.8913
                                  216
                                        TE
                                             21
                                                        28.8156
                                                   2
177
      TM
            1
                 8
                      25.9037
                                  217
                                        TM
                                             19
                                                        28.8317
178
      TE
            0
                 8
                      25.9037
                                  218
                                        TM
                                             10
                                                   5
                                                        28.8874
                      26.1778
                                                   8
179
      TE
           15
                 3
                                  219
                                        TM
                                              3
                                                        28.9084
180
      TE
           12
                 4
                      26.2460
                                  220
                                        TE
                                              2
                                                   9
                                                        28.9777
181
      TM
            8
                 5
                      26,2668
                                  221
                                        TM
                                              1
                                                   9
                                                        29.0468
                                                   9
182
      TE
           24
                 1
                      26.3555
                                  222
                                        TE
                                              0
                                                        29.0468
183
      TM
           21
                      26.4937
                                  223
                                        TE
                                              9
                                                   6
                                                        29.2186
                 1
184
      TE
            7
                 6
                      26.5450
                                  224
                                        TM
                                             13
                                                   4
                                                        29.2706
185
      TM
           17
                 2
                      26.5598
                                  225
                                        TM
                                             16
                                                   3
                                                        29.2909
186
      TE
           19
                 2
                      26,6055
                                  226
                                        TE
                                             27
                                                   1
                                                        29.4481
                                  227
                                                        29.5457
187
      TM
           11
                 4
                      26.7733
                                        TM
                                              8
                                                   6
                                  228
188
      TM
            6
                 6
                      26.8202
                                        TE
                                             18
                                                   3
                                                        29.6701
                                  229
                                                   1
189
      TM
           14
                 3
                      26.9074
                                        TM
                                             24
                                                        29.7105
190
      TE
            5
                 7
                      27.0103
                                  230
                                        TE
                                             12
                                                   5
                                                        29.7290
                 5
                                                   7
191
      TE
           10
                      27.1820
                                  231
                                        TE
                                              7
                                                        29.7908
            4
                 7
                                                   4
                                                        29.9066
192
      TM
                      27.1991
                                  232
                                        TE
                                             15
                                                   2
            3
193
      TE
                                  233
                                        TE
                                             22
                                                        29.9161
                      27.3101
                                                   27
                 3
                                             20
194
      TE
           16
                      27.3474
                                  234
                                        TM
                                                        29.9616
195
      TE
           25
                      27.3871
                                  235
                                        TM
                                                        30.0337
                 1
                                              6
196
            2
                                                   5
      TM
                      27.4206
                                  236
                                        TM
                                                        30.1791
                 8
                                             11
197
                      27.4571
                                                   8
      TE
            1
                 9
                                  237
                                        TE
                                                        30.2029
                                              5
198
      TE
           13
                 4
                      27.4743
                                  238
                                        TM
                                              4
                                                   8
                                                        30.3710
199
      TM
            0
                 9
                      27.4935
                                  239
                                        TE
                                              3
                                                   9
                                                        30.4703
200
      TM
           22
                      27,5680
                                  240
                                        TM
                                             17
                                                        30.4733
```

```
NO.
                                  NO.
            N
                         ka
                                              N
                                                           ka
241
                      30.4774
                                  281
      TE
           28
                 1
                                                   4
                                                        32.9537
                                        TM
                                             16
          14
                      30.5060
242
                 4
      TM
                                  282
                                        TE
                                              7
                                                   8
                                                        33.0152
                      30.5345
243
      TE
           10
                                             21
                 6
                                  283
                                        TE
                                                   3
                                                        33.1192
                      30.5692
244
      TM
            2
                 9
                                  284
                                                   6
                                        TE
                                             12
                                                        33.1315
                                                   2
245
      TE
            1
               10
                      30.6019
                                  285
                                        TE
                                             25
                                                        33,2023
246
                      30.6346
                                                   8
      TM
            0
               10
                                  286
                                        TM
                                             6
                                                        33.2330
247
      TM
           25
                      30.7790
                                  287
                                        TM
                                             23
                                                   2
                 1
                                                        33.3302
248
      TE
           19
                 3
                      30.8241
                                  288
                                              5
                                                   9
                                        TE
                                                        33.3854
                                                   5
4
249
      TM
            9
                 6
5
2
                      30.8854
                                             15
                                  289
                                        TE
                                                        33,4785
250
      TE
           13
                      30.9874
                                  290
                                        TE
                                             18
                                                        33,5039
251
      TE
           23
                      31.0140
                                  291
                                        TM
                                             11
                                                   6
                                                        33.5264
           21
                 2
252
      TM
                      31.0878
                                  292
                                        TM
                                              4
                                                   9
                                                        33.5371
253
           16
                 4
                      31.1119
                                             31
      TE
                                  293
                                        TE
                                                   1
                                                        33,5616
254
                 7
            8
                      31.1553
                                              3
      TE
                                  294
                                        TE
                                                  10
                                                        33,6270
255
            7
      TM
                 7
                      31.4228
                                  295
                                        TM
                                              2
                                                  10
                                                        33.7165
256
                 5
                      31.4600
                                                        33.7462
      TM
           12
                                  296
                                        TE
                                              1
                                                  11
257
      TE
           29
                 1
                      31.5062
                                  297
                                        TM
                                              0
                                                  11
                                                        33,7758
258
            6
                8
      TE
                      31.6179
                                  298
                                        TE
                                             10
                                                   7
                                                        33.8420
259
           18
                 3
                                                        33.9749
      TM
                      31.6501
                                  299
                                        TM
                                             28
                                                   1
260
      TM
           15
                 4
                      31.7334
                                  300
                                             20
                                                        33,9887
                                        TM
                                                   3
261
      TM
            5
                      31.8117
                                  301
                                        TM
                                             14
                                                   5
                                                        33,9932
                8
262
                      31.8384
                                                   7
      TE
           11
                 6
                                  302
                                        TM
                                              9
                                                        34.1544
263
      TM
           26
                 1
                      31.8459
                                  303
                                        TM
                                             17
                                                   4
                                                        34.1673
                                                   3
                                                        34.2608
264
      TE
            4
                 9
                      31.9385
                                  304
                                        TE
                                             22
265
      TE
           20
                 3
                      31.9737
                                  305
                                        TE
                                             26
                                                   2
                                                        34.2930
266
      TM
            3
                 9
                      32.0649
                                  306
                                             8
                                                   8
                                                        34.3966
                                        TE
                 2
267
      TE
           24
                      32,1093
                                        TE
                                             13
                                                   6
                                  307
                                                        34.4146
                                                   2
268
            2
      TE
               10
                      32.1273
                                  308
                                        TM
                                             24
                                                        34.4468
269
      TM
            1
               10
                      32.1897
                                  309
                                        TE
                                             32
                                                        34.5884
                                                   1
270
      TE
            0
               10
                      32.1897
                                  310
                                                   8
                                                        34.6371
                                        TM
                                             7
271
           22
                2
                      32.2106
                                                   4
      TM
                                             19
                                                        34.6915
                                  311
                                        TE
                                                   5
272
      TM
           10
                 6
                      32.2119
                                  312
                                             16
                                                        34.7125
                                        TE
           14
                 5
                                                   9
273
      TE
                      32.2370
                                  313
                                              6
                                                        34.8134
                                        TE
274
           17
                 4
                      32.3109
      TE
                                  314
                                        TM
                                             12
                                                   6
                                                        34.8300
275
            9
                 7
                      32.5052
                                        TM
                                                   9
                                                        34.9888
      TE
                                  315
                                             5
           30
                                        TM
                                             29
                                                   1
276
      TE
                 1
                      32.5341
                                  316
                                                        35.0373
           13
277
      TM
                 5
                      32.7311
                                  317
                                        TE
                                              4
                                                  10
                                                        35.1039
278
      TM
           8
                 7
                      32.7958
                                             21
                                  318
                                        TM
                                                   3
                                                        35.1511
279
      TM
           19
                 3
                      32.8218
                                  319
                                        TE
                                                   7
                                                        35.1667
                                             11
280
      TM
           27
                      32.9112
                                  320
                 1
                                        TM
                                              3
                                                  10
                                                        35,2187
```

#### APPENDIX B

## INCLUSION OF ALL MULTIPLE INTERACTIONS ACROSS THE APERTURE

As shown in Figure 16, the incident plane wave field, after double diffraction, gives rise to a non-ray optical field  $\overline{E}_3$  on the rim, which was described by Eqs. (91) and (94).

$$\overline{E}_3^i = \overline{E}_{3,1}^i + \overline{E}_{3,2}^i \qquad (A-1)$$

where  $\overline{E}_{3,1}^i$  and  $\overline{E}_{3,2}^i$  are the two ray optical components given in Eqs. (95)-(96). Now, the triply diffracted ray which traverses the aperture to produce  $\overline{E}_4^i$  (and therefore  $\overline{E}^b$ ) lies again on the reflection boundary of the doubly diffracted ray (which produces  $\overline{E}_3^i$  and therefore  $\overline{E}^b$ ). Accordingly, one can decompose the non-ray optical  $\overline{E}_4^i$  into four ray optical components as follows.

$$\overline{E_{4}} = \overline{E_{4,1}^{i1}} + \overline{E_{4,1}^{i2}} + \overline{E_{4,2}^{i1}} + \overline{E_{4,2}^{i2}}$$
due to  $\overline{E_{3,1}^{i}}$  due to  $\overline{E_{3,2}^{i}}$ 

Here,  $\overline{E}_{4,1}^{i1}$  and  $\overline{E}_{4,1}^{i2}$  are the two ray optical fields scattered by  $\overline{E}_{3,1}^{i}$ ;  $\overline{E}_{4,2}^{i1}$  and  $\overline{E}_{4,2}^{i2}$  are the two ray optical fields scattered by  $\overline{E}_{3,2}^{i2}$ . Proceeding the same as in Eqs. (95)-(96), one can write  $\overline{E}_{4,1}^{i1}$ ,  $\overline{E}_{4,1}^{i2}$ ,  $\overline{E}_{4,2}^{i1}$ , and  $\overline{E}_{4,2}^{i2}$ 

as

$$\frac{-i1}{E_{4,1}} = \frac{-i}{E_{3,1}} \cdot D_s^i \cdot \sqrt{\frac{\rho}{2a(\rho+2a)}} e^{-j2ka} ,$$
(A-3)

$$\overline{E}_{4,1}^{i2} = \frac{1}{2} \overline{E}_{3,1}^{i} (-1) \sqrt{\frac{\rho_{1}^{\Gamma} \rho_{2}^{\Gamma}}{(\rho_{1}^{\Gamma} + 2a)(\rho_{2}^{\Gamma} + 2a)}} e^{-j2ka}, \qquad (A-4)$$

$$\frac{-i1}{E_{4,2}} = \frac{-i}{E_{3,2}} \cdot n_s \cdot \sqrt{\frac{\rho}{2a(\rho+2a)}} e^{-j2ka}, \qquad (A-5)$$

$$\frac{12}{E_{4,2}} = \frac{1}{2} E_{3,2}^{\dagger} (-1) \cdot \sqrt{\frac{\rho_3^{\Gamma} \rho_4^{\Gamma}}{(\rho_3^{\Gamma} + 2a)(\rho_4^{\Gamma} + 2a)}} e^{-j2ka}, \qquad (A-6)$$

where

$$D_{S}^{i} = \frac{-e^{-j\frac{\pi}{4}}}{2\sqrt{2\pi k}} \qquad (A-7)$$

and

$$\rho = -a$$
;  $\rho_1^r = -a$ ,  $\rho_2^r = 2a$ ;  $\rho_3^r = -a$ ,  $\rho_4^r = 4a$ . (A-8)

Thus, E4 can be rewritten as

$$\frac{-1}{E_4} = \frac{-1}{E_{4,1}} + \frac{-1}{E_{4,2}} + \frac{-1}{E_{4,3}} , \qquad (A-9)$$

where

$$\overline{E}_{4,1}^{i} = \overline{E}_{4,1}^{i1} + \overline{E}_{4,1}^{i2}$$

$$= \overline{E}_{3}^{i} \cdot n_{s}^{i} \cdot j \cdot \sqrt{\frac{1}{2a}} e^{-j2ka} \cdot (A-10)$$

$$\frac{i}{E_{4,2}} = \frac{i^{2}}{E_{4,1}}$$

$$= \frac{1}{2} \frac{i}{E_{3,1}} (-1) \cdot j \cdot \sqrt{\frac{1}{2}} e^{-j2ka}$$
(A-11)

$$\frac{\overline{E}_{4,3}^{i}}{\overline{E}_{3,2}^{i}} = \overline{E}_{4,2}^{i2}$$

$$= \frac{1}{2} \overline{E}_{3,2}^{i} (-1) \cdot j \cdot \sqrt{\frac{2}{3}} e^{-j2ka} \qquad (A-12)$$

Proceeding the same, one is able to obtain

$$\overline{E}_{m}^{i} = \sum_{n=1}^{m-1} \overline{E}_{n}^{i} \qquad m \ge 3 \qquad . \tag{A-13}$$

where

$$\overline{E}_{m,1}^{i} = \overline{E}_{m-1}^{i} \cdot D_{s}^{i} \cdot j \cdot \sqrt{\frac{1}{2a}} e^{-j2ka}$$

$$= \overline{E}_{m-1}^{i} \left[ -\frac{e^{-j(2ka-\pi/4)}}{4\sqrt{\pi ka}} \right]$$

$$= \overline{E}_{m-1}^{i} \cdot A \quad . \tag{A-14}$$

and

$$\frac{1}{E_{m,n}} = \frac{1}{2} \frac{1}{E_{m-1,n-1}} (-1) \cdot j \cdot \sqrt{\frac{n-1}{n}} e^{-j2ka} \cdot 
= \frac{1}{E_{m-1,n-1}} \sqrt{\frac{n-1}{n}} \cdot jB , 2 < n < m-1 .$$
(A-15)

with

$$A = \frac{-e^{-j\left(2ka - \frac{\pi}{4}\right)}}{4\sqrt{\pi ka}} \qquad (A-16)$$

$$B = \frac{-1}{2} e^{-j2ka} \qquad (A-17)$$

From Eqs. (107)-(108), one can try to sum up  $\sum\limits_{m=2}^{\infty} \frac{i}{E_m}$  in terms of  $E_2^i$  to obtain a multiplication factor  $\widetilde{f}$ , then  $\sum\limits_{m=2}^{\infty} \overline{E}^{bsm}$  is just the product of

EbS2 and f. Now,

$$\sum_{m=2}^{\infty} \frac{-i}{E_{m}} = \sum_{m=2}^{\infty} \sum_{n=1}^{m-1} \frac{i}{E_{m,n}^{i}}$$

$$= \sum_{m=3}^{\infty} \sum_{n=2}^{m-1} \frac{E_{m,n}^{i}}{E_{m,n}^{i}} + A \cdot \sum_{m=3}^{\infty} \frac{E_{m-1}^{i}}{E_{m-1}^{i}} + E_{2}^{i}$$

$$= jB \cdot \sum_{m=2}^{\infty} \sum_{n=1}^{m-1} \frac{E_{m,n}^{i}}{E_{m,n}^{i}} \sqrt{\frac{n}{n+1}} + A \cdot \sum_{m=2}^{\infty} \frac{E_{m}^{i}}{E_{m}^{i}} + E_{2}^{i} \qquad (A-18)$$

Thus,

$$(1-A) \sum_{m=2}^{\infty} \overline{E}_{m}^{i} = jB \cdot \sum_{m=2}^{\infty} \sum_{n=1}^{m-1} \overline{E}_{m,n}^{i} \cdot \sqrt{\frac{n}{n+1}} + \overline{E}_{2}^{i} . \qquad (A-19)$$

Proceeding the same for K times, one can obtain

$$[1-A \cdot \sum_{\ell=1}^{K} (jB)^{\ell-1} \cdot \sqrt{\frac{1}{\ell}}] \sum_{m=2}^{\infty} \overline{E}_{m}^{i}$$

$$= (jB)^{K} \cdot \sum_{m=2}^{\infty} \sum_{n=1}^{\infty} \overline{E}_{m,n}^{i} \cdot \sqrt{\frac{n}{n+K}} + [\sum_{\ell=1}^{K} (jB)^{\ell-1} \sqrt{\frac{1}{\ell}}] \cdot \overline{E}_{2}^{i} . \tag{A-20}$$

However, |B| < 1. In the limiting case where  $K + \infty$ , the first term on the right hand side of Eq. (A-20) can be neglected. Thus, Eq. (A-20) is reduced to

$$\sum_{m=2}^{\infty} \overline{E}_{1}^{i} \approx \overline{E}_{2}^{i} \cdot \widetilde{f} \qquad (A-21)$$

where

$$\hat{f} = \frac{C}{1-AC} \qquad (A-22)$$

and

$$C = \sum_{k=1}^{K} (jB)^{k-1} \cdot \sqrt{\frac{1}{k}}, \quad K + \infty . \qquad (A-23)$$

From Eqs. (107)-(108), one can write

$$\sum_{m=2}^{\infty} \overline{E}^{bsm} (\theta=0) \approx \overline{E}^{bs2} (\theta=0) \cdot \widetilde{f} \qquad (A-24)$$

Combining Eqs. (87) and (A-24), one has

$$\sum_{m=1}^{\infty} E^{bsm} (\theta=0) = E^{bs1} (\theta=0) \cdot \{1+u_2 \cdot \hat{f}\} . \tag{A-25}$$

### APPENDIX C

# TO DETERMINE [ $S_{21}$ ] FROM [ $S_{12}$ ] USING THE RECIPROCITY THEOREM

As shown in Figure 26, one wants to find the coupled fields inside the waveguide due to an electric source  $\overline{J}_e$  in the far field. Let the electric and magnetic test sources  $\overline{J}_S$ ,  $\overline{M}_S$  be located at z=-L, then,

$$\overline{J}_{S} = \hat{n} \times \overline{H}_{n}^{+}$$

$$\overline{M}_{S} = \overline{E}_{n}^{+} \times \hat{n}$$
at  $z = -L$  . (A-26)

 $\overline{E}_n^+$  and  $\overline{H}_n^+$  represent the incident modal fields in the waveguide, and

$$\begin{bmatrix}
\vec{E}_{n} = \vec{c}_{n} & (\vec{e}_{n} + \vec{e}_{zn}) & e^{-j\beta_{n}z} \\
\vec{H}_{n} = \vec{c}_{n} & (\vec{h}_{n} + \vec{h}_{zn}) & e^{-j\beta_{n}z}
\end{bmatrix} \text{ at } z = -L .$$
(A-27)

where  $\overline{e}_n$  (or  $\overline{h}_n$ ) is the transverse electric (or magnetic) field, and  $\overline{e}_{Zn}$  (or  $\overline{h}_{Zn}$ ) is the longitudinal electric (or magnetic) field.  $C_n^+$  can be either  $A_{nm}^+$  or  $B_{nm}^+$  to denote the TE or TM case. The test sources  $\overline{J}_S$  and  $\overline{M}_S$  will generate  $\overline{E}^+$ , and  $\overline{H}^+$  in the far field which are assumed to be known (see Eqs. (131)-(133)). Now, let  $\overline{J}_e$  generate  $\overline{E}^e$  and  $\overline{H}^e$  internal and external to the guide. From reciprocity, one obtains

$$\iint_{\Sigma+S+S_0} [\overline{E}^r x \, \overline{H}^e - \overline{E}^e \, x \, \overline{H}^r] \cdot \hat{n} \, dS = \iiint_V J_e \cdot \overline{E}^r \, dV . \tag{A-28}$$

However,

$$\hat{n} \times \overline{E}^{\Gamma}$$
 = 0;  $\hat{n} \times \overline{E}^{e}$  = 0. (A-29)

Also,  $(\overline{E}^\Gamma$ ,  $\overline{H}^\Gamma)$  and  $(\overline{E}^e$ ,  $\overline{H}^e)$  satisfy the radiation conditions on  $\Sigma$ . Therefore, Eq. (A-28) can be reduced to

$$-\iint_{S_0} \overline{H}^e \cdot \overline{M}_s dS + \iint_{S_0} \overline{E}^e \cdot \overline{J}_s dS = \overline{P}_e \cdot \overline{E}(\overline{R}_p) . \qquad (A-30)$$

if  $\overline{J}_e = \overline{p}_e \cdot \delta(|\overline{R}-\overline{R}p|)$ , a point source in the far field.  $\overline{R}p$  is the position vector from the reference point to point P. Also, we let

$$\frac{e}{E} = \sum_{p} A_{p}^{-} (\overline{e}_{p} - \overline{e}_{zp}) e^{j\beta_{p}z} .$$

$$\overline{H}^{e} = \sum_{p} A_{p}^{-} (-\overline{h}_{p} - \overline{h}_{zp}) e^{j\beta_{p}z} .$$
(A-31)

in the waveguide region at z=-L. Again,  $A_p^-$  can be either  $A_{nm}^-$  or  $B_{nm}^-$  to denote the TE or TM case. Substituting Eqs. (A-26)-(A-27), and (A-31) into (A-30), one obtains

$$-\iint\limits_{S_0} \left\{ \left[ \sum\limits_{p} A_p^- \left( \overline{e}_p - \overline{e}_{zp} \right) \right] \times \left[ c_n^+ \left( \overline{h}_n + \overline{h}_{zn} \right) \right] e^{j \left( \beta_p - \beta_n \right) z} \right\} \cdot \hat{z} \ dS$$

$$+\iint\limits_{S_0} \left\{ \left[ c_n^+ \left( \overline{e}_n + \overline{e}_{zn} \right) \right] \times \left[ \sum\limits_{p} A_p^- \left( -\overline{h}_p + \overline{h}_{zp} \right) \right] e^{j \left( \beta_p - \beta_n \right) z} \right\} \cdot \hat{z} \, dS$$

$$= \overline{P}_{e} \cdot \overline{E}^{f}(\overline{R}p) \qquad . \tag{A-32}$$

Using the orthogonality property of the waveguide modes, one obtains

$$P_{e} \cdot \overline{E}(\overline{Rp}) = -2 c_{n}^{+} A_{n}^{-} \iint_{S_{0}} \overline{e}_{n} \times \overline{h}_{n} \cdot \hat{z} dS . \qquad (A-33)$$

Therefore,

$$A_{n}^{-} = -\frac{\overline{P}_{e} \cdot E^{r}(Rp)}{2c_{n}^{+} \iint \overline{e}_{n} \times \overline{h}_{n} \cdot \hat{z} dS} \qquad (A-34)$$

In order to produce an incident field  $\vec{E}^i = \hat{\theta} \hat{E}^i_{\theta} + \hat{\phi} \hat{E}^i_{\phi}$  at the opening of the waveguide, one can let

$$\overline{P}_{e} = - \left( \hat{\theta} E_{\theta}^{\dagger} + \hat{\phi} E_{\phi}^{\dagger} \right) \cdot \frac{4\pi}{J\omega\mu} \quad \cdot$$

Thus,

$$A_{n} = \frac{\left(\hat{\theta}E_{\theta}^{\dagger} + \hat{\phi}E_{\phi}^{\dagger}\right) \cdot \overline{E}^{r}(Rp) \cdot Rp e^{jkRp}}{2 c_{n}^{+} \iint_{S_{0}} \overline{e_{n}} \times \overline{h_{n}} \cdot \overline{z} dS} \cdot \frac{4\pi}{j\omega\mu}$$
 (A-36)

Replacing A- with A- or B- , and  $c_{n}^{+}$  with  $A_{nm}^{+}$  or  $B_{nm}^{+}$  , one obtains

$$A_{nm}^{-} = \frac{(\widehat{\theta}\widehat{E}_{\theta}^{i} + \widehat{\phi}\widehat{E}_{\phi}^{i}) \cdot \widehat{E}_{TE}^{r} (\widehat{R}p) \cdot Rp \cdot e^{jkRp}}{2 A_{nm}^{+} \iint_{S_{0}} \widehat{e}_{nm}^{i} \times \widehat{h}_{nm}^{i} \cdot \widehat{z} dS} \cdot \underbrace{4\pi}_{j\omega\mu} \cdot (A-37)$$

$$B_{nm}^{-} = \frac{(\hat{\theta}E_{\theta}^{\dagger} + \hat{\phi}E_{\phi}^{\dagger}) \cdot E_{TM}^{r} (\overline{R}p) \cdot Rp \cdot e^{jkRp}}{2 B_{nm}^{+} \iint_{S_{0}} \overline{e_{nm}} \times \overline{h_{nm}} \cdot \hat{z} dS} \cdot \frac{4\pi}{j\omega\mu}$$
 (A-38)

## APPENDIX D

## RADAR RECOGNITION OF CAVITY STRUCTURES

It was demonstrated in Part II of this report that a set of complex natural resonances could be associated with the rim or aperture of the cavity. These resonances are independent of any loading (engine) or external termination. The rim or aperture scattering is most dominant at frequencies just below the cutoff frequency of the first propagating mode. The on-axis radar cross section of the rim (for a circular waveguide) just below cutoff is some 9db greater than its nominal value at higher frequencies and is roughly equal to the average cross sections obtained when a short circuit terminates the guide. A target recognition algorithm based on the most dominant aperture natural resonance (oscillatory part ~ 0.35 guide diameters in wavelengths) would not require penetration of the cavity. If the spectrum of the interrogating radar signal lies below the cutoff frequency for the first propagating mode for the cavity then direct exploitation of the two (possibly) complex natural resonances excited does not appear too promising. The amplitude only approach using synthetically generated matched-filter response waveforms, Moffatt, Rhoads [48] would be one

possibility. Another possibility which should be tested is the low frequency classification scheme discussed by Ksienski and Lin in Moffatt, Young, Ksienski, Lin and Rhoads [49].

If somewhat more sophisticated interrogating signals are considered then two procedures can be suggested; prediction-correlation Chuang, Moffatt [38] and the K-pulse, Kennaugh [44] both of which would be based on the aperture complex natural resonances of the cavity or a combination of these and the load resonances (see below). The K-pulse seems particularly attractive in that very distinctive waveforms should result. Briefly, the K-pulse relates a single excitation invariant interrogating waveform to a unique family of excitation-dependent (aspect and polarization) response waveforms. The integrating K-pulse spectrum has, as zeros, the complex natural resonances of the scatterer and is defined to elicit a response waveform of minimum duration, Kennaugh [44].

Consider the solution for the backscattered field from a loaded open circular waveguide using the generalized scattering matrix technique (GSMT), Johnson, Moffatt [12]. The scattered field is given by

$$u^{bs} = \left\{ S_{11} + S_{12} \left[ (T_{b2}S_bT_{2b})^{-1} - S_{22} \right]^{-1} S_{21} \right\} u^{\dagger} , \qquad (A-39)$$

where  $S_{11}$ ,  $S_{12}$ ,  $S_{21}$  and  $S_{22}$  are matrices representing respectively the rim scattering, radiation characteristics of the rim, coupling characteristics of the rim and reflection of waveguide modes at the open

(rim) end of the guide and  $u^{\dagger}$  is the incident field.  $T_{2b}$  and  $T_{b2}$  are diagonal matrices representing respectively transmission down the guide (rim to load) and transmission back from the load (load to rim).  $S_b$  is a matrix for the reflection of waveguide modes from the load. The matrices  $S_{11}$ ,  $S_{12}$ ,  $S_{21}$  and  $S_{22}$  have been found using the exact Wiener-Hopf solution, Johnson, Moffatt [12]. Based on these matrices, Part II of this report suggests the characteristic equation

$$[1 - f_n^2] = [1 + f_n][1 - f_n] = 0.$$
 (A-40)

for the aperture or rim complex natural resonances. The point is that each element in the matrices  $S_{11}$ ,  $S_{12}$ ,  $S_{21}$  and  $S_{22}$  has  $(1-f_n{}^2)$  as a multiplication factor in the denominator. If we write these matrices as

$$S_{ij} = \frac{S_{ij}}{[1 - fn^2]}$$
, (A-41)

then

$$u^{bs} = \left\{ \frac{s_{11}'}{[1-f_n^2]} + \frac{s_{12}'}{[1-f_n^2]^2} \left[ (T_{b2}s_b^{\dagger}T_{2b})^{-1} - \frac{s_{22}'}{[1-f_n^2]} \right]^{-1} s_{21}' \right\} u^{\dagger} ,$$
(A-42)

or

$$u^{bs} = \frac{1}{[1-f_n^2]^2} \left\{ s_{11}^{'}[1-f_n^2] + s_{12}^{'}[(T_{b2}s_b^{T}T_{2b})^{-1} - \frac{s_{22}^{'}}{[1-f_n^2]}] - s_{21}^{'} \right\} u^{4}.$$

Equations (A-42) and (A-43) illustrate on important point which it is felt will be true for all cavity structures. The K-pulse spectrum desired is the square of the aperture pole spectrum as zeros. Such a spectrum still does not contain the poles of the load, i.e., the poles affected by  $(T_{b2}S_bT_{2b})^{-1}$ . A K-pulse which included these would apparently be quite long. An excitation with the square of the aperture pole spectrum as zeros however would result in response waveforms very highly characteristics of the load. From Equation (A-42) it is clear that a K-pulse with the zeros of  $1-f_n^2$  alone would not eliminate ringing in the response due to the rim.

The discussion at this time is somewhat academic since, as discussed in Section 5, of Part II, we have not yet been completely successful in extracting the zeros of  $1-f_n^2$ . However, development of the K-pulse concept is in its infancy. The K-pulse waveforms for a few representative scatterers including the sphere, circular disk and circular loop are presently being studied on other programs\*. We envision however that applications of the K-pulse concept will grow in much the same way as those of the impulse response concept, Kennaugh, Cosgriff [42] and complex natural resonances for target identification, Moffatt, Mains [47].

•

<sup>\*</sup>Contract No. 710816, etc.

## REFERENCES

- [1] Kouyoumjian, R.G. and P.H. Pathak, "A Uniform Geometrical Theory of Diffraction for an Edge in a Perfectly Conducting Surface," Proc. IEEE, Vol. 62, No. 11, November 1974, pp. 1448-1461.
- [2] Chu, L.J., "Calculation of the Radiation Properties of Hollow Pipes and Horns," J. Appl. Phys., Vol. 11, September 1940, pp. 630-610.
- [3] Levine, H. and J. Schwinger, "On the Radiation of Sound from an Unflanged Circular Pipe," Phys., Rev. 2nd ser., Vol. 73, No. 4, 1948, pp. 383-406.
- [4] Jones, D.S., "The Scattering of a Scalar Wave by a Semi-Infinite Rod of Circular Cross-Section," Phil. Trans. Roy. Soc. London, ser A., Vol. 247, 1955, pp. 499-528.
- [5] Noble, B., Methods Based on the Wiener-Hopf Technique, Pergamon Press, Los Angeles, 1958.
- [6] Pearson, J.D., "The Diffraction of Electromagnetic Waves by a Semi-Infinite Circular Waveguide," Proc. Cambridge Phil. Soc., Vol. 49, No. 4, 1953, pp. 659-667.
- [7] Weinstein, L.A., The Theory of Diffraction and the Factorization Method, The Golem Press, Boulder, Colorado, 1969.
- [8] Bowman, J.J., "Comparison of Ray Theory with Exact Theory for Scattering by Open Waveguides," SIAM J. Appl. Math., Vol. 18, 1970, pp. 781-829.
- [9] Lee, S.W., V. Jamnejad, and R. Mittra, "Near Field of Scattering by a Hollow Semi-Infinite Cylinder and Its Application to Sensor Booms," IEEE Trans. Ant. Prop., Vol. AP-21, No. 2, March 1973, pp. 182-188.
- [10] Mittra, R., S.W. Lee, and C.A. Chuang, "Analytical Modeling of the Radar Scattering Characteristics of Aircraft," Report No. UILU-ENG-74-2548, University of Illinois, January 1974.
- [11] Chuang, C.A., C.S. Liang, and S.W. Lee, "High Frequency Scattering from an Open Ended Semi-Infinite Cylinder," IEEE Trans. Antennas and Porpagation, Vol. AP-23, No. 6, November 1975, pp. 770-776.

- [12] Johnson, T.W., and D.L. Moffatt, "Electromagnetic Scattering by Open Circular Waveguides," Report No. 710816-9, The Ohio State University Electroscience Laboratory, Department of Electrical Engineering, prepared under contract No. NOO014-78-C-0049 for Department of Navy, Office of Naval Research. Also a dissertation to the Ohio State University, December 1980.
- [13] Witt, H.R. and E.L. Price, "Scattering from Hollow Conducting Cylinders," Proc. IEE (London), Vol. 115, No. 1, January 1968, pp. 94-99.
- [14] Moll, J.W. and R.G. Seecamp, "Calculation of Radar Reflecting Properties of Jet Engine Intakes Using a Waveguide Model," IEFE Trans. Aero. Elec. Sys., Vol. AES-6, No. 5, September 1970, pp. 675-683.
- [15] Kao, C.C., "Electromagnetic Scattering from a Finite Tubular Cylinder: Numerical Solutions," Radio Science, Vol. 5, No. 3, 1970, pp. 617-624.
- [16] Pace, J. and R. Mittra, "Generalized Scattering Matrix Analysis of Waveguide Discontinuity Problems," Quasi-Optics, Vol. XIV, pp. 177-197, Polytechnic Institute of Brooklyn Press, New York, 1964.
- [17] Mittra, R. and S.W. Lee, Analytic Techniques in the Theory of Guided Waves, MacMillan Company, New York, 1971.
- [18] Narasimhan, M.S., "A GTD Analysis of the Radiation Patterns of Open-Ended Circular Cylindrical Waveguide Horns," IEEE Trans. Ant. Prop., Vol. AP-27, No. 3, May 1979, pp. 438-441.
- [19] Felsen, L.B. and H.Y. Yee, "Ray Method for Sound-Wave Reflection in an Open-Ended Circular Pipe," The Journal of the Acoustical Society of America, Vol. 44, No. 4, 1968, pp. 1028-1039.
- [20] Collin, R.E., Foundations for Microwave Engineering, McGraw-Hill Book Co., New York, 1966.
- [21] Keller, J.B., "Geometrical Theory of Diffraction," J. Opt. Soc. Amer., Vol. 52, 1962, pp. 116-130.
- [22] Ryan, C.L., and L. Peters, Jr., "Evaluation of Edge-Diffracted Fields Including Equivalent Currents for the Caustic Regions," IEEE Trans. Antennas and Propagation, Vol. AP-17, No. 3, May 1969, pp. 292-299.
- [23] Knott, E.F. and T.B.A. Senior, "Comparison of Three High-Frequency Diffraction Techniques," IEEE Proc., Vol. 62, 1969, pp. 1468-1474.

- [24] Ufimtsev, P. Ya. "Method of Edge Waves in the Physical Theory of Diffraction," Translation prepared by the U.S. Air Force Foreign Technology Division, Wright-Patterson AFB, Ohio; released for public distribution Sept. 7, 1971.
- [25] Silver, S. (Ed.), Microwave Antenna Theory and Design, MIT Radiation Lab Series, re-published by Boston Technical Publishers, Lexington, Mass. 1964.
- [26] Sommerfeld, A., "Mathematische Theorie der Diffraktion," Math. Ann., Vol. 47, pp. 317-374, 1896.
- [27] Kouyoumjian, R.G., W.D. Burnside, and P.H. Pathak, A Uniform GTD for the Diffraction by Edges, Vertices, adn convex Surfaces, Book Chapter in Theoretical Methods for Determining the Interaction of Electromagnetic Waves with Structures, edited by J.K. Skwirzynski, and published by Sijthoff and Noordhoff, Netherlands, 1981.
- [28] Pathak, P.H., "A GTD Analysis of the Radiation from Slots in Planar and Cylindrical Perfectly-Conducting Structures with a Surface Impedance Patch," Report No. 4396-2, The Ohio State University Electroscience Laboratory, Department of Electrical Engineering, February 1977.
- [29] Sartwell, T. of Wright Patterson Air Force Base, private communication.
- [30] Chuang, C.W. and A.A. Ksienski, "Backscatter of a Large Rotating Conducting Cylinder with Arbitrary Cross Section," Report No. 78315-4, February 1978, Electroscience Laboratory, The Ohio State University.
- [31] Mikulski, J.J., "The Scattering Matrix, Polarization, Power and Periodic Bodies from the Viewpoint of Matrix Theory," Group Report No. 47-48, March 1960, MIT Lincoln Laboratory.
- [32] Kennaugh, E.M., "Effects of Type of Polarization on Echo Characteristics," Quarterly Progress Report No. 389-13, March 1962, ElectroScience Laboratory, The Ohio State University.
- [33] Borison, S.L., "Diagonal Representation of the Radar Scattering Matrix for an Axially Symmetric Body," IEEE Trans. Antennas and Propagation, Vol. AP-13, 1965.
- [34] Chuang, C.W., Pathak, P.H. and C.C. Huang, "On Wave Modulation by a Rotating Object," IEEE Transaction on Antennas and Propagation, Vol. AP-30, No. 3, May 1982.
- [35] Chuang, C.W., The Ohio State University, private communication.

- [36] Volakis, J.L., "Electromagnetic Scattering from Inlets and Plates Mounted on Arbitrary Smooth Surfaces," Ph.D. dissertation, The Ohio State University ElectroScience Laboratory, Department of Electrical Engineering, August 1982.
- [37] Cerrillo, Manuel, <u>Transient Phenomena in Waveguides</u>, Technical Report #33, MIT Research Laboratory of Electronics, Cambridge, MA, DDC #ATI-28023, 1948.
- [38] Chuang, C.W. and D.L. Moffatt, "Natural Resonances via Prony's Method and Target Discrimination,"
  IEEE Trans. Aerosp. Electron Syst., Vol. AES, 1976.
- [39] Chuang, C.A., C.S. Liang, and Shung-Wu Lee, "Correction to 'High Frequency Scattering from an Open-Ended Semi-Infinite Cylinder'," IEEE Trans. Antennas Propag., AP-28(6), pp. 949-950, 1980.
- [40] Guillemin, Ernest Adolph, The Mathematics of Circuit Analysis, 1949, John Wiley and Sons, Inc.
- [41] Johnson, T.W. and D.L. Moffatt, "Electromagnetic Scattering by Open Circular Waveguides," submitted for publication in Radio Science, 1981.
- [42] Kennaugh, E.M. and R.L. Cosgriff, "The Use of Impulse Response in Electromagnetic Scattering Problems," IRE National Convention Record Part 1, 1958.
- [43] Kennaugh, E.M. and D.L. Moffatt, "Transient and Impulse Response Approximation," <u>Proceedings of the IEEE</u>, Vol. 53(8), 1965.
- [44] Kennaugh, E.M., "The K-Pulse Concept," IEEE Trans. Antennas and Propag., Vol. AP-29(2), 1981.
- [45] Mithouard, Didien P. and Daniel B. Hodge, "Electromagnetic Scattering by a Metallic Disk," The Ohio State University ElectroScience Laboratory, Department of Electrical Engineering; prepared under Contract No. NO0014-76-A-0039 for the Department of the Navy, Office of Naval Research, 800 N. Quincy Street, Arlington, Virginia, Report No. 810816, 1979.
- [46] Moffatt, David L., "Interpretation and Application of Transient and Impulse Response Approximations in Electromagnetic Scattering Problems," Scientific Report No. 1, AFCRL, Office of Aerospace Research, USAF, Bedford, MA, DDC #AD-668 124, pp. 186-211, 1968.
- [47] Moffatt, D.L. and R.K. Mains, "Detection and Discrimination of Radar Targets," IEEE Trans. Antennas Propagation, Vol. AP-23, pp. 358-367, 1975.

- [48] Moffatt, D.L. and C.M. Rhoads, "Radar Identification of Naval Vessels," IEEE Trans. Aerospace Electronic Systems, Vol. AES-18, No. 2, March 1982.
- [49] Moffatt, D.L., J.D. Young, A.A. Ksienski, H.C. Lin and C.M. Rhoads, "Transient Response Characteristics in Identification and Imaging," IEEE Trans. Antennas Propag., AP-29(2), pp. 192-205, 1981.
- [50] Pathak, P.H. and C.C. Huang, "Analysis of EM Backscatter from a Jet Intake Configuration," The Ohio State University ElectroScience Laboratory, Department of Electrical Engineering; prepared under Contract No. F19628-80-C-0056 for the Department of the Air Force, Electronic Systems Division, Hanscom AFB, Massachusetts, Report No. 712661, 1981.
- [51] Singaraju, B.K., D.V. Giri and Carl E. Baum, "Further Developments in the Application of Contour Integration to the Evaluation of the Zeros of Analytic Functions and Relevant Computer Programs," Math-ematics Notes, Note 42, March 1976, Air Force Weapons Laboratory.
- [52] Skolnik, Merrill I., <u>Introduction to Radar Systems</u>, McGraw-Hill, 1980.
- [53] Moffatt, D.L., "Impulse Response Waveforms of a Perfectly Conducting Right Circular Cylinder", Proc. IEEE, Vol. 57, No. 5, pp. 816-817, May 1969.

. Ata

<sup></sup>COLCOLCOLCOLCOLCOLCOLCOLCOLCOLCOLCO

## MISSION of

Rome Air Development Center

RADC plans and executes research, development, test and selected acquisition programs in support of Command, Control Communications and Intelligence  $\{C^3I\}$  activities. Technical and engineering support within areas of technical competence is provided to ESN Program Offices  $\{POs\}$  and other ESD elements. The principal technical mission areas are communications, electromagnetic guidance and control, surveillance of ground and aerospace objects, intelligence data collection and handling, information system technology, ionospheric propagation, solid state sciences, microwave physics and electronic reliability, maintainability and compatibility.

とめことめことかことかことかことかことかことかことかっとかっとかっとかっことかっ

Printed by United States Air Force Houseom AFB, Moss, 01731